学位論文

Mass Distribution of Primordial Stars: Various Paths of Star Formation in the Early Universe

(始原星の質量分布: 宇宙初期における星形成の多様性)

平成 26 年 12 月　博士(理学)申請

東京大学大学院理学系研究科
天文学専攻

平野 信吾

Doctoral Dissertation

Mass Distribution of Primordial Stars: Various Paths of Star Formation in the Early Universe

Shingo Hirano

Department of Astronomy, Graduate School of Science
The University of Tokyo

December, 2014

Abstract

This thesis presents theoretical study on various formation paths of the first-generation stars and the distribution of their final masses. A series of numerical simulations from the formation of star-forming cloud to the end of the mass accretion onto the protostar are performed to determine the initial stellar mass. The simulation results show a certain dependence of the stellar masses on the initial state of star-forming clouds. By using such a correlation, a large sample of primordial star-forming clouds in the cosmological volume is converted to the mass distribution of the primordial stars. This is the first study to directly calculate the stellar mass distribution in the early universe theoretically.

Primordial stars, so-called Population III stars, play vital roles in the early cosmic evolution by initiating cosmic reionization and chemical enrichment of the intergalactic medium. The stellar evolution and death, which regulate the dynamical, radiative, and chemical feedbacks to the surrounding medium, are largely determined by its stellar mass (e.g., Heger & Woosley, 2002). The characteristic mass of Pop III stars and the initial mass function are thus essential to understand the formation and evolution of the first galaxy (e.g., Bromm & Yoshida, 2011).

The star formation process involves various different physics and it is highly complicated. Theorists have performed numerical simulations to reveal the nature of Pop III stars (e.g., Abel *et al.*, 2002; Yoshida *et al.*, 2008; Clark *et al.*, 2011b). Recent simulations (Hosokawa *et al.*, 2011; Stacy *et al.*, 2012a; Susa, 2013) show that the stellar mass is determined when the mass accretion onto the protostar ceases with the stellar UV radiative feedback (McKee & Tan, 2008). They, however, calculate only a limited number of cases, in the other words, the calculated case is not necessarily the standard case of primordial star-formation. In general, the star formation greatly depends on the initial state of a natal cloud. The evolution of an accreting protostar can differ with different accretion histories resulting from different initial states. The stellar UV luminosity depends on the protostellar evolution, so that the different accretion histories affect the strengths of radiative feedback and also the final masses. Thus such studies cannot mention about the characteristic mass of Pop III stars and their overall mass distribution.

The goal of this thesis is to directly calculate the primordial mass distribution. First, 110 formation processes of Pop III.1 stars (so-called fist stars which are unaffected by any external feedback) are calculated in a fully cosmological context to study the dependences of primordial star formation on different accretion histories. There is a great diversity

of accretion histories among primordial star-forming clouds. With more rapid accretion, the UV radiative feedback which can prevent the mass accretion becomes less efficient and the protostar can grow in mass further more. The final result shows a wide scatter of stellar masses, $M_* = 10 \sim 1000\ M_\odot$. Interestingly, the calculated stellar masses show good correlations with the physical properties of star-forming clouds. Such correlations are useful because one can estimate the stellar mass using the initial state of a natal cloud without following the long-term evolution from the cloud's collapse to the protostellar evolution.

The above study is not sufficient yet to mention about the mass distribution of primordial stars. This is because primordial stars should have several sub-populations, so-called Pop III.2 stars, which form within clouds whose chemical compositions are affected by the external radiation background. Several studies show that they have different typical masses compared with Pop III.1 cases (Yoshida *et al.*, 2007; O'Shea & Norman, 2008; Hosokawa *et al.*, 2012b). This thesis studies the star-formation processes with primordial clouds affected by the photodissociating far-ultraviolet radiation, Pop III.$2_{\rm D}$ cases. A series of simulation of primordial star-formation is performed to investigate the dependence of stellar masses on the strengths of the photodissociating radiation. The calculations show that the external radiation overall increases the final stellar masses though their dependence is not simple with some exceptional cases. Pop III.$2_{\rm D}$ cases, however, also have the same dependence of stellar masses on the natal cloud's property as for Pop III.1 stars. The Pop III.$2_{\rm D}$ stellar masses also correlate with the local FUV intensity J_{21}.

To construct the mass distribution of primordial stars, one has to construct a non-biased, sufficiently large, cosmological sample. Finally, a cosmologically non-biased sample of 1540 primordial star-forming clouds is constructed and classified into two sub-populations, Pop III.1 and III.$2_{\rm D}$ cases. The stellar masses for each halo are determined by considering the physical properties of the cloud for Pop III.1 cases and intensity of the local FUV radiation field for Pop III.$2_{\rm D}$ cases. At high redshifts, about half of the clouds are exposed by intense photodissociating radiation and give birth to Pop III.$2_{\rm D}$ stars. These stars have a characteristic mass around a few hundred solar masses at $z \sim 25$, which gradually shifts to lower masses with decreasing redshifts. The relative fraction of Pop III.$2_{\rm D}$ stars becomes smaller at the lower redshifts. In such an epoch, the FUV radiation field is weaker because the typical Pop III stellar mass is lower and the mean separation between stars is larger owing to the cosmic expansion. At $z < 15$, most of the clouds host Pop III.1 stars and about half of them are formed via enhanced radiative cooling of H_2 and HD molecules, having masses of several tens of solar masses.

The past studies have discussed about *how massive a primordial star is*. This thesis shows that the primordial stars have a wide mass distribution reflecting the diversity of the initial states of star-forming clouds. Both low-mass and massive primordial stars should form with a finite probability. Moreover, it is also found that the presence of typical stellar mass which decreases with decreasing redshift. These suggestions are based on the diversity of initial cloud's states and independent with the uncertainty of primordial star-formation.

Contents

Abstract **i**

Contents v

List of Figures xv

List of Tables xviii

1 Introduction **1**
1.1 Primordial Star . . . 1
1.2 Standard Model of Primordial Star Formation . . . 2
1.2.1 Dark Matter Minihalo . . . 3
1.2.2 Primordial Star-Forming Gas Cloud . . . 6
1.2.3 Early Collapse Phase . . . 7
1.2.4 Later Accretion Phase . . . 9
1.2.5 Evolution of Accreting Protostar . . . 10
1.3 Nature of Primordial Stars . . . 13
1.3.1 Stellar Evolution and Final Fates . . . 13
1.3.2 Observational Clues . . . 14
1.3.3 Primordial Initial Mass Function . . . 16
1.4 Aims . . . 16
1.5 Structure of This Thesis . . . 19

2 Mass Diversity of Primordial Stars and its Origins **21**
2.1 Overview . . . 21
2.2 Population III.1 Stars . . . 21
2.2.1 Method . . . 22
2.2.2 Early Collapse Stage . . . 26
2.2.3 Later Accretion Stage . . . 31
2.2.4 Wide Range of Stellar Masses . . . 36
2.2.5 Discussions . . . 44
2.3 Population III.2$_{\mathbf{D}}$ Stars . . . 48
2.3.1 Method . . . 49
2.3.2 Results . . . 51
2.3.3 General Properties . . . 53

2.3.4 Individual Cases . . . 55
2.3.5 Mass Estimating Formula . . . 58
2.4 Summary . . . 59

3 Cosmological Sample of Primordial Gas Clouds 62
3.1 Overview . . . 62
3.2 Method . . . 64
3.3 Results . . . 66
3.3.1 Virial Scale: Dark Matter Minihalos . . . 67
3.3.2 Jeans Scale: Gravitationally Unstable Clouds . . . 69
3.3.3 Distribution of Gas Infall Rates . . . 72
3.3.4 Estimating Pop III.1 Stellar Masses . . . 73
3.4 Discussion . . . 76

4 Mass Distribution of Primordial Stars 78
4.1 Overview . . . 78
4.2 Method . . . 79
4.3 Results . . . 81
4.3.1 Classification into Population III.1 and III.$2_{\rm D}$ Stars . . . 81
4.3.2 Stellar Mass Distribution . . . 82
4.3.3 Star Formation Rate Density . . . 84
4.4 Discussion . . . 85
4.4.1 The Final Fate of Primordial Stars . . . 85
4.4.2 Uncertainty in the Number Fraction of Pop III.2 Stars . . . 86
4.4.3 Alternative Formulae for Mass Estimation . . . 90

5 Conclusions 92
5.1 Summary . . . 92
5.2 Future Prospects . . . 95

A Cosmological Simulation 98
A.1 *N*-body Dynamics . . . 98
A.2 Smoothed Particle Hydrodynamics . . . 99
A.3 Primordial Chemistry . . . 100
A.3.1 Chemical Reaction Rates . . . 100
A.3.2 Updated Rates for H_2- and HD-Cooling . . . 106
A.3.3 H_2 and HD Self-Shielding . . . 107
A.4 Numerical Resolution . . . 107
A.4.1 Hierarchical Zoom-In . . . 108
A.4.2 Particle Splitting . . . 108

B Simulation of Accreting Protostar 110
B.1 Radiation Hydrodynamics . . . 110
B.1.1 Angular Momentum Transport in the Accretion Disk . . . 111

B.2 Protostellar Evolution 112
B.2.1 Oscillating Protostar (P2) 113
B.2.2 Super-Giant Protostar (P3) 114

C Thermal Evolution Depending on the Collapsing time-scale 118

D 110 Population III.1 Stars 122

E Remaining Pop III.2$_{\mathrm{D}}$ Cases 126

Acknowledgments 130

Bibliography 132

List of Figures

1.1 Fractional abundances of primordial chemical species as a function of redshift. The calculated is performed by the same chemical network with the cosmological simulation. 5

1.2 Evolution of the accreting protostar's radius for three constant accretion rates $\dot{M} = 1\times10^{-3}$, 6×10^{-3}, and 6×10^{-2} $M_\odot$ yr^{-1} (taken from Hosokawa *et al.*, 2012a). The dotted and dashed lines represent the mass-radius relations for super-giant protostars (Eq. 1.26) and ZAMS stars. 11

1.3 Various paths during the primordial star formation which is considered in this thesis. The star formation process is divided into three different phases; a) formation of star-forming gas cloud, b) thermal evolution of collapsing cloud, and c) evolution of accreting protostar. The top three panels represent pictures of corresponding simulations. The below squares represent each path and the arrows between paths reveal the evolutionary connections. The paths enclosed by red squares and the red arrows represent the newly found paths and links in this thesis. The detail explanations for each path are found in the text. 17

2.1 Projected density distribution at $z = 25$ in one of the cosmological simulations. There are five primordial star-forming clouds in a cube of 15 kpc on a side. The small figures show the zoom-in to the central 1 pc region of the clouds at the respective formation epoch. The masses of the Population III.1 stars formed in these clouds are 60, 76, 125, 303, and 343 $M_\odot$, respectively. 22

2.2 Distributions of dark matter minihalos that host primordial star-forming clouds as a function of the formation redshift at $n_{\rm H,cen} = 10^6$ cm^{-3}. The bin width is $\Delta = 1$ and the different colors indicate the different ranges of the virial masses: $M_{\rm vir}/{\rm M}_\odot < 10^{5.4}$, $10^{5.4} < M_{\rm vir}/M_\odot < 10^{5.6}$, $10^{5.6} < M_{\rm vir}/M_\odot < 10^{5.8}$, $10^{5.8} < M_{\rm vir}/M_\odot < 10^{6.0}$, and $10^{6.0} < M_{\rm vir}/M_\odot$. The black line shows the sums over all virial masses. The redshifts and virial masses are measured when $n_{\rm H,cen} = 10^7$ cm^{-3}. 26

2.3 Radial gas density profiles for nine selected star-forming clouds. The colors indicate the different stellar evolutionary paths P1 (4 black lines), P2 (3 blue), and P3 (2 red). For one P1 case it is also plotted the time evolution of the density profile at the time when the central density is 10^4, 10^6, 10^8, 10^{10}, and 10^{12} cm^{-3}. For all other clouds, snapshots at $n_{\rm H,cen} \simeq 10^{12}$ cm^{-3} are used. The dashed line shows an averaged DM density profile for 110 cases. The dotted line shows a power-law density distribution with $n_{\rm H} \propto r^{-2.2}$ for reference. 27

2.4 Averaged profiles of primordial star-forming clouds as a function of gas number density, $n_{\rm H}$, for the same nine clouds in Figure 2.3: (a) gas temperature, (b) H_2 fraction, and (c) HD fraction which are the mass-weighted mean values of the SPH (gas) particles for each density bin when the central (highest) density is $n_{\rm H,cen} = 10^{12}$ cm^{-3}. The dashed lines in panel (a) show the $n_{\rm H} - T$ relation for the given Jeans masses $M_{\rm Jeans} \propto T^{3/2}/n_{\rm H}^{1/2}$. The dashed line in panel (d) shows the critical value $f_{\rm HD}/f_{\rm H_2} = 10^{-3}$ above which the HD cooling becomes efficient to cool the primordial cloud further more. 28

2.5 Averaged profiles of the degree of rotational support, $f_{\rm Kepler} = v_{\rm rot}/v_{\rm Kepler}$, for the same nine clouds in Figure 2.3at the moment when $n_{\rm H,cen} = 10^{12}$ cm^{-3}. The lowest line represents the case for which the cloud is most slowly rotating in the sample (see Fig. 2.15a and Table 2.3). Generally, $f_{\rm Kepler}$ is large for P1, P2, and P3 in this order. 30

2.6 Projected gas density distributions for three representative cases at the moment when $n_{\rm H,cen} = 10^{12}$ cm^{-3} whereby the protostars go through three characteristic evolutionary paths (P1, P2, and P3 from left to right) in the later accretion phase. The panels show the gas distribution in regions of 500, 1, and 0.01 pc on a side, respectively and both the face-on and edge-on views are shown for the last two. Note the rotationally supported disk-like structure for the P1 case. 31

2.7 Accretion rates (panel a) and stellar radii (b) as a function of stellar mass for the entire sample. The colors represent the different paths of the protostellar evolution as in Figure 2.3. The two horizontal lines in panel (a) are critical values of accretion rates $\dot{M}_{\rm P2} = 0.004\ M_\odot$ yr^{-1} (dashed; Eq. 1.24) and $\dot{M}_{\rm P3} = 0.04\ M_\odot$ yr^{-1} (dotted; Eq. 1.25) . The two diagonal lines in panel (b) indicate $260 \times M^{0.5}\ R_\odot$ (dotted; super-giant protostar, Eq. 1.26) and $0.31 \times M^{0.58}\ R_\odot$ (dashed; ZAMS track derived from the calculation). 32

2.8 Averaged radial distribution for 110 cases of (a) the gas infall rate $\dot{M}_{\rm cloud} = 4\pi r^2 \rho(r) v_{\rm rad}(r)$, (b) the density, and (c) infall velocity profiles when $n_{\rm H,cen} = 10^{12}$ cm^{-3}. The colors represent the three paths of the protostellar evolution as in Figure 2.3. 33

2.9 Three representative cases of the protostellar evolution as a function of the stellar mass: (a) accretion rates, (b) stellar radius, (c) surface temperature, and (d) ionized photon intensity. In panel (a), the solid and dashed lines represent the evolution with and without UV radiative feedback from the accreting protostar. The dashed and dotted lines in the panels (a) and (b) are the same as in Figure 2.7. Two horizontal lines in panel (c) indicate $T_{\rm eff} = 10^5$ K (dotted) and 5000 K (dashed). The filled circle marks the epoch when a bipolar H II region first appears in each case with UV radiative feedback. 35

2.10 Expanding H II regions around the primordial protostar from top to bottom panels for the same three cases as in Figure 2.9. The plotted regions are cubes with 60000 AU on a side. The colors indicate gas temperature and the contours show the density structure. The main accretion takes place through the accretion disk on the equatorial plane. As the central protostar becomes more massive and the surface temperature increases, the ionizing photon production of the central star increases. H II regions are launched into the polar direction and the opening angles grow with time, eventually stopping the accretion. 36

2.11 Final distribution of the calculated stellar masses for 110 Population III.1 cases. Histograms' colors represent the different paths of protostellar evolution; KH contracting protostar (P1; black), oscillating protostar (P2; blue), and super-giant protostar (P3; red). P1 cases are classified into two populations according to whether the HD cooling is inefficient, P1(H_2), or efficient, P1(HD). $P3_{\rm pred}$ indicates the same cases as P3, except that the final masses are calculated from a correlation between the properties of the cloud and the resulting stellar mass (Eq. 2.1; see Appendix B.2.2). 37

2.12 Final stellar masses as a function of gas infall rates over Jeans scales (left panels) or virial scales (right) at $n_{\rm H,cen} = 10^7$ cm^{-3}. Three colors represent the evolutionary paths of the protostellar evolution. The dotted lines in panels (a) and (b) represent the fitting functions given by Eqs. (2.1) and (2.2). The panel (b) shows the ratio of the calculated stellar mass to the estimated one by the fitting formula (Eq. 2.1). 39

2.13 Dependences of final stellar masses on two properties at the Jeans and virial scales; the cloud mass and the rotation parameter $\beta_{\rm Jeans}$ at the Jeans scale (panel a) and the formation redshift and the halo mass (c), for each of the sample of 110 clouds. The different colors are indicative of the final stellar masses (see color scale at the top). The dotted lines represent the fitting functions given by Eq. (2.4) for $M_{\rm III} = 10$, 32, 100, 320, and 1000 $M_\odot$. The panels (b) and (d) show ratios of estimated masses by Eqs. (2.4) and (2.6) to final stellar masses. 41

2.14 Virial temperature for all the calculated cases shown in this thesis when $n_{\rm H,cen} \sim 10^7$ cm^{-3} as a function of the formation redshift. The circles and triangles correspond to H_2- and HD-cooling clouds, respectively. . . 43
2.15 Projected gas density distributions when the central density reaches 10^{12} cm^{-3} for two extreme cases: the most rapidly (*top*) and the most slowly (*bottom*) rotating clouds. Table 2.3summarizes the physical properties of theses clouds. 45
2.16 Projected gas density distributions for six clouds which have multiple density peaks when the central density reaches 10^{12} cm^{-3}. Table 2.4summarizes the clump properties 47
2.17 Accretion histories of mass accreting protostars, which from the same cloud (ID = 4 in Table 2.5) but with different FUV intensities $J_{21} = 0$, 0.1, 1, and 10, as a function of the stellar mass. When the mass accretion rates fall below 10^{-4} $M_\odot$ yr^{-1}, the simulations stop and the masses at this moment are considered as the final stellar masses, 50, 61, 883, and 496 $M_\odot$, respectively. 49
2.18 Final stellar masses obtained in 2D RHD simulations as a function of the gas infall rate measured at the Jeans scale when $n_{\rm H,cen} = 10^7$ cm^{-3}. The open circles represent 16 cases with $J_{21} > 0$ (Pop III.2$_{\rm D}$ stars; red) and 5 cases with $J_{21} = 0$ (Pop III.1 stars; blue), in which the 2D RHD simulations successfully follow the evolution until the final stellar masses are fixed. The crosses depict the results for Pop III.1 stars obtained for the same central density (Fig. 2.12). The dotted line shows the fitting formula for Population III stars (Eq. 2.1). 52
2.19 Physical properties of collapsing clouds with different FUV intensity J_{21} for the different cases ID = 4 (left), 8 (center), and 9 (right) listed in Table 2.5. Line colors in each panel represent the different FUV intensity $J_{21} = 0$, 0.1, 0.316, 1, and 10 from black to yellow. The three rows show the evolution of the gas temperature (panels a), chemical abundances (b), and the ratio between the collapsing time and free-fall time $f_{\rm collapse} = t/t_{\rm ff}$ (c; the same definition in appendix C) measured at the cloud center. The dotted lines in panel (a) show the Jeans scale as a function of the gas density and temperature. In the panels (b), the solid and dotted lines represent the number fraction of H_2 molecules $f_{\rm H_2}$ and the fractional abundance of HD molecules $f_{\rm HD}/f_{\rm H_2}$. 53
2.20 Different physical properties of collapsing clouds for the same cases in Figure 2.19. The three rows show the radial profiles of the gas infall rate (a), number density (b), and radial velocity (c) as functions of the enclosed mass for $n_{\rm H,cen} = 10^{11}$ cm^{-3}. The dotted lines in panels (a) show the mass accretion histories seen in the 2D RHD simulations following the evolution after the birth of protostars. Note that the horizontal axis represents the protostellar mass for these cases. 54

2.21 Density (color and line contours) and velocity (arrows) distributions around the collapsing center when $n_{\rm H,cen} = 10^{11}$ cm^{-3} for the same cases as in Figure 2.19. The box size is 0.1 pc on a side. The top and bottom panels show the slices through the X-Y and X-Z planes, whereby the Z-axis corresponds to the rotational axis. There is a blank panel for ID = 8 with $J_{21} = 10$, because the collapse is prevented by the photodissociating radiation in this case. 56

2.22 Stellar masses for the Pop III.2$_{\rm D}$ cases with different FUV intensity J_{21}. The left panel shows the stellar mass of Pop III.2$_{\rm D}$ cases $M_{\rm III.2_D}$ ($J_{21} > 0$) plotted versus Pop III.1 cases $M_{\rm III.1}$ ($J_{21} = 0$), whose different values represent different gas clouds (for ID = $1 \sim 9$ from left to right). The filled symbols indicate the stellar masses determined by 2D RHD simulations. The values marked with the open symbols, on the other hand, are calculated using the analytic formula (Eq. 2.1). The solid line represents the equal mass boundary $M_{\rm III.1} = M_{\rm III.2_D}$. The dotted lines show the fitting functions which follow the dependence of $M_{\rm III.2_D}$ on J_{21}. The right panel shows the correlation of $M_{\rm III.2_D}$ with J_{21}. The symbols with error bars depict the averaged masses and variances of the same J_{21} cases. The stellar masses for cases without 2D RHD simulations are given by the estimated values. The line shows the simplified relation $M_{\rm III.2_D}$ as a function of J_{21} (Eq. 2.10; $M_{\rm III.2_D}$ = 100, 300, 500, and 400 M$_\odot$ for J_{21} = 0.1, 0.316, 1, and 10), which is used for evaluating Pop III.2$_{\rm D}$ stellar masses. 58

3.1 Schematic view of the cosmological simulation to obtain the non-biased sample of primordial star-forming clouds. The color contour reveals the projected density level of dark matter which increase from blue to yellow. In a parent simulation (the background panel), 55 zoomed initial conditions are generated which cover each cradle region (the red circle shows one of them). Finally 1540 star-forming clouds are obtained from zoom-in simulations (a part of them is shown as white circles in the foreground panel) and their formation and evolution are followed. 63

3.2 Mass function of dark matter halos. The crosses show the result of the parent simulation at $z = 9$ which is constructed by performing the Friend-Of-Friend (FOF) halo finder with linking length $b = 0.2$ and counting halos containing more than 50 N-body particles. The solid lines show the analytically calculated model function, Press-Schechter mass function, at $z = 9$ (thick), 20, and 30 (thin) using the Reed *et al.* (2007) code. The dashed horizontal line represents the number density of 1 (3 h^{-1}Mpc)$^{-3}$, with which one halo should be found in the cosmological volume of the parent simulation. 64

3.3 Distributions of dark matter minihalos that host primordial star-forming clouds as functions of the formation redshift (panel a) or the virial mass (b). In the panel (a), the bin width is $\Delta z = 1$ and the different colors indicate the different ranges of the virial masses: $M_{\rm vir}/M_\odot < 10^{5.4}$, $10^{5.4} < M_{\rm vir}/M_\odot < 10^{5.6}$, $10^{5.6} < M_{\rm vir}/M_\odot < 10^{5.8}$, $10^{5.8} < M_{\rm vir}/M_\odot < 10^{6.0}$, and $10^{6.0} < M_{\rm vir}/M_\odot$. In the panel (b), the bin width is logarithmically equal, $\Delta M_{\rm vir}(M) = (10^{0.1} - 1) \times M$, and the different colors indicate the different ranges of the redshifts: $10 < z < 14$, $14 < z < 18$, $18 < z < 22$, $22 < z < 26$, and $26 < z < 30$. The black lines show the sums over all virial masses or redshifts. 66

3.4 Scatter plots and histograms of basic properties of the gas clouds on the virial scale. The left panels show, from top to bottom, spin parameters of dark matter, spin parameters of baryonic components, and the offset angles between angular momentum vectors of the two components. The right panels show their histograms; the colors represent the same redshift ranges as in the right panel of Figure 3.3. The circles and triangles correspond to H_2- and HD-cooling clouds, respectively. 68

3.5 Scatter plots of (a) the spin parameters of baryonic components and (b) the offset angles as a function of the spin parameters of dark matter components. The dashed lines show the equal relation $\lambda_{\rm DM} = \lambda_{\rm gas}$ in panel (a) and a given angle $\theta = 90^\circ$ in panel(b). 69

3.6 Averaged profiles of primordial star-forming clouds when $n_{\rm H,cen} = 10^7$ cm^{-3}; (a) gas temperature, (b) H_2 fraction and ratio of HD to H_2, (c) gas infall rate, and (d) Keplerian factor ($f_{\rm Kepler} = v_{\rm rot}/v_{\rm Kepler}$). In panel (b), the colored lines show averaged H_2 fractions for H_2-cooling cases at 5 redshift ranges. The grey region shows the maximum and minimum for all clouds at each radius. The colored lines show averaged profiles for H_2-cooling clouds at five redshift ranges and the black line shows the averaged profile for HD-cooling clouds. The dotted and dashed lines show averaged $f_{\rm HD}/f_{\rm H_2}$ for all HD-cooling and H_2-cooling cases, respectively. In panel (c), the dotted lines show the fitting functions for the averaged infall rates at the protostellar formation and are characterized by $\{0.34, 0.34, 0.23, 0.17, 0.14\} \times (M_{\rm enc}/M_\odot)^{-0.7}\ M_\odot$ yr^{-1} in order of higher- to lower-redshift groups. 70

3.7 Radial gas density profiles of primordial star-forming clouds when $n_{\rm H,cen} = 10^7$ cm^{-3} in the same manner as in Figure 3.6. The solid lines show the gas component and the dashed line shows the DM component. The dotted line shows the power-law slope, $n_{\rm H} \propto r^{-2.2}$ (e.g., Omukai & Nishi, 1998). 71

3.8 Histogram of the gas infall rates measured at the Jeans scale when $n_{\rm H,cen} = 10^7$ cm^{-3}. The lines with the different colors represent the different redshift ranges from high (red) to low redshift (blue). The top axis gives the stellar mass estimated from $\dot{M}_{\rm Jeans}$ by Eq. (2.1). 73

3.9 Variation of the gas infall rate at the virial scale as a function of formation redshift and virial mass. The different colors depict the different mass infall rates, according to the color scale at the top. The distributions of the filled circles and dotted lines represent the variation of the sample data and its fitting function Eq. (3.4). 74

3.10 Correlation between the gas infall rates at the virial scale $\dot{M}_{\rm vir}$ and at the Jeans scale $\dot{M}_{\rm Jeans}$ when $n_{\rm H,cen} = 10^7$ cm^{-3} for two samples; 1540 cases shown in this chapter and 110 cases shown in Section 2.2. The circles and triangles correspond to H_2- and HD-cooling clouds, respectively. The dotted and dashed lines show the fitting formulae for H_2- and HD-cooling cases (Eq. 3.5) 75

4.1 Time evolution of the FUV intensity field, J_{21}, in the same comoving cosmological volume with (3 h^{-1}Mpc)^3 at z = 25, 20, 19.5, 19, and 15. The color contours indicate the FUV intensity ranging from $J_{21} = 0.025$ to 6.3 (blue to red). The yellow and red clumps show the active Pop III.1 and III.2$_{\rm D}$ stars, respectively. The FUV radiation field decreases with decreasing redshift, because the typical stellar mass becomes lower and separations between the stars are stretched by the cosmic expansion. . . 79

4.2 Histogram of the normalized intensity of photodissociating radiation J_{21} at the position of each primordial cloud when $n_{\rm H,cen} = 10$ cm^{-3}. The different colors depict the same redshift ranges as in the right panel of Figure 3.3. The dotted vertical line represents the critical value of $J_{21} = 0.1$, above which (right side) Pop III.2$_{\rm D}$ stars form. The halos with $J_{21} > 10$ and $J_{21} < 10^{-3}$ are included in the rightmost and leftmost bins, respectively. 82

4.3 Resultant mass distributions of Pop III.1 (left) and III.2$_{\rm D}$ (right) stars for the different redshifts. The different colors represent the same redshift ranges as in the right panel of Figure 3.3. The black solid lines show the total distributions over all redshifts for each population whereas the dotted lines show the sum of them. 83

4.4 Redshift evolution of star formation rate densities (SFRD) of Population III.1 and III.2$_{\rm D}$ stars (panel a) and the averaged J_{21} for clouds with its variance (b). In panel (a), the dotted line represents the total of them. In panel (b), the gray dots show the scatter of J_{21} at each cloud and the dotted line represents the critical value of $J_{21} = 0.1$, above which Pop III.2$_{\rm D}$ stars form. 84

4.5 Resultant mass distribution of Population III.1 (blue line) and III.2$_{\rm D}$ (red) stars but calculated by decreasing the estimated stellar masses obtained from Eq. (2.1) by factors of 0.5 (panel a) and 0.2 (b). 87

4.6 Number distribution of clouds which have the nearby density peak within a physical 1 kpc from their own density centers. The solid line shows the total number of clouds which have the nearby peaks within the corresponding radius. 88
4.7 Accretion rates at (a) the Jeans scale and (b) the virial scale are plotted against the spin parameter of the parent dark matter halo to demonstrate the degree of correlation between the two quantities. The circles and triangles correspond to H_2- and HD-cooling clouds, respectively. 88
4.8 Comparison the resultant stellar mass with the calculation result of Susa *et al.* (2014). Panel (a) plots the 110 final stellar masses as a function of the spin parameter at the Jeans scale when $n_{\rm H,cen} = 10^7$ cm^{-3}. The dotted line is the fitting function shown in Susa *et al.* (2014), $M_{\rm prim} \sim 14\ \lambda_{\rm Jeans}^{-0.7}\ M_\odot$. Panel (b) shows the mass distribution of the primary star estimated by the alternative formula depending on the spin parameter. 91

5.1 Good correlation between the early states of gravitationally unstable star-forming cloud and the final stellar masses for both Pop III.1 and III.$2_{\rm D}$ cases. 93
5.2 Resultant mass distribution of primordial stars which are classified into Pop III.1 and III.$2_{\rm D}$ cases. The dotted line shows the sum of the two populations. 94
5.3 Various paths during the primordial star formation which is the similar with Figure 1.3. The blue dotted squares and arrows represent the ignored evolutionary paths in this thesis. 96

A.1 Various reaction rates for the three-body H_2 formation (Eq. 1.14; left panel) and variety of the thermal evolution of collapsing clouds depending on the rates (right). 101
A.2 Cooling rates of H_2 (panel a) and HD (b) molecules as a function of temperature at different densities. The lines show the updated functions used in this thesis whereas the dots are the previously used functions (e.g., Yoshida *et al.*, 2006). There is only a bit modification. 106

B.1 Evolution of the minimum Toomre Q-parameter as a function of the stellar mass for the same cases as in Figure 2.3. $Q_{\rm min}$ is close to unity, which is generally expected for a self-gravitating circumstellar disk, in almost all the cases. Only one case, for which the cloud rotation is the slowest of the entire sample, shows a very large $Q_{\rm min}$ (see discussion in text). 112
B.2 Evolution of the stellar radius (panel a) and effective temperature (b) as a function of the stellar mass. The solid lines show the numerical results for $\dot{M} = 6 \times 10^{-3}\ M_\odot$ yr^{-1} taken from Hosokawa *et al.* (2012a). The dotted and short-dashed lines are the same as in Figures 2.9(b) and (c). 114

C.1 Comparison of the thermal evolution during the cloud collapse between the simulation results (dashed lines and filled circles) and one-zone models (solid lines). The solid lines with the different colors represent the different collapse time-scales, $t_{\rm coll} = f \cdot t_{\rm ff}$, with f = 0.6, 1.0, 1.8, 3.2, 5.6, and 10, which is a parameter for one-zone modeling. The red, blue, and black dashed lines represent the same 3D simulation cases shown in Figure 2.10, whereas the green line is for the most rapidly rotating cloud shown in Figure 2.15. The black dashed lines in the top panel present $\rho - T$ relations for given values of the Jeans mass. 119

C.2 Correlation between the ratio $f = t/t_{\rm ff}$ of the averaged relative collapse time-scale to the free-fall time-scale and the final stellar masses in the numerical simulations. 120

D.1 Density maps of 110 dark matter with a physical 500 pc in a side. . . . 122

E.1 Same as Figures 2.19 and 2.20 for ID = 1, 2, and 3 cases. 127

E.2 Same as Figures 2.19 and 2.20 for ID = 5, 6, and 7 cases. 128

List of Tables

1.1 Cosmic age as a function of redshift calculated with the cosmological parameters in Tale 1.2. 2

1.2 Cosmological parameters obtained from table 5 in Planck Collaboration *et al.* (2014) used for a part of cosmological simulations in this thesis. . 3

1.3 Column 1: Paths of the protostellar evolution, and Column 2: Accretion rate for each path. The critical accretion rates are refereed in Omukai & Palla (2003) and Hosokawa *et al.* (2012a). 11

1.4 Column 1: Final fate of stellar evolution: neutron star (NS), low-mass black hole (LMBH), pulsational pair-instability supernovae (PPISN), pair-instability supernovae (PISN), and high-mass black hole (HMBH), Column 2: Stellar mass range at ZAMS for the non-rotating star, Column 3: Stellar mass range at ZAMS for the highly rotating star. The values is based on Yoon *et al.* (2012). 14

2.1 Parameters of cosmological initial conditions for calculations of Pop III.1 stars. Column 1: Number of star-forming clouds, Column 2: Simulation box size (comoving), Column 3: Gravitational softening length (comoving), Column 4: Mass of zoom-in N-body particle (dark matter), Column 5: Mass of zoom-in SPH particle (gas), and Column 6: Reference of the adopted cosmological parameters. 23

2.2 Column 1: Evolutionary paths of protostar, Column 2: Number of samples for each path, Column 3: Final stellar mass, Column 4: Redshift when the central density reaches 10^6 cm^{-3}, Column 5: Virial mass of dark matter minihalos, Column 6: Jeans mass of star-forming cloud, and Column 7: Ratio of the rotation to gravitational energy of the cloud. All quantities are the averaged amount for each evolutionary path. Appendix Dshows the list of original data. 37

2.3 Each column header has the same meaning as in Table 2.2. 45

2.4 Column 2: Distance between the primary star and the clump, Column 3: Enclosed mass within $R/2$, Column 4: Central density of the clump, Column 5: Estimated free-fall time, and Column 6: The final stellar mass of the primary star. 47

2.5 Column 1: Cloud's index, Columns $2-11$: Final stellar masses in the unit of $M_\odot$ for different FUV intensities: $J_{21} = 0$, 0.1, 0.316, 1, and 10. The masses are determined by two different methods: the 2D RHD simulations (left) and from the estimating formula (2.1; right). The underbars indicate the cases cooled by HD molecules during the run-away collapse stage. The crosses indicate the un-collapsed cases by photodissociating radiation. The dashes indicate the cases without final stellar masses calculated by 2D RHD simulations. 50

3.1 Each column shows the same parameter as Table 2.1for the final cosmological simulation. 62

4.1 Column 1: Final fate of stellar evolution: neutron star (NS), low-mass black hole (LMBH), pulsation pair-instability supernovae (PPISN), pair-instability supernovae (PISN), and high-mass black hole (HMBH), Column 2: Corresponding mass ranges at ZAMS for each fate from figure 12 in Yoon *et al.* (2012) for the non-rotating case, Column 3 to 12: Fractions of each fate in the sample for each redshift range, Column 13: Sum over each row. 85

A.1 Column 1: ID, Column 2: Chemical Reaction, Column 3: Rate coefficient and cross section, and Column 4: References; AAZN97 (Abel *et al.*, 1997), B77 (Barsuhn, 1977), C11(Coppola *et al.*, 2011b), C92 (Cen, 1992) F13 (Forrey, 2013a), FK94 (Fukugita & Kawasaki, 1994), GA08 (Glover & Abel, 2008), GP98 (Galli & Palla, 1998), HG97 (Hui & Gnedin, 1997) J72 (de Jong, 1972), PSS83 (Palla *et al.*, 1983), Sav02 (Savin, 2002), Sch08 (Schleicher *et al.*, 2008), SK87 (Shapiro & Kang, 1987), Sta98(Stancil *et al.*, 1998), TT02 (Trevisan & Tennyson, 2002), WS02 (Wang & Stancil, 2002), ... 105

D.1 Column 1: ID, Column 2: Formation redshift, Column 3: Virial mass of minihalo Columns 4 and 5: Spin parameters of DM and gas components, Column 6: Offset angle, Column 7: Gas infall rate at the virial scale, Column 8: Gravitationally unstable cloud mass, Column 9: Rotation parameter, Column 10: Gas infall rate at the Jeans scale, Column 11: Final stellar mass, and Column 12: Evolutionary path of the accreting protostar. 125

Chapter 1

Introduction

About 13.8 billion years ago, the Universe gives its first cry with the Big-Bang. Through the inflation, the Universe reaches the state of quark-gluon plasma. About the "first 3 minutes" later (Weinberg, 1977), the cosmic temperature drops with the cosmic expansion to become low enough to create the atomic nuclei. Such Big-Bang nucleosynthesis (BBN) generates the primordial chemical species which are constructed only with the hydrogen (H), helium (He), and a tiny amount of deuterium (D), lithium, and beryllium (Alpher *et al.*, 1948). After about 380,000 years from the cosmic birth, the photons decouple with the electrons because the electrons couple with the atomic nuclei due to the temperature drop and the Universe becomes transparent to radiation (so-called the cosmic recombination). The radiation at this epoch is observed as the cosmic microwave background (CMB) today, which well proves the above standard scenario of the modern cosmology. Furthermore, the observed CMB anisotropies reveal the presence of initial perturbation at such primary Universe (redshift $z \simeq 1100$). The primordial density distribution is almost uniform over the Hubble scale but includes a slight perturbation which is the primitive origin of today's rich large-scale structure. The small perturbations grow via gravitational instability and hierarchically form the large scale structure (bottom-up scenario). Finally, in first a few hundred million years after the Big-Bang, the gas gravitationally collapses in the dark matter minihalo and forms the metal-free first-generation stars (primordial stars; so-called Population III stars). This event ends the cosmic "dark age" (Rees, 1999) and starts the stellar Universe.[*1] Table 1.1 summarizes the corresponding cosmic ages for important redshifts.

1.1 Primordial Star

Primordial stars play vital roles in the early evolution of the cosmos by initiating cosmic reionization and chemical enrichment of the intergalactic medium (e.g., Ciardi & Ferrara, 2005). Their first light initiated cosmic reionization (e.g., Barkana & Loeb, 2001; Meiksin, 2009) and the heavy elements synthesized by them enabled the formation of

[*1] Hoyle (1946) first demonstrate that the heavy metal which cannot been generated by BBN is produced from the hydrogen in the star (e.g., Burbidge *et al.*, 1957). The importance of primordial star on the chemical evolution is suggested by them.

Redshift	Cosmic Age (Gyr)
1100	4.7×10^{-4}
300	3.3×10^{-3}
100	0.017
50	0.048
30	0.10
20	0.18
10	0.47
7	0.67
2	3.3
1	6.1
0	13.8

Table 1.1. Cosmic age as a function of redshift calculated with the cosmological parameters in Tale 1.2.

subsequent ordinary stellar populations (e.g., Alvarez *et al.*, 2006; Johnson *et al.*, 2007; Maio *et al.*, 2011; Wise *et al.*, 2012; Karlsson *et al.*, 2013). The primordial stars could have also seeded the formation of super-massive black holes observed at high redshifts (so-called high-z quasars, e.g., Fan *et al.*, 2003; Willott *et al.*, 2010; Mortlock *et al.*, 2011). Understanding the formation of the first stars is thus necessary to understand the early history of the Universe (e.g., Bromm *et al.*, 2009). Stellar evolution and death, which regulate the dynamical, radiative, and chemical feedback to the surrounding medium, are largely determined by the stellar mass. Knowledge of the characteristic mass of primordial stars, or their initial mass function (IMF), is thus essential for understanding the initial stages of the first galaxy formation (e.g., Robertson *et al.*, 2010; Bromm & Yoshida, 2011). Whereas direct observations can be utilized to derive the stellar IMF in the present-day Universe, only limited and indirect observational constraints are available regarding the characteristic mass of the first generation of stars. For instance, the elemental abundance patterns of Galactic extremely metal-poor stars provide signatures of nucleosynthesis in primordial stars, from which the mass of the progenitor stars can be inferred (e.g., Caffau *et al.*, 2011; Keller *et al.*, 2014; Tominaga *et al.*, 2014; Aoki *et al.*, 2014).

1.2 Standard Model of Primordial Star Formation

Primordial stars have not been directly observed yet and theorists study their formation processes numerically starting from the cosmological initial condition (see Bromm, 2013; Glover, 2013; Greif, 2014, for recent reviews). The overall processes of star formation and evolution are similar with the present-day case for Population I stars. One can utilize the methodology and idea applied for the present-day case for the primordial star formation. Moreover, studying the primordial star formation has some advantages compared with the present-day star formation because the relevant physical processes are rather simple. The

Parameter	Value	
H_0	67.77	... Current expansion rate in km s^{-1} Mpc^{-1}
Ω_Λ	0.6914	... Dark energy density today divided by the critical density
Ω_m	0.3086	... Matter density today divided by the critical density
Ω_{baryon}	0.04825	... Baryon density today divided by the critical density
σ_8	0.8288	... RMS matter fluctuations today in linear theory
n_s	0.9611	... Scalar spectrum power-law index

Table 1.2. Cosmological parameters obtained from table 5 in Planck Collaboration *et al.* (2014) used for a part of cosmological simulations in this thesis.

primordial star formation takes place through the gravitational contraction of a primordial gas cloud formed under the dark matter dynamics whose initial condition is set by the modern cosmology. So the primordial star formation can be followed with "first principle" numerical simulations.

There is a long history of numerical studies on the primordial star formation. This section reviews the standard model of primordial star formation which has been obtained during last a few decade; the formation of a host dark matter (DM) minihalo which harbors a star-forming gas cloud, the thermal and dynamical evolution of the collapsing cloud until a protostellar core forms, and the evolution of the accreting protostar. The final stellar mass, which is the key parameter of the stellar evolution and feedback on the surrounding medium, is determined through these evolutionary stages.

1.2.1 Dark Matter Minihalo

The CMB observation tells us that the primordial Universe at recombination era is almost uniform but slightly perturbed. This tiny density fluctuation ($\sim 10^{-5}$) is the seed of all structure currently observed. The cosmological initial density distribution is defined by the modern cosmology and the recent CMB observations which constrain the cosmological parameters precisely (e.g., Planck Collaboration *et al.*, 2014, and a part of parameters are summarized in Table 1.2). The gravity amplifies the primordial perturbation which is randomly enhanced over the surrounding matter. The growing perturbation is finally decoupled from the cosmic expansion (the Hubble flow) and begins to collapse. Under the ΛCDM cosmology, the structure formation proceeds hierarchically; the low-mass dark matter halos (so-called "minihalos") appear at first and then these building blocks accrete and merge to grow up the high-mass halos. The primordial stars are considered to form in dark matter minihalo in the early Universe.

The collapsed halo is approximately characterized as the virial state. The virialization is defined as the state that the kinetic energy K and gravitational potential energy U satisfy $U = -2K$ (virial theorem), in the other words,

$$\frac{GM_{vir}}{R_{vir}} \sim v_{vir}^2 \ , \tag{1.1}$$

where $M_{\rm vir}$, $R_{\rm vir}$, and $v_{\rm vir}$ are the mass, radius, and rotational velocity at the virial scale. The analytic theory of gravitational instability shows that the minihalo becomes such a equilibrium state when its density reaches the virial density, $\rho_{\rm vir} = 18\pi^2\rho_{\rm univ} \simeq 178\rho_{\rm univ}$, where $\rho_{\rm univ}$ is the average density of the overall universe. The properties of virialized halo are also written as

$$R_{\rm vir} \simeq 84 \left(\frac{M_{\rm vir}}{10^6\ h^{-1}M_\odot}\right)^{1/3} \left(\frac{1+z}{20}\right)^{-1} \left(\frac{\Delta_c}{18\pi^2}\right)^{-1/3} h^{-1}{\rm pc}\ , \tag{1.2}$$

$$T_{\rm vir} \simeq 1838 \left(\frac{M_{\rm vir}}{10^6\ h^{-1}M_\odot}\right)^{2/3} \left(\frac{1+z}{20}\right) \left(\frac{\mu}{0.6}\right) \left(\frac{\Delta_c}{18\pi^2}\right)^{-1/3} {\rm K}\ , \tag{1.3}$$

(Barkana & Loeb, 2001; Bromm, 2013) where μ is the mean molecular weight and $\Delta_c = \rho_{\rm vir}/\rho_{\rm univ}$ is the overdensity so $\Delta_c/18\pi^2 \simeq 1$ when the halo becomes the virial state. These are the typical scale of minihalos which host the primordial star forming gas cloud; the typical halo mass is $\sim 10^6\ M_\odot$ at redshift $z \sim 20$.

DM minihalos are the gravitational potential earlier formed and the surrounding gas is contracted into them. The condensed gas is once heated up to the virial temperature ~ 1000 K and they have to cool for further collapse. The first primordial star-formation always occurs solely at the center of the dark matter minihalo where the gravitational potential energy of dark matter component achieve a minimum. (cf., multiple formation of the Population I/II stars). The primordial gas contains only limited species (hydrogen, deuterium, and helium) for coolant; none of metal and dust which are efficient coolants in the present-day star formation (Population I/II stars). The hydrogen atomic cooling becomes efficient only at $T \geq 8000$ K and cannot cool the gas contracting in a minihalo.[*2] Instead the cooling of molecular hydrogen (H_2) is efficient at lower temperature by emitting the radiation via the rotational excitation. The cloud collapse starts with this H_2 line cooling.

The cosmic chemical evolution is well studied from the recombination era at $z \simeq 1100$ to the primordial star formation at $z \simeq 20$ (the recent review is Galli & Palla, 2013). Figure 1.1 depicts the evolution history of main elements in this thesis. Because of the absent of dust grains which catalyze H_2 formation in the present-day star-formation, the molecules form via different channel in the early universe. The important formation channel changes with decreasing the CMB intensity: 1) radiative association of excited hydrogen atoms

$$\mathrm{H}(n=2) + \mathrm{H}(n=1) \rightarrow \mathrm{H_2(ground\text{-}state)} + h\nu\ , \tag{1.4}$$

or Raman association

$$\mathrm{H} + \mathrm{H} + h\nu \rightarrow \mathrm{H_2(excited)} \rightarrow \mathrm{H_2(ground)} + h\nu\ , \tag{1.5}$$

[*2] If the minihalo and contracted gas grow up to become $M_{\rm vir} \sim 10^8\ M_\odot$, the high-temperature gas ($T \sim 8000$ K) begin collapse via the atomic cooling (so-called "atomic-cooling halo"; see Fig. 5.3).

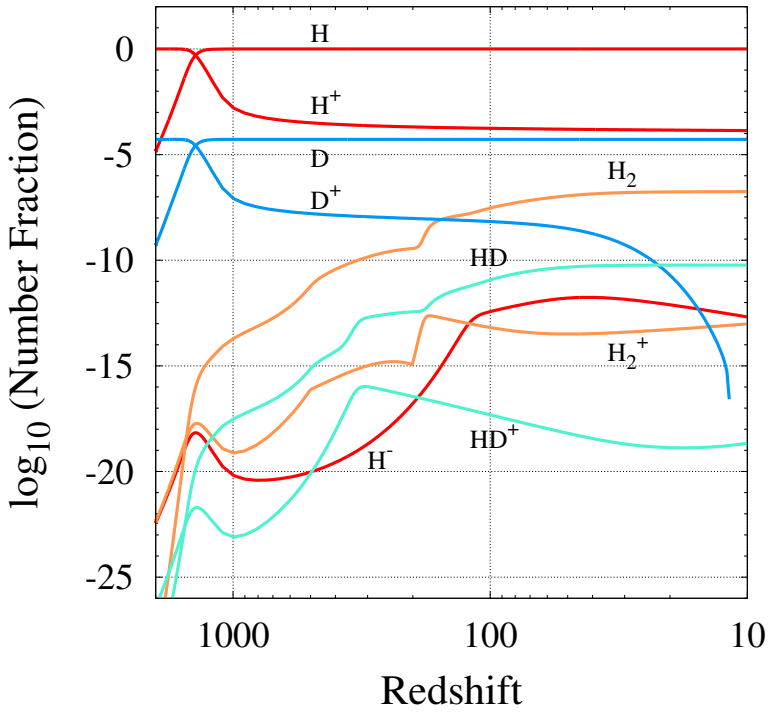

Figure 1.1. Fractional abundances of primordial chemical species as a function of redshift. The calculated is performed by the same chemical network with the cosmological simulation.

during the recombination era, 2) H_2^+ channel

$$H^+ + H \rightarrow H_2^+ + h\nu \ , \tag{1.6}$$
$$H_2^+ + H \rightarrow H_2 + H^+ \ , \tag{1.7}$$

which is prevented in the early epochs via the opposite reaction triggered by energetic CMB photon (photodissociation)

$$H_2^+ + h\nu \rightarrow H^+ + H \ , \tag{1.8}$$

at redshifts lower than $z \sim 800$, and 3) H^- channel

$$H + e^- \rightarrow H^- + h\nu \ , \tag{1.9}$$
$$H^- + H \rightarrow H_2 + e^- \ , \tag{1.10}$$

with the opposite reaction as (photodetachment)

$$H^- + h\nu \rightarrow H + e^- \ , \tag{1.11}$$

at redshifts lower than $z \sim 100$.

The H_2 abundance needed to cool the gas is estimated by comparing the cooling time-scale $t_{\rm cool} \equiv T/\dot{T}$ and the Hubble time-scale $t_{\rm Hubble}$ which is the same order as the free-fall

time-scale of the virialized gas cloud. If $t_{\rm cool} > t_{\rm Hubble}$, the cloud cannot cool sufficiently and maintain a pressure supported state. Whereas if $t_{\rm cool} < t_{\rm Hubble}$, the cloud can cool and collapse at a nearly free-fall time-scale. The critical value is evaluated as $f_{\rm H_2} \sim$ a few times 10^{-4} (e.g., Haiman *et al.*, 1996; Tegmark *et al.*, 1997; Yoshida *et al.*, 2003). The corresponding gas temperature is $T_{\rm crit} \sim 1000$ K so that the primordial gas inside the DM minihalo with $T_{\rm vir} \geq T_{\rm crit}$ can cool and collapse. Eq. 1.3 estimates the mass of host minihalo by substituting $T_{\rm vir} = 1000$ K as

$$M_{\rm vir,T_{vir}=1000\ K} \simeq 4 \times 10^5 \left(\frac{1+z}{20}\right)^{-3/2} \left(\frac{\mu}{0.6}\right)^{-3/2} \left(\frac{\Delta_c}{18\pi^2}\right)^{1/2} h^{-1} M_\odot \ . \quad (1.12)$$

In fact, the formation of host minihalo is stochastic processes which reflect the statistics of density perturbation as a rare higher peak can form the DM halo at higher redshift (e.g., $z \sim 50$ case is found in Gao *et al.*, 2005). Three dimensional cosmological simulations are performed to study the evolution of DM and the formation of gas cloud inside DM minihalos (Abel *et al.*, 2002; Bromm *et al.*, 2002; Yoshida *et al.*, 2003; Bromm & Loeb, 2004; O'Shea & Norman, 2007; Gao *et al.*, 2007). They have found almost similar results for the cloud formation as mentions above.

1.2.2 Primordial Star-Forming Gas Cloud

Inside the minihalo, a gravitationally compressed primordial gas becomes a star-forming cloud. There are some different conditions for the star formation occurred inside the pristine gas due to the radiative feedback from the other stars (both the Pop III and Pop II stars).[*3] Hereafter, the star formed from the primordial gas cloud is referred to as the primordial star (Population III star). The so-called first star (Population III.1 stars; the subscript "1" stands for the first generation in the strict sense) is the case unaffected by any external feedback from other nearby stars. The condition for the star formation (Eq. 1.12) is for such Pop III.1 stars. Primordial stars forming under any radiation feedback is referred to as the Population III.2 stars.

Furthermore, the Pop III.2 stars can be classified into two sub-classes depending on the hardness of the radiation: 1) the photodissociation-dominated case (Pop III.$2_{\rm D}$) and 2) the photoionization-dominated case (Pop III.$2_{\rm I}$), where the subscripts "D" and "I" stand for dissociation and ionization, respectively. In the former case, because H_2 and HD molecules which are the main coolants for the primordial gas are destroyed by photodissociating photons, the temperature in a collapsing cloud is higher than for the Pop III.1 case (e.g., Omukai & Palla, 2001; Omukai & Yoshii, 2003; O'Shea & Norman, 2008). In the latter Pop III.$2_{\rm I}$ case,[*4] external radiation fields affect the thermal evolution in the opposite direction; photoionization first enhances the abundance of free electrons, which are the catalyst for generating H_2 molecules as Eq. (1.9), and then a collapsing cloud evolves at low-temperature due to the enhanced H_2 and HD formation and cooling (e.g., Yoshida

[*3] The latter can contribute orders of magnitude more strongly, in particular, at low redshifts, $z < 15$, as shown in figure 6 of Agarwal *et al.* (2012).

[*4] In the previous studies, this path is usually called Population III.2.

et al., 2007; Hosokawa *et al.*, 2012b). Overall, these theoretical studies suggest that the mass of a primordial star should depend critically on the local strength of the radiation emitted by other stars.

1.2.3 Early Collapse Phase

The gravitationally contracting primordial gas evolves roughly isothermally, the temperature rises since the onset of run-away collapse is only a factor of ~ 10, whereas the density increases over 16 orders of magnitudes (Palla *et al.*, 1983; Omukai & Nishi, 1998). The one-dimensional simulations show that the nature of the collapse can be well explained by the Larson-type self-similarity solution $\rho \propto r^{-n}$ with $n \simeq 2.2$ (e.g., Omukai & Nishi, 1998). The fundamental process of star formation in the early universe is similar with the present-day one but the absence of metal (and strong magnetic field) causes the different thermal evolution. The chemical reactions and thermal processes during the primordial star formation are well studied (e.g., Abel *et al.*, 1997; Galli & Palla, 1998) and Galli & Palla (2013) have summarized the recent updates. By adopting such a primordial chemical network, the thermal evolution of collapsing primordial gas cloud is calculated numerically. The thermal evolution of collapsing primordial star-forming gas cloud until the protostellar core formation is summarized below. More detailed discussions and simulation results are shown in the later chapters.

After the gas is compressed and adiabatically heated upto $T_{\rm vir} \sim 1000$ K at the hydrogen number density $n_{\rm H} \sim 1$ cm^{-3}, the primordial gas contracts by releasing its internal energy via H_2 radiative cooling (e.g., Matsuda *et al.*, 1969; Palla *et al.*, 1983) and reaches the minimum temperature $T \sim 200$ K at $n_{\rm H} \sim 10^4$ cm^{-3}. This phase is called the quasi-hydrostatic "loitering phase" after that the H_2 cooling becomes less efficient and the cloud temperature rises again via the compressional heating. The gas cloud becomes gravitationally unstable at this loitering point, in the other words, the cloud mass reaches the so-called Jeans mass as

$$M_{\rm Jeans} \approx 1000 \left(\frac{T_{\rm Jeans}}{200\ {\rm K}}\right)^{3/2} \left(\frac{n_{\rm H}}{10^4\ {\rm cm^{-3}}}\right)^{-1/2} M_\odot \ , \tag{1.13}$$

(Abel *et al.*, 2002) and begins to rapidly collapse until the formation of a protostellar core. This Jeans mass $\sim 1000\ M_\odot$ is more massive than in the case of present-day star-formation $\sim 1\ M_\odot$ because the efficient dust cooling decreases the minimum temperature at the loitering phase to < 10 K.

During the collapse, a fully molecular cloud with $\sim 1\ M_\odot$ forms by the rapid H_2 formation via three-body reactions at $n_{\rm H} \sim 10^8$ cm^{-3} [*5]

$$\mathrm{H + H + H \rightarrow H_2 + H} \ , \tag{1.14}$$

$$\mathrm{H + H + H_2 \rightarrow H_2 + H_2} \ . \tag{1.15}$$

[*5] The rate of the three-body formation of hydrogen molecules has poorly been determined which results in substantial difference in the thermal evolution of a pre-stellar gas at high density (Turk *et al.*, 2011).

There are two different cooling mechanisms by abundant H_2 in the following collapse. One is the H_2 ro-vibrational line cooling which becomes dominant at $10^8 < n_H/cm^{-3} < 10^{14}$, and promotes the further collapse. It is known that chemo-thermal instability can be triggered in this phase (Sabano & Yoshii, 1977; Silk, 1983). At the following $10^{14} < n_H/cm^{-3} < 10^{17}$, where the gas is nearly opaque to H_2 lines (Ripamonti & Abel, 2004; Yoshida *et al.*, 2006; Clark *et al.*, 2011b),[*6] the other cooling by collision-induced emission (CIE) becomes effective. Finally the CIE cooling also becomes optically thick and inefficient at $n_H > 10^{17}$ cm^{-3} (Ripamonti & Abel, 2004; Yoshida *et al.*, 2007, 2008). The hydrostatic core forms at the collapsing center in which H_2 is collisionally dissociated. The initial mass of such final object, quasi-hydrostatic protostellar core, is $\sim 0.01\ M_\odot$ (e.g., Omukai & Nishi, 1998; Yoshida *et al.*, 2008) which is similar in the cases for Population I/II stars (e.g., Omukai, 2000).

1.2.3.1 Additional Cooling via HD line

The evolution of collapsing gas cloud are also classified into two distinct thermal paths depending on whether HD molecular cooling affects the thermal evolution of the cloud (Pop III.1_{HD}) or not (Pop III.1_{H_2}). As introduced in the section for standard model of primordial star formation, the main coolant of primordial gas is H_2. However, H_2 cooling becomes ineffective at low temperatures, $T < 200$ K, owing to the large energy difference that exists between its $J = 0$ and $J = 2$ rotational levels, and the fact that the lower energy $J = 1 \rightarrow 0$ transition is strongly forbidden (Glover, 2008). The alternative coolant HD becomes more effective if the gas temperature drops below ~ 200 K (see also Fig. A.2), which is close to the minimum temperature above which H_2 cooling operates (so-called the loitering temperature).

The small size of the cosmic D/H ratio means that in general HD is far less abundant than H_2 (see also Appendix A.3). The HD abundance is boosted at low temperatures in two ways: the H_2 fraction is larger and the HD/H_2 ratio is enhanced by chemical fractionation. The formation and destruction of HD in the primordial gas of low density is dominated by the ion-neutral reactions: [*7]

$$H_2 + D^+ \rightarrow HD + H^+ \ , \tag{1.16}$$

$$HD + H^+ \rightarrow H_2 + D^+ \ . \tag{1.17}$$

Reaction (1.16) is exothermic, but reaction (1.17) is endothermic by 462 K (Galli & Palla, 2002). The relative abundance in equilibrium is

$$\frac{n_{HD}}{n_{H_2}} = 2\frac{n_D}{n_H} \exp\left(\frac{462\ \mathrm{K}}{T}\right) \ . \tag{1.18}$$

[*6] Recently, Greif (2014) perform the multifrequency radiation hydrodynamics simulations and find that the detail radiation transfer is well modeled by the one-dimensional fitting function (see also Hartwig *et al.*, 2014).

[*7] Whereas the neutral-neutral reactions (No. 23 and 26 in Table A.1) become more important in conditions of high density and temperature (e.g., collapsing cloud, shocked gas).

Thus at low gas temperatures, considerable chemical fractionation occurs: the equilibrium value of the HD/H_2 ratio is enhanced over the cosmic D/H ratio by a factor $\exp(462\ \mathrm{K}/T)$ (Solomon & Woolf, 1973). Even though the HD cooling rate per molecule decrease with decreasing temperature, the HD cooling rate per unit volume can actually increase, owing to the increase in the HD abundance produced by this fractionation process.

The HD cooling becomes important in the Pop III.$2_{\rm I}$ star formation. The increase of electron fraction by the external ionization promotes H_2 formation via H^- channel (Eq. 1.10) and the abundant H_2 reduces the gas temperature even below the critical temperature to operate HD cooling. Once HD molecular line cooling begins to operate, the temperature decreases further down to a few tens of Kelvin. In one extreme case, the temperature attains the CMB temperature floor, $T_{\rm CMB} = 2.73\ (1+z) \simeq 50$ K at $z \simeq 20$. The average infall rate during the accretion phase extremely decreases following $\dot{M} \propto T^{3/2}$ and the ratio compared with the H_2-cooling case is $\sim (50/200)^{3/2} = 0.125$. So the final stellar mass is also expected to highly decrease.

Another possible route for HD-cooling primordial star-formation is suggested by some studies (Uehara & Inutsuka, 2000; Shchekinov & Vasiliev, 2006; Prieto *et al.*, 2012, 2014; Bovino *et al.*, 2014). In this scenario, the merging of multiple dark matter halos induces the formation of shock-waves. Such shock-waves trigger the ionized environment in which HD formation is enhanced (as the same mechanism mentioned above). Such merging often yields large mass halos with $M_{\rm halo} > 10^7[(1+z)/20]^{-2}\ M_\odot$ (Shchekinov & Vasiliev, 2006).

1.2.4 Later Accretion Phase

The newly-born protostellar core grows in mass via rapid gas accretion from the surrounding envelope. The final stellar mass critically depends on how long the gas accretion continues. One estimation is obtained by assuming that the collapsing gas with Jeans mass, $M_{\rm Jeans} \propto T_{\rm Jeans}^{3/2}/\rho^{1/2}$, collapses for the free-fall time-scale, $t_{\rm ff} \propto \rho^{-1/2}$, as

$$\dot{M} \simeq M_{\rm Jeans}/t_{\rm ff} \propto T_{\rm Jeans}^{3/2}\ . \tag{1.19}$$

The estimated accretion rate for the primordial case ($T_{\rm Jeans} \sim 200$ K) is much higher than for the present-day case ($T_{\rm Jeans} \sim 10$ K) and the ratio is about $(200/10)^{1.5} \simeq 100$. The typical accretion rate in a primordial gas cloud is $10^{-3} - 10^{-2}\ M_\odot\ \mathrm{yr}^{-1}$ (Gao *et al.*, 2007), with which most of the gas in the cloud can be accreted onto the star in its stellar lifetime $\sim$ Myr. It has been postulated that the final stellar mass is set by the mass of the natal cloud, which is as massive as $M_{\rm Jeans} \sim 100 - 1000\ M_\odot$. This is too naive an estimate, however. The final stellar mass is determined by a complex interplay between the growing central protostar and the accretion history.

One important issue is the multiplicity in the primordial star formation. There are some different scales where the fragmentations occur during the star-formation process. Turk *et al.* (2009) and Clark *et al.* (2011a) have shown that, before the protostellar formation, a primordial gas cloud can fragment into some clumps because of the rotation and turbulence in the cloud. Machida *et al.* (2008) and Saigo *et al.* (2008) have investigated the instability of a rotating protostellar core and its dependence on the rotational degree

by performing the parameterized studies. Recent 3D numerical simulations using sink-particle techniques study the time evolution of mass accretion disk around the protostar and show that a circumstellar disk becomes gravitationally unstable and fragments (e.g., Stacy *et al.*, 2010; Clark *et al.*, 2011b; Greif *et al.*, 2011a, 2012; Stacy & Bromm, 2013). Greif *et al.* (2013) have performed more realistic simulation without sink particles but for the first 10 yr after the protostar formation. This could lead to the formation of multiple stellar systems rather than a single star in each minihalo. In this case, the available gas in the envelope is divided among multiple protostars, so that the stars in such a multiple system could have relatively lower masses than in the case of a single star (e.g., Peters *et al.*, 2010; Susa *et al.*, 2014). However, there is an opposite effect; a large fraction of the protostars and fragments could rapidly migrate inward due to gravitational torque, resulting in frequent stellar mergers at the cloud centre (e.g., Greif *et al.*, 2012; Vorobyov *et al.*, 2013). This more efficient accretion could enhance the formation of massive stars.

Another key process in this later accretion stage is the protostellar radiative feedback, which sets the final stellar mass by terminating the mass accretion. McKee & Tan (2008) have evaluated the potential impacts of the ultraviolet (UV) radiative feedback using a semi-analytical model. They consider that, when a protostar becomes massive enough to emit a copious amount of ionizing photons, an $\mathrm{H\,II}$ region grows in polar directions of a circumstellar disk. The stellar ionizing photons heat up and photo-evaporate the gas on the disk surface. Their analytic model of the protostellar evolution finds the final stellar mass to be around 140 $M_\odot$ in a particular case. Numerical simulations are necessary to follow the growth of the protostar and the detailed interplay between the star and the surrounding gas self-consistently, because the UV feedback influences directly and almost instantaneously the mass accretion rate. More recently, the feedback process has been studied with two-dimensional radiation hydrodynamic (RHD) numerical simulations (Hosokawa *et al.*, 2011), demonstrating that UV radiative feedback does indeed shut off the mass accretion and the resulting stellar masses can be a few tens of solar masses. The final stellar masses are determined by the balance of the above competing effects; both fragmentation and radiative feedback (Stacy *et al.*, 2012a; Susa, 2013; Susa *et al.*, 2014).

1.2.5 Evolution of Accreting Protostar

The response of protostellar structure to the external mass accretion is a key property which determines the stellar UV feedback. The mass accretion rate onto the protostar increases following the well-known scaling relation $\dot{M} \propto T^{3/2}$. At the higher accretion rates, the protostar has a larger radius and lower effective temperature for a given stellar mass (the "bloating" phenomenon, see e.g. Zinnecker & Yorke, 2007; Hosokawa *et al.*, 2011). This weakens the stellar UV feedback, and the resulting final stellar mass becomes higher than the case with lower accretion rate.

It is known that an accreting protostar goes through a qualitatively different evolution depending on the accretion rate (e.g., Omukai & Palla, 2003; Hosokawa *et al.*, 2012a). The notably different protostellar evolutionary paths are classified into three characteristic cases (see also Table 1.3). For completeness the remaining paragraphs first review briefly

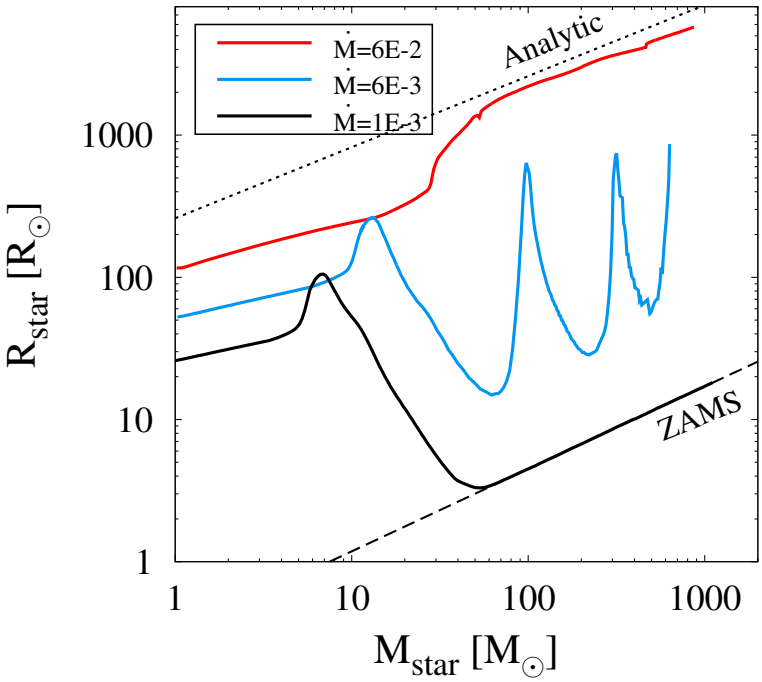

Figure 1.2. Evolution of the accreting protostar's radius for three constant accretion rates $\dot{M} = 1 \times 10^{-3}$, 6×10^{-3}, and 6×10^{-2} $M_\odot$ yr^{-1} (taken from Hosokawa *et al.*, 2012a). The dotted and dashed lines represent the mass-radius relations for super-giant protostars (Eq. 1.26) and ZAMS stars.

Evolution Path	$\dot{M}$ ($M_\odot$ yr^{-1})
P1 : KH Contracting Protostar	< 0.004
P2 : Oscillating Protostar	> 0.004
P3 : Super-Giant Protostar	> 0.04

Table 1.3. Column 1: Paths of the protostellar evolution, and Column 2: Accretion rate for each path. The critical accretion rates are refereed in Omukai & Palla (2003) and Hosokawa *et al.* (2012a).

each evolutionary path, in order to clearly describe the main results presented in the following sections. In the figures hereafter, the three evolutionary paths are distinguished by using different colors (black, blue, and red) for clarity.

1.2.5.1 KH Contracting Protostar (P1; $\dot{M} < 4 \times 10^{-3}$ $M_\odot$ yr^{-1})

The evolution of an accreting protostar is approximately determined by the balance between the following two physical time-scales. One is the stellar Kelvin-Helmholtz (KH)

time-scale, over which the protostar radiates away its gravitational energy,

$$t_{\rm KH} \equiv \frac{GM_*^2}{R_* L_*} \ , \tag{1.20}$$

where M_*, R_*, and L_* are the stellar mass, radius, and luminosity, respectively. This is an approximate time-scale for a non-accreting protostar to contract to the main-sequence. The other is the accretion time-scale, over which the protostar doubles its mass by accretion,

$$t_{\rm acc} \equiv \frac{M_*}{\dot{M}} \ , \tag{1.21}$$

where $\dot{M}$ is the mass accretion rate.

In Figure 1.2, the case with $\dot{M} = 10^{-3}\ M_\odot\ {\rm yr}^{-1}$ (black line) corresponds to the evolution of the KH contracting protostar. In an early evolutionary stage when $M_* \leq 5\ M_\odot$, the KH time-scale is longer than the accretion time-scale, $t_{\rm KH} \gg t_{\rm acc}$, so that the energy deposition by accretion is faster than the energy loss by radiation (this is called "adiabatic accretion"; Stahler *et al.*, 1986). When M_* exceeds 5 $M_\odot$ the stellar luminosity begins to increase sharply, and the KH time-scale quickly decreases with increasing stellar mass. The KH time-scale eventually falls below the accretion time-scale, and the protostar is able to efficiently radiate away its internal energy; it begins to contract ($M_* \geq 7\ M_\odot$; "KH contraction"). KH contraction continues until the star begins core hydrogen burning at $M_* \simeq 40\ M_\odot$, a point at which it has essentially reached the zero-age main-sequence (ZAMS).

1.2.5.2 Oscillating Protostar (P2; $\dot{M} > 4 \times 10^{-3}\ M_\odot\ {\rm yr}^{-1}$)

Omukai & Palla (2003) have shown that, with rapid mass accretion, the star begins expanding before reaching the ZAMS. Figure 1.2 illustrates this for the case $\dot{M} = 6 \times 10^{-3}\ M_\odot\ {\rm yr}^{-1}$ (blue line). Abrupt expansion occurs when the stellar total luminosity approaches the Eddington value during KH contraction. The stellar luminosity L_* cannot exceed the Eddington one $L_{\rm Edd}$ but there is additional effect of the mass accretion $L_{\rm acc}$. The critical accretion rate above which this abrupt expansion occurs has been studied by Omukai & Palla (2003). The total luminosity

$$L_{\rm env} = L_* + L_{\rm acc} \simeq L_* + \frac{GM_*\dot{M}}{R_*} \ , \tag{1.22}$$

becomes equal to the Eddington luminosity when the star reaches the ZAMS. The condition for the critical value is thus $L_{\rm env}|_{\rm ZAMS} = L_{\rm ZAMS} + L_{\rm acc,ZAMS} = L_{\rm Edd}$, from which one can obtain

$$L_{\rm Edd} = L_{\rm ZAMS} + \frac{GM_{\rm ZAMS}\dot{M}_{\rm P2}}{R_{\rm ZAMS}} \ , \tag{1.23}$$

$$\begin{aligned} \dot{M}_{\rm P2} &= \frac{R_{\rm ZAMS}}{GM_{\rm ZAMS}}(L_{\rm Edd} - L_{\rm ZAMS}) \ , \\ &\approx 4 \times 10^{-3}\ M_\odot\ {\rm yr}^{-1} \ . \end{aligned} \tag{1.24}$$

Note that $\dot{M}_{\rm P2}$ given by this equation is a function of M_*, but its dependence is weak (Omukai & Palla, 2003). If the mass accretion rate is higher than this critical value during KH contraction, $\dot{M} > \dot{M}_{\rm P2}$, the star's total luminosity approaches the Eddington value before arriving at the ZAMS. The star can not contract any more and begins to expand. This *bloating* results from the high specific entropy gain in surface layers, where the opacity is higher than the interior, as they absorb a part of the outward heat flux. However, only these surface layers begin to inflate; the bulk of the stellar mass continues KH contraction (see below). As the star inflates, the Eddington ratio $L_{\rm tot}/L_{\rm Edd}$ decreases with decreasing accretion luminosity. After reaching a significantly lower Eddington ratio the star resumes KH contraction, thereby completing one cycle of oscillation. The oscillatory time-scale in this evolutionary stage is approximately given by the KH time-scale, the thermal adjustment time-scale of the star.

1.2.5.3 Super-Giant Protostar (P3; $\dot{M} > 4 \times 10^{-2}\ M_\odot\ {\rm yr}^{-1}$)

Hosokawa *et al.* (2012a) have shown that, if the accretion rate is higher than

$$\dot{M}_{\rm P3} \approx 4 \times 10^{-2}\ M_\odot\ {\rm yr}^{-1}\ , \tag{1.25}$$

the protostar enters a third evolutionary path, whereby the stellar radius monotonically increases with stellar mass according to the relation

$$R_* \simeq 2.6 \times 10^2\ R_\odot\ \left(\frac{M_*}{\rm M_\odot}\right)^{1/2}\ , \tag{1.26}$$

for $M_* > 100\ M_\odot$. The above scaling is independent of the mass accretion rate as long as it is greater than the critical value, $\dot{M}_{\rm P3}$. In Figure 1.2, the case with $6 \times 10^{-2}\ M_\odot\ {\rm yr}^{-1}$ (red line) demonstrates this behavior. Note that, even in this case, the time-scale inversion to $t_{\rm KH} < t_{\rm acc}$ occurs at $M_* \simeq 30\ M_\odot$. This means that most of the stellar interior contracts, radiating the energy away and only a surface layer significantly inflates. The star thus has a highly inhomogeneous structure, whereby the contracting core is surrounded by a bloating envelope, similar to red-giant stars. This evolutionary path is appropriately called the "super-giant protostar" (Hosokawa *et al.*, 2012a).

1.3 Nature of Primordial Stars

Theorists have constructed the formation model of primordial stars and recently the final stellar masses are directly calculated from the cosmological initial condition. The stellar evolution and final fate are largely determined by the stellar mass (and stellar rotation speed). Now, one can discuss about the nature of *first* light, metal and so on whatever originates from primordial stars.

1.3.1 Stellar Evolution and Final Fates

The stellar evolution and its dependence on the stellar mass have been studied by performing the parameterized simulations of stellar evolution for different initial mass models.

Fate	$M_{\rm ZAMS}$ (non-rotating)	$M_{\rm ZAMS}$ ($f_{\rm Kepler,ZAMS} = 0.5$)
NS	$8 < M_*/M_\odot < 25$	$8 < M_*/M_\odot < 25$
LMBH	$25 < M_*/M_\odot < 80$	$25 < M_*/M_\odot < 65$
PPISN	$80 < M_*/M_\odot < 120$	$65 < M_*/M_\odot < 90$
PISN	$120 < M_*/M_\odot < 240$	$90 < M_*/M_\odot < 200$
HMBH	$240 < M_*/M_\odot$	$200 < M_*/M_\odot$

Table 1.4. Column 1: Final fate of stellar evolution: neutron star (NS), low-mass black hole (LMBH), pulsational pair-instability supernovae (PPISN), pair-instability supernovae (PISN), and high-mass black hole (HMBH), Column 2: Stellar mass range at ZAMS for the non-rotating star, Column 3: Stellar mass range at ZAMS for the highly rotating star. The values is based on Yoon *et al.* (2012).

For the primordial (no metal) stars, such calculations have been performed (e.g., Schaerer, 2002; Heger & Woosley, 2002). Recently, the influence of stellar rotational degree on its evolution is considered but the precise implementation of rotational effects, transformation of angular momentum, and matter mixing, is difficult. Also, the rotational speed of primordial stars is highly uncertain, which is different from the present-day field stars which have observational constraints.[*8]

Yoon *et al.* (2012) have performed stellar evolution calculations for zero-metallicity stars and categorize their final fates as a function of the stellar masses. Table 1.4 lists their results for different rotational degrees as $f_{\rm Kepler} = v_{\rm rot}/v_{\rm Kepler} = 0$ (non-rotator) and 0.5 (rapid-rotator). The final fates are different depending on the initial stellar parameters; neutron star (NS), low-mass black-hole (LMBH), pulsational pair-instability supernovae (PPISN), pair-instability supernova (PISN), and high-mass black-hole (HMBH). The feedback to the surrounding medium depends on the stellar mass (and the rotation degree Chatzopoulos & Wheeler, 2012); both the radiative feedback from bright main-sequence stars and the dynamic and chemical feedbacks mostly by supernova explosions at the moment of the stellar deaths.

1.3.2 Observational Clues

Ultimately, the theoretical predictions must be verified by observations. Currently, there have been no direct observational signatures of primordial stars unfortunately. To search the dark age of the primordial stars, scientists are waiting for next-generation projects with large telescopes which have the capacity for detecting the image of the early Universe; e.g., space-borne *James Webb Space Telescope* (JWST) and ground-based *Thirty Meter Telescope* (TMT). Theorists have to estimate the observational possibility based

[*8] Stacy *et al.* (2011b, 2013) have shown the calculations of the stellar rotation which is the second important parameter to determine the stellar evolution obtained from the cosmological simulations.

on predicted nature of primordial stars.

A simple plan is to search the bright end of primordial stars as supernovae (SN) or gamma-ray bursts (GRB). Some authors estimate that the massive primordial stars which end as energetic hypernovae, PISNe, and GRB can be detected by the future telescopes (e.g., Tanaka *et al.*, 2013; Whalen *et al.*, 2013b,a, 2014; Smidt *et al.*, 2014). The most distant observed astronomical objects are currently GRB at $z \simeq 8.2$ (GRB 090423; Salvaterra *et al.*, 2009; Tanvir *et al.*, 2009) or $z \sim 9.4$ (GRB 090429B; Cucchiara *et al.*, 2011) and galaxies at $z \simeq 10.8$ (MACS0647-JD; Coe *et al.*, 2013) or $z \simeq 11.9$ (UDFj-39546284; Bouwens *et al.*, 2011; Ellis *et al.*, 2013; Capak *et al.*, 2013). However, the primordial stars are predicted to be born at $z \sim 20$, which is still beyond the reach of the current observations.

Another strategy is to find the chemical fossil of primordial stars in the Galactic chemical evolution. The typical mass of the primordial stars can be inferred, for example, from the elemental abundance patterns of metal-poor stars in the Galaxy (Caffau *et al.*, 2011; Cooke & Madau, 2014). Interestingly, the abundance patterns found in the atmospheres of a few extremely metal-poor stars can be reconciled, if the metals are produced in supernovae of progenitor stars with a mass $\leq 100\ M_\odot$ (e.g., Umeda & Nomoto, 2005; Takahashi *et al.*, 2014). This relative small mass is consistent with the conclusion of recent theoretical studies on primordial star formation (Hosokawa *et al.*, 2011; Stacy *et al.*, 2012a; Susa, 2013). Very massive stars with $150 - 300\ M_\odot$ end their lives as pair-instability supernovae (PISNe; Barkat *et al.*, 1967; Bond *et al.*, 1984; Heger & Woosley, 2002) which would imprint a peculiar abundance pattern in metal-poor stars. There have been no clear observational indication (Tumlinson *et al.*, 2004; Frebel *et al.*, 2009) but recently Aoki *et al.* (2014) have reported a very metal-poor star which shows such peculiarity in the elemental abundances.

Some simulations of primordial star formation show that the accretion disk fragments and low-mass stars form (Clark *et al.*, 2011b; Greif *et al.*, 2011a). If Pop III stars are less massive than $\leq 0.8\ M_\odot$, their lifetimes of the main-sequence phase become longer than the cosmic age. Such stars may have still survived in the Galaxy but there have been no reports. Another possibility is that they have been chemically polluted by the accretion of surrounding medium (e.g., Yoshii, 1981; Hattori *et al.*, 2014) and scientists have already observed such surviving stars as the metal-poor stars.

Instead of the direct search of each primordial signature, some authors try to find clues of primordial stellar systems; 21 cm radiation (e.g., Furlanetto *et al.*, 2006; Barkana & Loeb, 2007), polarization of CMB radiation, and cosmic infrared background (CIB; e.g., Santos *et al.*, 2002; Kashlinsky *et al.*, 2005; Matsumoto *et al.*, 2011).

The evaluations of the observational possibilities depend on the assumed nature of primordial stars. The critical parameter is the initial stellar mass at the birth of a star. The probability function of stellar masses, so-called initial mass function, is useful to model the statistical signature.

1.3.3 Primordial Initial Mass Function

The ultimate goal of the theoretical study of primordial star formation is to derive the primordial Initial Mass Function (IMF) in the cosmological context. IMF is used to calculate the statistical stellar feedback for the evolution of stellar cluster, galaxy, and intergalactic medium. For the nearby Population I/II stars the present-day IMF is constrained by observations; i.e., Salpeter ($dN/dM_* \propto M_*^{-x}$ with $x = 2.35$), Kroupa, and Chabrier IMF. The primordial IMF should be different from the present-day IMF because their star formation processes and initial conditions are totally different. The metal-free gas cloud can cool onto about 200 K via the H_2 cooling and the gravitationally unstable Jeans mass becomes about thousand $M_\odot$ which is much higher than the present-day star formation. So the primordial stars are thought to have a top-heavy IMF because of the sufficient mass around the protostellar core.

Recently, some multi-dimensional radiation hydrodynamic simulations have been performed to determine the initial mass of the primordial star (Hosokawa *et al.*, 2011; Stacy *et al.*, 2012a; Hosokawa *et al.*, 2012b; Susa, 2013). These previous studies, however, calculate only several individual cases and thus it remains unclear if they represent fiducial cases. The characteristic mass and the overall mass distribution are yet unknown so that they cannot mention about the shape of primordial IMF, which is essential to model the role of primordial stars in the early universe. Obviously, large sampling is necessary to study the overall mass distribution of primordial stars; *how massive the typical primordial star* and *how their masses distribute*.

1.4 Aims

The goal of this thesis is to directly calculate the mass distribution of primordial stars theoretically. To obtain the mass distribution of primordial stars, it is needed to cover all possible modes of the primordial star formation which result in different stellar masses. The formation process differs according to the initial properties of star-forming clouds, so that the reported stellar masses are not the same between articles (Hosokawa *et al.*, 2011; Stacy *et al.*, 2012a; Susa, 2013). Furthermore, there are qualitatively different evolution paths during the primordial star formation. Figure 1.3 depicts the overall of primordial star formation by classifying the evolution paths as squares and representing the evolutionary links by arrows. While the previous studies found and investigated a part of paths and links (black), this thesis discover some new branches (red) in the simulations. The final stellar masses are different according to which route the primordial star formation goes through. It is needed to investigate the dependence of stellar mass on the formation paths and the probability fraction for each path. For this purpose, this thesis adopts the strategy of a series of simulations as below.

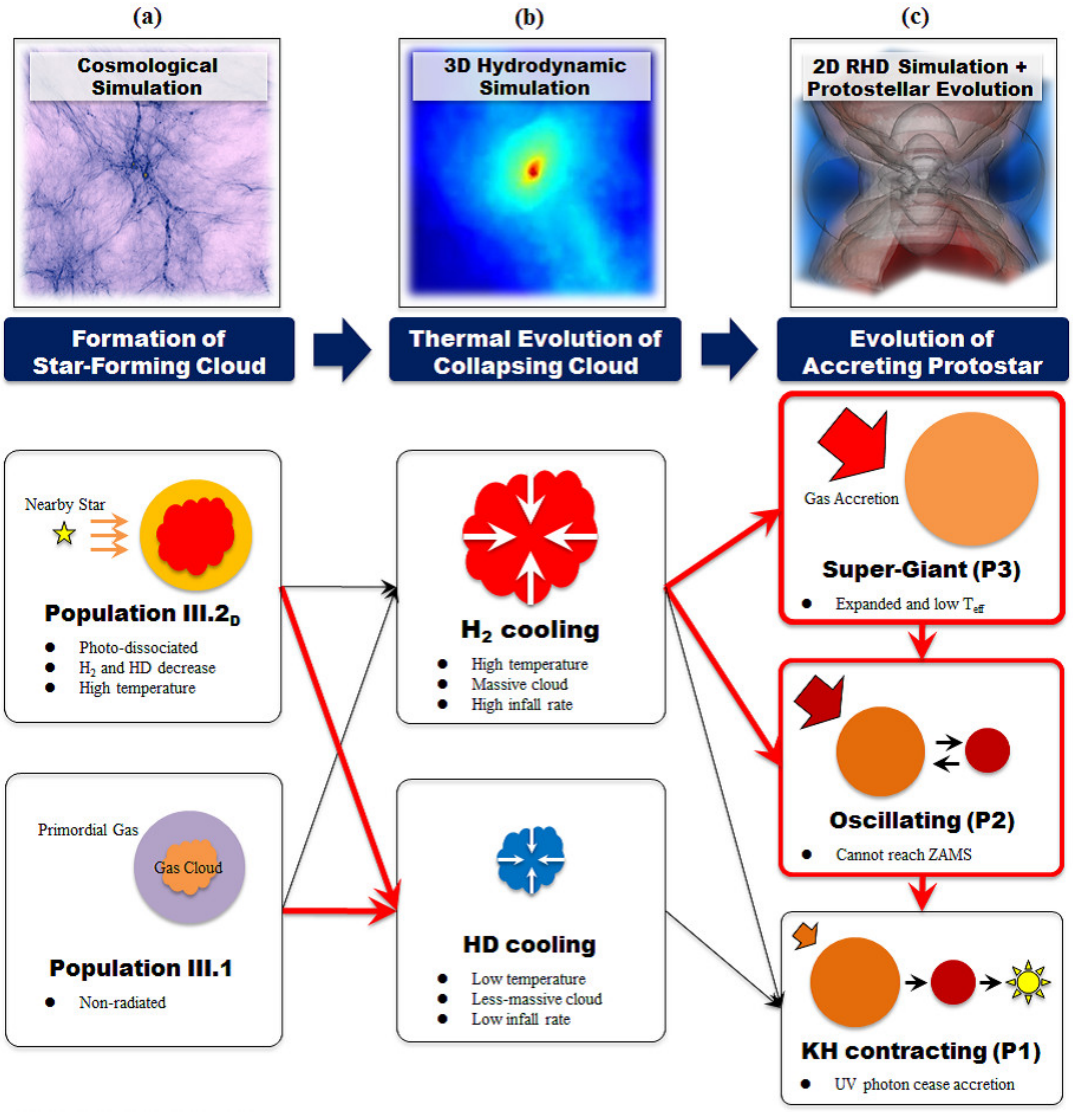

Figure 1.3. Various paths during the primordial star formation which is considered in this thesis. The star formation process is divided into three different phases; a) formation of star-forming gas cloud, b) thermal evolution of collapsing cloud, and c) evolution of accreting protostar. The top three panels represent pictures of corresponding simulations. The below squares represent each path and the arrows between paths reveal the evolutionary connections. The paths enclosed by red squares and the red arrows represent the newly found paths and links in this thesis. The detail explanations for each path are found in the text.

Various Paths of the Primordial Star Formation

First, the various properties of the primordial stars are investigated by performing a number of simulations which follow the whole evolutionary stages of the primordial star formation. The thesis considers both Pop III.1 and III.$2_{\rm D}$ stars but ignores the contribution of Pop III.$2_{\rm I}$ stars (see Sec. 4.4.2 for a discussion of this topic). The calculation for each star-formation is constructed of two different simulations. Large-volume three-dimensional (3D) cosmological simulations first follow the formation of primordial clouds in dark matter halos and their initial run-away collapse. Then the subsequent evolution in the mass accretion stage under the influence of protostellar UV feedback is calculated by performing 2D local radiation hydrodynamic simulations coupled with stellar evolution calculations (Hosokawa *et al.*, 2011). The protostellar evolution is calculated self-consistently by numerically solving the interior structure of the protostar (e.g., Omukai & Palla, 2003). The final stellar mass is determined, when the mass accretion onto the protostar is shut off by strong stellar UV feedback. For the Pop III.1 case, the star-formation processes and final masses are calculated for 110 star-forming clouds. A wide range of stellar masses is obtained which suggests a great diversity of the Pop III.1 star-formation. For the Pop III.$2_{\rm DIS}$ case, 21 cosmological simulations are performed under the influence of different UV radiation to study the dependence of final stellar mass on the strength of the photodissociating radiation field. Interestingly, calculation results show correlations between the final stellar masses and the physical properties of star-forming clouds for both Pop III.1 and III.$2_{\rm DIS}$ stars. Such correlations are useful to estimate the final stellar mass using the early physical state of the clouds or of the haloes, without following the detailed evolution from the cloud collapse up to the termination of mass accretion onto the protostellar core.

Mass Distribution of Primordial Stars

To construct the mass distribution of primordial stars, a number of different modes of the primordial star-formation should be gathered to get a large sample which contains both Pop III.1 and III.$2_{\rm D}$ star-formation. In order to generate non-biased cosmological samples of star-forming clouds, this thesis performs a large cosmological simulation with a comoving volume of $(3\ h^{-1}{\rm Mpc})^3$ and choose 1540 halos in the cosmological volume. The calculation for each halo ends when the cloud collapse proceeds enough to determine the final stellar mass from the cloud's property by using the derived formula. For each cloud, the local intensity of the photodissociating radiation is calculated by summing up contributions from nearby primordial stars distributed in the cosmological volume. This approach provides mass distributions of Pop III.1 and III.$2_{\rm D}$ stars at different epochs.

1.5 Structure of This Thesis

The rest of the thesis is organized as follows. The procedures of calculations are described in each chapter. Chapter 2 studies the diversity of primordial star formation and the origins of the wide stellar mass distributions; the former part is for the Population III.1 cases whereas the later part is for the Population III.$2_{\rm D}$ cases. Chapter 3 shows the sampling of the primordial star-forming gas clouds in the cosmological context. Chapter 4 finally represents the resulting mass distributions of primordial stars, classifying the large samples into Pop III.1 and III.$2_{\rm D}$ cases. The conclusion of this thesis is summarized in Chapter 5.

Chapter 2

Mass Diversity of Primordial Stars and its Origins

2.1 Overview

The first step is investigating the diversity of primordial stellar masses by performing the overall simulations of the primordial star-formation from the cosmological initial condition to the zero-age main-sequence stage. The results presented here are based on a sequence of simulations with different computer codes. First the cosmological simulations are performed to follow the formation of the primordial gas clouds which gravitationally collapse in the center of dark matter halos. After the formation of a protostellar core at the center of the collapsing cloud, the simulations are switched to the 2D RHD calculations for each individual cloud and follow the evolution during the later accretion stages. In each case a bipolar H_{II} region forms and it subsequently grows with time-dependent mass accretion as the stellar mass increases. The mass accretion onto the protostar is finally shut off by the strong UV radiative feedback caused by the dynamical expansion of the H_{II} region. The final stellar masses are determined for each case at this time. This chapter shows the dependences of the final stellar masses on the initial properties of the star-forming cloud.

The former part for Population III.1 cases has been already published in The Astrophysical Journal, Volume 781, 60 (Hirano *et al.*, 2014) whereas the later part for Population III.$2_{\rm D}$ cases has been submitted to Monthly Notices of the Royal Astronomical Society.

2.2 Population III.1 Stars

This section shows the 110 simulations of the primordial star-formation without any external feedback (i.e., Pop III.1) in the cosmological context. Figure 2.1 shows an example of simulations for five representative cases. The resulting gas density concentrations arise in five such dark matter halos. These primordial star-forming clouds show different structures of density, velocity, and temperature which results in the different accretion histories in the following accretion phases. Then the resulting stellar masses are also different from 60 to 343 $M_\odot$. The overall sample of 110 cases shows a large scatter of resulting stellar

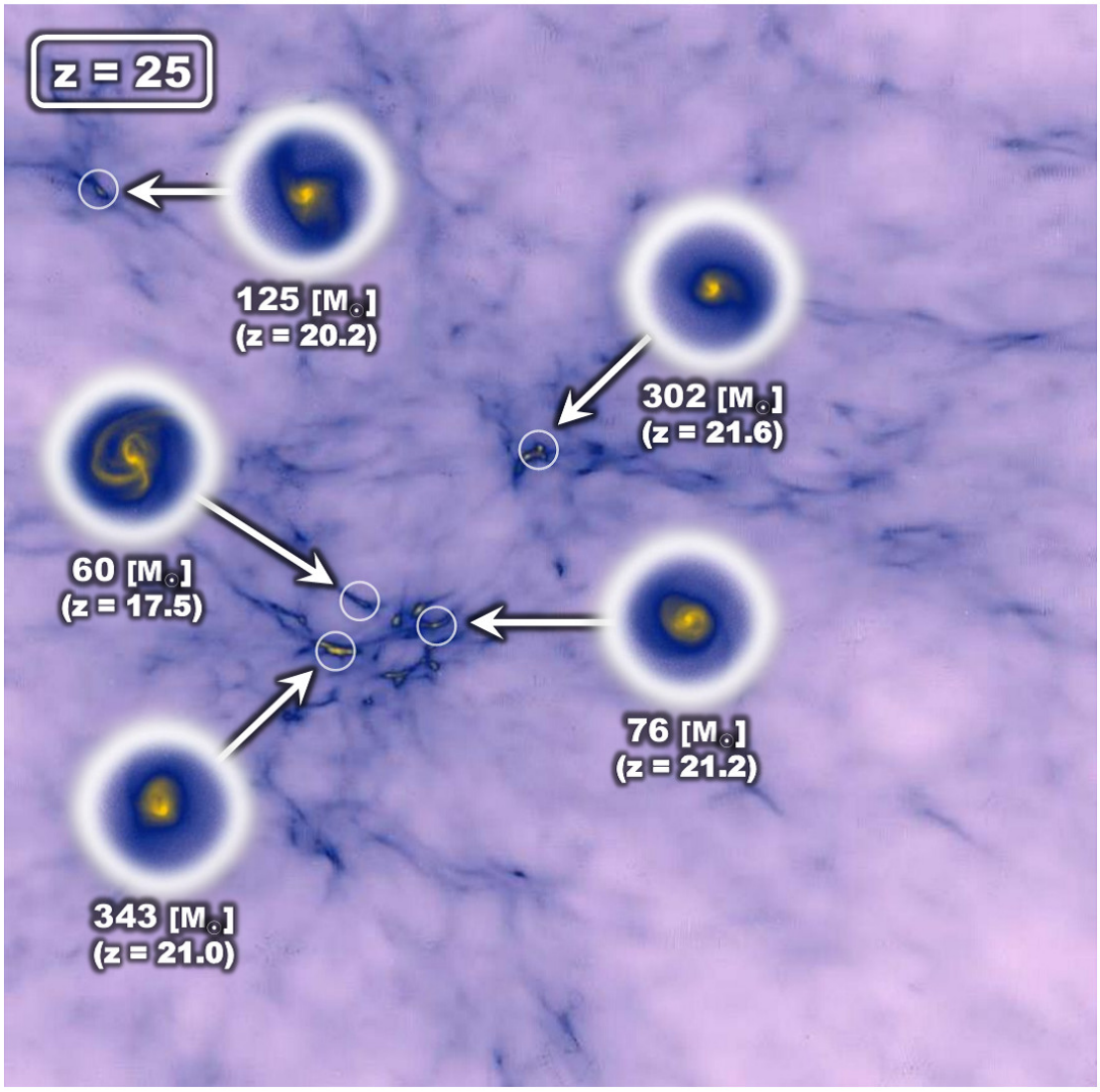

Figure 2.1. Projected density distribution at $z = 25$ in one of the cosmological simulations. There are five primordial star-forming clouds in a cube of 15 kpc on a side. The small figures show the zoom-in to the central 1 pc region of the clouds at the respective formation epoch. The masses of the Population III.1 stars formed in these clouds are 60, 76, 125, 303, and 343 $M_\odot$, respectively.

masses, ranging from 9.9 to 1621 $M_\odot$. The later subsections discuss the origin of this diversity.

2.2.1 Method

The calculations consist of two simulations performed by different codes: formation of the protostellar core ("early collapse phase") and following growth of the accreting protostar ("later accretion phase"). The former phase is followed by the three-dimensional cosmological hydrodynamic simulations. The calculation then switches to two-dimensional

$N_{\rm cloud}$	$L_{\rm box}$ (h^{-1}kpc)	$l_{\rm soft}$ (h^{-1}pc)	$m_{\rm DM}$ ($h^{-1}M_\odot$)	$m_{\rm gas}$ ($h^{-1}M_\odot$)	Cosmological Parameters
3	50	1.0	0.0142	0.00288	Larson *et al.* (2011)
3	150	1.5	0.0478	0.00971	Larson *et al.* (2011)
1	300	2.9	0.383	0.0772	Larson *et al.* (2011)
7	1000	6.5	2.16	0.436	Komatsu *et al.* (2009)
75	1000	13.5	17.3	3.49	Komatsu *et al.* (2011)
21	2000	13.5	17.3	3.49	Komatsu *et al.* (2009)

Table 2.1. Parameters of cosmological initial conditions for calculations of Pop III.1 stars. Column 1: Number of star-forming clouds, Column 2: Simulation box size (comoving), Column 3: Gravitational softening length (comoving), Column 4: Mass of zoom-in N-body particle (dark matter), Column 5: Mass of zoom-in SPH particle (gas), and Column 6: Reference of the adopted cosmological parameters.

axisymmetric radiation hydrodynamics simulations that start with the final output of the cosmological simulations. The more detailed code descriptions are summarized in Appendixes A and B.

2.2.1.1 Cosmological Simulations: Formation of Primordial Gas Clouds

Three dimensional (3D) cosmological simulations are performed using the parallel N-body / Smoothed Particle Hydrodynamics (SPH) solver GADGET-2 (Springel, 2005) in its version suitably adopted for primordial star formation. Chemical rate equations are solved for 14 primordial species (e^-, H, H^+, H^-, He, He^+, He^{++}, H_2, H_2^+, D, D^+, HD, HD^+, and HD^-) as in Yoshida *et al.* (2006, 2007). To accurately evaluate trapping effects of cooling radiation, the code employs the Sobolev method for H_2 line cooling and a ray-tracing method for continuum cooling by H_2 collision-induced emission (Yoshida *et al.*, 2006, 2008; Hirano & Yoshida, 2013). Some chemical rates have been updated: the cooling rates for H_2 and HD (see Galli & Palla, 2013) and the three-body H_2 formation rates (Forrey, 2013a,b).

The cosmological initial conditions are generated by using the modified version of N-GENIC (Springel, 2005). The basic simulation parameters are summarized in Table 2.1. All the cosmological simulations are initialized at $z_{\rm ini} = 99$. The main parent simulations have a volume of $L_{\rm box} = 1$ and 2 h^{-1}Mpc on a side. A part of samples come from a few additional simulations with smaller volumes. The simulations adopt the periodic boundary condition.

In order to achieve sufficient spatial resolution to resolve the primordial gas clouds with masses of $\sim 1000\ M_\odot$, hierarchical zoom-in technique is used with a progressively larger number of particles. A Friends-Of-Friends (FOF) halo finder locates dense, clustered regions in the parent cosmological simulations. Then the zoom-in initial conditions are generated for the selected regions, where the mass- and spatial-resolutions are increased.

The corresponding small-scale density fluctuations are added suitably as given by the adopted ΛCDM cosmology. Each refined region has a spherical shape of radius 130 h^{-1}kpc in the case of $L_{\rm box} = 1\ h^{-1}$Mpc. All the re-simulations are started from $z_{\rm ini} = 99$.

The selection of the gas clouds is done as follows. The first step is selecting a virialized dark matter halo whose mean density within the virial radius is 200 times greater than the mean density of the universe, $\rho_{\rm DM} > \rho_{\rm vir} \sim 200\ \rho_{\rm univ}$ (Sec. 1.2.1). Then, if the halo is the densest structure within a two physical kpc radius around itself, the halo is assumed to have not been influenced by nearby supernova explosions (e.g., Ritter *et al.*, 2012) nor by stellar radiation (e.g., O'Shea & Norman, 2008; Agarwal *et al.*, 2012; Johnson *et al.*, 2013). Primordial gas clouds forming at the centers of such halos are thought to bear the first generation of stars. In this way, a sample of 110 gas clouds is located from the parent cosmological simulations.

The zoom-in simulations follow the formation and gravitational run-away collapse of the selected primordial gas clouds. The code uses the particle-splitting technique of Kitsionas & Whitworth (2002) to achieve a wide dynamic range for both N-body and SPH particles. By this method, the radius of DM density core is always resolved by 2 times the gravitational softening length of the N-body particles, whereas the local Jeans length is always resolved by more than 10 times the local smoothing length of the SPH particles. There is one more condition that the ratio of neighbor particles' masses should be less than a certain value to avoid the artificial dynamical friction. The N-body particles are split as long as the local DM density overcomes the local gas density ($n_{\rm H,cross} \sim 10^3$ cm^{-3}; see also Fig. 2.3). The zoom-in simulations stop when the central density of the cloud reaches $n_{\rm H,cen} = 10^{13}$ cm^{-3}. At this moment, the mass of the lightest gas particle is $m_{\rm gas} \sim 10^{-5}\ M_\odot$, and thus the nominal mass resolution is $\sim 0.01\ M_\odot$, which is equal to the mass of a protostellar core (Sec. 1.2.3). The model outputs at this time are used to generate the *initial* conditions for the following radiation hydrodynamic simulations.

2.2.1.2 Radiation Hydrodynamic Simulations: Evolution of Accreting Protostars

The evolution of the protostars in the accretion phase is followed by two-dimensional (2D) axisymmetric radiation hydrodynamic (RHD) calculations coupled with the stellar structure evolution (Hosokawa *et al.*, 2011). The nested-grid method is employed in order to achieve an extremely wide dynamic range (e.g., Yorke & Kaisig, 1995; Yorke & Bodenheimer, 1999; Yorke & Sonnhalter, 2002). The calculations utilize 9 level hierarchical grids, whereby the coarsest grid size is $\sim$ 6400 AU (level 1) and the finest is $\sim$ 25 AU (level 9) in a $\sim$ 1 pc volume. Data from the 3D cosmological simulation are mapped onto 2D axisymmetric meshes as follows. First, the principal rotational axis is determined by calculating the average angular momentum vector of the gas within a 0.01 pc region around the cloud center. Then the physical quantities are averaged along the azimuthal direction around the rotational axis under the 8 level hierarchical grids. The free flow boundary condition is adopted in the RHD simulations; the material can escape through the edges of the simulation domains assuming that the density at the boundary is the

same as that of the outermost grid. To eliminate the additional effects of this boundary condition, the simulation sets a sufficiently large box size so that the inflow cannot affect the accretion onto the central protostar. The computational domain is 1.2 pc on a side, which typically contains a few thousands solar masses of gas.

The calculations consistently follow the structure and evolution of the central accreting star and the hydrodynamics of the accreting gas which is irradiated by the stellar radiation as in Hosokawa *et al.* (2011). The mass accretion rate onto the protostar is directly obtained from the inflow rate of gas into the central sink cell in the RHD simulation. The code treats non-equilibrium chemistry and radiative processes in a primordial gas (summary of the reactions are found in Hosokawa *et al.*, 2011). A test calculation verifies that HD cooling, which sometimes operates in the pre-collapse stage, is unimportant in the vicinity of the protostar and in the accretion disk. So the HD chemistry is switched off when following the accretion stage (Hosokawa *et al.*, 2012b). The evolution of the protostar is calculated by numerically solving the interior structure with this accretion rate (e.g., Omukai & Palla, 2003; Hosokawa & Omukai, 2009). The stellar luminosity and the effective temperature are provided by the stellar model. The spectral energy distribution is calculated from these basic properties of the star.

The sample of 110 cases show different mass accretion histories and different protostellar evolution (as introduced in Sec. 1.2.5). To this end, the code used in Hosokawa *et al.* (2011, 2012b) needs several modifications to calculate those various evolution.

- In reality (3D), angular momentum transport in a rapidly accreting circumstellar disk is driven mainly by its non-axisymmetric structures such as spiral arms. Hosokawa *et al.* (2011) adopt the so-called α-viscosity model (Shakura & Sunyaev, 1973) using a constant gravo-viscous parameter α everywhere on the equator of the disk (e.g., Yorke & Sonnhalter, 2002). Recent 3D numerical simulations suggest that, in a self-gravitating disk, the effective α can be estimated as a function of the Toomre Q-parameter (Zhu *et al.*, 2010b; Takahashi *et al.*, 2013). Motivated by this, the code adopts a functional form proposed by Gammie (1996), and allows α to spatially vary with the Toomre Q-parameter evaluated at each cell on the equator, $\alpha(Q(r))$. Details of this procedure are described in Appendix B.1.1.
- Some of 110 cases show rather high accretion rates, exceeding 0.01 $M_\odot$ yr^{-1}. For sufficiently high accretion rates, the protostellar evolution differs significantly from the fiducial case, whereby the star contracts to reach the zero-age main-sequence (Omukai & Palla, 2003; Hosokawa *et al.*, 2012a). In practice, the calculations occasionally encounter convergence difficulties with time-dependent accretion histories resulting from the RHD simulations. To avoid this technical problem, the code employs an analytic model of stellar evolution. In essence, the rapidly accreting star, whose envelope experiences expansion and oscillations, nevertheless evolves on a certain averaged track on the mass-radius plane. The details of the analytic model are described in Appendix B.2.

The calculation ends when the mass accretion rate falls below 10^{-4} $M_\odot$ yr^{-1} assuming

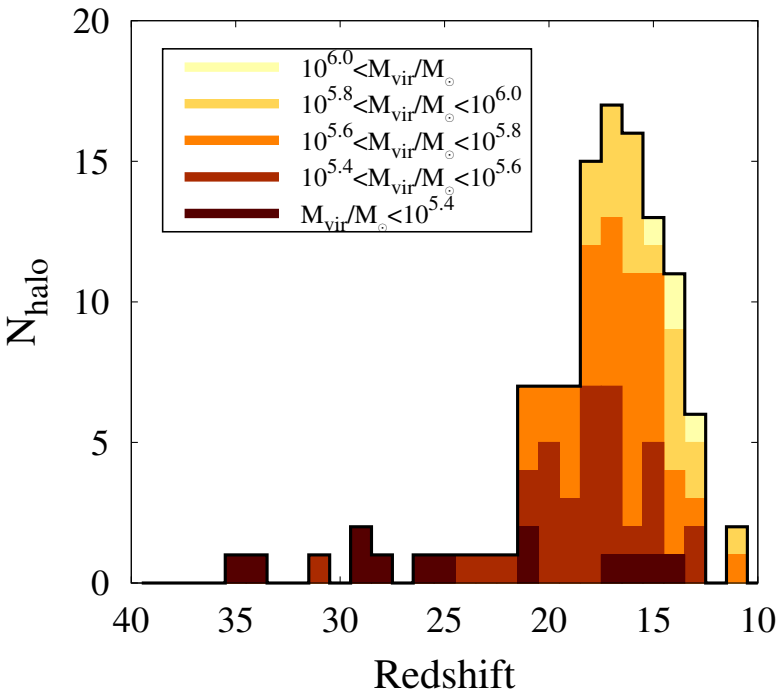

Figure 2.2. Distributions of dark matter minihalos that host primordial star-forming clouds as a function of the formation redshift at $n_{\rm H,cen} = 10^6$ cm^{-3}. The bin width is $\Delta = 1$ and the different colors indicate the different ranges of the virial masses: $M_{\rm vir}/{\rm M}_\odot < 10^{5.4}$, $10^{5.4} < M_{\rm vir}/M_\odot < 10^{5.6}$, $10^{5.6} < M_{\rm vir}/M_\odot < 10^{5.8}$, $10^{5.8} < M_{\rm vir}/M_\odot < 10^{6.0}$, and $10^{6.0} < M_{\rm vir}/M_\odot$. The black line shows the sums over all virial masses. The redshifts and virial masses are measured when $n_{\rm H,cen} = 10^7$ cm^{-3}.

that the mass accretion and hence the growth of the central star are halted due to stellar radiative feedback. In fact Hosokawa *et al.* (2011, 2012a) have shown that the accretion rate continues to decrease after that and further stellar growth in mass is negligible. The calculation results of the 110 collapsing clouds and accreting protostars represent a large sample of the final masses of the first stars (Pop III.1 stars), $M_{\rm III.1}$.

2.2.2 Early Collapse Stage

This section describes the early evolution of the star-forming clouds up to the moment when a central hydrostatic core is formed. The following paragraphs show the evolution in nine representative cases, which include four P1 (black), three P2 (blue), and two P3 (red) cases for the protostellar evolution. By performing the cosmological simulations, 110 dark matter minihalos which host the primordial star-forming clouds are obtained. Figure 2.2 shows a wide range of masses $M_{\rm vir} = 10^5 - 10^6$ $M_\odot$ distributed over redshifts $z = 35-11$, most of which are at $z = 20-15$. The initial conditions of the primordial star-

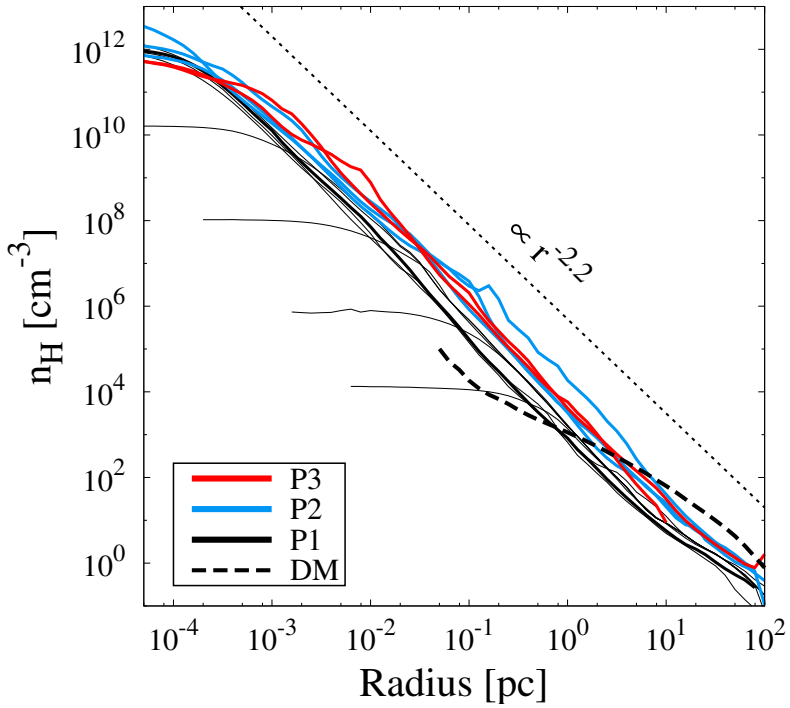

Figure 2.3. Radial gas density profiles for nine selected star-forming clouds. The colors indicate the different stellar evolutionary paths P1 (4 black lines), P2 (3 blue), and P3 (2 red). For one P1 case it is also plotted the time evolution of the density profile at the time when the central density is 10^4, 10^6, 10^8, 10^{10}, and 10^{12} cm^{-3}. For all other clouds, snapshots at $n_{\rm H,cen} \simeq 10^{12}$ cm^{-3} are used. The dashed line shows an averaged DM density profile for 110 cases. The dotted line shows a power-law density distribution with $n_{\rm H} \propto r^{-2.2}$ for reference.

formation have the great diversity, which results in different evolution in the subsequent evolutionary stages. The following subsections show the dynamical and thermal features of gravitationally collapsing clouds.

2.2.2.1 Run-away Collapse of the Clouds

Figure 2.3 shows that the gravitational collapse of a primordial cloud proceeds in the well-known self-similar manner. The cloud has a central collapsing core and a surrounding envelope during the collapse. Whereas the collapsing core has an approximately homogeneous density distribution, the envelope develops a power-law profile, $n_{\rm H} \propto r^{-2.2}$ (e.g., Omukai & Nishi, 1998; Ripamonti *et al.*, 2002). Figure 2.3 also shows the radially-averaged density profiles in the nine different clouds at the time when the central density reaches 10^{12} cm^{-3}. Densities at the same radial distance can differ among the clouds by more than a factor of ten. The variation of the density structure is attributed to the different thermal evolution during the collapse. Some bumps in the density profiles indicate the presence of neighboring density peaks, large disk- or bar-like structure, and/or

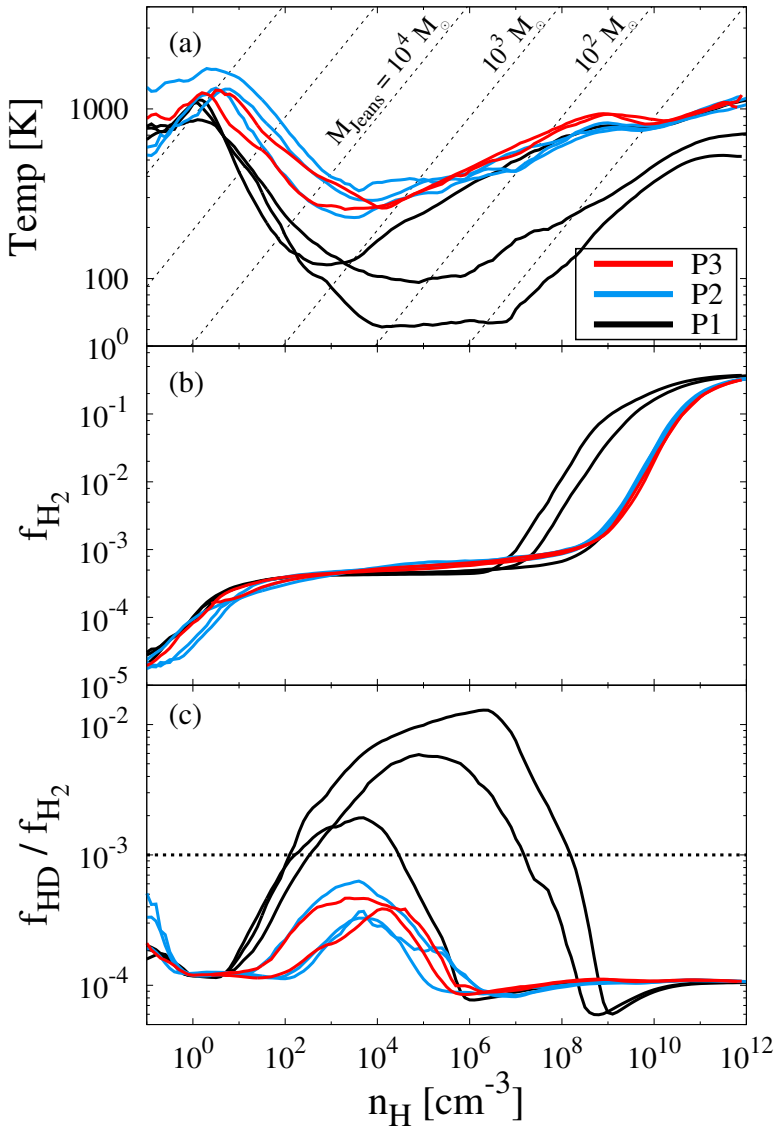

Figure 2.4. Averaged profiles of primordial star-forming clouds as a function of gas number density, $n_{\rm H}$, for the same nine clouds in Figure 2.3: (a) gas temperature, (b) H_2 fraction, and (c) HD fraction which are the mass-weighted mean values of the SPH (gas) particles for each density bin when the central (highest) density is $n_{\rm H,cen} = 10^{12}$ cm^{-3}. The dashed lines in panel (a) show the $n_{\rm H} - T$ relation for the given Jeans masses $M_{\rm Jeans} \propto T^{3/2}/n_{\rm H}^{1/2}$. The dashed line in panel (d) shows the critical value $f_{\rm HD}/f_{\rm H_2} = 10^{-3}$ above which the HD cooling becomes efficient to cool the primordial cloud further more.

fragmenting clumps in the collapsing clouds (discussed later in Sec. 2.2.5.2.2).

2.2.2.2 Thermal Evolution During the Collapse

The thermal evolution of a collapsing cloud is largely determined by non-equilibrium cooling and heating processes. The so-called $\rho - T$ profiles in the envelope at a particular

time essentially trace the thermal evolution of the contracting core due to the self-similar nature of the collapse. The most important coolant of the primordial gas is molecular hydrogen H_2. Figure 2.4(a) shows that the cloud is heated up to $\sim$ 1000 K due to virialization at $n_{\rm H} < 10^2$ cm^{-3}, as the H_2 fraction slowly increases (Fig. 2.4b) via the two-body reaction (Eqs. 1.9 and 1.10). When a sufficient amount of H_2 is formed, the gas temperature begins to decrease to $100 - 200$ K due to H_2 line cooling.

Figure 2.4(a) shows that, in several cases, the gas temperature becomes lower than 200 K, which is unexpectedly low for the so-called Pop III.1 star formation scenario (Bromm *et al.*, 2009). The low temperature tracks are rather similar to that expected from Pop III.2$_{\rm I}$ star formation where HD molecular cooling operates. Indeed, Figure 2.4(c) shows that HD molecules are efficiently formed in these cases, suggesting that the low temperatures are due to HD line cooling. HD cooling has been thought to be usually negligible for Pop III.1 star formation (Ripamonti, 2007). In the Pop III.2$_{\rm I}$ star formation scenario H_2 formation is enhanced if the initial electron abundance is high (see Eq. 1.9). As a result, the temperature becomes low enough to form HD molecules, and even drops below 100 K with the additional HD molecular cooling. This is not the case, however, since there is no significant enhancement of the electron abundance.

Interestingly, the time-scale of the cloud collapse plays an important role in determining the thermal evolution. Although the collapse time-scale is always comparable to the free-fall time-scale for an average given density, the collapse can be decelerated, e.g., by rotational support if the cloud has finite angular momentum. When the collapse is slower, more H_2 molecules are produced via reactions (1.10). With the enhanced radiative cooling from the more abundant H_2, the temperature becomes sufficiently low to allow HD formation and cooling. Note that the slight difference in molecular binding energy triggers chemical fractionation at low temperatures. Once HD molecular line cooling begins to operate, the temperature decreases further down to a few tens of Kelvin. One extreme case in Figure 2.4(a) shows that the temperature attains the floor of the cosmic microwave background (CMB), $T_{\rm CMB} = 2.73\ (1+z) \simeq 50$ K at $z \simeq 20$. This clearly shows the effects of the slow collapse are significant indeed. When the collapse time is only a few times longer than the free-fall time, the resulting thermal evolution becomes similar to that of the Pop III.2$_{\rm I}$ case driven by HD cooling. This behavior has been also confirmed by using one-zone models for following the thermal evolution during the cloud collapse (e.g., Omukai, 2000) and by using 1D hydrodynamic simulations (Ripamonti, 2007). This thesis finds this HD-cooling mode in the 3D cosmological simulations.[*1] The detailed analysis is described in Appendix C.

HD cooling becomes inefficient at densities greater than 10^8 cm^{-3}. However, the abundance of H_2 molecules begins to increase as the so-called three-body formation process (Eq. 1.14) comes into play, which converts nearly all the hydrogen to molecules before the density reaches 10^{12} cm^{-3}. After that, the cooling process in the collapsing cloud is dominated by H_2 molecules.

[*1] Section 1.2.3.1 suggests the alternative route for HD cooling due to shock-waves driven by halos' merger but the obtained HD-cooling clouds in these simulations are not the mode.

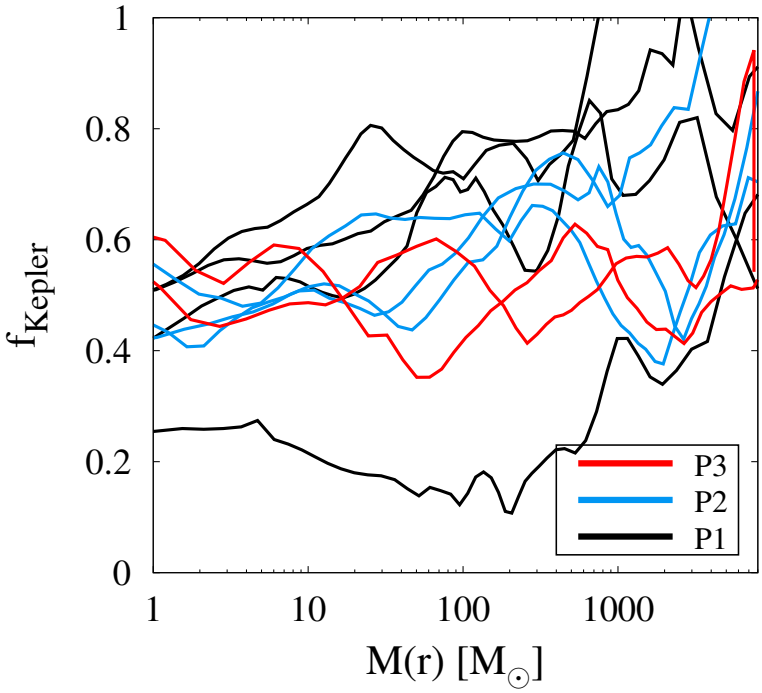

Figure 2.5. Averaged profiles of the degree of rotational support, $f_{\rm Kepler} = v_{\rm rot}/v_{\rm Kepler}$, for the same nine clouds in Figure 2.3 at the moment when $n_{\rm H,cen} = 10^{12}$ cm^{-3}. The lowest line represents the case for which the cloud is most slowly rotating in the sample (see Fig. 2.15a and Table 2.3). Generally, $f_{\rm Kepler}$ is large for P1, P2, and P3 in this order.

2.2.2.3 Cloud Collapse and Angular Momentum

The angular momentum of a cloud is one of the key factors which influence the radial infall velocity and thermal evolution during the collapse. A cloud with a low angular momentum gravitationally contracts roughly over a free-fall time. Figure 2.5 shows for the nine representative cases the radial distributions of $f_{\rm Kepler}$, the ratio of the azimuthal rotation velocity $v_{\rm rot}$ (defined as the azimuthally averaged velocity perpendicular to the total angular momentum vector inside the enclosed mass $M(r)$) to the Keplerian velocity $v_{\rm Kepler} = \sqrt{GM(r)/r}$.

The profiles of $f_{\rm Kepler}$ are moderately correlated to the thermal evolution of the clouds, albeit with a large variance at each mass scale $M(r)$. On average, clouds with low temperatures have higher $f_{\rm Kepler}$ (recall that the red, blue, and black lines represent clouds with progressively lower temperatures in this order; see also Figure 2.4a). Interestingly, the variance of $f_{\rm Kepler}$ decreases with decreasing enclosed mass $M(r)$ whereas the median value is nearly constant around $\simeq 0.5$ (see also Abel *et al.*, 2002), independent of $M(r)$.

The cloud's degree of rotation also influences the density distribution during the collapse. Figure 2.6 shows the projected density distributions for three clouds with different

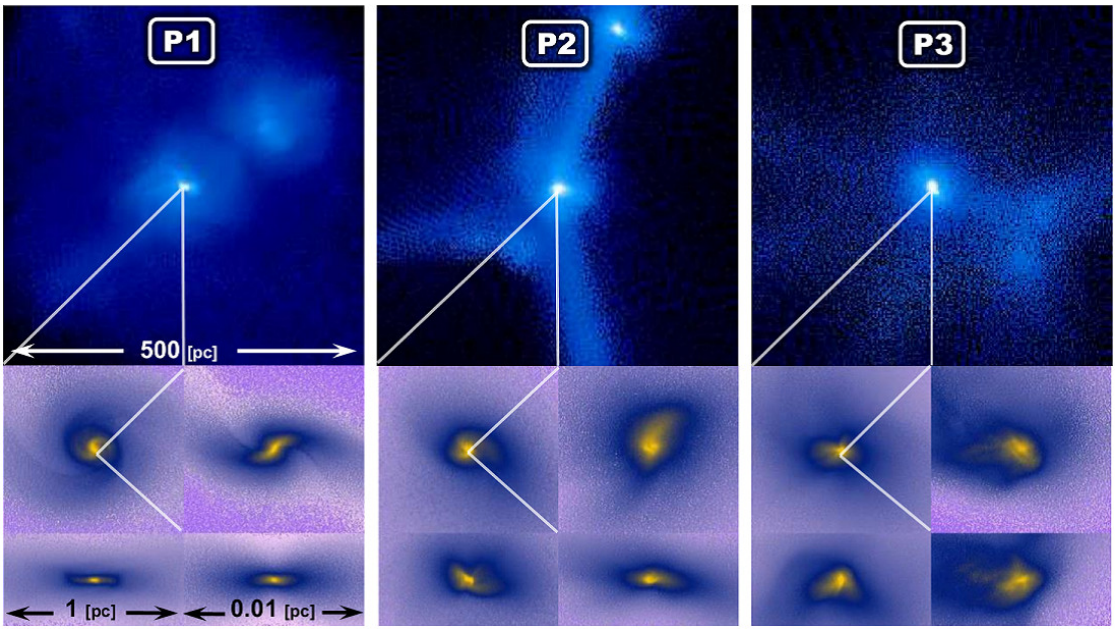

Figure 2.6. Projected gas density distributions for three representative cases at the moment when $n_{\rm H,cen} = 10^{12}$ cm^{-3} whereby the protostars go through three characteristic evolutionary paths (P1, P2, and P3 from left to right) in the later accretion phase. The panels show the gas distribution in regions of 500, 1, and 0.01 pc on a side, respectively and both the face-on and edge-on views are shown for the last two. Note the rotationally supported disk-like structure for the P1 case.

initial angular momenta. The left panel clearly shows a disk-like structure with notable spiral arms, suggesting that a self-gravitating disk is forming around the protostar. Although the disk-like structure disappears for the lower angular momentum cases, the middle and right panels still show a variety of non-spherical structures. This suggests a variety of dynamics in the gravitational collapse of the primordial clouds.

2.2.3 Later Accretion Stage

This section shows the calculation results for the later accretion stage, the period during which a protostar gains most of its final mass.

2.2.3.1 Mass Accretion Histories and the Final Stellar Masses

Figure 2.7(a) shows the accretion histories for the entire sample of 110 protostars. The accretion rates gradually decrease with increasing protostellar mass in all the cases. There are, however, substantial variations among the clouds and the accretion rates differ more than a factor of 10 when the stellar masses are only a few solar masses.

Figure 2.7(b) shows the response of protostellar evolution which also differ significantly, reflecting the variation of the mass accretion rates. The stellar effective temperature and the UV luminosity rapidly increase when a protostar approaches the ZAMS. At this point

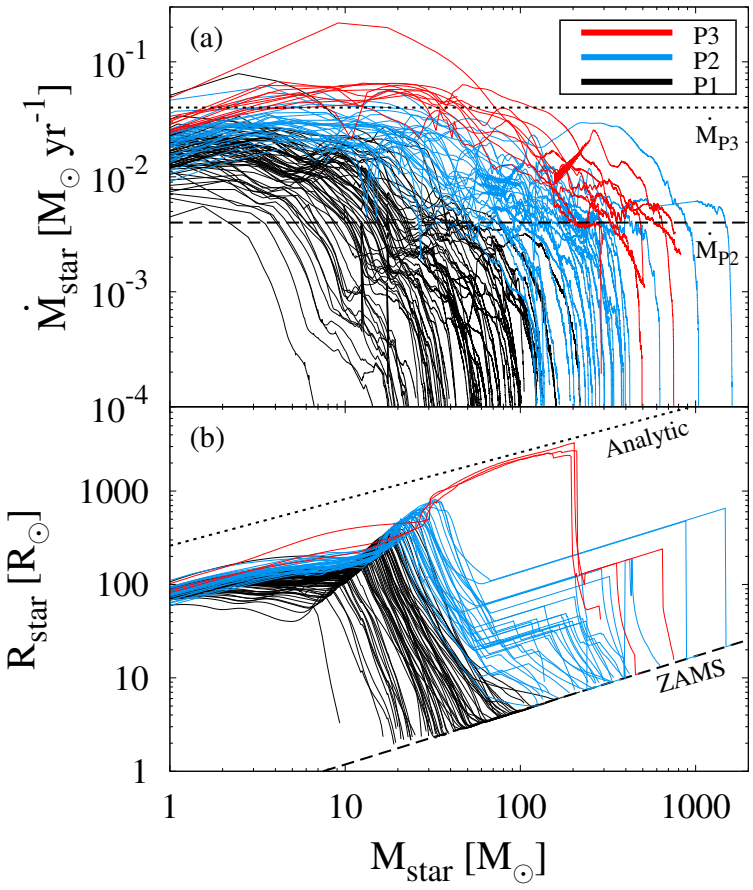

Figure 2.7. Accretion rates (panel a) and stellar radii (b) as a function of stellar mass for the entire sample. The colors represent the different paths of the protostellar evolution as in Figure 2.3. The two horizontal lines in panel (a) are critical values of accretion rates $\dot{M}_{\rm P2} = 0.004\ M_\odot\ {\rm yr}^{-1}$ (dashed; Eq. 1.24) and $\dot{M}_{\rm P3} = 0.04\ M_\odot\ {\rm yr}^{-1}$ (dotted; Eq. 1.25) . The two diagonal lines in panel (b) indicate $260 \times M^{0.5}\ R_\odot$ (dotted; super-giant protostar, Eq. 1.26) and $0.31 \times M^{0.58}\ R_\odot$ (dashed; ZAMS track derived from the calculation).

UV feedback becomes efficient and ultimately terminates the mass accretion onto the protostar. For high accretion rates, the protostar reaches the ZAMS when the mass is typically larger than one hundred solar masses. In general, the final stellar masses are greater in cases with higher mass accretion rates.

The wide variety of mass accretion profiles are caused by differences in the structure of the gas envelope at the birth of the protostellar core. Figure 2.8 shows the radially averaged profiles of the mass accretion rate estimated from the instantaneous density and velocity distributions of the envelope, $4\pi r^2 \rho(r) v_{\rm rad}(r)$. Note that this is not the accretion history plotted in Figure 2.7(a). The "predicted" accretion rates differ quite substantially, being qualitatively consistent with the actual accretion histories found in the radiation hydrodynamic simulations (compare Figs. 2.7a and 2.8a). The thermal

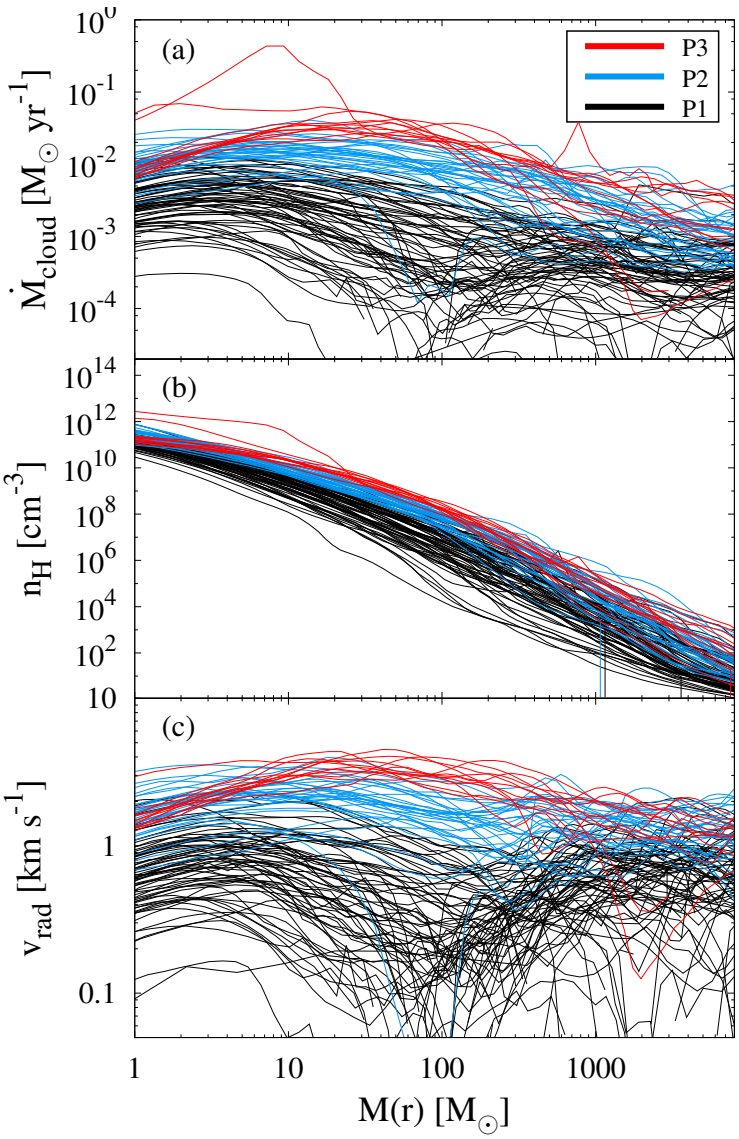

Figure 2.8. Averaged radial distribution for 110 cases of (a) the gas infall rate $\dot{M}_{\rm cloud} = 4\pi r^2 \rho(r) v_{\rm rad}(r)$, (b) the density, and (c) infall velocity profiles when $n_{\rm H,cen} = 10^{12}$ cm^{-3}. The colors represent the three paths of the protostellar evolution as in Figure 2.3.

evolution during the pre-stellar collapse phase plays a key role in shaping the structure of the accreting envelope. Because the thermal evolution depends on the contraction time-scale, mechanisms that affect the gravitational collapse such as the cloud's angular momentum likely affect the overall gas accretion rate. The origin of the various accretion histories is discussed in Section 2.2.4.2.

2.2.3.2 Three Evolutionary Paths of Accreting Protostars

This subsection focuses on three representative cases characterized by the evolution of the protostellar radius: the KH contracting protostar (P1: 67 cases), the oscillating protostar

(P2: 31), and the super-giant protostar (P3: 12). Figure 2.9 shows the accretion histories for these three cases selected from the sample. The accretion rates are highest for P3 and lowest for P1. The figure also presents the accretion histories for the same cases but with the UV radiative transfer module switched off, which demonstrates that stellar UV feedback does indeed reduce the accretion rates and the final mass of the protostar late in the evolution. In all the cases, a bipolar $\mathrm{H\,II}$ region forms and finally shut off the mass accretion. Figure 2.10 shows the dynamical expansion of the $\mathrm{H\,II}$ region for three cases in which one can find apparent differences between three cases; density distribution, temperature of irradiated gas, and the expansion trend.

Case P1 exemplifies the KH contracting protostar studied in Hosokawa *et al.* (2011, 2012a). The panels (b) − (d) show that, in the adiabatic accretion phase when the protostellar mass is less than 10 $M_\odot$, the effective temperature and ionizing photon (EUV) luminosity is so low that stellar UV feedback is negligible. However, the EUV luminosity rapidly increases once the protostar begins KH contraction at $M_* \simeq 10\ M_\odot$. As the stellar radius decreases the effective temperature and the EUV luminosity rise. At first, the high accretion rate squelches the $\mathrm{H\,II}$ region (e.g., Yorke, 1986; Omukai & Inutsuka, 2002), but eventually the EUV flux is sufficient to ionize the infalling neutral material, driving an expanding bipolar $\mathrm{H\,II}$ region into the accretion envelope (see also Fig. 2.10). The expanding $\mathrm{H\,II}$ region accelerates the envelope gas outward. At the same time the circumstellar disk is irradiated by the stellar UV, creating a thermally driven disk wind as the disk gradually photo-evaporates. As the accretion rate rapidly decreases, the protostar contracts faster, further increasing the effective surface temperature, and the UV feedback becomes stronger. Figure 2.9 shows that the final stellar mass for the P1 case is fixed at $\simeq 30\ M_\odot$, just before the star's arrival to the ZAMS.

The evolution of P2 looks similar to P1's before KH contraction ceases at $M_* \simeq 60\ M_\odot$, when the stellar total luminosity reaches the Eddington value. The evolution after this differs from P1's. The stellar radius begins to increase with increasing mass, entering an oscillating phase.[*2] The effective temperature remains almost constant at $\simeq 3 \times 10^4$ K during this phase, and thus the stellar EUV luminosity does not increase. A bipolar $\mathrm{H\,II}$ region first appears late, when the stellar mass reaches $\simeq 100\ M_\odot$. The oscillating phase is over at $M_* \simeq 200\ M_\odot$, when the accretion rate falls below the critical rate $\dot{M}_{\rm P2} = 4 \times 10^{-3}\ M_\odot\ \mathrm{yr}^{-1}$ (Eq. 1.24), allowing the protostar to resume contraction toward the ZAMS. Mass accretion onto the star is finally halted at $M_* \simeq 300\ M_\odot$. It is remarkable that, in this case, a large portion of the surrounding gas, 200 $M_\odot$, is accreted onto the star well after the breakout of the $\mathrm{H\,II}$ region.

The protostar of representative P3 case enters the super-giant phase soon after the adiabatic accretion phase, when $M_* \simeq 30\ M_\odot$. The stellar radius monotonically increases with increasing mass, according to the relation (1.26). The radius exceeds 3000 $R_\odot$ when the stellar mass is $M_* \simeq 200\ M_\odot$. The effective temperature is still around 5000 K during this super-giant phase, which means that the EUV luminosity is too low to launch an

[*2] By using the simplified model for P2, the radius does *not* oscillate, see Appendix B.2.1.

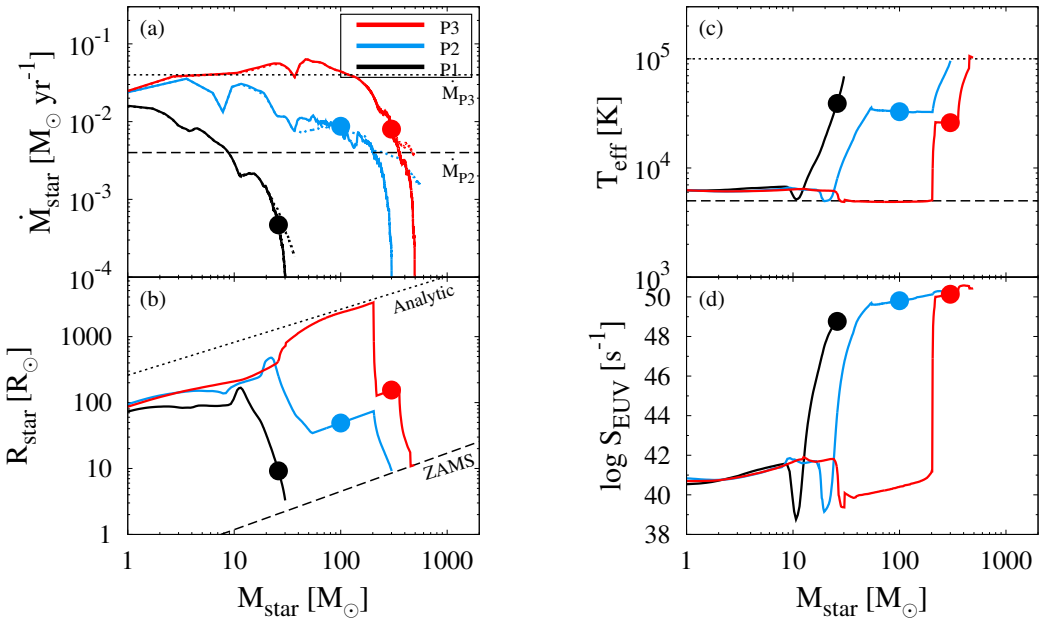

Figure 2.9. Three representative cases of the protostellar evolution as a function of the stellar mass: (a) accretion rates, (b) stellar radius, (c) surface temperature, and (d) ionized photon intensity. In panel (a), the solid and dashed lines represent the evolution with and without UV radiative feedback from the accreting protostar. The dashed and dotted lines in the panels (a) and (b) are the same as in Figure 2.7. Two horizontal lines in panel (c) indicate $T_{\rm eff} = 10^5$ K (dotted) and 5000 K (dashed). The filled circle marks the epoch when a bipolar H II region first appears in each case with UV radiative feedback.

H II region. The protostar begins to contract after the accretion rate falls below a few $\times 10^{-2}\ M_\odot\ {\rm yr}^{-1}$, the critical rate given by Eq. (1.25). The final contraction is very rapid because the KH time-scale of the super-giant protostar is very short, less than 10^3 years (e.g., Hosokawa *et al.*, 2012a). Shortly thereafter, KH contraction is interrupted, and the protostellar evolution becomes similar to P2. The H II region begins expanding when the stellar mass is $\simeq 300\ M_\odot$, which in turn reduces the accretion rate below the critical value $\dot{M}_{\rm P2}$. As the star contracts once again toward the ZAMS, the stellar UV feedback becomes stronger, and the stellar mass is finally fixed at $M_* \simeq 500\ M_\odot$.

Note that, in the cases of P2 and P3, the effective temperature of the expanding protostar remains low, which mostly explains why the breakout of the H II region occurs late, when the mass is $\simeq 200$ and $300\ M_\odot$, respectively. However, Figure 2.9(d) also shows that the EUV photon luminosity is in fact higher than the case of P1 when the H II region first emerges. This is explained by the fact that the accretion envelope is denser in P2 and P3 because of the higher accretion rates. More ionizing photons are needed to create an H II in dense regions, where hydrogen atoms recombine rapidly (see also Hosokawa *et al.*, 2012b).

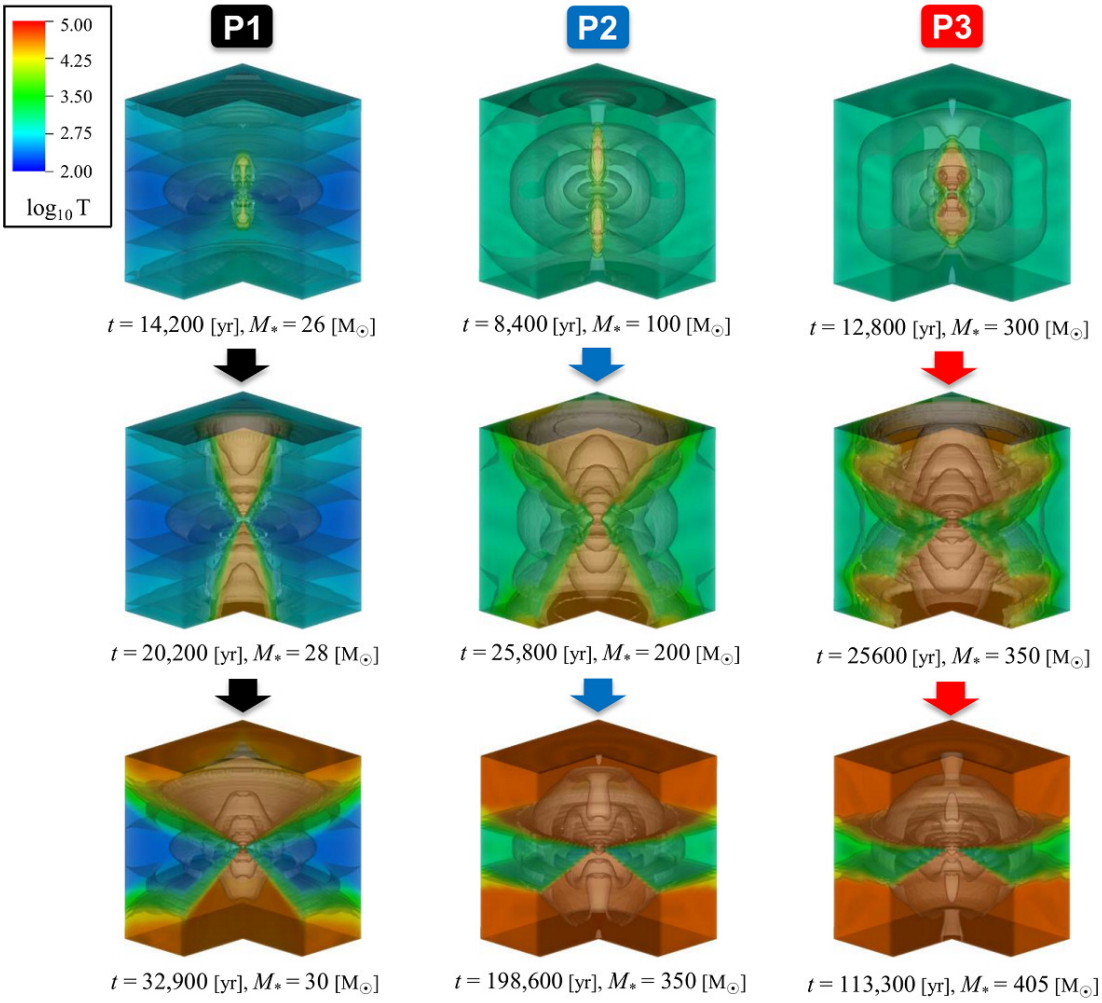

Figure 2.10. Expanding H II regions around the primordial protostar from top to bottom panels for the same three cases as in Figure 2.9. The plotted regions are cubes with 60000 AU on a side. The colors indicate gas temperature and the contours show the density structure. The main accretion takes place through the accretion disk on the equatorial plane. As the central protostar becomes more massive and the surface temperature increases, the ionizing photon production of the central star increases. H II regions are launched into the polar direction and the opening angles grow with time, eventually stopping the accretion.

2.2.4 Wide Range of Stellar Masses

Above simulations have followed the process of primordial star formation in a number of cosmological halos until the final stellar masses are determined. Figure 2.11 shows the resultant mass distribution of Population III.1 stars covering the wide range from 10 to 1600 $M_\odot$. The average mass is more massive for P3, P2, and P1 cases in this order (see

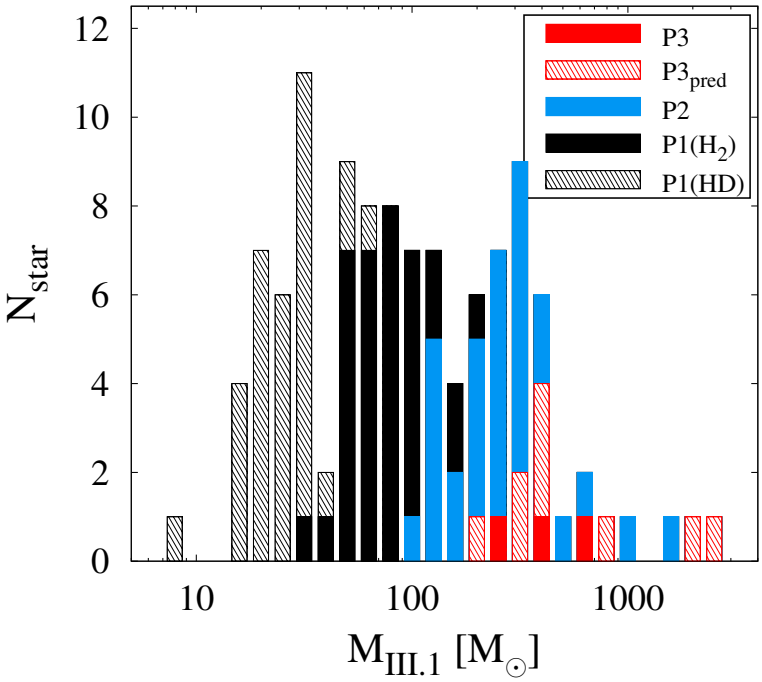

Figure 2.11. Final distribution of the calculated stellar masses for 110 Population III.1 cases. Histograms' colors represent the different paths of protostellar evolution; KH contracting protostar (P1; black), oscillating protostar (P2; blue), and super-giant protostar (P3; red). P1 cases are classified into two populations according to whether the HD cooling is inefficient, P1(H_2), or efficient, P1(HD). $P3_{pred}$ indicates the same cases as P3, except that the final masses are calculated from a correlation between the properties of the cloud and the resulting stellar mass (Eq. 2.1; see Appendix B.2.2).

Path	N_{sample}	$\overline{M_{III}}$ ($M_\odot$)	$\overline{z_{form}}$	$\overline{M_{vir}}$ ($10^5\ M_\odot$)	$\overline{M_{Jeans}}$ ($M_\odot$)	$\overline{\beta_{Jeans}}$
P1	67	51 ± 4	18.0 ± 0.6	3.1 ± 0.2	171 ± 20	0.35 ± 0.02
P2	31	282 ± 30	18.9 ± 0.8	4.1 ± 0.4	626 ± 81	0.30 ± 0.05
P3	12	483 ± 128	17.6 ± 0.7	5.1 ± 0.6	838 ± 119	0.21 ± 0.06

Table 2.2. Column 1: Evolutionary paths of protostar, Column 2: Number of samples for each path, Column 3: Final stellar mass, Column 4: Redshift when the central density reaches 10^6 cm^{-3}, Column 5: Virial mass of dark matter minihalos, Column 6: Jeans mass of star-forming cloud, and Column 7: Ratio of the rotation to gravitational energy of the cloud. All quantities are the averaged amount for each evolutionary path. Appendix D shows the list of original data.

Table 2.2) reflecting the different protostellar evolution which determines the strength of the stellar radiative feedback. In general, the final stellar mass is more massive with higher accretion rates onto the protostar (Fig. 2.7).

The final stellar masses is determined by the protostellar evolution depending on the accretion history. First, the stellar radiative feedback is ineffective unless $\dot{M}_{\rm star} > \dot{M}_{\rm P2}$ because of the radial expansion of the protostar. Figure 2.7 clearly shows the increase of freely accreted masses where the accretion rates first fall below $\dot{M}_{\rm P2}$ with increasing the average $\dot{M}_{\rm star}$. Furthermore, higher accretion rate prolongs much more the timescale of the following contraction phase because of the additional gravitational energy imported into the protostar. So one can evaluate how massive the protostar becomes from the accretion history, $\dot{M}_{\rm star}$. Such the accretion history is never known until the mass growth of accreting protostar is calculated but can estimated from the gas distribution around the protostar before the accretion phase, $\dot{M}(r)$. Figure 2.8 has already shown that $\dot{M}(r)$ largely depends on the cloud's properties: the density and velocity structure of the envelope around the protostar.

This section examines the origin of the wide distribution of stellar masses. First the following section focuses on the overall gas infall rates at two different mass scales of the parent gas cloud ("Jeans scale") and the host dark matter halo ("virial scale"). The final stellar masses are correlated to the infall rates measured at both of these scales. Then the following section shows how the infall rates are related to fundamental properties of the star-forming gas clouds and those of the host halos.

2.2.4.1 Stellar Masses and Gas Infall Rates

2.2.4.1.1 Infall Rates in Gas Clouds

A characteristic mass scale of a gravitationally contracting gas cloud would be the Jeans mass $M_{\rm Jeans}$ (Eq. 1.13). A cloud is expected to collapse when the mass within a given radius $M(r)$ exceeds the local Jeans mass. For a primordial gas cloud, this run-away collapse occurs when the first temperature dip appears in the thermal evolutionary track (Fig. 2.4a), i.e., at the so-called loitering regime (e.g., Bromm *et al.*, 2002). In several of the dark matter halos, run-away collapse occurs even though the ratio $M_{\rm enc}(r)/M_{\rm Jeans}$ is (slightly) smaller than unity. This is because the above Jeans mass provides a critical mass for gravitational stability only under some idealized conditions, e.g., assuming static motion for the initial condition, which is not realized in 3D simulations, and the isothermal equation of state. Here, the mass of the collapsing cloud is defined to be the mass within a radius at which the ratio of the enclosed mass to the Jeans mass takes the maximum value during the collapse. The loitering regime appears at $n_{\rm H} \simeq 10^7$ cm^{-3} on the lowest temperature model (Fig. 2.4a) so the Jeans masses are determined for the collapsed clouds when $n_{\rm H,cen} = 10^7$ cm^{-3}. Typically, a primordial gas cloud that cools via H_2 line cooling has a large mass $M_{\rm Jeans} \sim 1000\ M_\odot$. Note that HD line cooling also operates in some clouds. Such clouds have relatively small masses $M_{\rm Jeans} \sim 10-100\ M_\odot$ when they collapse gravitationally.

As mentioned above, how massive the final stellar mass depends on how large the ac-

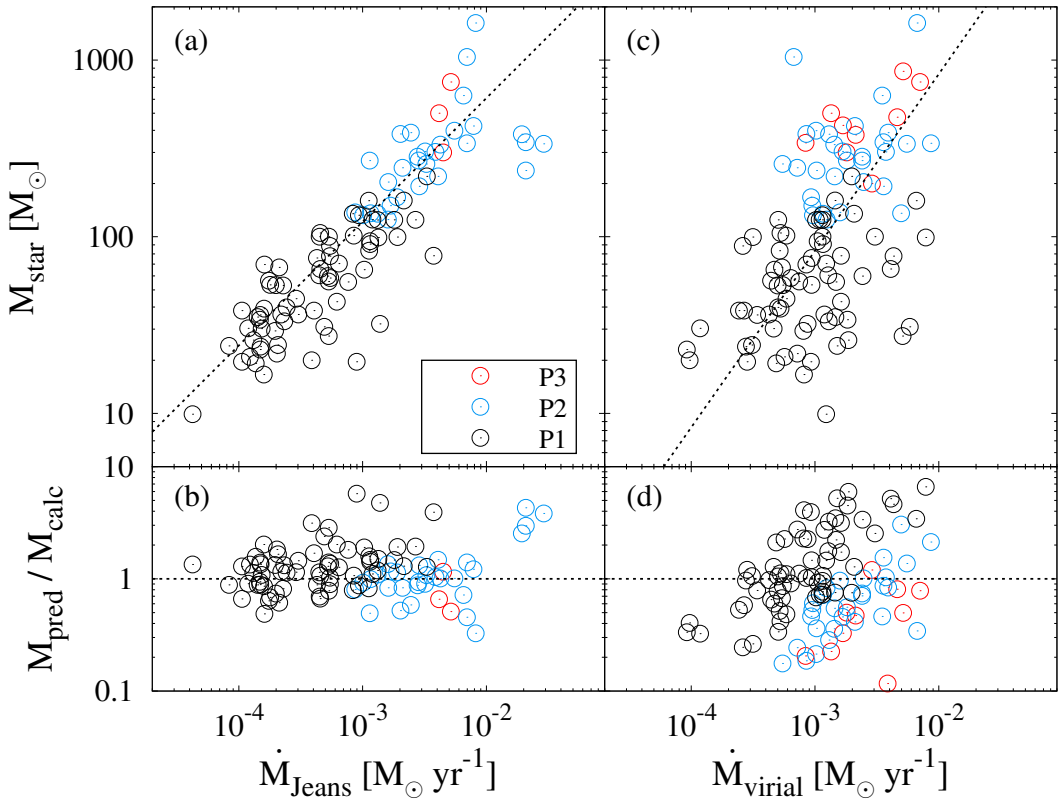

Figure 2.12. Final stellar masses as a function of gas infall rates over Jeans scales (left panels) or virial scales (right) at $n_{\rm H,cen} = 10^7$ cm^{-3}. Three colors represent the evolutionary paths of the protostellar evolution. The dotted lines in panels (a) and (b) represent the fitting functions given by Eqs. (2.1) and (2.2). The panel (b) shows the ratio of the calculated stellar mass to the estimated one by the fitting formula (Eq. 2.1).

cretion history onto the protostar, in other words, $\dot{M}(r)$ just before the accretion phase. For simplicity, how large $\dot{M}(r)$ is substituted by the instantaneous mass infall rate at the Jeans scale $\dot{M}_{\rm Jeans} = 4\pi r^2 \rho(r) v_{\rm rad}(r)$ evaluated at radius within which the enclosed gas mass is $M_{\rm Jeans}$. Figure 2.12(a) supports the above notion, showing a good correlation between the final stellar masses and $\dot{M}_{\rm Jeans}$. The fitting formula for the correlation between the stellar masses and infall rates

$$M_{\rm III.1} = 250 \left(\frac{\dot{M}_{\rm Jeans}}{2.8 \times 10^{-3}\ M_\odot\ {\rm yr}^{-1}} \right)^{0.7} M_\odot\ , \tag{2.1}$$

is shown in Figure 2.12(a) as the dotted line.[*3] Both accretion time, $t_{\rm acc}$, and averaged accretion rate, $M_{\rm star}/t_{\rm acc}$, are positively correlated with $\dot{M}_{\rm Jeans}$. Figure 2.12(b) suggests that the deviations from the above relation are indeed small. This relationship should

[*3] The coefficients of the formula depends on the evaluating condition, i.e., $M_{\rm III.1} \propto \dot{M}_{\rm Jeans}^{0.8}$ if the Jeans masses are determined when $n_{\rm H,cen} = 10^{12}$ cm^{-3}.

be quite useful, because one can estimate the final stellar mass from $\dot{M}_{\rm Jeans}$ when the primordial cloud reaches the loitering regime without following the detailed protostellar evolution.

2.2.4.1.2 Infall Rates at Large Scales

Primordial gas clouds are formed in dark matter minihalos, and one can thus expect that some properties of the host dark halos will affect the structure of the gas clouds and possibly the in situ formation of primordial stars as well. By evaluating the density and radial velocity at the virial radius of a halo $r_{\rm vir}$, the infall rates at the virial scale are determined as $\dot{M}_{\rm vir} = 4\pi r_{\rm vir}^2 \rho(r_{\rm vir}) v_{\rm rad}(r_{\rm vir})$. The gas infall rates at the virial scale indeed correlate with the infall rates at the Jeans scale. Similar to Eq. (2.1), Figure 2.7(c) shows a good correlation

$$M_{\rm III.1} = 100 \left(\frac{\dot{M}_{\rm vir}}{1.2 \times 10^{-3}\ M_\odot\ {\rm yr}^{-1}} \right)\ M_\odot\ , \tag{2.2}$$

for 110 simulation results. The correlation at the halo scale is somewhat weaker than that at the cloud scale. This is probably because there is a time gap between the virialization of the halos and the onset of collapse. Nonetheless, the presence of such correlation suggests that the chemo-thermal evolution of the star-forming cloud, the resulting accretion history and the final stellar mass are affected, at least partially, by the very early conditions of the dark matter halos.

2.2.4.2 Key Quantities Shaping the Mass Distribution

Figure 2.12 has shown a positive correlation between the final stellar masses and the gas infall rates. This motivates us to further investigate the origin of the diversity of infall rates. To this end this section first considers the effects of rotation.

2.2.4.3 Correlation at the Jeans Scale

To first order the gas mass accretion rate of a Jeans unstable cloud is approximately $\dot{M} \propto T^{3/2}$ (Eq. 1.19). Note that the collapsing cloud mass is not strictly equal to the Jeans mass. Gravitational collapse does not always proceed over a free-fall time-scale because rotation can prevent or delay the collapse. The actual *collapse time* likely depends on the rotation parameter, the ratio of the rotational energy to gravitational energy,

$$\beta_{\rm Jeans} = \frac{\Omega_{\rm Jeans}^2 R_{\rm Jeans}^3}{3GM_{\rm Jeans}}\ , \tag{2.3}$$

where $\Omega(r) = |(\vec{r} \times \vec{v(r)})/r^2| = v_\perp(r)/r$ with $v_\perp(r)$ at distance r being the velocity perpendicular to the rotational axis and $\Omega_{\rm Jeans}$ is defined at the cloud radius. Naively, a cloud with a large $M_{\rm Jeans}$ and a low $\beta_{\rm Jeans}$ is expected to collapses quickly and therefore that the gas accretion rate onto the protostar in the cloud is large (see also Table 2.2).

Figure 2.13(a) shows how the final stellar masses depend on the various Jeans masses and rotation parameters. As expected, the final stellar mass is higher for larger cloud

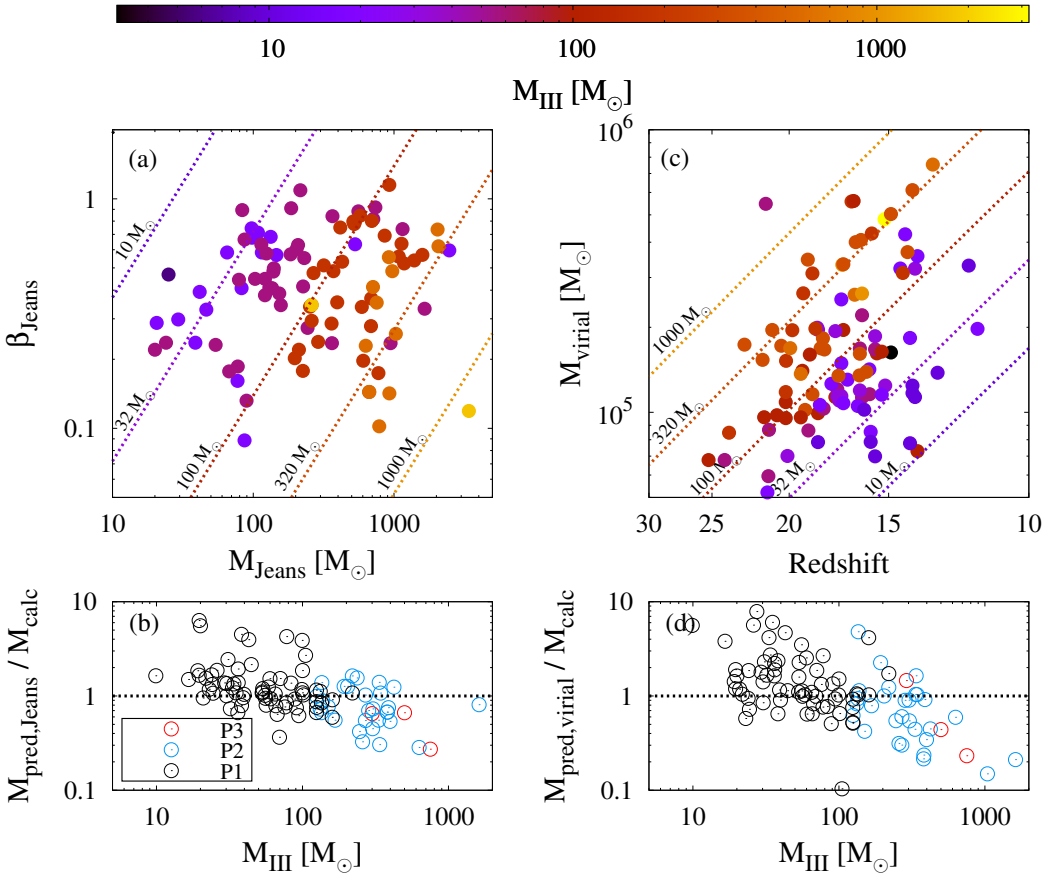

Figure 2.13. Dependences of final stellar masses on two properties at the Jeans and virial scales; the cloud mass and the rotation parameter $\beta_{\rm Jeans}$ at the Jeans scale (panel a) and the formation redshift and the halo mass (c), for each of the sample of 110 clouds. The different colors are indicative of the final stellar masses (see color scale at the top). The dotted lines represent the fitting functions given by Eq. (2.4) for $M_{\rm III} = 10$, 32, 100, 320, and 1000 $M_\odot$. The panels (b) and (d) show ratios of estimated masses by Eqs. (2.4) and (2.6) to final stellar masses.

mass and/or for lower rotation parameter. The dependence is approximately

$$M_{\rm III.1} = 250 \left(\frac{M_{\rm Jeans}}{800\ M_\odot} \cdot \frac{0.3}{\beta_{\rm Jeans}} \right)^{0.7} M_\odot \ , \tag{2.4}$$

which also shows the dependences of the infall rates on Eq. (2.1),

$$\dot{M}_{\rm Jeans} = 2.8 \times 10^{-3} \left(\frac{M_{\rm Jeans}}{800\ M_\odot} \cdot \frac{0.3}{\beta_{\rm Jeans}} \right) M_\odot\ {\rm yr}^{-1} \ . \tag{2.5}$$

The relation (2.4) is plotted for several different stellar masses in Figure 2.13(a). Whereas Eq. (2.4) approximately follows the variations of the stellar mass, there are substantial deviations from the fit as shown in Figure 2.13(b).

2.2.4.4 Correlation at the Virial Scale

The infall rates at the halo virial radii are also correlated with two quantities, the redshift at which a halo forms and the mass of the dark halo. Thus the resulting final stellar mass likely depends on these parameters of the host halo. Figure 2.13(c) shows the final stellar masses for different sets of z and $M_{\rm vir}$; massive stars preferentially form at higher redshifts and in more massive dark halos. A good fit providing the estimate for the stellar mass is

$$M_{\rm III.1} = 100 \left(\frac{1+z}{20}\right)^3 \left(\frac{M_{\rm vir}}{3\times10^5\ M_\odot}\right)^2 M_\odot\ , \tag{2.6}$$

which with use of Eq. (2.2) can be converted to

$$\dot{M}_{\rm vir} = 1.2\times10^{-3} \left(\frac{1+z}{20}\right)^3 \left(\frac{M_{\rm vir}}{3\times10^5\ M_\odot}\right)^2 M_\odot\ {\rm yr}^{-1}\ . \tag{2.7}$$

Although there is substantial scatter for small cloud masses (Fig. 2.13d), Eq. (2.6) provides a reasonable estimate of the final stellar mass using basic properties of the host dark halo.

2.2.4.4.1 Origin of Dependence

It is interesting to study why the two parameters z and $M_{\rm vir}$ control the infall rates at the virial scale, and why the final stellar masses correlate with the large-scale infall rates. The final stellar mass sensitively depends on the thermal evolution of a collapsing cloud. Let us suppose that the infall rate is approximately proportional to $M_{\rm vir}/t_{\rm ff}$ with some variance due to rotation. Since the mean density within a collapsed halo scales with the mean density of the universe at the epoch z as

$$\rho_{\rm crit}(z) \equiv \frac{3H^2(z)}{8\pi G}\ , \tag{2.8}$$

$$\frac{H^2(z)}{H_0^2} \simeq \Omega_{\rm m}(1+z)^3 + \Omega_\Lambda\ . \tag{2.9}$$

The above estimate should display a dependence $M_{\rm vir}/t_{\rm ff} \propto M_{\rm vir}/\rho_{\rm vir} \propto M_{\rm vir}(1+z)^{3/2}$. This qualitatively explains the overall trend, but the actual dependences are stronger (Eq. 2.7).

The additional dependence could be attributed to the degree of halo spin. As presented later in Chapter 3, on average the spin parameter decreases with increasing redshift. At high redshifts, dark matter halos with a given mass are formed from high σ fluctuations of the initial density field. Such halos acquire systematically smaller amounts of angular momentum via tidal interaction with the surrounding structure. The rotational support at the halo scale would be thus inefficient at the higher redshift, which explains the additional dependence on redshift in Eq. (2.7).

2.2.4.4.2 Comparison with the Previous Studies

It is worth comparing above findings with the conclusion of previous studies. Gao *et al.* (2007) have presented simulations of eight primordial gas clouds. Their gas clouds show

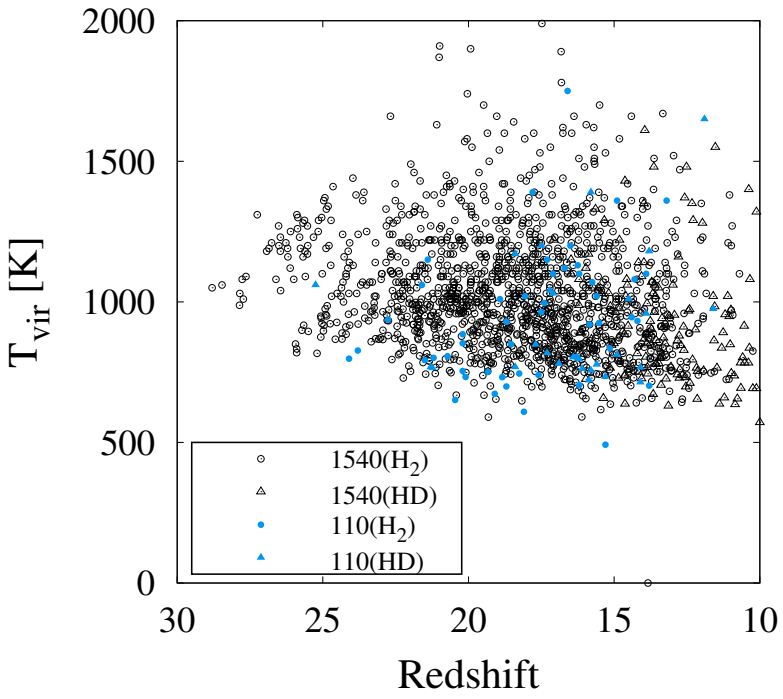

Figure 2.14. Virial temperature for all the calculated cases shown in this thesis when $n_{\rm H,cen} \sim 10^7$ cm^{-3} as a function of the formation redshift. The circles and triangles correspond to H_2- and HD-cooling clouds, respectively.

significant scatter in the instantaneous mass accretion rate, over one order of magnitude (see figure 11 in Gao *et al.*, 2007). However, they did not study in detail correlations between the accretion rate and halo mass etc., and thus the origin of scatter among the collapsing clouds remained unclear. It is likely that the scatter is caused by a combination of rotation, halo mass, and the collapse epoch, as discussed in this section. O'Shea & Norman (2007) have presented a statistical study of primordial cloud formation. On the assumption that the stellar mass is proportional to the overall gas infall rate at some initial epoch, they argue that smaller mass stars would form at higher redshifts. This appears inconsistent with the obtained correlation $M_{\rm III} \propto (1+z)^{2.45}$. O'Shea & Norman (2007) have claimed that the redshift-dependence of the virial temperature of a halo with a given mass $T_{\rm vir} \propto M_{\rm vir}^{2/3}$ $(1+z)$ (Eq. 1.3) is essential for determining accretion rates onto the protostar. In an early stage of primordial cloud formation, H_2 molecules are produced via the H^- channel (Eq. 1.10), which occurs efficiently at higher temperatures. The above dependence of $T_{\rm vir} \propto (1+z)$ can be understood because slightly more H_2 molecules are formed in a cloud at high redshifts. The resulting temperature of the cloud is lower, and the mass accretion rate onto a protostar would be correspondingly lower because of the relation $\dot{M} \propto T^{3/2}$. This argument holds for halos with a fixed mass. This study has a larger number of halos that have a wide range of the virial mass. Figure 2.14 shows that, for the calculated cosmological halos that form at different redshifts, the virial

temperatures do not simply scale with the collapse redshifts and they are approximately constant $T_{\rm vir} \simeq 1000$ K for collapse.[*4] This is reasonable because chemical reactions should take place at the same rate at a constant gas temperature (e.g., Glover, 2013). Therefore, if the virial temperature (instead of mass) is fixed, the corresponding halo mass is lower at higher redshifts, which cancels out the z-dependence in Eq. (1.3).

Note that, whereas the equilibrium H_2 abundance is an increasing function of the temperature, the amount of H_2 molecules necessary to cool the gas is a *decreasing* function of the gas temperature (see figure 2 in Glover, 2013). The balance between the two processes sets the critical temperature above which the gas can cool and condense (Yoshida *et al.*, 2003). Because the calculation selects the dark halos where the primordial gas clouds are formed via H_2 cooling, the gas temperatures as well as H_2 abundances do not differ much between members of the sample. Note also that the z-dependence in the relation (3.6) is attributed to the collapse time rather than the virial temperature, as explained above. Overall, with those large number of gas clouds, one is able to explore a large parameter space such as halo mass and collapse epoch and thus is able to find correlations between multiple quantities.

2.2.5 Discussions

2.2.5.1 Effect of DM treatment

The cosmic gravitational source is dominated by DM component and the first object inside which the primordial stars form is dark matter minihalo (Virial scale). After the star-forming cloud reaches the gravitationally unstable state (Jeans scale), it collapses under own gravity with releasing its internal energy via the radiative cooling. Then when does the dominant material which controls the primordial star-formation switch from DM to gas? The fact is that the DM density is more than gas density until the cloud begins the gravitational collapse. So the simulation should resolve the DM cusp structure inside the minihalo to correctly calculate the formation of gas cloud and its properties (e.g., Umemura *et al.*, 2012).

The calculation in this thesis adopt the particle-splitting technique (Sec. 2.2.1.1) to keep the numerical resolution of DM component. Figure 2.3 shows the resultant DM density profile averaged for 110 cases which crosses the gas density profile at 1 pc and $n_{\rm H,cen} = 10^3 - 10^4$ cm^{-3}. Such the crossing phase corresponds to the loitering phase of collapsing gas cloud (Fig. 2.4). If the calculation switches off the particle splitting of DM component, the formation of gas cloud inside the DM minihalo delay and the cloud's properties at the Jeans scale must be mistaken. Furthermore, such high-resolutional DM calculation is also necessary to study the sub-structures which may cite the star-forming cloud nearby and inside the DM minihalo (Fig. D.1 and Sec. 2.2.5.2.2). The next

[*4] The set of samples in O'Shea & Norman (2007) also shows a large scatter of halo mass in the range of $1.5 \times 10^5 < M_{\rm vir}/M_\odot < 7 \times 10^5$. However, they suggest that the accretion rates depend only on the collapse redshift. One speculation is that the apparent discrepancy is seen simply because the statistical set of 12 samples is too small to find the dependence on two variables, $\{z_{\rm vir}, M_{\rm vir}\}$.

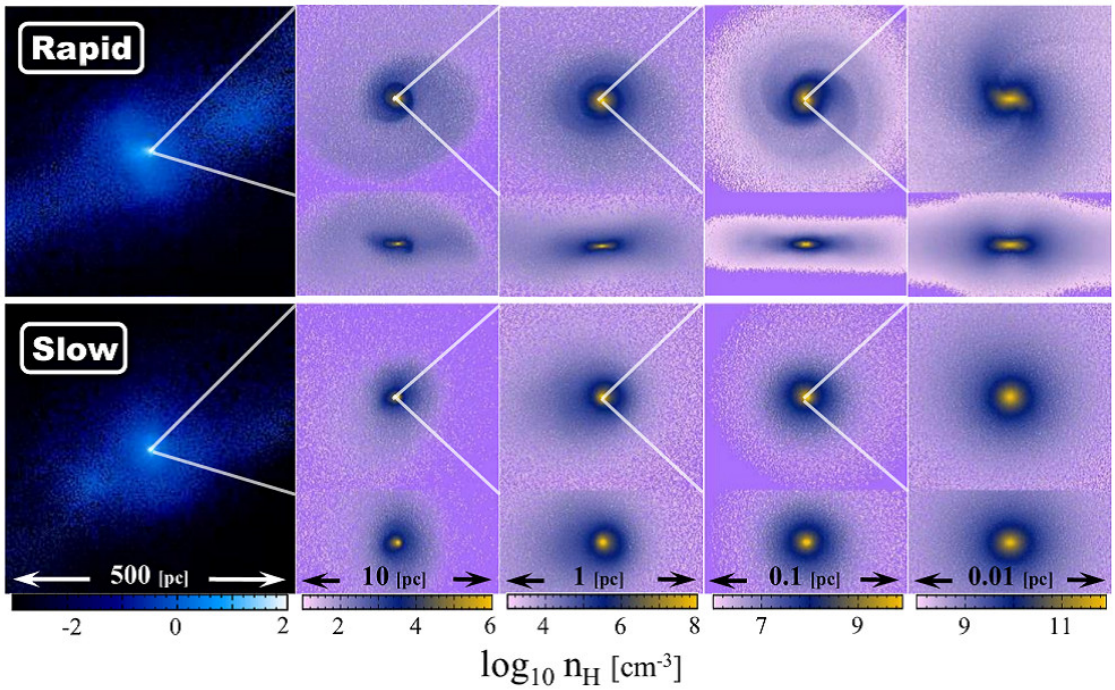

Figure 2.15. Projected gas density distributions when the central density reaches 10^{12} cm^{-3} for two extreme cases: the most rapidly (*top*) and the most slowly (*bottom*) rotating clouds. Table 2.3 summarizes the physical properties of theses clouds.

Case	$M_{\rm III}$ ($M_\odot$)	$z_{\rm form}$	$M_{\rm vir}$ (10^5 $M_\odot$)	$M_{\rm Jeans}$ ($M_\odot$)	$\beta_{\rm Jeans}$
Rapid	9.9	14.90	5.24	25	0.579
Slow	105.0	13.80	2.86	278	0.088

Table 2.3. Each column header has the same meaning as in Table 2.2.

chapters find the similar results from more than 10 times sample (DM density profile in Fig. 3.7 whereas sub-structures in Fig. 4.6). It is necessary to calculate the primordial star formation correctly that the DM component is always resolved until its density reaches $\sim 10^4$ cm^{-3} at least.

2.2.5.2 Various Sub-structure of Star-forming Clouds

The variety of mass accretion histories and hence the final stellar masses likely originate from different initial conditions during formation of gas clouds. The overall shapes and structures of collapsing gas clouds reflect different initial conditions. More than one hundred sample members in the simulations contains a few cases which show very different properties. The following paragraphs discuss these clouds in greater detail.

2.2.5.2.1 The Most Rapidly and the Most Slowly Rotating Clouds

Rotation of a cloud plays a critical role in determining the thermal evolution during the pre-stellar collapse. Figure 2.15 presents the density distributions at multiple epochs for the two extreme cases of very rapidly and very slowly rotating clouds (*top* and *bottom* panels; Table 2.3 shows their properties). With fast rotation, the cloud has a disk-like structure that is nearly rotationally supported. Interestingly, this particular cloud is prominent also in the other figures; it shows the lowest temperature evolution track in Figure 2.4 and the slowest accretion history in Figure 2.7. The cloud collapses slowly because of rotational support, and cools down to $\simeq$ 50 K, almost reaching the CMB temperature floor at $T_{\rm CMB} \sim 2.73(1+z)$ K. The resulting final stellar mass is only 9.9 $M_\odot$, which is the smallest among samples.

The opposite limiting case of the most slowly rotating cloud is presented in the lower panels of Figure 2.15. The cloud shows little indication of a flattened structure and almost no difference between the face-on and edge-on views. This case corresponds to the case with the lowest value of $f_{\rm Kepler}$ plotted in Figure 2.5. It has $f_{\rm Kepler} \simeq 0.2$, less than half of the average. Without strong rotational support, the cloud quickly collapses and the gas mass accretion rate onto the central protostar is large, yielding the final mass of $\simeq 100\ M_\odot$ (The slowest rotating cloud does not form the most massive star because the protostellar evolution depends also on the cloud mass at the onset of collapse, $M_{\rm Jeans}$; see Figure 2.13a). Clearly, nearly spherical accretion is a favored condition for the formation of very massive primordial stars.

2.2.5.2.2 Multiple Density Peaks

Some of samples show the formation of multiple density peaks in and around a single gas cloud. Figure 2.3 has already shown their signatures as humps in the radial density profiles. The sample contains seven close density peaks in six cases and Figure 2.16 shows the projected gas density distributions around them. Note that "Frag5" has two neighboring clumps. Several properties of the neighboring gas clumps are summarized in Table 2.4. The clumps are located at distances $0.05 \sim 2$ pc from the central collapsing core. Note that the simulations in this thesis only follow the protostellar evolution of the central core. The clumps in the surrounding are smeared out in the subsequent 2D RHD simulations by averaging the physical quantities over the azimuthal direction. Therefore, whether or not stars can be formed in the neighboring clouds remains unclear in the calculations. Fully three dimensional calculations of protostellar evolution are necessary to determine the final stellar mass(es) for these cases.

The cosmological simulation of Turk *et al.* (2009) also shows two fragments forming with a 800 AU separation during the run-away collapse of a cloud. The simulations performed here find similar multiple clumps but with even wider separations, though only in a handful of cases out of sample of 110 clouds. Note also that the clump formation is different from those seen in a self-gravitating circumstellar disk (e.g., Stacy & Bromm, 2013, and see also the next section), which produce small separation ($<$ 1000 AU) multiple protostellar

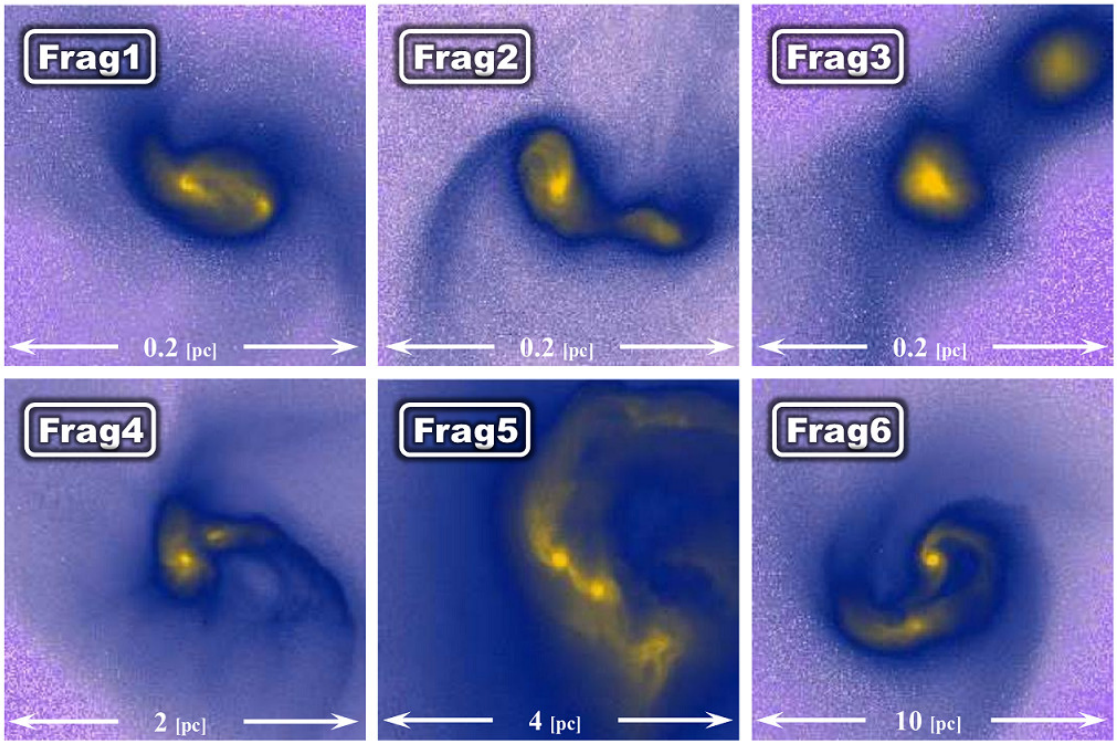

Figure 2.16. Projected gas density distributions for six clouds which have multiple density peaks when the central density reaches 10^{12} cm^{-3}. Table 2.4 summarizes the clump properties

No.	R (pc)	$M(< R/2)$ ($M_\odot$)	$n_{\rm H,cen,frag}$ (cm^{-3})	$t_{\rm ff,frag}$ (yr)	$M_{\rm III,prim}$ ($M_\odot$)
1	0.05	170	1.5×10^{10}	436	380
2	0.08	50	1.9×10^{8}	3820	53
3	0.10	170	2.6×10^{8}	3300	381
4	0.20	120	2.3×10^{7}	11100	340
5a	0.60	270	6.6×10^{7}	6530	27
5b	1.50	900	3.6×10^{5}	88700	27
6	2.00	1300	7.2×10^{5}	62500	56

Table 2.4. Column 2: Distance between the primary star and the clump, Column 3: Enclosed mass within $R/2$, Column 4: Central density of the clump, Column 5: Estimated free-fall time, and Column 6: The final stellar mass of the primary star.

systems. Recently, Greif *et al.* (2013) have shown the possibility of the chemo-thermal instability which makes fragments on a scale of a few tens of au.

2.2.5.3 Accretion Disk Fragmentation

Recently, Clark *et al.* (2011a) and Greif *et al.* (2011a) have studied the evolution of primordial protostellar disks over one hundred years using sink particle techniques. In their simulations, multiple protostars are formed in a disk via gravitational instability. Although two-dimensional calculations cannot follow the evolution of multiple protostars in a disk, it is worth discussing the possible effect and outcome in such cases.

If disk fragmentation occurs during the mass accretion phase, there are two mechanisms that can reduce the final stellar mass of the central main protostar. One is the reduction of the total gas mass that can be accreted onto the central star, simply because additional sinks are present (fragmentation-induced starvation; i.e., Peters *et al.*, 2010). The other is that the structure and evolution of the protostar itself are affected by the reduced accretion rate in a complicated nonlinear way, as the discussion in the previous sections. With a lower accretion rate, the protostar begins KH-contraction at a lower stellar mass so that the mass accretion is halted by UV radiative feedback in accordance to P1 evolution. Both of these effects are expected to reduce the final mass of the central protostar.

There is another physical process which has not included. Primordial magnetic fields are generally considered to be much weaker than in the present-day star-forming cloud, and thus their effects are often ignored in the study of primordial star formation. However, as shown by Machida *et al.* (2010), even *pico-gauss* magnetic fields are sufficient to transfer angular momentum in the accretion flow via magnetic braking. The accretion disk disappears in cases with a weak magnetic field, and the surrounding gas is accreted onto the protostar directly in a roughly spherical manner. More recently, Turk *et al.* (2012) and Sur *et al.* (2012) have performed magneto-hydrodynamic simulations of primordial star formation. They show that turbulent velocity fluctuations resolved in their simulations can amplify the magnetic field via the dynamo effect. They argue that magnetic fields can influence the formation and the structure of the accretion disk. Further studies on the effects of magnetic fields are needed to determine the overall impact on the characteristic masses of the first stars.

2.3 Population III.2$_{\rm D}$ Stars

The next step is to study the Population III.2$_{\rm D}$ cases, the primordial star-formation under the influence of the far-ultraviolet (FUV) radiation. Figure 2.17 shows the mass accretion histories onto a protostar, obtained from the 2D RHD simulations which are computationally expensive but necessary to examine the correlation between the final stellar mass and the intensity of the photodissociating radiation. In all of the cases presented, the mass accretion rate decreases sharply at some point; i.e., the protostellar feedback finally shuts off the mass accretion. In general, for the larger J_{21}, the gas temperature in the accretion envelope is higher (e.g., Omukai, 2001; O'Shea & Norman, 2008), causing higher

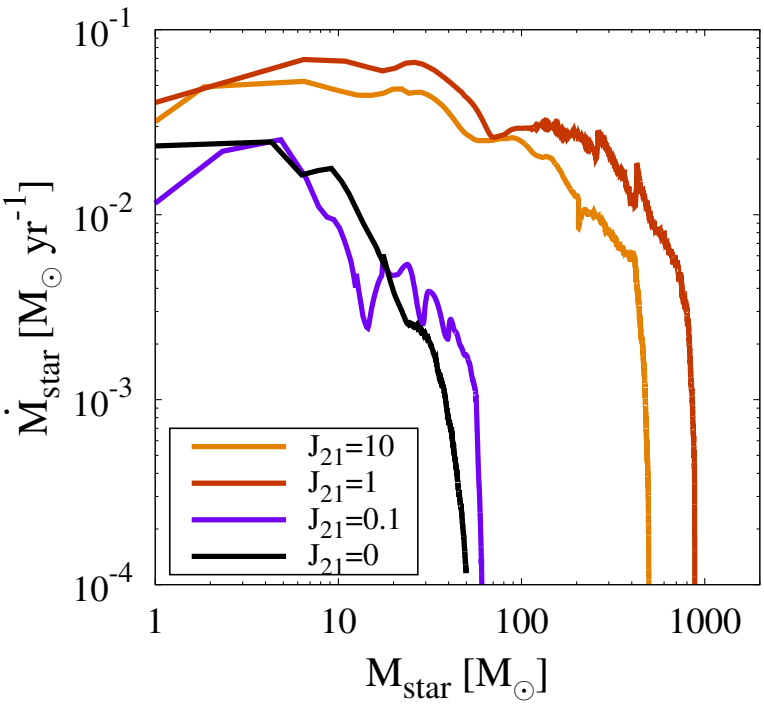

Figure 2.17. Accretion histories of mass accreting protostars, which from the same cloud (ID = 4 in Table 2.5) but with different FUV intensities J_{21} = 0, 0.1, 1, and 10, as a function of the stellar mass. When the mass accretion rates fall below 10^{-4} $M_\odot$ yr^{-1}, the simulations stop and the masses at this moment are considered as the final stellar masses, 50, 61, 883, and 496 $M_\odot$, respectively.

accretion rates onto the protostar. The final stellar mass is consequently larger for higher FUV intensity.

2.3.1 Method

The various formation processes and final stellar masses of Pop III.1 stars are characterized by the initial properties of star-forming cloud. Pop III.2$_{\rm D}$ star-formation, however, has additional parameters that could affect the star-formation process. One is the intensity of photodissociating FUV radiation in Lyman-Werner (LW) bands, which is often normalized as $J_{21} = J_{\rm LW}/(10^{21}$ erg s^{-1} Hz^{-1} sr^{-1}). This radiation destroys H_2 and HD molecules and prevents the cooling and collapse of the cloud. This thesis investigates the dependence of Pop III.2$_{\rm D}$ star-formation on the parameter J_{21}.

Another parameter is the central density when the photodissociating photons reach the cloud, $n_{\rm H,cen,rad}$. This thesis fixes this parameter at $n_{\rm H,cen,rad} = 10$ cm^{-3} for the following reasons. In reality, the FUV photons might affect the earlier phase of the collapse ($n_{\rm H,cen,rad} < 10$ cm^{-3}). Pop III.2$_{\rm D}$ stars could then form with less efficient self-

ID	J_{21}=0		J_{21}=0.1		J_{21}=0.316		J_{21}=1		J_{21}=10	
	RHD	estimate								
1	–	12.5	–	872.6	–	352.3	238.1	368.3	×	
2	15.7	23.7	89.1	93.6	–	286.4	–	449.8	183.2	203.7
3	25.7	32.1	–	150.8	×		–	809.5	–	2438.7
4	49.9	49.4	61.0	100.7	–	425.7	883.3	433.7	496.1	373.6
5	–	59.1	152.0	317.5	177.7	236.7	126.6	176.3	–	503.8
6	197.2	142.2	40.9	33.0	–	608.2	29.1	70.6	×	
7	–	328.2	235.4	268.5	175.7	544.4	–	522.7	–	473.8
8	–	352.3	60.1	20.8	–	397.5	–	655.6	×	
9	291.1	384.0	323.7	406.1	–	367.8	–	593.6	618.8	176.3

Table 2.5. Column 1: Cloud's index, Columns $2-11$: Final stellar masses in the unit of $M_\odot$ for different FUV intensities: J_{21} = 0, 0.1, 0.316, 1, and 10. The masses are determined by two different methods: the 2D RHD simulations (left) and from the estimating formula (2.1; right). The underbars indicate the cases cooled by HD molecules during the run-away collapse stage. The crosses indicate the un-collapsed cases by photodissociating radiation. The dashes indicate the cases without final stellar masses calculated by 2D RHD simulations.

shielding. However, in the calculations it takes ~ 100 Myr for such a low-density cloud to begin to collapse with the reduced amount of H_2 molecules. It is unlikely that the intensity of FUV radiation remains strong enough for the Pop III.2_D star formation mode for such long time; typical stellar lifetimes of the light sources are only a few million years. For the opposite case ($n_{H,cen,rad} > 10$ cm^{-3}), the photodissociating photon is absorbed by the outer dense gas and cannot photodissociate the inner collapsing region. Such self-shielding mechanism prevents photodissociation and the cloud forms a Pop III.1 star; test simulation shows that self-shielding becomes sufficiently efficient in the cloud at densities $\sim 10^2 - 10^3$ cm^{-3}. Furthermore, the collapse time-scale of such a dense cloud is short and it is difficult that the photodissociating photon arrives at the time. This thesis thus adopts the critical value $n_{H,cen,rad} = 10$ cm^{-3}.

The initial conditions of simulations are nine different primordial star-forming clouds in 110 cases irradiated by photodissociating photons. The effects of external irradiation is studied by varying the intensity as a free parameter with J_{21} = 0, 0.1, 0.316, 1, and 10. The cases with $J_{21} = 0.01$ have been calculated and their thermal evolution of the cloud collapse is nearly identical to the Pop III.1 cases ($J_{21} = 0$). On the other hand, the collapse is almost completely prohibited for intensities exceeding $J_{21} = 10$. Thus the parameter range is examined as $J_{21} = 0.1 - 10$.

The formation of Pop III.2_D stars is studied in a two-step manner which is the modification of Pop III calculations. First, the evolution of collapsing clouds under the FUV fields is calculated by GADGET-2 by assuming a uniform FUV radiation field. The code em-

ploys the self-shielding functions (Wolcott-Green & Haiman, 2011; Wolcott-Green *et al.*, 2011) for H_2 and HD molecules. For each SPH particle, the column densities are calculated along six directions ($\pm X,\ \pm Y,\ \pm Z$) to account for the directional dependence of the self-shielding effect. The collapse calculations end when the central density reaches $n_{\rm H,cen} = 10^{13}$ cm^{-3} and an optically thick hydrostatic object (protostar) is assumed to have formed at this point. The final configuration is used to generate the *initial* conditions for the 2D RHD grid-based simulations of the subsequent protostellar accretion stage by azimuthal averaging around the rotational axis (ϕ-direction).

Then the subsequent evolution after the birth of the protostar is followed by conducting 2D axisymmetric RHD simulations of the collapsing cloud coupled with the simultaneous stellar evolution of the central accreting protostar located in a central sink cell (Hosokawa *et al.*, 2011, 2012b). The simulations continue until the mass accretion rate falls below $10^{-4}\ M_\odot$ yr^{-1} in each case and the mass at this moment is assumed as the final stellar mass. Whereas the accreting protostar's evolution is normally followed by solving for the stellar interior structure, it occasionally becomes difficult to construct a stellar model with highly variable mass accretion histories. This often happens in Pop III.2$_{\rm D}$ cases, when the mass accretion rates are relatively high and the protostar has an extremely large radius (e.g., Hosokawa *et al.*, 2012a). In order to continue the calculations in these cases, the stellar evolution calculation switches to an analytic stellar model, which agrees with the numerical results well, only when the accretion rate exceeds $10^{-2}\ M_\odot$ yr^{-1} (see also Appendix B.2).

2.3.2 Results

In the former 3D hydrodynamical simulations, the primordial cloud gravitationally collapses in 41 cases out of the total 45 cases. In the other 4 cases, gas condensation and the gravitational collapse are prevented because H_2 molecules are completely photodissociated (crosses in Table 2.5). The later 2D RHD calculations are finished in 21 cases of the 41 collapsed cases and the resultant stellar masses are shown in left columns for each J_{21} in Table 2.5 (HD-cooling clouds are marked by underbars). In the remaining 20 cases (dashes in Table 2.5), it was difficult to numerically follow the stellar evolution with time-dependent rapid mass accretion, so that their stellar masses are estimated by using the procedure described below.

Figure 2.18 shows that the final stellar masses obtained from the 2D RHD simulations are well correlated with $\dot{M}_{\rm Jeans}$. The correlation for Pop III.2$_{\rm D}$ stars is similar to that for Pop III.1 stars given by Eq. (2.1). This can be understood by noting that, for the Pop III.2$_{\rm D}$ cases, photodissociating radiation affects the thermal structure of the envelope only in the early stage of the collapse. Once the collapse proceeds and the density increases, gas self-shielding becomes effective and the subsequent evolution is unaffected by the external radiation. The evolution after the birth of the protostar is only modified with a different accretion history resulting from the different temperature in the envelope.

Having derived the above correlation, one can estimate the stellar mass without computing the detailed long-term evolution after the birth of the protostar. Instead, this study

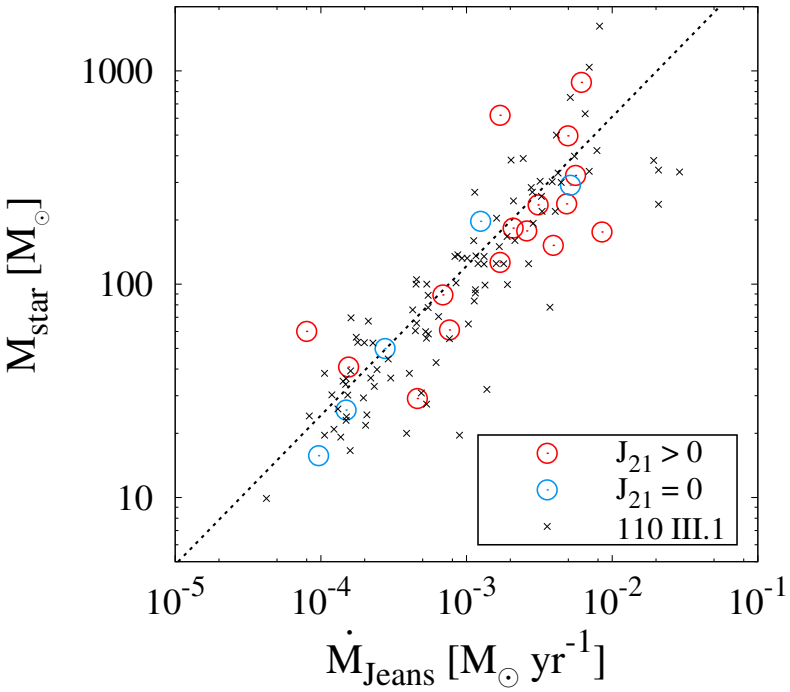

Figure 2.18. Final stellar masses obtained in 2D RHD simulations as a function of the gas infall rate measured at the Jeans scale when $n_{\rm H,cen} = 10^7$ cm^{-3}. The open circles represent 16 cases with $J_{21} > 0$ (Pop III.2$_{\rm D}$ stars; red) and 5 cases with $J_{21} = 0$ (Pop III.1 stars; blue), in which the 2D RHD simulations successfully follow the evolution until the final stellar masses are fixed. The crosses depict the results for Pop III.1 stars obtained for the same central density (Fig. 2.12). The dotted line shows the fitting formula for Population III stars (Eq. 2.1).

only follows the early collapse stage in 3D until the central density reaches 10^7 cm^{-3}. The final stellar mass is determined for the remaining 20 cases by using the calculated $\dot{M}_{\rm Jeans}$ and Eq. (2.1) which are shown in the right columns for each J_{21} in Table 2.5.

Overall, external radiation increases the resulting final stellar masses, though the dependence can be quite complex in some cases. Table 2.5 shows that the stellar mass does not always increase with increasing FUV intensity. For the clouds with ID = 6 and 8, for instance, the stellar mass decreases somewhat from the III.1 value, when a weak FUV intensity ($J_{21} = 0.1$) is present. Interestingly, the thermal evolution during the collapse actually changes from an H_2-cooling mode to the HD-cooling mode (marked with the overbars) for these cases: i.e., a weak FUV field sometimes triggers the HD-cooling mode. The following subsections shall examine the interesting cases in greater detail. Section 2.3.3 first reviews the overall trend of those results, and then Section 2.3.4 examines the detailed evolution for the clouds ID = 4, 8, and 9. Finally, Section 2.3.5 describe how these results are used to derive the mass distributions of Pop III.2$_{\rm D}$ stars.

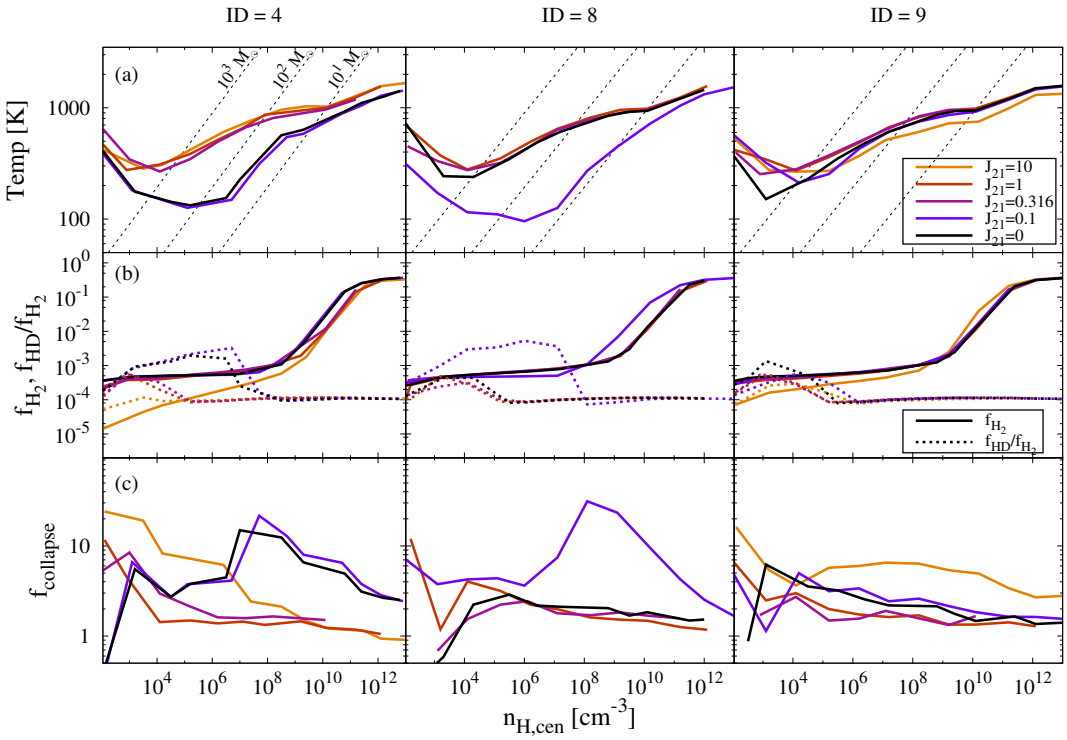

Figure 2.19. Physical properties of collapsing clouds with different FUV intensity J_{21} for the different cases ID = 4 (left), 8 (center), and 9 (right) listed in Table 2.5. Line colors in each panel represent the different FUV intensity $J_{21} = 0$, 0.1, 0.316, 1, and 10 from black to yellow. The three rows show the evolution of the gas temperature (panels a), chemical abundances (b), and the ratio between the collapsing time and free-fall time $f_{\rm collapse} = t/t_{\rm ff}$ (c; the same definition in appendix C) measured at the cloud center. The dotted lines in panel (a) show the Jeans scale as a function of the gas density and temperature. In the panels (b), the solid and dotted lines represent the number fraction of H_2 molecules f_{H_2} and the fractional abundance of HD molecules f_{HD}/f_{H_2}.

2.3.3 General Properties

Figure 2.19 depicts the thermal and dynamical evolution during the cloud collapse. The columns represent ID = 4, 8, or 9 from left to right (Appendix E shows the rest). For ID = 4 and 8 with the weak FUV intensity $J_{21} = 0.1$, HD cooling becomes efficient enough to alter the thermal evolution. The decrease of the temperature at $n_{\rm H,cen} < 10^7$ cm^{-3} is explained by the increase of HD fraction and hence of the cooling rate (panels a and b). As described in Section 2.2.2.2, HD cooling becomes efficient when the cloud collapse is slow. Figure 2.19(c) shows that the time-scale ratio $f_{\rm collapse} \equiv t/t_{\rm ff}$ exceeds 3 in the early

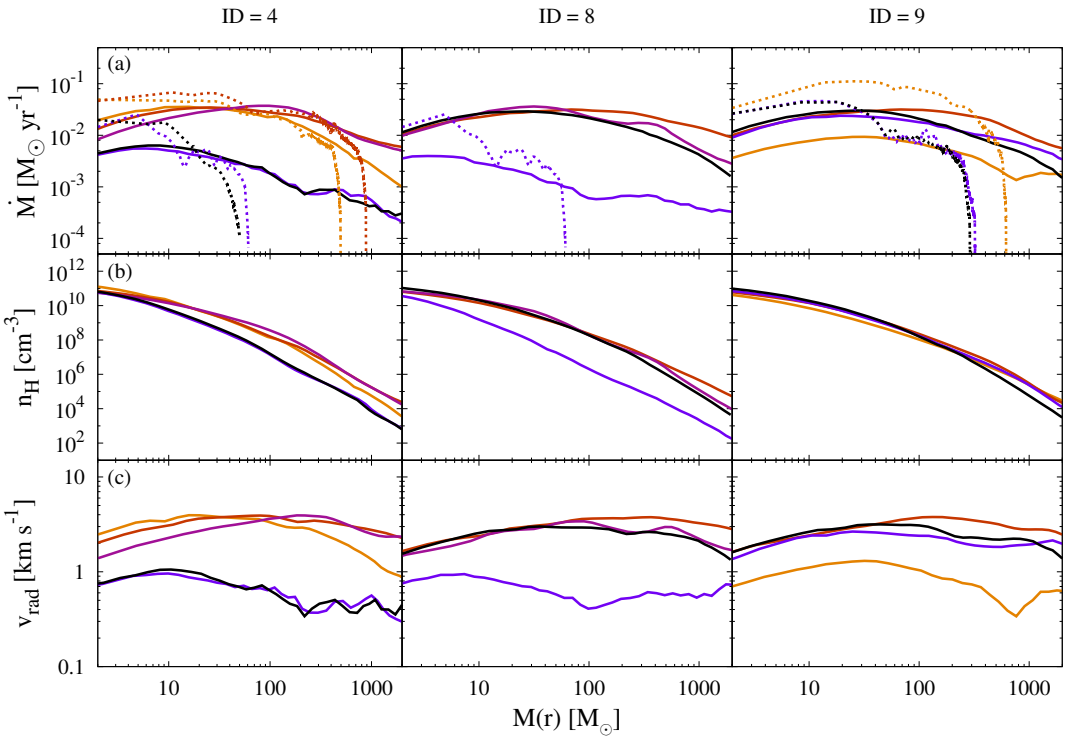

Figure 2.20. Different physical properties of collapsing clouds for the same cases in Figure 2.19. The three rows show the radial profiles of the gas infall rate (a), number density (b), and radial velocity (c) as functions of the enclosed mass for $n_{\rm H,cen} = 10^{11}$ cm^{-3}. The dotted lines in panels (a) show the mass accretion histories seen in the 2D RHD simulations following the evolution after the birth of protostars. Note that the horizontal axis represents the protostellar mass for these cases.

stage.[*5] The collapse is decelerated around $n_{\rm H,cen} \sim 10^8$ cm^{-3}, when HD cooling becomes inefficient. In addition to the effect of HD cooling, the H_2-cooling cases show substantial variations of the temperature, depending on the FUV intensity (for instance, the ID = 9 case). The conclusion is that the accretion histories after the birth of a protostar are also dependent on the local FUV radiation field.

Figure 2.20 shows the dynamical properties of collapsing clouds at the point in time when $n_{\rm H,cen} = 10^{11}$ cm^{-3}. The instantaneous gas infall rate $4\pi r^2 \rho v_{\rm rad}$ (panel a) depends on the radial distributions of the density (b) and velocity (c). The variations seen in the profiles originate from the different thermal evolution during the collapse. Figure 2.20(a) also shows that the mass accretion rates observed in the 2D RHD simulations (dotted lines), which follow the subsequent evolution after the birth of a protostar (the abscissa is now the protostellar mass), obey the dependence on FUV intensity expected with the

[*5] Appendix C has confirmed that the thermal evolution seen in the 3D simulations is well explained with the one-zone models using $f_{\rm collapse}$ as a free parameter.

snapshots before the birth of the protostar (solid lines).

Overall, the photodissociating radiation has a stronger impact on those clouds that evolve on low temperature tracks for $J_{21} = 0$ (see e.g., ID = 4 in Table 2.5 and Fig. 2.19). In such cases, the thermal evolutionary path moves towards higher temperatures with increasing J_{21}, which results in larger accretion rates and hence ultimately more massive stars. The effect is most significant for the clouds that would normally evolve on a HD-cooling path when FUV radiation is absent (e.g., ID = 1 − 5 cases). However, the dependence of the thermal evolution on the FUV intensity is not always simple nor even monotonic in some cases. For ID = 8, whose thermal evolution follows the typical H_2-cooling mode for $J_{21} = 0$, HD cooling dominates when J_{21} is increased to 0.1. The following section shows the individual cases in more detail to understand this complex behavior.

2.3.4 Individual Cases

To study the evolution of individual cases, it is useful to examine the 3D distributions of gas density and velocity for the different FUV intensities. Figure 2.21 displays such distributions in the central region with 1 pc on a side. Overall, the morphology of a cloud changes from a disc-like shape to a more spherical one with increasing J_{21} (from left to right). This can be understood as follows. At the higher FUV intensity, H_2 and HD molecules are photodissociated more efficiently, which makes the Equation of State (EoS) of the primordial gas stiffer. The collapse is decelerated in such a case and there is more time for angular momentum redistribution within the cloud. As a result, the cloud becomes more spherical. Once the density increases to the point that self-shielding effect becomes important, the collapse occurs rapidly with a weaker rotational support. This partly explains why the strong FUV irradiation increases the gas infall rate. An exceptional case is for ID = 9 with $J_{21} = 10$, which has significant rotation, resulting in a disk-like structure with spiral arms. The evolution of each case is described below.

2.3.4.1 ID = 4: disabling the HD cooling with FUV radiation

The first case is ID = 4, for which the cloud evolves on the HD-cooling path for the Pop III.1 case ($J_{21} = 0$). Figure 2.21 shows that the cloud rotates rapidly, which is also inferred from the low infall velocity shown in Figure 2.20(c). Please remind that the HD-cooling path emerges when the collapse is slow, which could be the result of rapid rotation (Appendix C). For $J_{21} = 0.1$ the evolution does not change much. The photodissociation of molecules hardly affects the evolution because of efficient self-shielding. The resulting stellar mass is almost the same as for the Pop III.1 case.

With the higher FUV intensities $J_{21} = 0.316$ and 1, however, the thermal evolution tracks shift from the HD-cooling path to the H_2-cooling path, because of the enhanced photodissociation of H_2 and HD molecules. The decreased coolants cannot cool the cloud sufficiently to follow a HD-cooling evolution. Once the thermal evolution begins to follow the H_2-cooling path, the cloud becomes more spherical as described above. With the reduced rotational support, the collapse proceeds more rapidly and the gas infall rates are

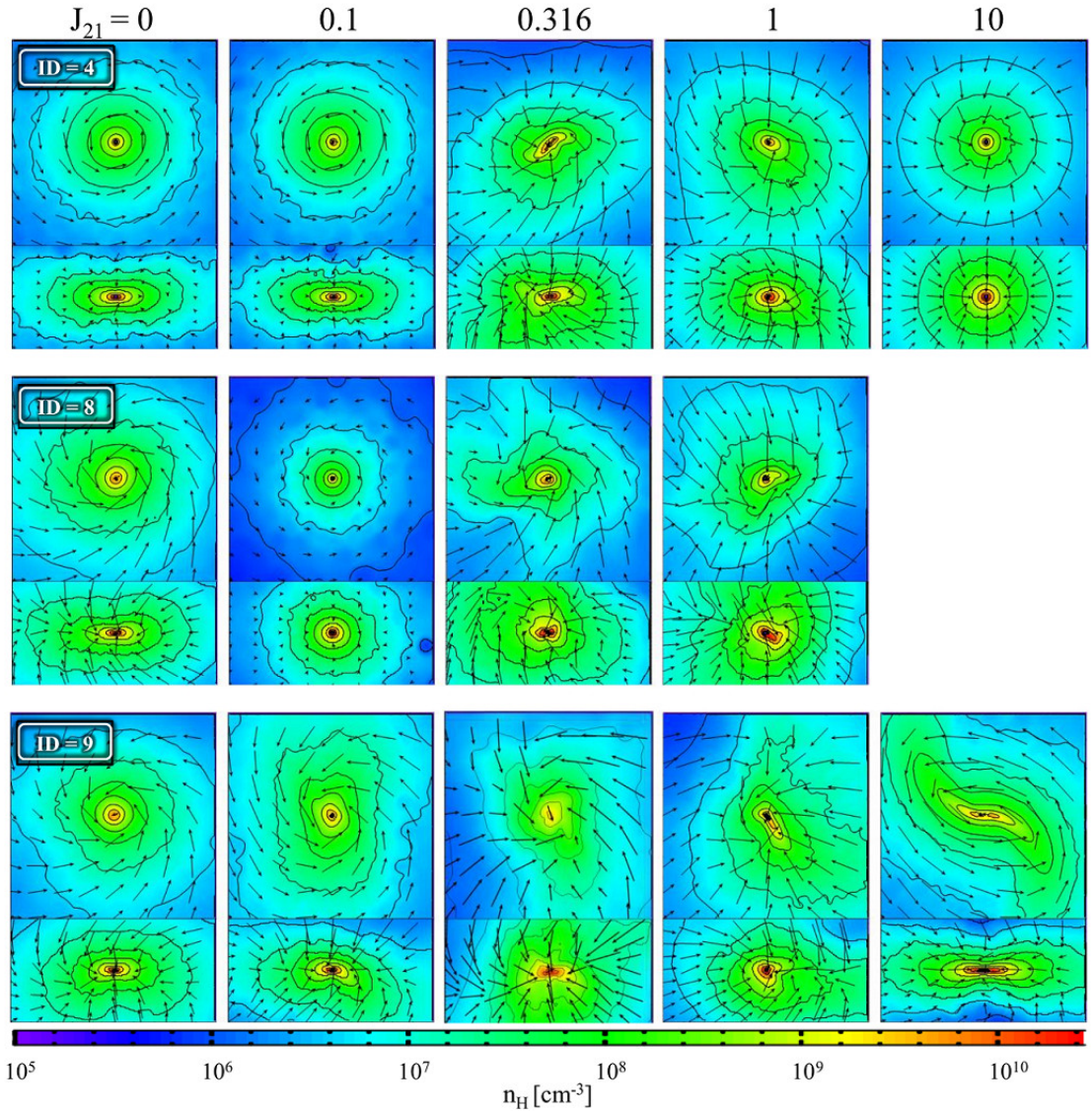

Figure 2.21. Density (color and line contours) and velocity (arrows) distributions around the collapsing center when $n_{\rm H,cen} = 10^{11}$ cm^{-3} for the same cases as in Figure 2.19. The box size is 0.1 pc on a side. The top and bottom panels show the slices through the X-Y and X-Z planes, whereby the Z-axis corresponds to the rotational axis. There is a blank panel for ID = 8 with $J_{21} = 10$, because the collapse is prevented by the photodissociating radiation in this case.

consequently higher than for the cases with weaker FUV irradiation $J_{21} < 0.1$.

The strong FUV irradiation with $J_{21} = 10$ photodissociates H_2 molecules even up to $n_{\rm H} = 10^9$ cm^{-3} (see Fig. 2.19b). With the reduced abundance of coolants, the cloud collapses slowly until three-body H_2 formation begins. The cloud has a spherical shape as a result of angular momentum redistribution over such a prolonged collapse time. The small rotational support results in the highest gas infall rates for $M(r) < 100\ M_\odot$ (or $n_{\rm H} > 10^9$ cm^{-3}) among the five cases examined. In the outer part of the envelope, however, the infall rate is lower than for $J_{21} = 0.316$ and 1, because of the slow collapse before self-shielding becomes effective. Due to the low infall rates in the outer low density regions (e.g., for $n_{\rm H,cen} = 10^7$ cm^{-3}, see Fig. 2.20a), the final stellar mass with $J_{21} = 10$ is lower than with weaker FUV irradiation.

The ID = 4 cases represent the typical variation of the stellar mass with external photodissociating radiation: the stellar mass increases with FUV intensity J_{21}. However, the trend saturates around $J_{21} \sim 10$ and then the stellar mass *decreases* for even higher FUV intensity. Cloud collapse would ultimately be prevented with very strong FUV irradiation, which is actually seen in some other cases (crosses in Table 2.5).

2.3.4.2 ID = 8: triggering the HD cooling with weak FUV radiation

The next cases are for ID = 8, whereby for $J_{21} = 0$ the cloud collapses along the H_2-cooling path. Interestingly, the HD-cooling path appears only for the weak FUV irradiation $J_{21} = 0.1$ in this case. The main effect of the FUV radiation is photodissociating molecules. Without molecules, the EoS becomes stiffer and the gas collapses slowly. However, the slow collapse actually promotes the formation of H_2 and HD molecules. Enhanced self-shielding eventually stops further photodissociation, triggering the HD-cooling mode in the subsequent evolution. At higher intensities $J_{21} = 0.316$ and 1, the thermal evolution tracks return to the H_2-cooling path, because the self-shielding is insufficient to prevent photodissociation. With $J_{21} = 10$, the cloud does not collapse even after 10^8 years. The strong photodissociation completely quenches star formation in this case. Calculation results suggest that the critical FUV intensity for preventing collapse depends on the physical properties of the cloud such as its morphology and the degree of rotation. This is likely because the strength of the self-shielding effect depends on the radial profiles of the density within the cloud.

2.3.4.3 ID = 9: reducing temperature with strong FUV radiation

The final cases are for ID = 9, which show an exceptional behavior for strong FUV irradiation. The gas infall rate and resulting final stellar mass monotonically increase with increasing J_{21} for $J_{21} \leq 1$. For $J_{21} = 10$, however, in spite of the intense FUV irradiation, the cloud evolves through the lowest temperature path among all cases examined (Fig. 2.19a). This is because the strong photodissociation decelerates the collapse even after the density becomes very high. In fact, Figure 2.19(c) shows that the time-scale ratio $f_{\rm collapse}$ is around 5 at $n_{\rm H} > 10^9$ cm^{-3}. Once three-body H_2 formation becomes effective, the gas temperature is lower for the longer collapse time-scales; i.e. more H_2 molecules, the coolant, are formed with the slower collapse (Appendix C). The enhanced coolant

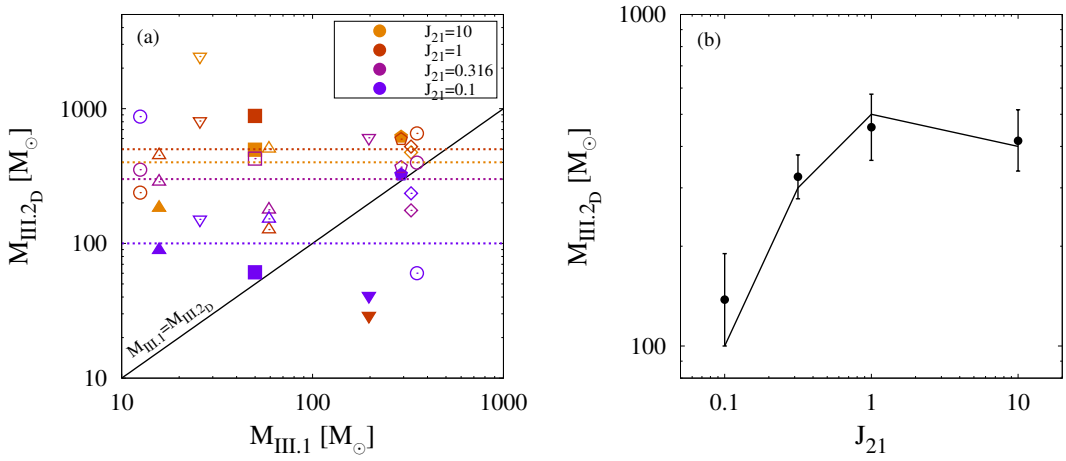

Figure 2.22. Stellar masses for the Pop III.2$_{\rm D}$ cases with different FUV intensity J_{21}. The left panel shows the stellar mass of Pop III.2$_{\rm D}$ cases $M_{\rm III.2_D}$ ($J_{21} > 0$) plotted versus Pop III.1 cases $M_{\rm III.1}$ ($J_{21} = 0$), whose different values represent different gas clouds (for ID $= 1 \sim 9$ from left to right). The filled symbols indicate the stellar masses determined by 2D RHD simulations. The values marked with the open symbols, on the other hand, are calculated using the analytic formula (Eq. 2.1). The solid line represents the equal mass boundary $M_{\rm III.1} = M_{\rm III.2_D}$. The dotted lines show the fitting functions which follow the dependence of $M_{\rm III.2_D}$ on J_{21}. The right panel shows the correlation of $M_{\rm III.2_D}$ with J_{21}. The symbols with error bars depict the averaged masses and variances of the same J_{21} cases. The stellar masses for cases without 2D RHD simulations are given by the estimated values. The line shows the simplified relation $M_{\rm III.2_D}$ as a function of J_{21} (Eq. 2.10; $M_{\rm III.2_D} = 100$, 300, 500, and 400 M$_\odot$ for $J_{21} = 0.1$, 0.316, 1, and 10), which is used for evaluating Pop III.2$_{\rm D}$ stellar masses.

abundance results in a softer EoS, which in turn leads to a more flattened morphology as the collapse advances (Hanawa & Matsumoto, 2000). In fact, the cloud morphology accordingly changes from disc-like to a more spherical structure for the cases with $J_{21} \leq 1$, but shows the highly rotating disc-like shape for $J_{21} = 10$ as seen in Figure 2.21.

2.3.5 Mass Estimating Formula

The calculations suggest that the masses of Pop III.2$_{\rm D}$ stars $M_{\rm III.2_D}$ vary not only among different gas clouds but also by the effect of FUV irradiation. Despite the fact that $M_{\rm III.2_D}$ is dependent on multiple parameters in a complicated way, the overall trend can be modeled by using the numerical simulation results obtained in this thesis. Figure 2.22(a) summarizes how the stellar mass $M_{\rm III.2_D}$ varies with the parameters ($M_{\rm III.1}$ and J_{21}). Note that, in the figure, the different Pop III.1 stellar masses indicate that the gas clouds are different. Overall, the mass ratio $M_{\rm III.2_D}/M_{\rm III.1}$ increases with decreasing $M_{\rm III.1}$ for a given FUV intensity; gas clouds with low temperatures are more susceptible to FUV

irradiation. On the other hand, the mass increase is relatively small for the cases with the higher Pop III.1 masses, i.e., $M_{\rm III.1} > 100\ M_\odot$. Figure 2.22(a) shows that the same colors for a given J_{21} are distributed around the similar values of $M_{\rm III.2_D}$. The Pop III.$2_{\rm D}$ stellar mass does not change radically within a given FUV intensity J_{21}. Table 2.5 shows the diversity of stellar masses for a given J_{21} over a factor of 10 but there are also a systematic dependence. Figure 2.22(b) shows the averaged values and variances for given values of J_{21}. To obtain the averaged values and its deviations, the estimated stellar masses are used for the cases without the 2D RHD results. There is a general trend that $M_{\rm III.2_D}$ increases for $0.1 \leq J_{21} \leq 1$ but *decreases* gradually for $J_{21} \geq 1$. The formula models such variations of $M_{\rm III.2_D}$ for different J_{21} by the solid line as

$$M_{\rm III.2_D}(J_{21}) = \begin{cases} 900 \cdot 10^{+0.96x} & (\text{if} \quad -1 < x < -0.5)\,, \\ 500 \cdot 10^{+0.44x} & (\text{if} \ -0.5 < x < 0)\,, \\ 500 \cdot 10^{-0.10x} & (\text{if} \quad 0 < x < 1)\,, \\ 400 & (\text{if} \quad 1 < x)\,, \end{cases} \tag{2.10}$$

where $x = \log_{10}(J_{21})$.

2.4 Summary

To study the mass diversity and its origins of the Population III.1 and III.$2_{\rm D}$ stars, this chapter has performed a number of simulations in a proper cosmological context. In both cases, the resultant stellar masses show wide distributions from 10 to 1600 $M_\odot$

The collapse time-scale is the key quantity that determines the thermal evolution of the gas clouds. Rapidly collapsing clouds follow the well-known evolution path which is controlled by H_2 cooling. Slowly collapsing clouds cool efficiently because of the less effective compressional heating and the longer time scale for the coolants to be produced. When the temperature decreases to ~ 100 K, HD molecules are formed efficiently, and the additional HD molecular cooling further lowers the temperature to the CMB temperature. The physical structure of the gas envelope around a protostellar core also differs among the sample of clouds, reflecting the different thermal evolution during the collapse. If the star-forming gas cloud is irradiated by intense UV radiation (Population III.$2_{\rm D}$ case), the main coolants, H_2 and HD molecules, are photodissociated and the gas cloud follows higher temperature track. This in turn leads to different accretion histories as seen in the subsequent evolutionary stage after the formation of protostars.

The main self-regulation mechanism of protostellar growth is UV feedback. Since the strength of the UV feedback depends on the protostellar evolution, which differs with different accretion histories, the resulting stellar mass also differs considerably among the sample. On average, the final stellar mass is larger for more rapid mass accretion. Protostars approach the ZAMS at larger stellar masses in such cases. Interestingly, with very rapid accretion $\dot{M} > 4 \times 10^{-3}\ M_\odot\ {\rm yr}^{-1}$, the protostar greatly expands, so that the stellar effective temperature remains below 10^4 K. The ionizing photon luminosity remains so low that UV feedback never becomes strong enough to prevent mass accretion

(e.g., Hosokawa *et al.*, 2012a). Rapid mass accretion is a promising path for forming very massive ($> 10^3\ M_\odot$) stars in the early universe (see e.g. Hosokawa *et al.*, 2012a, 2013).

The overall accretion rate can be estimated from the structure of the gas envelope around a protostellar core. The structure itself is affected by the thermal evolution during the run-away collapse. One can predict the final stellar mass from the conditions in the early state of the gas cloud formation and to a less rigorous extent even from the properties of dark matter halos. There are the correlations between the final stellar masses and infall rates at both the Jeans and virial scales (Eqs. 2.1 and 2.2). Eq. 2.1 can be used for both the Population III.1 and III.$2_{\rm D}$ cases. There are key physical quantities that determine the infall rates: the parent cloud mass and the rotation parameter for the cloud scale, and the formation redshift and the virial mass of the virial scale.

Chapter 3

Cosmological Sample of Primordial Gas Clouds

3.1 Overview

The mass distribution of primordial stars is constructed by sampling the star-forming clouds in the cosmological volume. Chapter 2 has presented the correlation between the initial properties of star-forming cloud and the final stellar masses. Such correlations are useful because one can estimate the final stellar mass using the early physical state of the cloud (or the halo) without following the detailed evolution up to the termination of mass accretion onto the protostellar core. Thus this thesis constructs the non-biased cosmological samples of primordial star-forming clouds at $n_{\rm H} = 10^7$ cm^{-3}, whose properties are used to estimate the final stellar masses with the correlations.

This section studies the physical properties of 1540 primordial star-forming clouds found in a certain cosmological volume. This section ignores the effect of stellar FUV fields and assumes that all the clouds bear Pop III.1 stars, allowing a direct comparison with the sample with 110 cases presented in Section 2.2. The dependencies of cloud properties and stellar mass distribution on the formation redshifts are discussed.

The content in this and next chapters has been submitted to Monthly Notices of the Royal Astronomical Society.

$N_{\rm cloud}$	$L_{\rm box}$ (h^{-1}kpc)	$l_{\rm soft}$ (h^{-1}pc)	$m_{\rm DM}$ ($h^{-1}M_\odot$)	$m_{\rm gas}$ ($h^{-1}M_\odot$)	Cosmological Parameters
1540	3000	29	116	19	Planck Collaboration *et al.* (2014)

Table 3.1. Each column shows the same parameter as Table 2.1 for the final cosmological simulation.

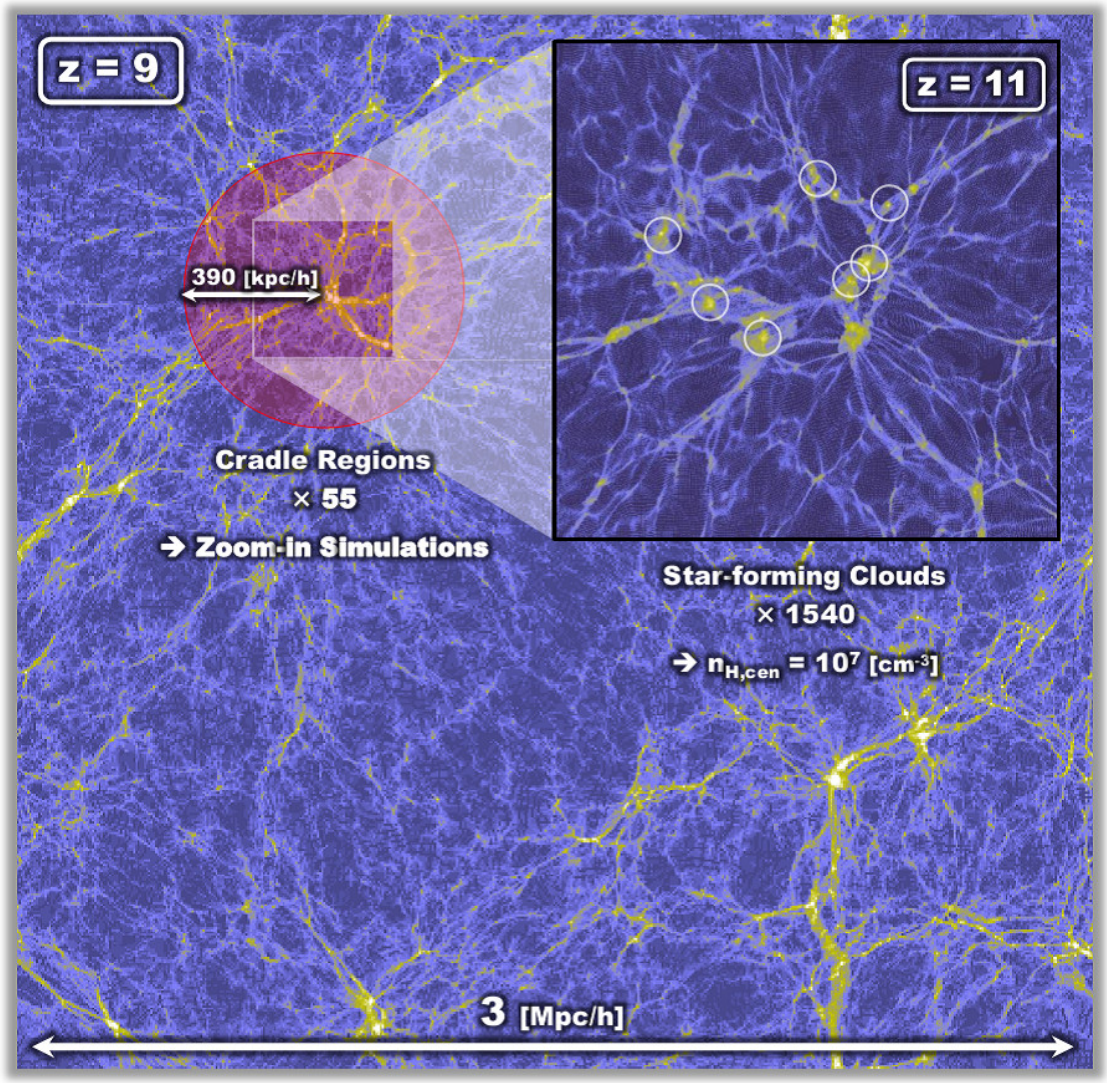

Figure 3.1. Schematic view of the cosmological simulation to obtain the non-biased sample of primordial star-forming clouds. The color contour reveals the projected density level of dark matter which increase from blue to yellow. In a parent simulation (the background panel), 55 zoomed initial conditions are generated which cover each cradle region (the red circle shows one of them). Finally 1540 star-forming clouds are obtained from zoom-in simulations (a part of them is shown as white circles in the foreground panel) and their formation and evolution are followed.

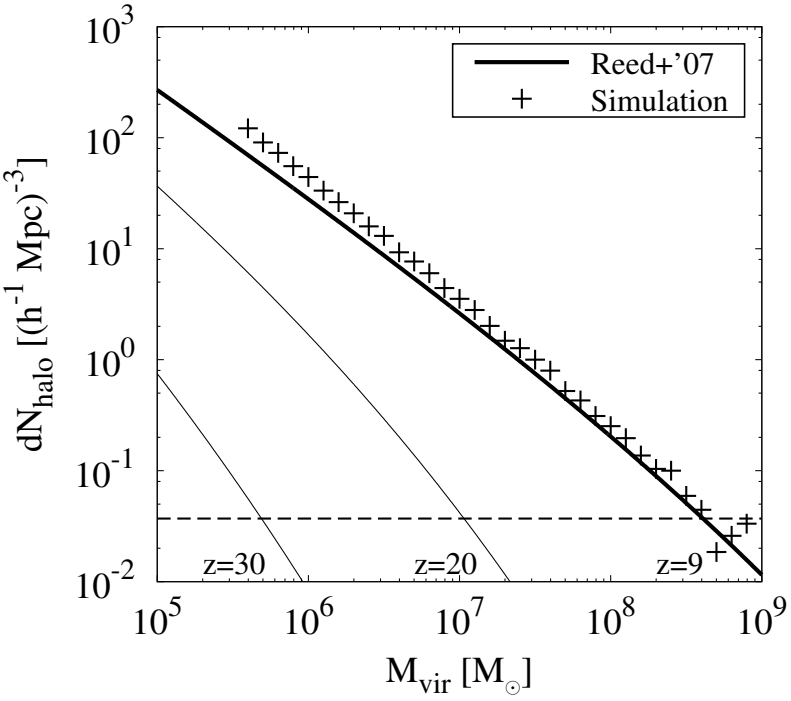

Figure 3.2. Mass function of dark matter halos. The crosses show the result of the parent simulation at $z = 9$ which is constructed by performing the Friend-Of-Friend (FOF) halo finder with linking length $b = 0.2$ and counting halos containing more than 50 N-body particles. The solid lines show the analytically calculated model function, Press-Schechter mass function, at $z = 9$ (thick), 20, and 30 (thin) using the Reed *et al.* (2007) code. The dashed horizontal line represents the number density of 1 $(3\ h^{-1}\mathrm{Mpc})^{-3}$, with which one halo should be found in the cosmological volume of the parent simulation.

3.2 Method

The first step is performing a large parent cosmological simulation with relatively low spatial resolution and identifying dark matter halos. Then the evolution is recalculated using the so-called hierarchical zoom-in technique for 55 cradle regions which contain a lot of halos. From these zoom-in simulations, the star-forming clouds are picked out to calculate the subsequent collapse until the central density reaches 10^7 cm^{-3}. The cloud state at this moment is used to infer the final stellar mass. Here, each step of the procedure is shown.

The first calculation is the parent N-body (DM-only) simulation with a large cosmological volume of $L_{\mathrm{box}} = 3\ h^{-1}$Mpc (comoving) on a side employing 768^3 DM particles which follows the evolution from $z = 99$ to 9. The particle mass of the DM component is 7400 $M_\odot$ and the gravitational softening length is set to be 115 pc. The parameters

of cosmological initial condition are summarized in Table 3.1 (as the same manner in Table 2.1). The background panel in Figure 3.1 shows the final output of this simulation. Primordial clouds form within the DM halos located at the densest parts of the cosmic filaments. Then all candidate sites for primordial star formation in the simulated volume are picked out. DM halos are identified by running the Friends-Of-Friends (FOF) halo finder. Figure 3.2 shows the obtained mass function of DM halos. The simulation result agrees well with the analytical prediction (Press-Schechter mass function), confirming that the parent simulation represents a typical cosmological volume. Note that the halo selection should be non-biased if all of the star-forming sites are selected from this simulation volume.

Figure 3.1 shows that the dark halos are strongly clustered. 55 zoom-in spherical regions with the radius of 390 h^{-1}kpc are located to cover such cradle regions (one of them is marked with the red circle in Fig. 3.1). Only the inner 3/4 volume of each zoom-in region are used to look for gas clouds in order to exclude non-physical halos which appear in the outer part of the zoom-in regions. The net volume considered as primordial star-forming regions is about 20 per cent of the total simulation volume. Then 55 zoomed initial conditions are generated with baryonic components (SPH particles) with increased mass resolution by a factor of 4^3. The resulting effective number of particles in a zoom-in region is 3072^3. The corresponding small-scale density fluctuations are added suitably as given by the adopted ΛCDM cosmology. The masses of DM particles and of the gas particles within the zoom-in region are 116 and 19 $M_\odot$ respectively. The gravitational softening length is set to be 29 pc. The zoom-in simulations are continued down to redshifts $z \simeq 30 - 25$, when the first gravitationally collapsing cloud is formed.

When non-linear objects are formed, the densest part are clipped out of the zoom-in regions with the following cutout criteria:

1. Because each zoom-in simulation stops when a cloud begins to collapse, the subsequent evolution of the other clouds is not followed in the same single simulation. Potential sites where other clouds are later formed are tagged by identifying the regions with densities a few times greater than the cosmic mean value. These zoomed-in regions normally have $\sim 10 - 100$ candidates.
2. Halos which lie in the densest region within 1 physical kpc radius around the density peak are selected, implicitly assuming that the halo forming there will not be affected by any external feedback from nearby sources except the photodissociating feedback, including photoionizing, chemical, and dynamical feedbacks. Primordial clouds forming at the centers of such halos will host Pop III.1 or III.$2_{\rm D}$ stars.

After that, the simulations for each selected gas cloud are restarted. When a cloud collapses, the spatial resolution is continually increased by adopting the particle-splitting technique (Kitsionas & Whitworth, 2002) to insure that the DM core radius is always resolved by 2 times the gravitational softening length of the N-body particles whereas the local Jeans length is always resolved by 15 times the local smoothing length of the SPH particles. The collapse of each cloud is followed until its central density reaches

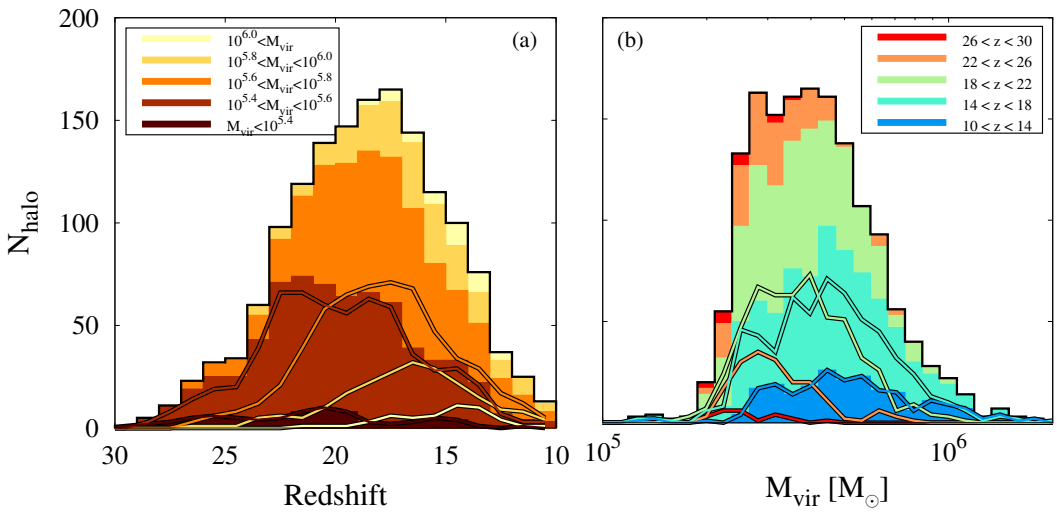

Figure 3.3. Distributions of dark matter minihalos that host primordial star-forming clouds as functions of the formation redshift (panel a) or the virial mass (b). In the panel (a), the bin width is $\Delta z = 1$ and the different colors indicate the different ranges of the virial masses: $M_{\rm vir}/M_\odot < 10^{5.4}$, $10^{5.4} < M_{\rm vir}/M_\odot < 10^{5.6}$, $10^{5.6} < M_{\rm vir}/M_\odot < 10^{5.8}$, $10^{5.8} < M_{\rm vir}/M_\odot < 10^{6.0}$, and $10^{6.0} < M_{\rm vir}/M_\odot$. In the panel (b), the bin width is logarithmically equal, $\Delta M_{\rm vir}(M) = (10^{0.1} - 1) \times M$, and the different colors indicate the different ranges of the redshifts: $10 < z < 14$, $14 < z < 18$, $18 < z < 22$, $22 < z < 26$, and $26 < z < 30$. The black lines show the sums over all virial masses or redshifts.

10^7 cm^{-3}, which ultimately results in 1540 primordial star-forming regions within one parent cosmological volume.

In the present study, the gas metal enrichment and hence the formation of Pop II stars is not considered. Previous studies show that the FUV radiation from nearby Pop II stars dominates over the Pop III component at $z < 10 - 15$ (e.g., Agarwal *et al.*, 2012; Johnson *et al.*, 2013). Thus, the simulations stop at $z = 10$.

3.3 Results

The following sections consider the statistical properties at two different scales; the gravitationally trapped gas in the virialized dark matter halos and the gravitationally collapsing gas at the Jeans scale. The cloud's properties are calculated by averaging over such two scales. The boundary for the former is defined to be the halo virial radius, within which the average matter density is 200 times higher than the cosmic mean value (Sec. 1.2.1). For the latter mass scale, the boundary is defined as the cloud radius, where the ratio of the enclosed mass to the local Jeans mass (Eq. 1.13) has its maximum value (Sec. 2.2.4.1). The following sections present the statistical analyses for the cloud properties calculated for the two mass scales.

3.3.1 Virial Scale: Dark Matter Minihalos

Figure 3.3(a) shows the redshift distribution of 1540 minihalos found in the cosmological simulation. The obtained sample ranges from $z = 30 - 10$ and peaks around $z \sim 20$. Figure 3.3(b) shows the halo mass distribution over $M_{\rm vir} = 2 \times 10^5 - 1 \times 10^6\ M_\odot$, which presents a peak around $M_{\rm vir} \simeq 3 \times 10^5\ M_\odot$. The virial temperature of a star-forming halo is about $T_{\rm vir} \simeq 1000$ K,[*1] and thus the virial mass is $M_{{\rm vir},3\sigma} \sim 4 \times 10^5\ [(1+z)/20)^{-3/2}\ M_\odot$ (Eq. 1.12) which gives $M_{\rm vir} = 2.1 \times 10^5$ and $9.9 \times 10^5\ M_\odot$ at $z = 30$ and 10, in good agreement with the typical masses of minihalos. As shown in Figure 3.3(b), the average halo mass increases with decreasing redshift, which is also consistent with the redshift dependence in Eq. (1.12). There are more than 100 halos per each redshift bin in the range of $z = 22 - 14$, which allows one to study even redshift evolution of the properties of samples.

The physical properties of the star-forming clouds may depend on the initial angular momentum of the host halo. One of the important quantities at the halo scale is the spin parameter which characterizes the rotational degree of a halo; following the definition of Bullock *et al.* (2001),

$$\lambda' \equiv \frac{j_{\rm vir}}{\sqrt{2} R_{\rm vir} V_{\rm vir}}\ , \tag{3.1}$$

where $j_{\rm vir}$ is the specific angular momentum and $V_{\rm vir} = \sqrt{GM_{\rm vir}/R_{\rm vir}}$ is the circular velocity of the halo. The angle between the two angular momentum vectors are also computed as

$$\theta = \cos^{-1}\left[\frac{\mathbf{J}_{\rm DM} \cdot \mathbf{J}_{\rm gas}}{|\mathbf{J}_{\rm DM}||\mathbf{J}_{\rm gas}|}\right]\ . \tag{3.2}$$

Figure 3.4 shows the spin parameters for both dark matter and baryonic components and the relative angle of their angular momentum vectors. The distribution of the spin parameters can be fitted by a log-normal distribution which is consistent with previous studies (e.g., Bullock *et al.*, 2001);

$$p(\lambda)d\lambda = \frac{1}{\lambda\sigma_\lambda\sqrt{2\pi}} \exp\left[-\frac{\ln^2(\lambda/\overline{\lambda})}{2\sigma_\lambda^2}\right] d\lambda\ , \tag{3.3}$$

where $\overline{\lambda}$ is the location parameter and σ_λ is the shape parameter of the distribution. The χ^2-fitting suggests $\overline{\lambda}_{\rm DM} = 0.0344$ and $\sigma_{\lambda_{\rm DM}} = 0.586$ for the dark matter whereas $\overline{\lambda}_{\rm gas} = 0.0283$ and $\sigma_{\lambda_{\rm gas}} = 0.782$ for the baryon. At high redshifts ($z > 14$), the baryon spin parameter is lower than that of dark matter (Fig. 3.5a). The distribution of baryon spin parameter becomes close to that of dark matter at lower redshift (after $z \sim 14$) because of the momentum redistribution between the two components (de Souza *et al.*,

[*1] This is the critical temperature for a primordial cloud to collapse with efficient H_2 molecular cooling which is weakly dependent on redshift (e.g., Glover, 2013). In fact, samples of dark matter minihalos have temperatures close to the critical value.

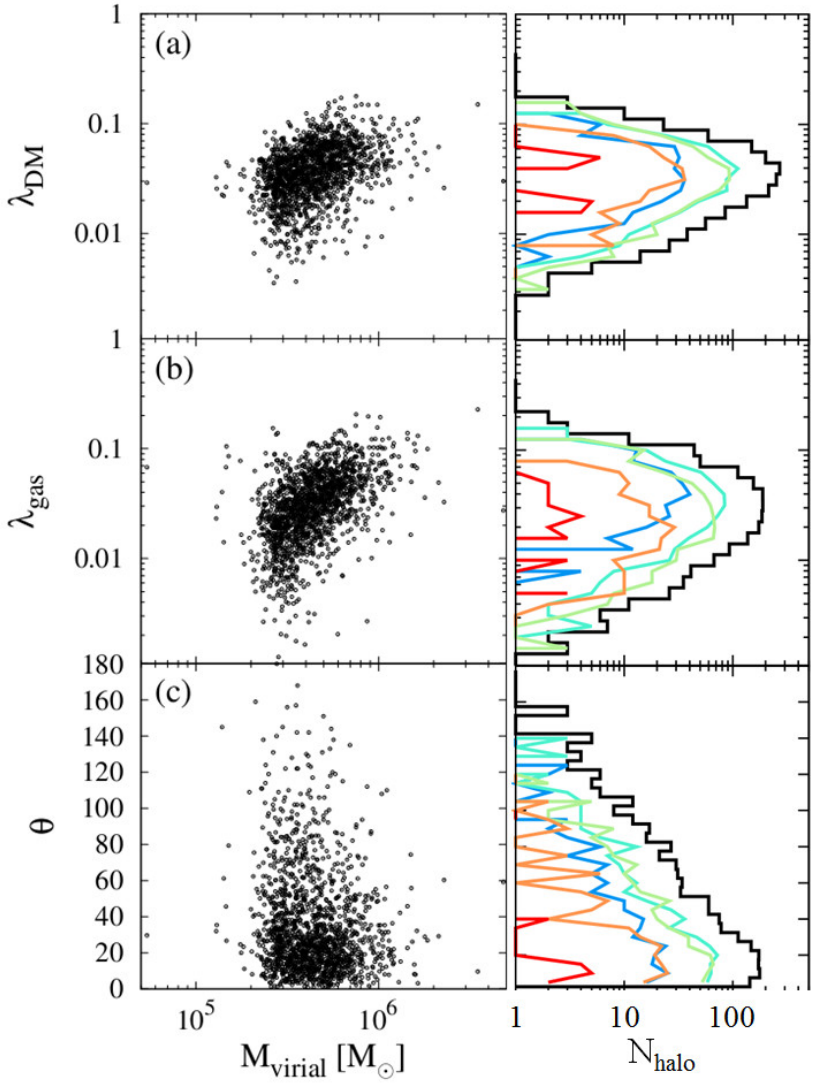

Figure 3.4. Scatter plots and histograms of basic properties of the gas clouds on the virial scale. The left panels show, from top to bottom, spin parameters of dark matter, spin parameters of baryonic components, and the offset angles between angular momentum vectors of the two components. The right panels show their histograms; the colors represent the same redshift ranges as in the right panel of Figure 3.3. The circles and triangles correspond to H_2- and HD-cooling clouds, respectively.

2013). The average angle is $\theta_{\rm ave} \simeq 35°$, suggesting that the spin vectors of the two components are roughly aligned with each other in most of the halos, although with a few exceptions whereby $\theta > 90°$ (Fig. 3.5b). Interestingly, there is a trend that the offset angle and the spin parameter are anti-correlated, i.e., the gas and the dark matter components rotate differently in slowly rotating halos.

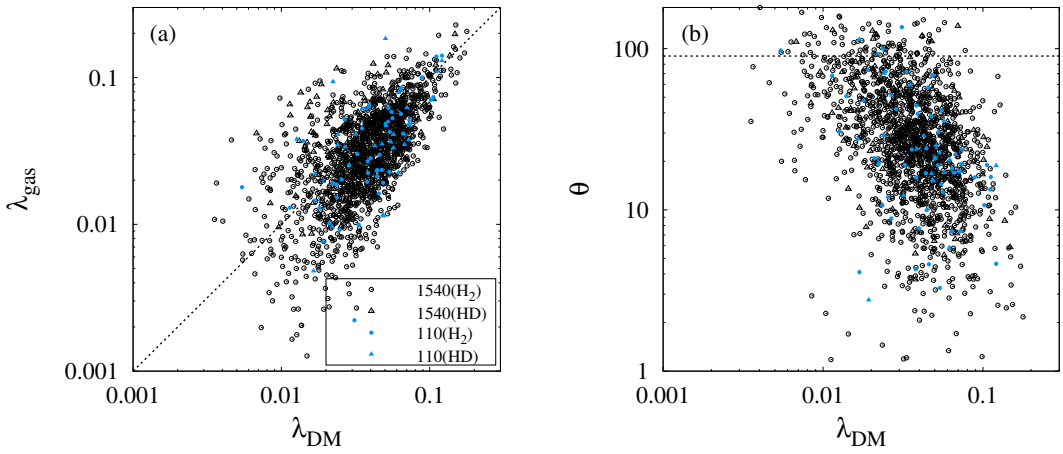

Figure 3.5. Scatter plots of (a) the spin parameters of baryonic components and (b) the offset angles as a function of the spin parameters of dark matter components. The dashed lines show the equal relation $\lambda_{\rm DM} = \lambda_{\rm gas}$ in panel (a) and a given angle $\theta = 90^\circ$ in panel(b).

3.3.2 Jeans Scale: Gravitationally Unstable Clouds

In a minihalo, the collapsing gas is initially heated adiabatically until H_2 molecular cooling overcomes the compression heating. When the H_2 fraction reaches the critical value ($f_{\rm H_2,crit}$ = a few $\times 10^{-4}$; Section 1.2.1), the temperature begins to decrease rapidly with increasing density. The simulation follows the collapse until the central hydrogen number density reaches 10^7 cm^{-3}. Among the samples, the time duration of the cloud collapse, from from $n_{\rm H,cen} = 10$ to 10^7 cm^{-3}, increases with decreasing the formation redshifts. For instance, the duration averaged over samples for five different redshift ranges are 29.5 ($10 < z < 14$), 18.0 ($14 < z < 18$), 12.0 ($18 < z < 22$), 7.9 ($22 < z < 26$), and 5.5 Myr ($26 < z < 30$). The clouds collapse more slowly at lower redshifts. The similar dependence is also reported by Gao *et al.* (2007). The following studies the evolution of clouds forming at different redshifts.

In the Pop III.1 case, the thermal evolution proceeds in one of two different modes depending on whether or not HD molecular cooling is effective. In most cases, the evolution is driven by H_2 cooling alone, whereas HD cooling becomes efficient only under limited conditions. In a rapidly rotating cloud, for instance, H_2 cooling reduces the temperature to $T < 200$ K because of the slower collapse and hence less efficient compressional heating. HD formation begins at these low temperatures and the resulting HD cooling further reduces the temperature to the CMB floor at $T_{\rm CMB}(z) \simeq 2.73\ (1+z)$ K.

How efficiently does HD cooling operate during the collapse in samples? Figure 3.6(b) shows the difference between the HD-cooling cases and others by analyzing simulation results. The averaged profile of fraction ratios of HD to H_2, $f_{\rm HD}/f_{\rm H_2}$, sharply increases at $n_{\rm H} \sim 10^4$ cm^{-3} in HD-cooling clouds because the cloud's temperature drops below

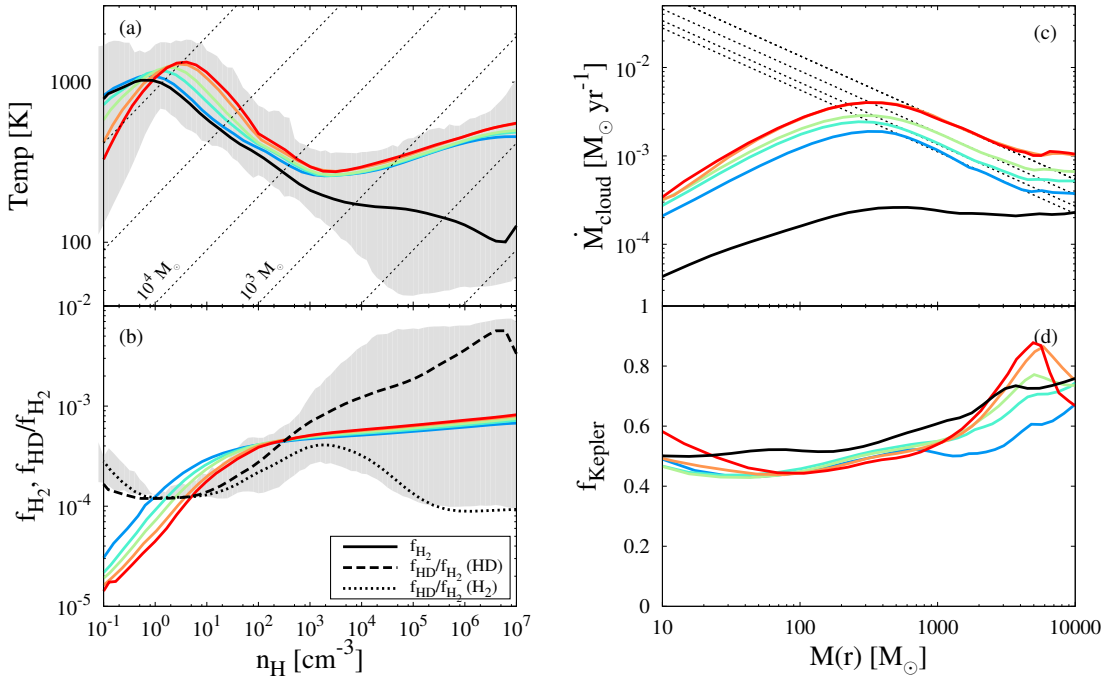

Figure 3.6. Averaged profiles of primordial star-forming clouds when $n_{\rm H,cen} = 10^7$ cm^{-3}; (a) gas temperature, (b) H_2 fraction and ratio of HD to H_2, (c) gas infall rate, and (d) Keplerian factor ($f_{\rm Kepler} = v_{\rm rot}/v_{\rm Kepler}$). In panel (b), the colored lines show averaged H_2 fractions for H_2-cooling cases at 5 redshift ranges. The grey region shows the maximum and minimum for all clouds at each radius. The colored lines show averaged profiles for H_2-cooling clouds at five redshift ranges and the black line shows the averaged profile for HD-cooling clouds. The dotted and dashed lines show averaged $f_{\rm HD}/f_{\rm H_2}$ for all HD-cooling and H_2-cooling cases, respectively. In panel (c), the dotted lines show the fitting functions for the averaged infall rates at the protostellar formation and are characterized by $\{0.34, 0.34, 0.23, 0.17, 0.14\} \times (M_{\rm enc}/M_\odot)^{-0.7}\ M_\odot$ yr^{-1} in order of higher- to lower-redshift groups.

the critical value to make the HD formation be efficient. In this thesis, following this result and previous studies (e.g. McGreer & Bryan, 2008), the HD-cooling case is defined as the mode where the fraction ratio exceeds 10^{-3} at $n_{\rm H,cen} < 10^6$ cm^{-3}. Among the samples, there are also intermediate cases, whereby the onset of HD cooling is somewhat delayed; i.e., $f_{\rm HD}/f_{\rm H_2}$ increases sharply in the density range $10^6 < n_{\rm H,cen}/{\rm cm}^{-3} < 10^7$ and eventually exceeds 10^{-3}. The 1540 samples of primordial clouds are classified as one of three possible cases, depending on the behavior of $f_{\rm HD}/f_{\rm H_2}$ during the collapse: H_2-cooling cases (1186 cases), HD-cooling cases (151), and the intermediate cases (203), where the numbers in parentheses indicate the numbers of the corresponding samples. The H_2-cooling cases show a broad range of formation redshifts: $10 < z < 14$ (98), $14 < z < 18$ (423), $18 < z < 22$ (474), $22 < z < 26$ (168), and $26 < z < 30$ (23), which allows to study the redshift-dependence of the physical properties of the primordial clouds. On the other

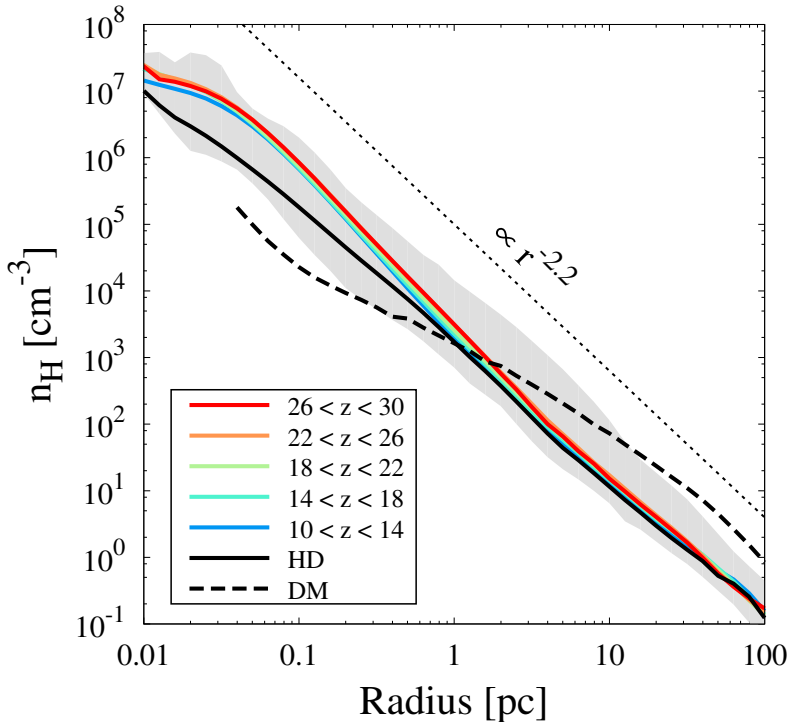

Figure 3.7. Radial gas density profiles of primordial star-forming clouds when $n_{\rm H,cen} = 10^7$ cm^{-3} in the same manner as in Figure 3.6. The solid lines show the gas component and the dashed line shows the DM component. The dotted line shows the power-law slope, $n_{\rm H} \propto r^{-2.2}$ (e.g., Omukai & Nishi, 1998).

hand, the HD cooling and intermediate cases appear only at low redshifts ($z < 18$).

Figure 3.7 shows the averaged radial profiles of gas density when $n_{\rm H,cen} = 10^7$ cm^{-3}. They are well fitted by the power-law function $\rho \propto r^{-2.2}$ in the envelope (e.g, Omukai & Nishi, 1998).[*2] The slopes of profiles look very similar, but, for any given radius, the clouds' densities can differ by more than an order of magnitude (see the gray region). Such differences between the clouds will lead to differences of the gas infall rates onto a central protostar during the subsequent accretion stage. For the H_2-cooling clouds, the densities tend to be lower with decreasing formation redshifts. The densities of the HD-cooling clouds tend to be even lower than for H_2-cooling cases, a result of the lower temperature during the collapse as shown below.

Figure 3.6 displays the averaged thermal (panel a), chemical (b), and dynamical (c and d) properties of the collapsing clouds. Figure 3.6(a) shows the temperature distribution as a function of gas density, which reflects the variation of H_2 and HD abundances shown in Figure 3.6(b). There is a small but systematic redshift-dependence of the effectiveness of H_2 cooling: the cloud's temperature averagely lower at lower redshifts.

The similar redshift-dependence has been found in the previous section, where possible

[*2] The dark matter density profiles also represent power-law features which at $r \sim 10$ pc transition from $n_{\rm DM} \propto r^{-2}$ to $r^{-1.5}$.

origins of such dependence is considered (see Sec. 2.2.4.2).

For the HD-cooling cases, the higher $f_{\rm HD}/f_{\rm H_2}$ leads to an even lower temperature. The typical mass of a gravitationally unstable cloud is given by the Jeans scale at the local minimum of the temperature profile, which is around several $\times 10^3$ $M_\odot$ for H_2-cooling cases and several $\times 10$ $M_\odot$ for HD-cooling cases.

Figure 3.6(c) shows the radial distributions of the instantaneous gas infall rate $\dot{M}_{\rm cloud} = 4\pi r^2 \rho v_{\rm rad}$ as a function of enclosed gas mass, extending well outside the Jeans mass. For the H_2-cooling cases, the expected gas infall rates decrease with decreasing formation redshifts. For the HD-cooling cases, the infall rates are about 10 times lower (the next section addresses this issues). The dotted lines show the expected profiles after further collapse. By extrapolating the profiles from the outer regions, power-law profiles $\dot{M}_{\rm cloud} \propto M_{\rm enc}^{0.7}$ are obtained, which agree with previous results (e.g., Gao *et al.*, 2007).

Figure 3.6(d) displays the degree of rotational support, the azimuthal rotation velocity $v_{\rm rot}$ normalized by the local Keplerian velocity $v_{\rm Kepler} = \sqrt{GM(r)/r}$, where $M(r)$ is the gas mass within a given radius r. $v_{\rm rot}$ is calculated by averaging the velocity perpendicular to the total angular momentum vector for the gas within r. All clouds have similar values clustered around $f_{\rm Kepler} = 0.5$, which agrees with the results of previous studies (e.g., Yoshida *et al.*, 2006).

McKee & Tan (2008) has modeled the accretion histories as a function depending on two parameters: $f_{\rm Kepler}$ and $K^{'}$, a measure of the entropy of the accreting gas. By comparing their modeled accretion rates (fig. 9 in McKee & Tan, 2008) and the calculation results in this thesis (Fig. 3.6c), one can determine the corresponding parameters. By assuming $f_{\rm Kepler} = 0.5$, the other parameter $K^{'}$ is estimated to be $1 \sim 2$. They also estimate the final stellar masses when the photoevaporative mass-loss rate overcomes the accretion rate. The estimated final masses with above parameters range over $150 - 300$ $M_\odot$, which are consistent with the results presented in later sections.

3.3.3 Distribution of Gas Infall Rates

After the onset of collapse, the newly-formed protostar grows in mass via accretion from the surrounding envelope. It is well known that the accretion history in this phase significantly affects the protostar's evolution and the strength of the UV radiative feedback against the accretion flow. Since the stellar radiative feedback ultimately shuts off the mass accretion, the mean accretion rate is a key parameter that determines the final stellar mass.

Figure 3.8 shows the histograms of gas infall rates. The black line represents the entire collection of samples covering all formation redshifts. There are two peaks that correspond to the different thermal evolution during the collapse stages: the right peak at $\sim 3 \times 10^{-3}$ $M_\odot$ yr^{-1} is primarily associated with the H_2-cooling case and the left peak at $\sim 10^{-4}$ $M_\odot$ yr^{-1} is primarily associated with the HD-cooling case. As expected from the redshift-dependence of the thermal evolution, the high-rate (high-mass) peak associated with H_2-cooling cases is found at all epochs, whereas the low-rate peak associated with HD cooling appears only at low redshifts. Thus, the infall rate distribution changes from

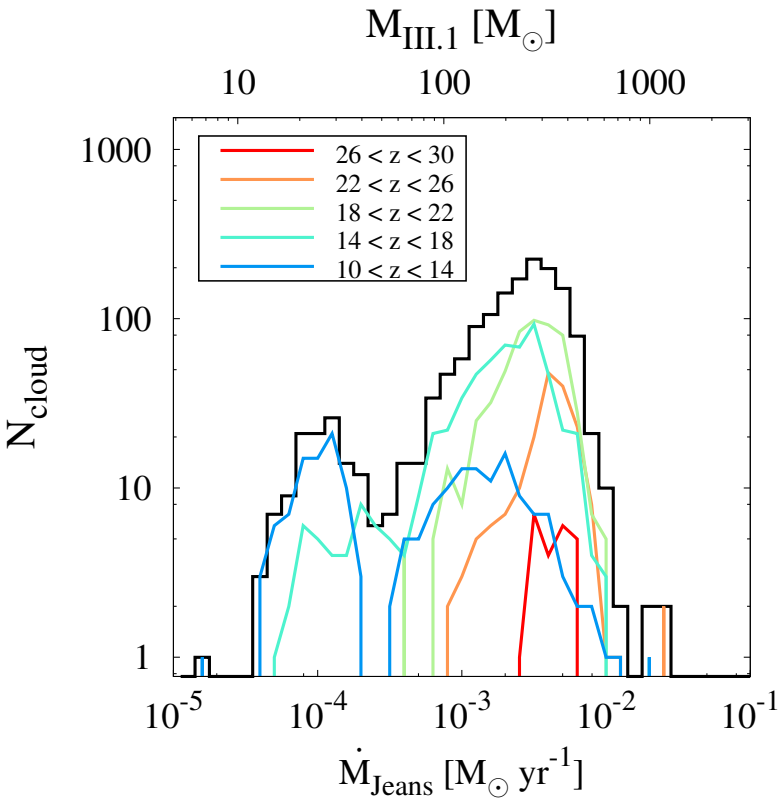

Figure 3.8. Histogram of the gas infall rates measured at the Jeans scale when $n_{\rm H,cen} = 10^7$ cm^{-3}. The lines with the different colors represent the different redshift ranges from high (red) to low redshift (blue). The top axis gives the stellar mass estimated from $\dot{M}_{\rm Jeans}$ by Eq. (2.1).

a single peaked function at high redshifts to the bimodal function for low redshifts, as shown by the colored lines.

110 cosmological samples of the primordial star-forming regions in Chapter 2.2 show that the large variation of the gas infall rates leads to a spread of final stellar masses ranging from 10 to 1600 $M_\odot$. The results of this chapter, with 10 times more samples, show that the infall rates at each formation epoch has their characteristic value, which decreases with decreasing redshifts. Thus, it is expected that the stellar mass distribution should also have analogous redshift-dependent characteristic values.

3.3.4 Estimating Pop III.1 Stellar Masses

This section revisits the correlations between the stellar masses and the gas infall rates, which have been examined in Section 2.2.4.2. Eq. 2.1 represents that the gas infall rates measured at the Jeans scale can be used as an accurate estimator, via empirical fit, of the final stellar masses. The top axis in Figure 3.8 depicts the stellar mass calculated by Eq. 2.1. In this diagram, the positions of the right and left peaks correspond to $M_* \simeq 264$ and

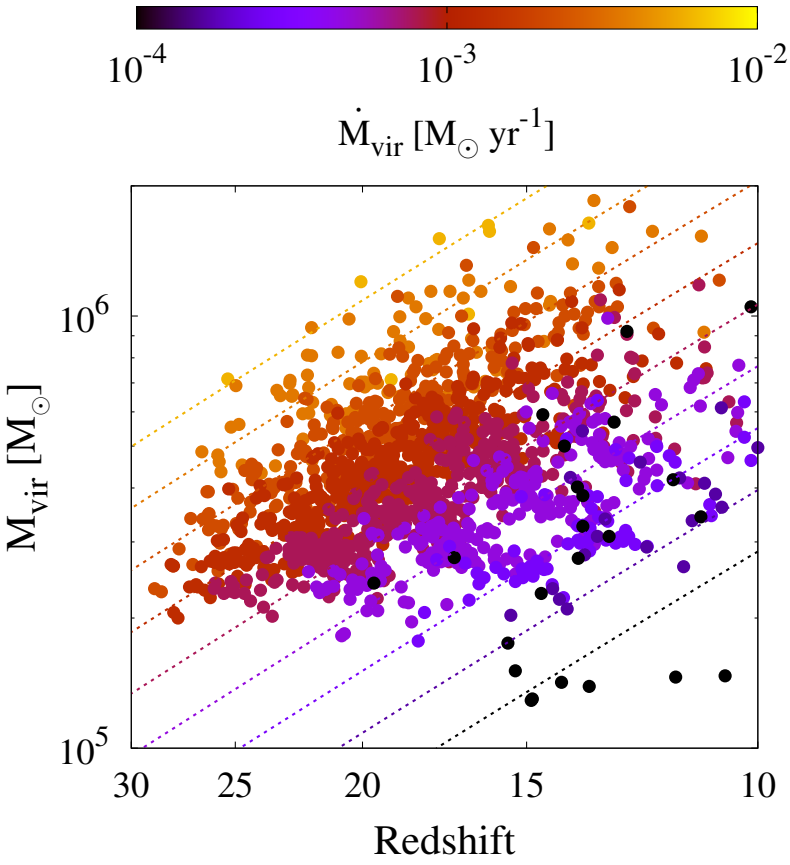

Figure 3.9. Variation of the gas infall rate at the virial scale as a function of formation redshift and virial mass. The different colors depict the different mass infall rates, according to the color scale at the top. The distributions of the filled circles and dotted lines represent the variation of the sample data and its fitting function Eq. (3.4).

$\simeq 24\ M_\odot$, which represent the typical masses of Pop III.1 stars forming via H_2-cooling and HD-cooling modes, respectively.

Section 2.2.4.1.2 shows that the gas infall rate at the halo scale $\dot{M}_{\rm vir}$ is also correlated to the stellar mass, but the correlation is somewhat weaker. Newly obtained much larger sample size, however, can derive more reliable correlations than the previous section. The infall rates at the virial scale are correlated with two quantities; the redshift at which a halo forms $z_{\rm form}$ and the mass of the dark halo $M_{\rm vir}$ (see Eq. 2.7). Figure 3.9 shows the scatter plot of three halo's properties; $z_{\rm form}$, $M_{\rm vir}$, and $\dot{M}_{\rm vir}$. The presence of the alignment of each color (different $\dot{M}_{\rm vir}$) suggests that the accretion rate at the virial scale $\dot{M}_{\rm vir}$ systematically depends on the two parameters of $z_{\rm form}$ and $M_{\rm vir}$. Thus the resulting final stellar mass likely depends on these parameters of the host halo; higher accretion rates, namely the higher final stellar masses, are preferentially found at higher redshifts

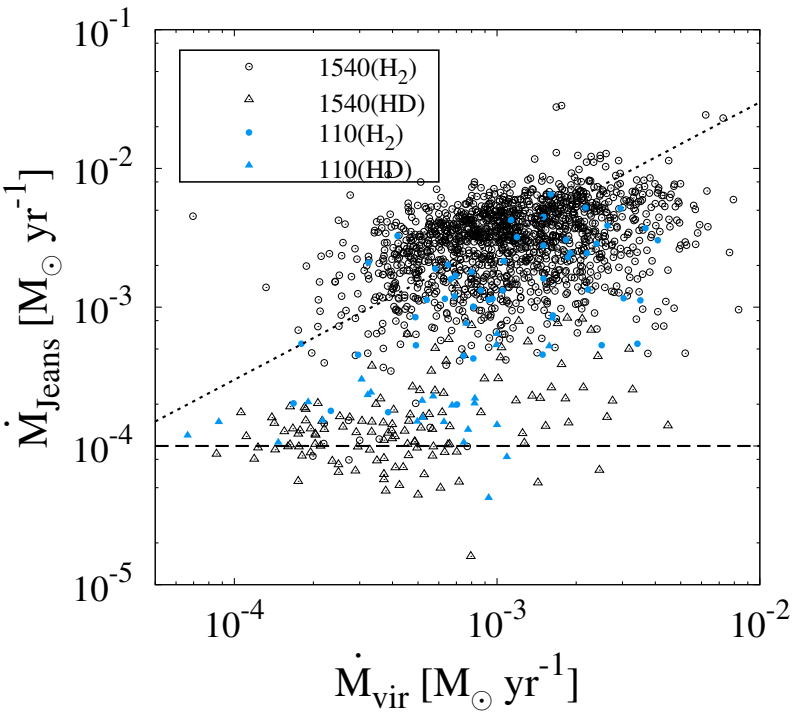

Figure 3.10. Correlation between the gas infall rates at the virial scale $\dot{M}_{\rm vir}$ and at the Jeans scale $\dot{M}_{\rm Jeans}$ when $n_{\rm H,cen} = 10^7$ cm^{-3} for two samples; 1540 cases shown in this chapter and 110 cases shown in Section 2.2. The circles and triangles correspond to H_2- and HD-cooling clouds, respectively. The dotted and dashed lines show the fitting formulae for H_2- and HD-cooling cases (Eq. 3.5)

and in more massive minihalos. A good fit providing the estimate for the infall rate is

$$\dot{M}_{\rm vir} = 1.1 \times 10^{-3} \left(\frac{1+z}{20}\right)^{3.5} \left(\frac{M_{\rm vir}}{4 \times 10^5\ M_\odot}\right)^{1.75} M_\odot\ {\rm yr}^{-1}\ . \tag{3.4}$$

Although there is substantial scatter, Eq. (3.4) provides a reasonable estimate of the stellar mass using basic properties of the host dark halo.

By assuming the dependence of the cloud's properties on the halo's properties, the redshift dependence of the gas infall rates (or the stellar masses) shown as the colored lines in Figure 3.8 can be understood as follows. For the H_2-cooling cases, the infall rates at the halo scale are well correlated with those at the Jeans scale as shown in Figure 3.10. On the other hand, such a correlation is not found for the HD-cooling cases, because the infall rates at the Jeans scale are within a narrow range of $\dot{M}_{\rm Jeans} \sim 10^{-4}\ M_\odot\ {\rm yr}^{-1}$ (see also Fig. 3.10). The relative scaling of $\dot{M}_{\rm vir}$ and $\dot{M}_{\rm Jeans}$ are described by

$$\dot{M}_{\rm Jeans} = \begin{cases} 3 \times \dot{M}_{\rm vir} & \text{if } \dot{M}_{\rm vir} > 10^{-3}\ M_\odot\ {\rm yr}^{-1}\ ({\rm H_2})\ , \\ 10^{-4}\ M_\odot\ {\rm yr}^{-1} & \quad < 10^{-3}\ M_\odot\ {\rm yr}^{-1}\ ({\rm HD})\ . \end{cases} \tag{3.5}$$

By substituting them into Eq. (2.1), mass estimating formulae for two thermal evolution paths are obtained as

$$M_{\mathrm{III.1(H_2)}} = 264 \left(\frac{\dot{M}_{\mathrm{vir}}}{10^{-3}\ M_\odot\ \mathrm{yr}^{-1}} \right)^{0.7} M_\odot\ , \tag{3.6}$$

$$M_{\mathrm{III.1(HD)}} = 24\ M_\odot\ . \tag{3.7}$$

Eq. (3.6) for $M_{\mathrm{III.1(H_2)}}$ is modified by eliminating $\dot{M}_{\mathrm{vir}}$ with Eq. (3.4) as

$$M_{\mathrm{III.1(H_2)}} = 282 \left(\frac{1+z}{20} \right)^{2.45} \left(\frac{M_{\mathrm{vir}}}{4 \times 10^5\ M_\odot} \right)^{1.23} M_\odot\ . \tag{3.8}$$

Under the assumption that primordial star formation mostly occurs in 3σ minihalos with $T_{\mathrm{vir}} = 1000$ K, the typical value of $M_{\mathrm{III.1(H_2)}}$ is evaluated by substituting $M_{\mathrm{vir},3\sigma}$ shown in Section 3.3.1 into Eq. (3.8),

$$M_{\mathrm{III.1(H_2)}} = 282 \left(\frac{1+z}{20} \right)^{0.65} M_\odot\ . \tag{3.9}$$

This equation provides the typical stellar mass for the H_2-cooling mode of 282 $M_\odot$ at $1+z = 20$, which is consistent with the redshift dependence shown in Figure 3.8. Eq. (3.9) is also consistent with the fact that, at low redshifts, the mass distribution peak moves to lower stellar masses.

3.4 Discussion

There is a variety of physical processes involved in the formation of primordial stars. Most of the uncertainties which have been discussed are attributed to the complexity of the star formation process itself, in particular, during the stage of mass accretion onto the embryo protostar and the protostar's UV feedback on the collapsing parent cloud. By contrast, the early evolutionary phases until the formation of a primordial gas cloud is relatively well understood (Yoshida *et al.*, 2008; Greif *et al.*, 2012) and obtained results provide statistics of the physical properties of the cosmological primordial gas clouds, such as the radial profiles of density, temperature, and velocities. In future, one shall discuss the variety of cloud properties and resultant stellar mass. Furthermore, there is a certain normal initial condition of the primordial star formation and its redshift-dependence.

Previous studies adopted *different* initial conditions and used *different* numerical codes with *different* physical processes implemented. It is thus often difficult to identify the origin of differences between studies. Direct comparison would be easier if the same initial conditions are used. The sample of halos can provide a convenient test set as well as statistical properties of halos under normal initial conditions.[*3]

Ultimately, the final stellar masses will be determined more accurately by conducting detailed 3D radiation magnetohydrodynamic simulations, including the additional physics.

[*3] The author is willing to provide data for individual sample halos, or even for all the halos to the interested reader.

Alternatively, it is possible to do the same more efficiently with knowledge of the distribution of initial conditions. Instead of repeating the entire multi-step procedure performed in the present study, the future work only needs to update the estimation formula of the final stellar masses such as Eq. (2.1) by simulating the evolution for several representative cases. In this manner, the primordial stellar mass distribution can be easily reconstructed from a very large cosmological simulation.

Chapter 4

Mass Distribution of Primordial Stars

4.1 Overview

The previous chapters have shown that the final masses of Pop III.1 and III.2$_{\rm D}$ stars can be estimated reasonably well from a few physical properties of their host clouds. In principle, one can derive the "cosmological" mass distribution of primordial stars theoretically by investigating the probability distribution of such a property, e.g., gas infall rate at the Jeans scale.*1 The results can be used, for example, to predict the early chemical evolution and the characteristic signatures of the first galaxies.

It is definitely worth developing such a global evolution model using large-scale cosmological simulations. This section constructs the mass distribution of Pop III.1 and III.2$_{\rm D}$ stars using the non-biased cosmological samples of the primordial star-forming clouds. The stellar mass for each halo is determined by considering the physical properties of the cloud for Pop III.1 case (Eq. 2.1) and intensity of the local FUV radiation field for Pop III.2$_{\rm D}$ cases (Eq. 2.10). The obtained cosmological sample of 1540 primordial clouds in Chapter 3 is classified into Pop III.1 and III.2$_{\rm D}$ cases, according to the criteria based on the local photodissociating FUV intensity ($J_{21} < 0.1$ or not). Figure 4.1 shows the spatial distribution of the FUV intensity J_{21} (color contour) and both of Pop III.1 (yellow dots) and III.2$_{\rm D}$ stars (red) in the cosmological volume. There are small clusters of Pop III.2$_{\rm D}$ stars at high redshifts, where the photodissociating radiation is very strong. The stellar masses are determined from the cloud properties and the computed FUV intensity.

The content in this chapter has been submitted to Monthly Notices of the Royal Astronomical Society, together with the results shown in Chapter 3.

*1 Such a correlation between the cloud properties' distribution and mass distribution is similar to the observational relationship between the core mass function and initial mass function for the present-day star.

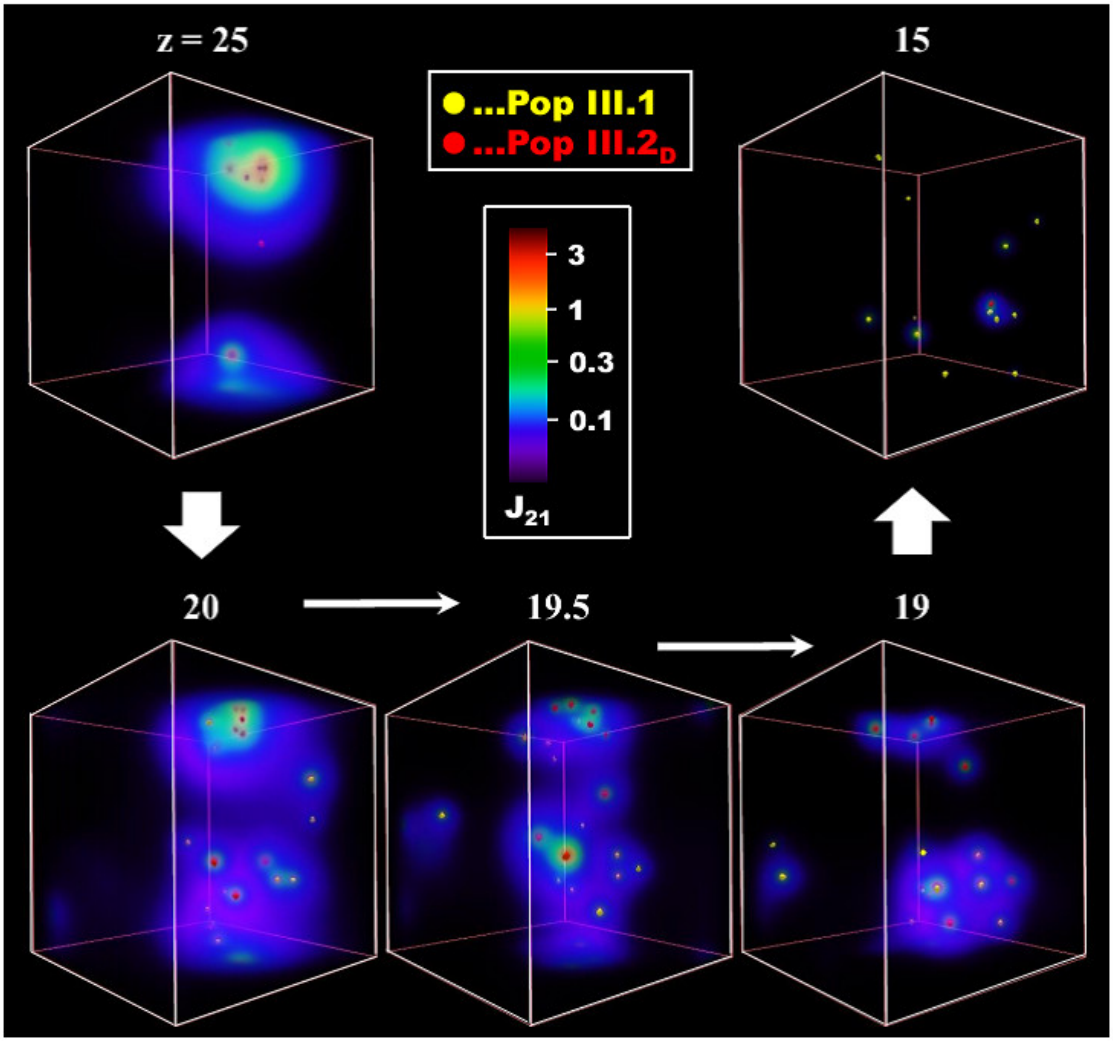

Figure 4.1. Time evolution of the FUV intensity field, J_{21}, in the same comoving cosmological volume with $(3\ h^{-1}\mathrm{Mpc})^3$ at $z = 25$, 20, 19.5, 19, and 15. The color contours indicate the FUV intensity ranging from $J_{21} = 0.025$ to 6.3 (blue to red). The yellow and red clumps show the active Pop III.1 and III.2$_\mathrm{D}$ stars, respectively. The FUV radiation field decreases with decreasing redshift, because the typical stellar mass becomes lower and separations between the stars are stretched by the cosmic expansion.

4.2 Method

To derive the primordial stellar mass distribution including both Pop III.1 and III.2$_\mathrm{D}$ stars, it is needed to evaluate the local intensity of the photodissociating radiation at each cloud in a self-consistent manner with the spatial distribution of the primordial stars. For this purpose, the following post-processing calculations are performed:

1. The primordial gas clouds are sorted by their formation redshifts z_{*1}, the epoch when the cloud's central density reaches 10^7 cm^{-3}. The procedure first begins with assigning the stellar mass to the halo which has the highest z_{*1}.
2. Then the local FUV intensity for the clouds forming at the lower redshifts are evaluated. This thesis assumes that the star radiates at a constant luminosity $Q_{\rm LW}$ during its lifetime t_* and dies at redshift $z_{*2} = z_{*1} - \Delta z(t_*)$ and adopts the numerical results of Schaerer (2002), who present the values of $Q_{\rm LW}$ and t_* as functions of the stellar mass. The FUV intensity is evaluated when a cloud is in the pre-collapse stage $z_{\rm ini}$ ($n_{\rm H,cen} = 10$ cm^{-3}). The FUV intensity from stars which have $z_{*1} > z_{\rm ini} > z_{*2}$ are counted to obtain the local field.
3. The stellar mass in a halo forming at the lower redshift is determined using the correlation derived from the 2D RHD simulations. The star is classified as Pop III.2$_{\rm D}$, if the local FUV intensity is higher than the critical value $J_{21,\rm crit} = 0.1$. In this case, the stellar mass depends on the local FUV intensity as well as the cloud properties. The mass of a star formed within the irradiated cloud is determined by the cloud's properties for Pop III.1 cases whereas by the local FUV intensity for Pop III.2$_{\rm D}$ cases.
4. Steps 2 and 3 are repeated for the clouds one by one in the order of decreasing formation redshift. The stellar masses are accordingly determined by the above procedure.

The intensity of the FUV radiation at the location of the i-th cloud contributed by the star in the j-th cloud is given by (Agarwal *et al.*, 2012),

$$J^j_{{\rm LW},i} = \frac{f_{\rm esc}}{\pi} \frac{h\nu_{\rm avg}}{\Delta\nu_{\rm LW}} \frac{Q_{{\rm LW},j}}{4\pi d^2_{ij}} \ , \tag{4.1}$$

where $f_{\rm esc}$ is the fraction of LW photons that escape from the j-th halo, $h\nu_{\rm avg}$ is the average photon energy emitted from a Pop III star in the LW band, $\Delta\nu_{\rm LW}$ is the difference between the maximum and minimum frequencies of the LW bands,[*2] and d_{ij} is the distance between the centers of the i-th and j-th clouds. According to Kitayama *et al.* (2004), the escape fraction $f_{\rm esc}$ should be around $0.1 - 1$ for the minihalos considered with $M_{\rm vir} = 2 \times 10^5 - 2 \times 10^6\ M_\odot$. This procedure adopts the fiducial value of $f_{\rm esc} = 0.5$. The local FUV intensity at the i-th cloud $J_{21,i}$ is then calculated by summing up the contributions from all the nearby clouds with $z_{*1,j} > z_{{\rm ini},i} > z_{*2,j}$,

$$J_{{\rm LW},i} = \sum_j^N J^j_{{\rm LW},i} \ . \tag{4.2}$$

This thesis only considers the contemporary sources in the simulation box and ignores the background radiation.

[*2] $\nu_{\rm avg} = \nu_{\rm max} = 13.6$ eV (3.288×10^{15} Hz) and $\nu_{\rm min} = 11.2$ eV (2.708×10^{15} Hz).

4.3 Results

4.3.1 Classification into Population III.1 and III.2$_{\rm D}$ Stars

In the cosmological context, as shown in Figure 3.1, the earliest generation of stars are formed in filaments or knots of the large scale structure and hence the star-forming regions are distributed in a biased manner. Radiation emitted by stars formed early affects subsequent star formation in nearby regions. The local FUV intensity at each cloud are evaluated considering the spatial distribution of other stars at the moment when the cloud central density reaches 10 cm^{-3}. This thesis assumes that Pop III.2$_{\rm D}$ stars form at the cloud with $J_{21} > 0.1$. Figure 4.1 shows the resultant FUV radiation fields in the cosmic volume at five different redshifts. The mean FUV intensity decreases with decreasing redshift mostly because spatial separations between stars are stretched by cosmic expansion. At $z = 25$, there is a small cluster of Pop III.2$_{\rm D}$ stars that are formed under the influence of a strong FUV field. Once the bright massive stars form in a dense region, the resulting FUV field could trigger the sequential formation of Pop III.2$_{\rm D}$ stars in nearby halos. At $z = 15$, on the other hand, there are no Pop III.2$_{\rm D}$ stars in the simulation volume because of the weak FUV radiation field resulting from the large physical separation between star-forming regions.

Figure 4.2 shows the histogram of the calculated FUV intensity and its redshift dependence. About one third of halos is irradiated by a strong FUV field and thus satisfies the criterion for Pop III.2$_{\rm D}$ star formation. At $z > 20$, the clouds have a large variation of J_{21}, ranging from 0.01 to 10; about half of the clouds are exposed to FUV radiation with $J_{21} > 0.1$. At $z < 20$, however, the fraction of III.2$_{\rm D}$ stars rapidly decreases. The transition is caused by a combination of the increase of physical separations between the clouds, the decrease of the number of FUV-active stars, and the systematic decrease of stellar masses by the promoted HD-cooling mode of star-formation. At $15 < z < 25$, almost all the clouds have non-zero intensity $J_{21} > 0.01$. However, such a weak FUV irradiation causes negligible effects on the cloud collapse.

Regarding clouds under strong FUV irradiation with $J_{21} > 10$, the sample have 5 such samples at $z = 21 - 26$ with intensities of $J_{21} = 12.1$, 14.1, 17.7, 70.3, and 97.3. However, these are still below the critical value of $J_{21}^{\rm crit} \propto \mathcal{O}(1000)$, above which the so-called direct collapse might be triggered in atomic-cooling haloes (e.g., Wolcott-Green & Haiman, 2011). In the current cases with the weaker FUV radiation and lower-mass haloes, massive Pop III.2$_{\rm D}$ stars should form but not provide the massive seed BHs as prospected in the direct collapse scenario.

In the next section, the stellar mass for each of 1540 star-forming clouds is determined according to the star-formation mode by using Eq. (2.1) for Pop III.1 stars and by using Eq. (2.10) for Pop III.2$_{\rm D}$ stars.

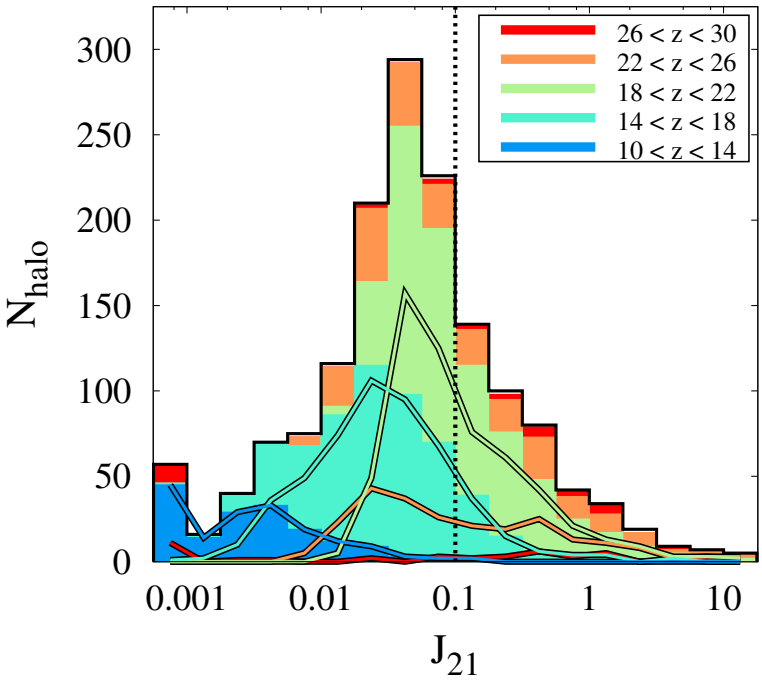

Figure 4.2. Histogram of the normalized intensity of photodissociating radiation J_{21} at the position of each primordial cloud when $n_{\rm H,cen} = 10$ cm^{-3}. The different colors depict the same redshift ranges as in the right panel of Figure 3.3. The dotted vertical line represents the critical value of $J_{21} = 0.1$, above which (right side) Pop III.2$_{\rm D}$ stars form. The halos with $J_{21} > 10$ and $J_{21} < 10^{-3}$ are included in the rightmost and leftmost bins, respectively.

4.3.2 Stellar Mass Distribution

Figure 4.3 displays the mass distributions of Pop III.1 and III.2$_{\rm D}$ stars. The black solid lines show the mass distributions integrated over redshifts. As expected from Figure 2.1, the Pop III.1 mass distribution has two peaks around $M_* \simeq 250$ and 25 $M_\odot$, which reflect the contributions of the H_2-cooling and the HD-cooling modes. The mass distribution of Pop III.2$_{\rm D}$ stars is shifted to larger masses $M_* \simeq 400\ M_\odot$. Each population has a wide mass range,

$$\begin{aligned} 10\ M_\odot < & M_{\rm III.1_{HD}} < \quad 50\ M_\odot\ , \\ 50\ M_\odot < & M_{\rm III.1_{H_2}} < 1000\ M_\odot\ , \text{and} \\ 100\ M_\odot < & M_{\rm III.2_D} < 1000\ M_\odot\ , \end{aligned}$$

respectively. About a half of $M_* > 200\ M_\odot$ stars are Pop III.2$_{\rm D}$ stars. The mass distributions for the different redshifts are represented by lines with different colors. For Pop III.1 cases, as suggested by Eq. (3.9), the high-mass peak, corresponding to the H_2-cooling

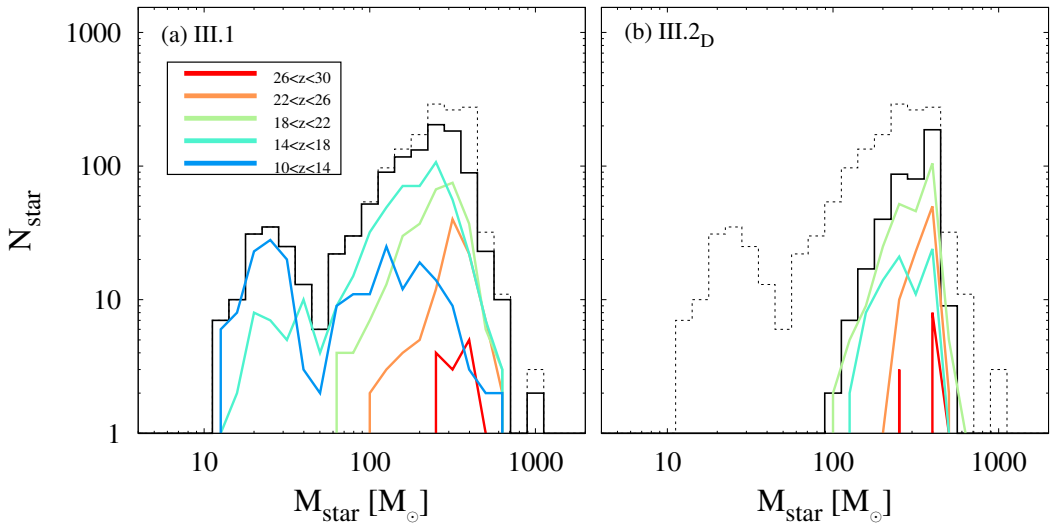

Figure 4.3. Resultant mass distributions of Pop III.1 (left) and III.$2_{\rm D}$ (right) stars for the different redshifts. The different colors represent the same redshift ranges as in the right panel of Figure 3.3. The black solid lines show the total distributions over all redshifts for each population whereas the dotted lines show the sum of them.

mode, gradually shifts to lower stellar masses with decreasing redshift; from 375 $M_\odot$ at $z = 30$ to 191 $M_\odot$ at $z = 10$. The mass distribution of Pop III.$2_{\rm D}$ stars also depends on the redshift, which is caused by the decrease of the average FUV intensity as shown in Figure 4.2. There is no such shift for the HD-cooling cases, probably because of the small sample size at lower redshifts. Overall, the decrease of the Pop III.$2_{\rm D}$ fraction, the decrease of Pop III.$1_{\rm H_2}$ stellar masses, and the increase of low-mass Pop III.$1_{\rm HD}$ fraction explain the shift of the distribution to the lower masses with decreasing redshift.

Because the Pop III.1 stellar masses are estimated from the gas infall rates at the Jeans scale by using the analytic function Eq. (2.1), the mass distribution reflects that of the infall rates. Interestingly, except for Pop III.1 cases formed via the HD-cooling mode, the stellar mass distributions are well described by power-law functions at both the low-mass and high-mass ends. For example, the mass distribution of Pop III.$1_{\rm H_2}$ stars is approximately proportional to $M_*^{2.5}$ at the low-mass end and to M_*^{-4} at the high-mass end. This allows to define the normalized stellar mass function,

$$\Psi(M_*) = \begin{cases} \frac{1.62}{M_{\rm p}/{\rm M}_\odot} \left(\frac{M_*}{M_{\rm p}}\right)^{2.5} & \text{for } M_* < M_{\rm p} \ , \\ \frac{1.62}{M_{\rm p}/{\rm M}_\odot} \left(\frac{M_*}{M_{\rm p}}\right)^{-4} & \text{for } M_* > M_{\rm p} \ , \end{cases} \tag{4.3}$$

where $M_{\rm p}$ is the peak mass given by Eq. (3.9) and $\Psi(M_*)$ is normalized by $\int \Psi(M_*)\, dM_* = 1$. This is obviously quite different from the well-known Salpeter function, $\Psi(M_*) \propto M_*^{-2.35}$. The above equation can model the time-dependent mass function of primordial stars and is useful when the large scale structure formation in the early universe.

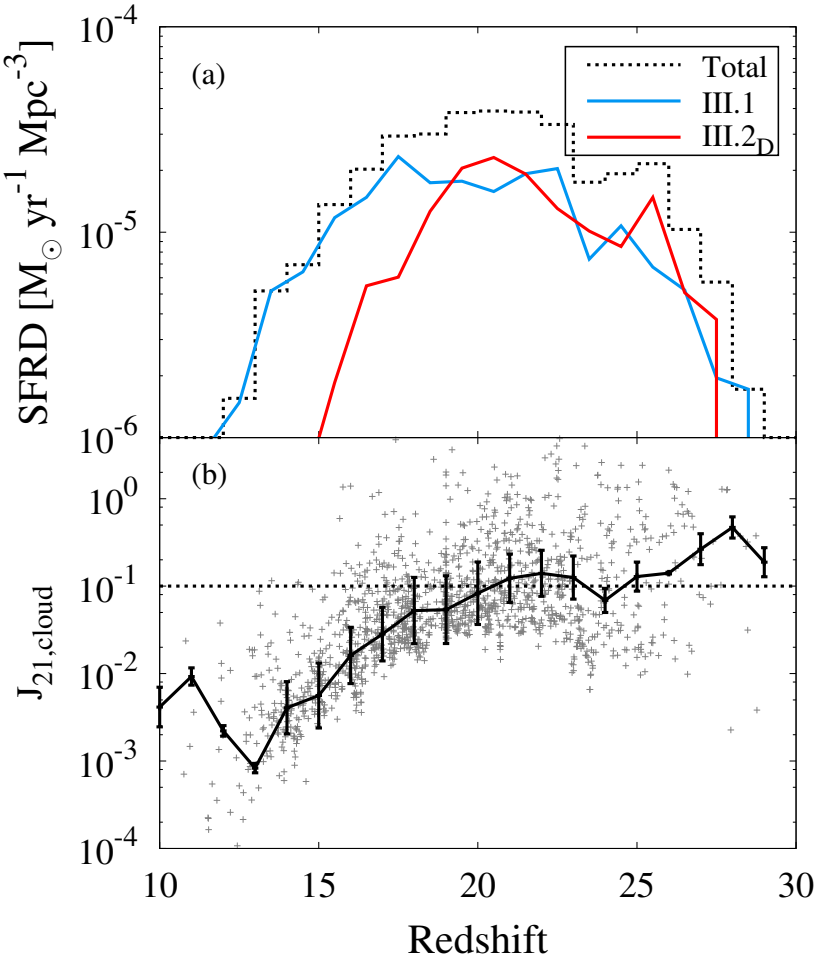

Figure 4.4. Redshift evolution of star formation rate densities (SFRD) of Population III.1 and III.2$_{\rm D}$ stars (panel a) and the averaged J_{21} for clouds with its variance (b). In panel (a), the dotted line represents the total of them. In panel (b), the gray dots show the scatter of J_{21} at each cloud and the dotted line represents the critical value of $J_{21} = 0.1$, above which Pop III.2$_{\rm D}$ stars form.

4.3.3 Star Formation Rate Density

Figure 4.4(a) shows the star formation rate densities (SFRD) as a function of redshift. The primordial SFRD rises until $z \sim 20$ and decreases afterwards (as Pop II star formation becomes the main mode). This evolution of the total SFRD is consistent with previous studies (e.g., Agarwal *et al.*, 2012; Johnson *et al.*, 2013), but the current results show clearly the contribution of Pop III.2$_{\rm D}$ stars. Significant Pop III.2$_{\rm D}$ star formation occurs after Pop III.1 stars are formed and emit copious amounts of FUV photons. Remarkably, SFRD$_{\rm III.2_D}$ approaches the same level as SFRD$_{\rm III.1}$ at $z > 20$. At $z < 20$, the fraction of Pop III.2$_{\rm D}$ stars rapidly decreases as shown in Figure 4.2. Note, however, one may be underestimating SFRD$_{\rm III.2_D}$ at this point, because this thesis ignores the contributions of

Final	III.1	III.2$_{\rm D}$								
Fate	$(10 < z < 14)$		$(14 < z < 18)$		$(18 < z < 22)$		$(22 < z < 26)$		$(26 < z < 30)$	
NS	2.4%		0.7%							
LMBH	4.2%		2.3%		0.3%					
PPISN	1.4%		2.7%		0.7%	0.1%	0.1%			
PISN	3.7%		12.1%	1.4%	4.8%	2.2%	0.7%	0.1%		
HMBH	2.0%	0.1%	13.8%	4.0%	13.0%	14.2%	5.6%	5.7%	0.9%	0.8%

Table 4.1. Column 1: Final fate of stellar evolution: neutron star (NS), low-mass black hole (LMBH), pulsation pair-instability supernovae (PPISN), pair-instability supernovae (PISN), and high-mass black hole (HMBH), Column 2: Corresponding mass ranges at ZAMS for each fate from figure 12 in Yoon *et al.* (2012) for the non-rotating case, Column 3 to 12: Fractions of each fate in the sample for each redshift range, Column 13: Sum over each row.

Pop II stars to the local and global FUV radiation field. The FUV background radiation intensity may exceed $J_{21} = 0.1$ at $z < 10$ and the Pop II SFRD may dominate at $z < 15$ (e.g., Agarwal *et al.*, 2012). If a large number of Pop II stars are formed during the epoch considered here, the number fraction of Pop III.2$_{\rm D}$ stars could be enhanced and the mass distribution at $z < 15$ may be significantly modified. There are a number of $M_* < 100\ M_\odot$ Pop III.1 stars forming via the HD-cooling mode, which is easily changed to the H_2-cooling mode for even weak FUV fields (see Sec. 2.3). The enhancement of the stellar mass by photodissociating molecules is significant for these cases (Fig. 2.22). However, because the total primordial SFRD decreases for $z < 20$, the uncertainties described above would not greatly change the overall mass distribution integrated over redshifts.

Figure 4.4(b) shows the redshift evolution of averaged local FUV intensity at each cloud. The averaged value decreases with decreasing redshift and falls below the critical value at $z \sim 20$, which is consistent with the decline of SFRD for Pop III.2$_{\rm D}$ cases (Fig. 4.4a). In comparison to the background FUV field calculated by Agarwal *et al.* (2012) and Johnson *et al.* (2013), the local J_{21} is in the same levels for $z > 15$ but starts to decline earlier for $z < 15$. This earlier decline is because of the ignorance of Pop II stars for calculating the FUV radiation fields in this thesis.

4.4 Discussion

4.4.1 The Final Fate of Primordial Stars

The derived stellar mass distribution can be used to predict the fates of primordial stars. Yoon *et al.* (2012) have performed stellar evolution calculations and categorize the final fates of primordial stars as a function of the stellar masses. Here, obtained sample of primordial stellar masses is classified into five different populations depending on their final fates for non-rotating cases (Table 1.4): neutron stars (NS; $M_*/M_\odot < 25$), low-mass

black holes (LMBH; $25 < M_*/M_\odot < 80$), pulsational pair-instability supernovae (PPISN; $80 < M_*/M_\odot < 120$), pair-instability supernovae (PISN; $120 < M_*/M_\odot < 240$), and high-mass black holes (HMBH; $240 < M_*/M_\odot$). Table 4.1 summarizes the respective number fractions and their redshift-dependence. Because the mass distribution itself evolves over time, the relative occurrence of the various fates of primordial stars also change over cosmic time.

First of all, a large fraction of the primordial stars end their lives as HMBHs. They do not contribute to the early chemical evolution but leave remnant black holes that might have seeded the formation of super-massive black holes (Li *et al.*, 2007). A fraction of Pop III.$1_{\rm H_2}$ stars die as PISN that chemically pollute the surrounding interstellar medium, leaving the peculiar elemental abundance patterns associated with this type of supernovae. It has been a long-standing puzzle, however, that such distinct abundance patterns are not observed in Galactic metal-poor stars. Very recently, however, Aoki *et al.* (2014) have reported the discovery of a metal-poor star whose elemental abundance patterns can be explained by a supernova explosion of a very massive star with $M_* > 100\ M_\odot$. Intriguingly, they also estimate from their data obtained from the Sloan Extension for Galactic Understanding and Exploration (SEGUE) survey that such peculiar stars are rare, comprising only a few per cent of metal-poor stars, in reasonable agreement with the simulation result. One explanation for the challenges in finding PISN signatures may be that minihalos hosting such massive primordial stars have masses too low to retain the halo gas after an energetic supernova explosion (e.g., Cooke & Madau, 2014). Heavy elements produced in the stellar interior might be expelled to intergalactic space and are therefore absent from the gas out of which the metal-poor stars form. At lower redshifts, the Pop III.$1_{\rm HD}$ stars with $M_* \simeq 25\ M_\odot$ die leaving LMBHs or NSs. Nucleosynthesis in core-collapse supernovae or hypernovae (e.g., Umeda & Nomoto, 2003), which are expected for such progenitors, are likely to dominate in the early Galactic chemical evolution.

4.4.2 Uncertainty in the Number Fraction of Pop III.2 Stars

The present investigation has used simple analytic formulae for estimating the stellar mass from local properties such as the gas infall rate $\dot{M}_{\rm Jeans}$ and the FUV intensity J_{21}. It would be important to improve the estimates by including physical effects that have not been considered here.

The number fraction of Pop III.$2_{\rm D}$ stars is dependent on the estimated mass of the Pop III.1 stars, which in turn determines the strength of the FUV radiation field. It is possible to see how critical this effect is by artificially modifying the scaling relation Eq. (2.1). Figure 4.5 shows the mass distributions obtained using modified scaling relations, whereby the masses obtained from Eq. (2.1) are multiplied by either 0.5 or 0.2. The local FUV intensity decreases because of the lower stellar masses, and the fraction of the clouds with $J_{21} > 0.1$ that form Pop III.$2_{\rm D}$ stars also decreases. In panel (a), the numbers of the two populations are still comparable at the high-mass end, whereas in panel (b), the overall mass distribution is dominated by Pop III.1 stars. Uncertainties in the masses of the Pop III.1 stars affect the masses of the Pop III.$2_{\rm D}$ stars in this manner.

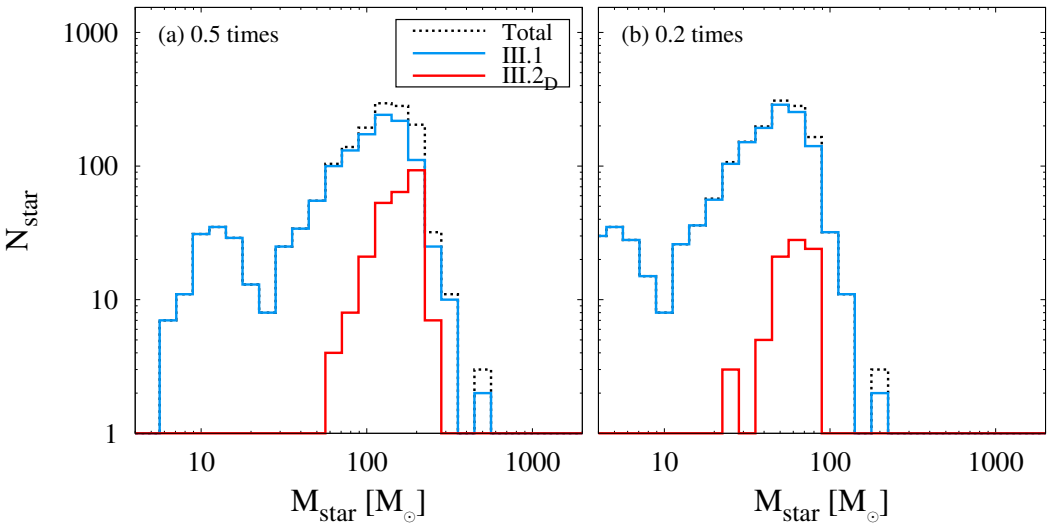

Figure 4.5. Resultant mass distribution of Population III.1 (blue line) and III.$2_{\rm D}$ (red) stars but calculated by decreasing the estimated stellar masses obtained from Eq. (2.1) by factors of 0.5 (panel a) and 0.2 (b).

There are also uncertainties regarding the local FUV intensity. This thesis only has counted photodissociating radiation emitted by primordial stars. However, there could be other FUV emitters such as Pop II stars. Pop II stars dominate the cosmic star formation rate at low redshifts. As noted in Section 3.2, however, including their FUV radiation should not largely modify the stellar mass distributions because a large fraction of the primordial stars form at sufficiently high redshifts.

There is another type of Pop III.2 stars that is formed under the influence of external radiation, the so-called Pop III.$2_{\rm I}$ stars (see also Sec. 1.2.2). In fact, about a half of sample has one $\sim$ ten close halo(s) which are excluded from the cosmological sample according to the selection rule (Sec. 3.2). Furthermore, about a few per cent of them contain the simultaneous peak within the minihalo ($R < 100$ pc), which is the similar probability found for 110 cases (6 fragmented cloud) in the previous chapter. Figure 4.6 shows the number distribution of the star-forming clouds which have the nearby density peak(s) within a physical 1 kpc as a function of the distance between them. The calculated cases have indeed suggested potential sites of Pop III.$2_{\rm I}$ star formation, i.e., stars forming in gas clouds that were previously ionized by radiation from nearby stars. In principle, one can simulate the evolution of such clouds and nearby H II regions by solving the transfer of EUV ($h\nu > 13.6$ eV) radiation (e.g., Yoshida *et al.*, 2007). This will likely add an additional population of lower mass primordial stars (e.g., $M_* = 17\ M_\odot$; Hosokawa *et al.*, 2012b), which can be verified in future studies. However, for the stellar mass distribution at the redshifts of interest in this thesis ($10 < z < 30$), Pop III.$2_{\rm I}$ stars comprise a minor component and do not affect the conclusions of this study.

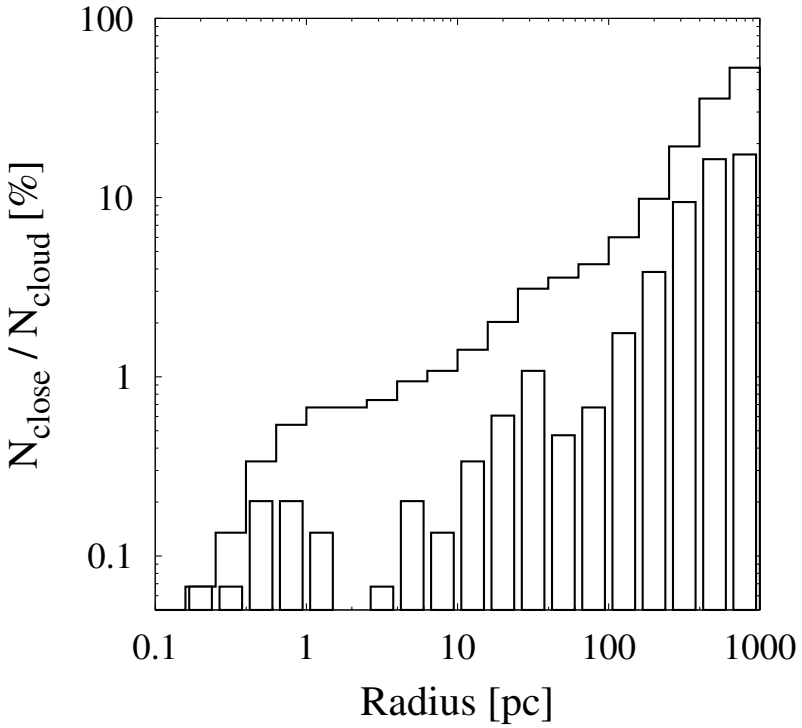

Figure 4.6. Number distribution of clouds which have the nearby density peak within a physical 1 kpc from their own density centers. The solid line shows the total number of clouds which have the nearby peaks within the corresponding radius.

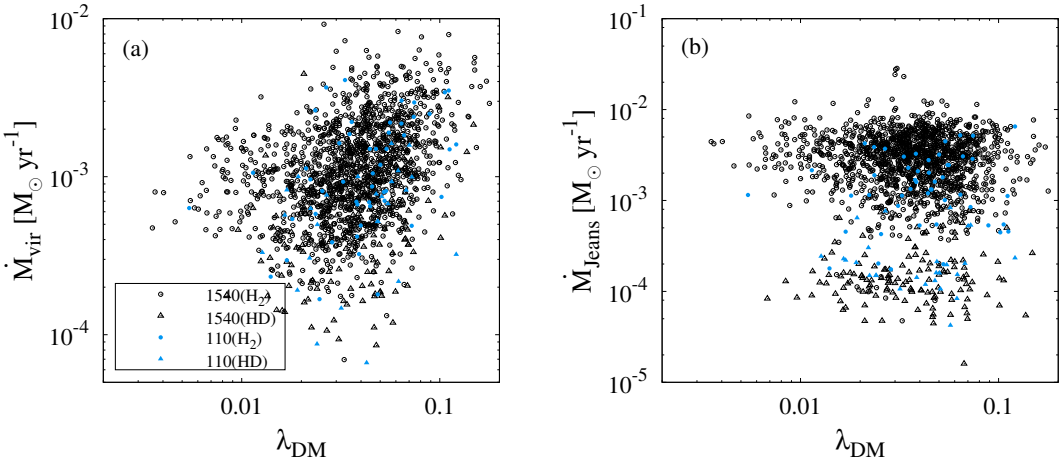

Figure 4.7. Accretion rates at (a) the Jeans scale and (b) the virial scale are plotted against the spin parameter of the parent dark matter halo to demonstrate the degree of correlation between the two quantities. The circles and triangles correspond to H_2- and HD-cooling clouds, respectively.

4.4.2.1 Beyond the Standard Model

There are some possible (alternative) physics which may affect the primordial star-formation process but has not considered in the current work. This section enumerates such remaining theoretical uncertainties.

Up to now, the effect of magnetic fields, which becomes essential in the present-day star formation by driving outflows and jets, has been ignored by assuming the primordial magnetic field is negligible. Recent magnetohydrodynamic (MHD) simulations show that even a small amount of turbulence can amplify magnetic fields by a dynamo mechanism (Sur *et al.*, 2010; Federrath *et al.*, 2011; Sur *et al.*, 2012; Turk *et al.*, 2012). The existence of magnetic fields would increase angular momentum transfer in the disk via magnetic braking, preventing disk fragmentation as well as enhancing accretion rates onto the protostars (e.g., Machida & Doi, 2013). Simulating the long-term evolution including all of these effects is still challenging, but should be tackled in future studies.

The structure formation is explained by the "standard" ΛCDM cosmology. The dark matter particle, however, has not been identified and there are other dark matter candidates, including hot dark matter (HDM) and warm dark matter (WDM). These particles have different velocity dispersions, which define different scales below which perturbations are vanished by the DM motion (collisionless free-streaming damping). The damping scale is larger with CDM, WDM, and HDM in this order. In the HDM universe, even supercluster structure vanishes, and the structure formation proceeds is a *top-down* fashion (larger to smaller). However, this fails to explain the formation of small objects, like minihalos. The CDM cosmology provides the hierarchical *bottom-up* structure formation, which well accords with observations as the standard model. The intermediate WDM model is suggested to solve the remaining problems in the CDM cosmology. In the WDM cosmology, the structure formation of small-scale object is suppressed. The primordial star formation is delayed and the minihalo's mass increases, which may change the final mass of the first stars formed inside them.

The nature of dark matter still remains unknown, but a possible candidate is the so-called Weakly Interacting Massive Particles (WIMPs; e.g., neutralinos), which have a large self-annihilation cross-section. DM annihilation can produce an enormous amount of energy essentially equal to the net mass energy of the annihilated DM particles (e.g, 100 GeV). The formation of primordial star occurs near the center of a minihalo, where the DM density is high enough that the efficient annihilation is expected. Spolyar *et al.* (2008) have suggested the new-type star whose self-gravity is supported by energy production via the DM annihilation (so-called "Dark Star"). The star highly inflates due to the sufficient energy release by DM annihilation and its surface temperature decreases accordingly (e.g., Spolyar *et al.*, 2009; Umeda *et al.*, 2009; Hirano *et al.*, 2011). Because such star hardly emits ionizing UV photons, the stellar radiative feedback should be so weak that the growth of stellar mass continues via the mass accretion. Moreover, the DM annihilation could affect the thermal evolution of a collapsing cloud. The Jeans mass of the collapsing gas is enhanced with the additional heating, which could cause fragmentation of the cloud

(Smith *et al.*, 2012; Stacy *et al.*, 2012b).

There is the more generic effect that, before recombination (decouple time), the baryon which couples with the photon moves on the acoustic oscillation and has relative velocity which is coherent over a few comoving Mpc with the dark matter (Tseliakhovich & Hirata, 2010). The relative streaming motion prevents the gas contraction into dark matter minihalo and delays the star formation in the early universe (e.g., Greif *et al.*, 2011b; Stacy *et al.*, 2011a). The effect may be larger for early low-mass, highly biased, halos; in other words, minihalos which host the primordial star formation. Such the suppression reduces the abundance of early halos and changes their spatial distribution, then this effect plays an important role in statistical properties of primordial stars in the overall universe.

4.4.3 Alternative Formulae for Mass Estimation

Recently, de Souza *et al.* (2013) have developed an analytic model assuming a tight correlation between the stellar mass and the spin parameter of the host halo. They argue that the mass distribution of the primordial stars would be determined by the angular momentum distribution of the host halos that is well given by a log-normal function. The rotational support possibly delays or prevents cloud collapse and effectively reduces the accretion rate onto the central protostar. Calculated results, however, show a weaker correlation between the spin parameter and the gas infall rates both at the virial and Jeans scale which tightly correlate with the stellar mass (see Fig. 4.7) than the dependence on the other two parameters, $z_{\rm form}$ and $M_{\rm vir}$. Furthermore, Figure 4.7(a) represents the anti-correlation between the spin parameters of dark matter components and infall rates at the virial scale; higher rotating halo has higher infall rate. de Souza *et al.* (2013) have used the semi-analytic model of McKee & Tan (2008) to calculate the stellar mass as a function of the angular momentum of the host halos. It is important to point out that McKee & Tan (2008) have used $f_{\rm Kepler}$ of a gas cloud, rather than that of a halo, in their accretion model. Although the parent gas cloud properties almost directly affect the pre-stellar collapse, it is less clear how the spin of dark halos affect the *small-scale* processes. Indeed there is no clear trend and thus the stellar mass cannot be estimated from the host halo spin.

If there will be an updated formula which determines the final stellar mass from some properties of star-forming cloud, one can re-construct the primordial mass distribution easily. It is one of the useful point of this work and this paragraph introduces a demonstration of such a procedure. Susa *et al.* (2014) have performed a number of cosmological simulations and following 3D RHD simulations for the primordial star-formation which allow the fragmentation of the star-forming regions. They finally obtain 60 cases and the two-thirds of them show the formation of multiple stellar systems. Their results show a good correlation between the masses of primary stars (first formed star in each system) and the spin parameters of gas components at the Jeans scale as $M_{\rm prim} \sim 14\ \lambda_{\rm Jeans}^{-0.7}\ M_\odot$; more massive star forms in the more slowly rotating cloud. Figure 4.8(a) shows that, however, there is no correlation between such two values for 110 cases calculated in this

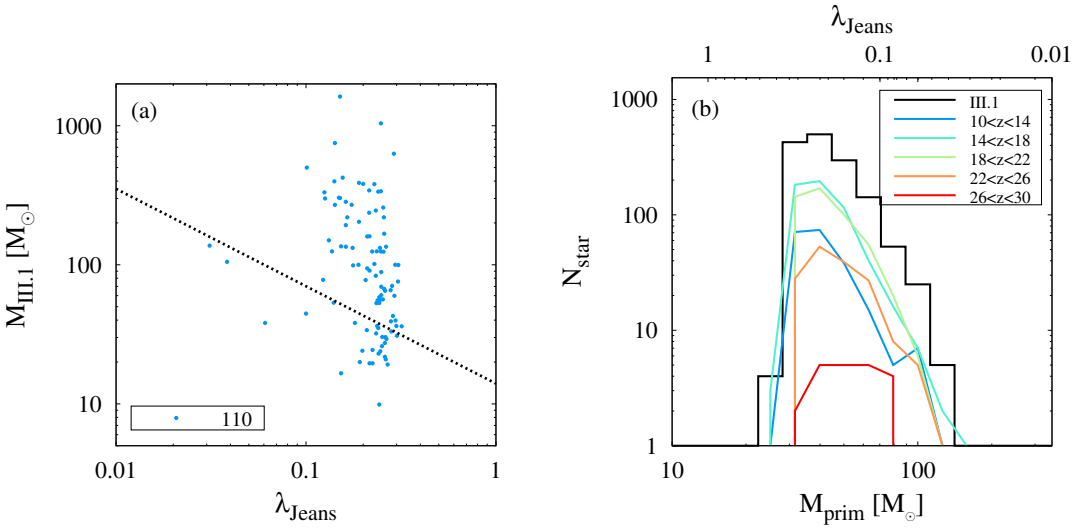

Figure 4.8. Comparison the resultant stellar mass with the calculation result of Susa *et al.* (2014). Panel (a) plots the 110 final stellar masses as a function of the spin parameter at the Jeans scale when $n_{\rm H,cen} = 10^7$ cm^{-3}. The dotted line is the fitting function shown in Susa *et al.* (2014), $M_{\rm prim} \sim 14\ \lambda_{\rm Jeans}^{-0.7}\ M_\odot$. Panel (b) shows the mass distribution of the primary star estimated by the alternative formula depending on the spin parameter.

thesis. Equally, they also find that their results do not obey the correlation (2.4) (see figure 18 in Susa *et al.*, 2014). They explain that the discrepancy is caused by performing different dimensional code, 2D or 3D, and whether the fragmentation can be taken into account.

If their correlation is more correct, the mass distribution must be reconstructed. On trial, Figure 4.8(b) shows the recalculated mass distribution based on the alternative formula. The stellar mass ranges over $25 < M_{\rm prim}/M_\odot < 200$ and centers at 30 $M_\odot$, which agree well with their results but are smoother and sharper. The mass distribution ranges around lower mass compared with the current results (Fig. 4.3) probably because of the consideration of the multiple formation. Here, the current understanding should be too limited to conclude which model is more precise, however, this is a good demonstration to show how easily one will be able to update the mass distribution in future when theorists obtain the better estimation formula. Note that their simulations do not include the HD cooling. If they update the calculation, the low-mass side in the distribution might rise as shown in this thesis.

Chapter 5

Conclusions

5.1 Summary

This thesis performs a series of simulations to obtain the mass distribution of primordial stars in the cosmological context. There are various evolutionary paths in the primordial star formation, which determines the resulting final stellar masses. The dependences of final stellar masses on the initial conditions of the primordial star formation at two different scales, virial and Jeans, are found from a number of simulations. Figures 5.1 and 5.2 summarizes the overall results of this thesis.

Various Evolutionary Paths and Mass Diversity of Primordial Stars

The first branch of primordial star formation appears when the gas cloud forms under the influence of the external radiation. Inside the pristine and non-irradiated gas, Population III.1 stars (so-called first stars) form with the high stellar mass. If the primordial gas is irradiated by other sources and the primordial coolant, hydrogen molecules, has been photodissociated, the gas cloud collapses with higher temperature and finally forms more massive Population III.$2_{\rm D}$ stars than in Pop III.1 case. The critical intensity is measured as $J_{21} > 0.1$ by the parameterized studies.

The new-born star-forming clouds within the dark matter minihalos begin the gravitational collapse by releasing the internal energy via radiative cooling mainly with H_2 molecules. The thermal evolution of collapsing clouds can be classified into two paths according to the cooling modes; whether or not the HD cooling is inefficient. If $f_{\rm HD}/f_{\rm H_2} > 10^{-3}$ at $n_{\rm H,cen} < 10^6$ cm^{-3}, both H_2 and HD coolings become efficient to reduce the temperature down to the background CMB temperature floor. Since the gas infall rate is proportional to the temperature as $\dot{M} \propto T^{3/2}$, various thermal evolution causes the diversity of following accretion history onto the protostar.

Accreting protostars grow in mass in the final phase of star formation. In the primordial case, as in the present-day case, the gas accretion is finally halted by the stellar radiative feedback. Because there is no dust which can feel the radiative pressure, the accreting gas is blow off via different mechanism; H II region expanding from the polar region photo-evaporates the accretion disk. This feedback is self-regulated by the protostellar evolution

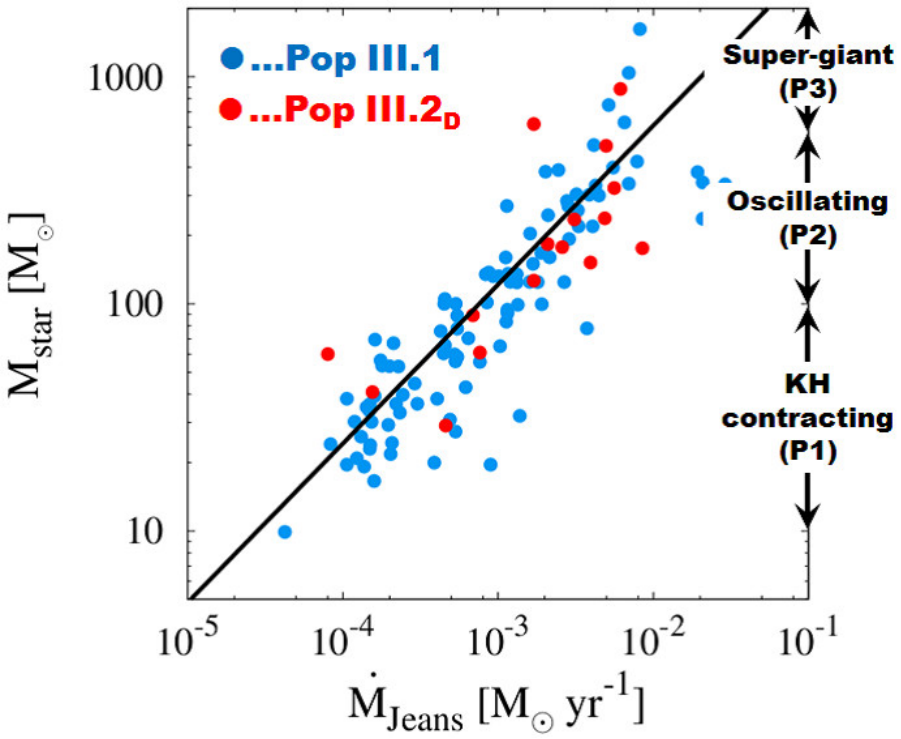

Figure 5.1. Good correlation between the early states of gravitationally unstable star-forming cloud and the final stellar masses for both Pop III.1 and III.$2_{\rm D}$ cases.

which depends on the mass accretion history. The protostar can approach the ZAMS and increase its surface temperature for emitting the UV photon if the accretion rate drops below a certain critical value, $\dot{M} < 4 \times 10^{-3}\ M_\odot\ {\rm yr}^{-1}$ (KH contracting protostar). Under more rapid accretion with $\dot{M} > 4 \times 10^{-3}\ M_\odot\ {\rm yr}^{-1}$, the protostellar radius greatly oscillates and cannot contract to become the ZAMS so that the stellar effective temperature remains below 10^4 K (oscillating protostar). The protostar with further rapid accretion $\dot{M} > 4 \times 10^{-2}\ M_\odot\ {\rm yr}^{-1}$ largely expands like the red super-giant star (super-giant protostar). The ionizing photon luminosity remains so low that UV feedback never becomes strong enough to prevent mass accretion. Such a rapid mass accretion is a promising path for forming very massive ($> 1000\ M_\odot$) stars in the early universe.

Formulae for Estimating the Final Stellar Masses

The overall accretion rate can be estimated from the structure of the gas envelope around a protostellar core. The structure itself is affected by the thermal evolution during the run-away collapse. The large sample of simulations until the mass accretion ceases show the dependence of final stellar mass on the initial property of the star-forming cloud,

$$M_{\rm III} = 250 \left(\frac{\dot{M}_{\rm Jeans}}{2.8 \times 10^{-3}\ M_\odot\ {\rm yr}^{-1}} \right)^{0.7} M_\odot\ , \tag{5.1}$$

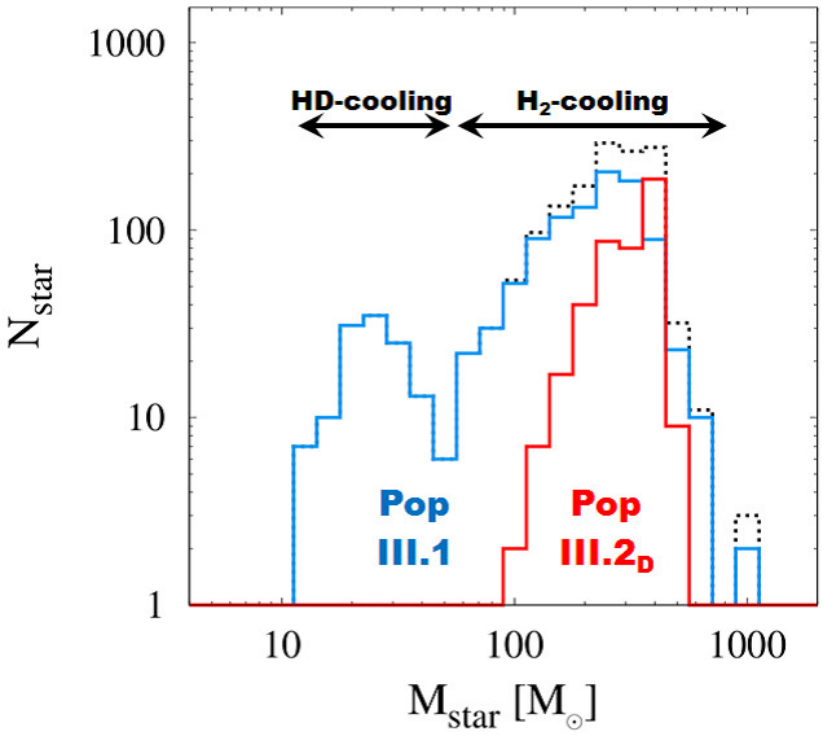

Figure 5.2. Resultant mass distribution of primordial stars which are classified into Pop III.1 and III.$2_{\rm D}$ cases. The dotted line shows the sum of the two populations.

and to a less rigorous extent even on the properties of dark matter halos,

$$M_{\rm III.1(H_2)} = 282 \left(\frac{1+z}{20}\right)^{2.45} \left(\frac{M_{\rm vir}}{4\times10^5\ M_\odot}\right)^{1.23} M_\odot\ . \tag{5.2}$$

In Pop III.$2_{\rm D}$ cases, the thermal evolution of the collapsing cloud is altered depending on the external radiation. Their masses, however, can be estimated by the same formula (5.1) as Pop III.1 cases (Fig. 5.1). This is because that, after the self-shielding becomes effective, the cloud's thermal evolution is decoupled from the external radiation field and become similar with Pop III.1 cases. By using the above correlation, one can determine the stellar masses for both cases without the computationally expensive simulations.

Mass Distribution of Primordial Stars

Finally, by combining the non-biased cosmological sample of 1540 primordial star-forming gas clouds and the mass estimating formulae, the mass distribution of primordial stars are obtained as in Figure 5.2. This is the first theoretical prediction in the cosmological context. The mass distribution has the sharp peak at $\simeq 250\ M_\odot$, which causes from the presence of a fiducial initial condition of the primordial star formation. The Pop III.1 mass distribution has the sub peak at $\simeq 25\ M_\odot$, which reflects the HD-cooling evolutionary path. Pop III.$2_{\rm D}$ stars have relatively large masses, centering around $\simeq 400\ M_\odot$. Moreover, this large sample also shows the redshift evolution of the stellar mass

distribution. At the high-redshifts of $z > 15$, Pop III.1 and Pop III.$2_{\rm D}$ stars are comparable in number. Their mass distributions have the sharp single peak around $M_* \simeq 250\ M_\odot$, though the peak gradually shifts to the lower-mass range with decreasing the redshift. The number of Pop III.$2_{\rm D}$ stars also decreases with redshift, and finally becomes negligible for $z < 15$. The stellar mass distribution is dominated by Pop III.1 stars at such low redshifts, but about half of them builds up another peak around $M_* \simeq 25\ M_\odot$. These time dependence of the mass distribution suggests that the primordial stars play a different role on the early galaxy formation and evolution with decreasing the redshift; massive black hole and energetic supernovae at the early epoch and ordinary supernovae which work as the factory of heavy metal elements at the later epoch.

Future observations will exploit the next-generation facilities such as *James Webb Space Telescope (JWST)*, *Thirty Meter Telescope (TMT)*, and radio telescope arrays, to probe the evolution of the high-redshift Universe. Data from such observations, combined with detailed studies of the Galactic metal-poor stars, will ultimately constrain the characteristic mass of the first generation of stars. To uncover the observational signatures of the first galaxies, the current study should be extended to follow the evolution after the deaths of the primordial stars: the star formation in the low-metallicity environments. The results can be used, for example, to predict the early chemical evolution and the characteristic signatures of the first galaxies. It is definitely worth developing such a global evolution model using large-scale cosmological simulations.

5.2 Future Prospects

To complete the whole model of primordial star formation in the early universe, there are also a number of remaining issues; fragmentation of cloud and accretion disk (Sec. 1.2.4), magneto-hydrodynamics, and cosmological alternatives (Sec. 4.4.2.1). The later accretion phase have to be studied again by performing 3D radiation hydrodynamic simulations to investigate the occurrence of fragmentation (Susa *et al.*, 2014). This could reduce the final stellar masses on average, because of the possible formation of binary and multiple stellar systems. However, the final outcome is still unclear, because there should be opposite effects which could increase the stellar mass, e.g., stellar mergers, and magnetic braking in an accretion disk. The interplay between these effects and stellar UV radiative feedback should determine the final stellar masses.

The next target is the comprehensive simulation of multiple star formation which can affect each other via radiative, dynamical, and also chemical feedbacks, for instance, formation of the first clusters. This study is designed to investigate the star formation which is affected by the neighbor primordial stars: radiative, chemical, and dynamical feedback. Such first clusters should contain Population III.1, III.$2_{\rm D}$, III.$2_{\rm I}$ (see Fig. 5.3), and also the first Population II stars. The next goal will be the direct calculation of the first Pop II star formation and determination of its stellar mass in the cosmological context.

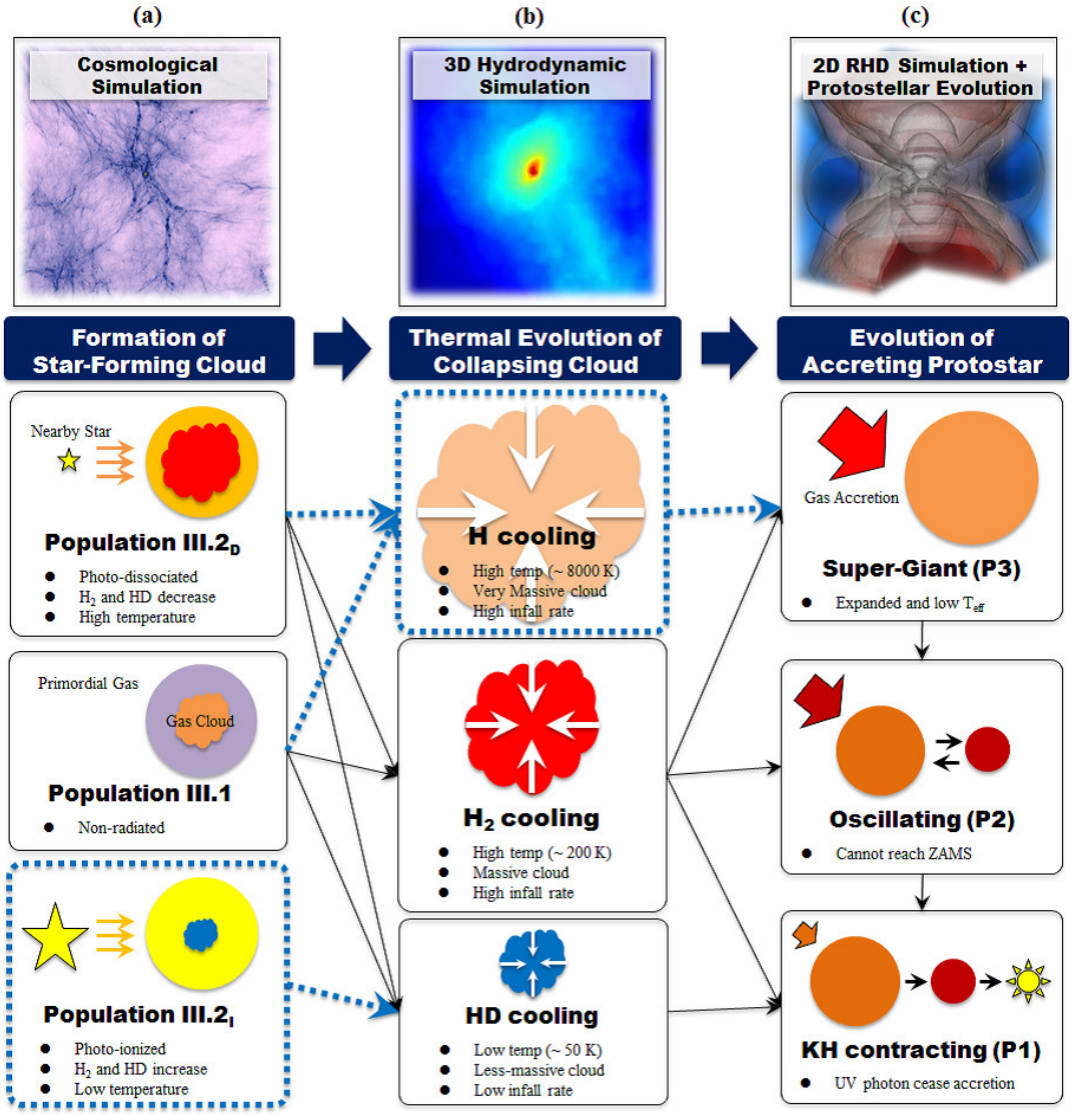

Figure 5.3. Various paths during the primordial star formation which is the similar with Figure 1.3. The blue dotted squares and arrows represent the ignored evolutionary paths in this thesis.

Appendix A

Cosmological Simulation

The simulations are performed by the public parallelized N-body / Smoother Particle Hydrodynamic (SPH) code GADGET-2 (Springel, 2005) which is suitably modified to treat the primordial star formation. You can find the detail code description and numerical techniques in the original paper (Springel, 2005). This chapter summarizes the basic equations of dynamics for N-body and SPH simulations (Secs. A.1 and A.2) and the chemical implementation (Sec. A.3). Section A.4 shows the methods to keep the numerical resolution during the overall cloud collapse with the wide dynamic range.

A.1 N-body Dynamics

In the astronomical field, there are many problems which can be considered to the particle dynamics driven via the gravitational force: e.g., stellar cluster, galaxy, and dark matter. The particle dynamic driven by the gravitational interaction is described as

$$\boldsymbol{g} = \frac{d^2\boldsymbol{x}_i}{dt^2} = -\sum_{j\neq i} G m_j \frac{x_j - x_i}{(x_j - x_i)^3}, \ , \tag{A.1}$$

where $\boldsymbol{x}$ is the particle position, t is the time, G is the gravitational constant, and m is the particle mass.

In the cosmological simulations, the time evolution of dark matter component is described by the collisionless Boltzmann equation coupled with the Poisson equation

$$\nabla^2\phi = 4\pi G\rho \ , \tag{A.2}$$

in the cosmic expansion. Such equations are solved by the N-body method in which the density field is divided and sampled with N collisionless particles.

To avoid the divergence of potential by the two-body contact diffusion as $\boldsymbol{g} \to \infty$ when $|\boldsymbol{x}_j - \boldsymbol{x}_i| \to 0$, the gravitational potential is in proportion not to $1/r$ but to $1/\sqrt{r^2+\epsilon^2}$ where ϵ is the gravitational softening length. In the thesis, the gravitational softening length is defined as $\epsilon = L_{\rm box}/N_{\rm mesh}/50$ for each simulation setting. This length determine the spatial resolution of N-body simulation.

A.2 Smoother Particle Hydrodynamics

Smoothed Particle Hydrodynamics (SPH) method first appears in Lucy (1977) and it has been widely used to solve many hydrodynamic problems (the recent review is Monaghan, 2005). SPH method is described by the Lagrange scheme which is suit to the problem in which there are many transforming voids in the simulation region.

The set of basic equations in the Lagrange scheme is

$$\frac{d\boldsymbol{v}}{\mathrm{d}t} = -\frac{1}{\rho}\nabla p - \boldsymbol{g} \ , \tag{A.3}$$

$$\frac{d\epsilon}{\mathrm{d}t} = -\frac{p}{\rho}\nabla \cdot \boldsymbol{v} \ , \tag{A.4}$$

where $\boldsymbol{g}$ is the gravitational acceleration, ϵ is the internal energy per the unit volume. In addition to this, there is the equation of state (EoS).

In SPH method, the fundamental particle which has a certain mass and scale is called SPH particle. The density of SPH particle is defined as

$$\rho(\boldsymbol{x}) = \sum_j m_j W(\boldsymbol{x} - \boldsymbol{x_j}, h) \ , \tag{A.5}$$

where $W(\boldsymbol{x}, h)$ is the kernel function which defines the normalized volume of SPH particle and h is the smoothing length which defines the radius of SPH kernel. The kernel function should be spherical symmetry and normalized as $\lim_{r\to\infty} W(r,h) = 0$ and $\int W(\boldsymbol{x},h)d\boldsymbol{x}^3 = 1$. GADGET-2 adopts the spline kernel as the SPH kernel function,

$$W(r,h) = \frac{8}{\pi h^3}\begin{cases} 1 - 6\left(\frac{r}{h}\right)^2 + 6\left(\frac{r}{h}\right)^3 & \left(\text{if } 0 \le \frac{r}{h} \le \frac{1}{2}\right) \ , \\ 2\left(1 - \frac{r}{h}\right)^3 & \left(\text{if } \frac{1}{2} \le \frac{r}{h} \le 1\right) \ , \\ 0 & \left(\text{if } 1 < \frac{r}{h}\right) \ . \end{cases} \tag{A.6}$$

GADGET-2 employs the adaptive soothing length h of each particle which is defined that the kernel volume contains a constant mass for the estimated density as

$$\frac{4\pi}{3}h^3\rho = N_{\mathrm{SPH}}\overline{m} \ , \tag{A.7}$$

where N_{SPH} ($= 64$ in the simulations) is the typical number of smoothing neighbors, and $\overline{m}$ is an average particle mass. The gravitational softening kernel for SPH particles is defined as $\min(2.8\epsilon, h)$.

The gravitational acceleration is computed as

$$\boldsymbol{g}(\boldsymbol{x}_i) = -G\sum_j W_2(|\boldsymbol{x}_i - \boldsymbol{x}_j|, h)\frac{\boldsymbol{x}_i - \boldsymbol{x}_j}{|\boldsymbol{x}_i - \boldsymbol{x}_j|^3} \ , \tag{A.8}$$

where $W_2(r,h)$ is defined as

$$W_2(r,h) = 4\pi\int_0^r W(s,h)s^2 ds \ . \tag{A.9}$$

To compute the gravitational collapse precisely, the smoothing length h is always smaller than the Jeans length. In other words, the SPH particle mass is always small enough to resolve the local Jeans mass.

A.3 Primordial Chemistry

SPH method is described by the Lagrange scheme and the chemical processes (cooling, heating, and reaction) are solved for each particle. In the Euler scheme, the distribution is changed when the chemical species move from cell to cell but SPH method does not have such a problem.

The initial abundances of chemical species at the start of simulations are defined in accordance with Stancil *et al.* (1998): $f_{\mathrm{e}^-} = 6.88 \times 10^{-4}$, $f_{\mathrm{H}} = 0.76$, $f_{\mathrm{H}^+} = 6.88 \times 10^{-4}$, $f_{\mathrm{He}} = 0.06$, $f_{\mathrm{He}^+} = 0$, $f_{\mathrm{He}^{++}} = 6 \times 10^{-12}$, $f_{\mathrm{H}_2} = 10^{-6}$, $f_{\mathrm{H}_2^+} = 10^{-12}$, $f_{\mathrm{H}^-} = 10^{-10}$, $f_{\mathrm{D}} = 2.30 \times 10^{-5}$, $f_{\mathrm{D}^+} = 3 \times 10^{-8}$, $f_{\mathrm{HD}} = 10^{-10}$, $f_{\mathrm{HD}^+} = 10^{-16}$, and $f_{\mathrm{D}^-} = 10^{-15}$. The initial ionization fractions are calculated by RECFAST (Seager *et al.*, 1999, 2000; Wong *et al.*, 2008) at the initial redshifts of simulations, $z_{\mathrm{ini}} = 99$.

A.3.1 Chemical Reaction Rates

In this thesis, simulations solve chemical reactions for fourteen species of primordial elements: e^-, H, H^+, He, He^+, He^{++}, H_2, H_2^+, H^-, D, D^+, HD, HD^+, and D^-. Table A.1 summarizes the latest version of the chemical reaction rates which is updated from Yoshida *et al.* (2006, 2007). In the table, T_e is temperature in the unit of electron volts (eV), T is in kelvin (K), $\ln T = \log_e T$ and $\log T = \log_{10} T$.

One of the most important reaction is the three-body H_2 formation (Eq. 1.14) which dominates the H_2 formation at $n_{\mathrm{H,cen}} > 10^8$ cm^{-3} but its reaction rate has a certain uncertainty. The rate is measured from the reverse reaction because one cannot provide such a dense and high temperature condition which is necessary for the three-body reaction (Savin *et al.*, 2012). Turk *et al.* (2011) have studies the effect of different reaction rates (Palla *et al.*, 1983; Abel *et al.*, 2002; Flower & Harris, 2007) on the primordial star formation by performing 3D hydrodynamical simulations and shown that the dependence of cloud's thermal and dynamical evolution on the adopting reaction rates. One should carefully treat this problem to consider the primordial star-formation precisely. This thesis adopts the recently presented rates from the quantum mechanical calculations (Forrey, 2013a,b). Figure A.1 shows the several reaction rates and the resultant thermal evolution of collapsing clouds. The new rate becomes the intermediate between the previously used rate, so that the critical density above which the three-body H_2 formation becomes efficient becomes also intermediate.

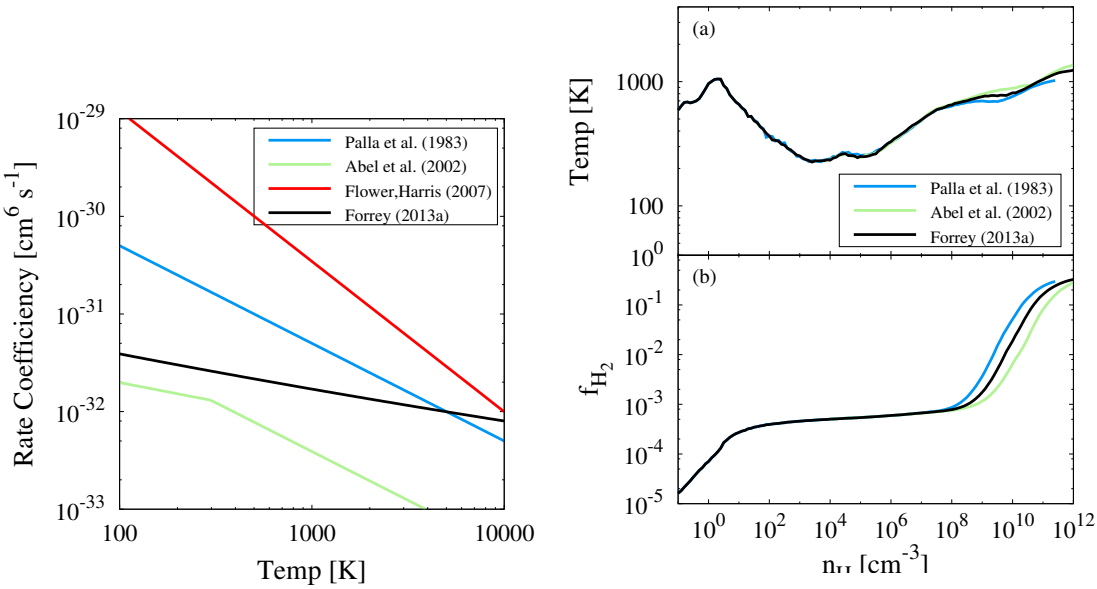

Figure A.1. Various reaction rates for the three-body H_2 formation (Eq. 1.14; left panel) and variety of the thermal evolution of collapsing clouds depending on the rates (right).

No.	Reaction	k (cm^3 s^{-1}, s^{-1}) and σ (cm^2)	Ref.
	Hydrogen reactions		
1	$H + e \rightarrow H^+ + 2e$	$k_1 = \exp[-32.71396786$	AAZN97
		$+ 13.536556\ (\ln T_e)$	
		$- 5.73932875\ (\ln T_e)^2$	
		$+ 1.56315498\ (\ln T_e)^3$	
		$- 0.2877056\ (\ln T_e)^4$	
		$+ 3.48255977 \times 10^{-2}\ (\ln T_e)^5$	
		$- 2.63197617 \times 10^{-3}\ (\ln T_e)^6$	
		$+ 1.11954395 \times 10^{-4}\ (\ln T_e)^7$	
		$- 2.03914985 \times 10^{-6}\ (\ln T_e)^8]$	
2	$H^+ + e \rightarrow H + h\nu$	$k_{2,A} = \exp[-28.6130338$	AAZN97
		$- 0.72411256\ (\ln T_e)$	
		$- 2.02604473 \times 10^{-2}\ (\ln T_e)^2$	
		$- 2.38086188 \times 10^{-3}\ (\ln T_e)^3$	
		$- 3.21260521 \times 10^{-4}\ (\ln T_e)^4$	
		$- 1.42150291 \times 10^{-5}\ (\ln T_e)^5$	
		$+ 4.98910892 \times 10^{-6}\ (\ln T_e)^6$	
		$+ 5.75561414 \times 10^{-7}\ (\ln T_e)^7$	
		$- 1.85676704 \times 10^{-8}\ (\ln T_e)^8$	
		$- 3.07113524 \times 10^{-9}\ (\ln T_e)^9]$	

No.	Reaction	k (cm^3 s^{-1}, s^{-1}) and σ (cm^2)	Ref.
		$k_{2,\mathrm{B}} = 2.753 \times 10^{-14}\ (315614/T)^{1.5}$	GA08
		$\cdot\ \left[1.0 + (115188/T)^{0.407}\right]^{-2.242}$	
3	$\mathrm{H} + e \rightarrow \mathrm{H}^- + h\nu$	$k_3 = 1.4 \times 10^{-18}\ T^{0.928}\ \exp\left(\frac{-T}{16200.0}\right)$	GP98
4	$\mathrm{H}^- + \mathrm{H} \rightarrow \mathrm{H}_2 + e$	$k_4 = 10^6 \times \mathrm{dex}[-14.4$	C11
		$-0.15\ (\log T)^2$	
		$-7.9 \times 10^{-3}\ (\log T)^4]$	
5	$\mathrm{H} + \mathrm{H}^+ \rightarrow \mathrm{H}_2^+ + h\nu$	$k_5 = 1.85 \times 10^{-23} T^{1.8}$ (if $T \leq 6700$ K)	SK87
		$5.81 \times 10^{-16} (T/56200)^{[-0.6657 \log_{10}(T/56200)]}$	
		(if $T > 6700$ K)	
6	$\mathrm{H}_2^+ + \mathrm{H} \rightarrow \mathrm{H}_2 + \mathrm{H}^+$	$k_6 = 6.4 \times 10^{-10}$	GP98
7	$\mathrm{H}_2 + \mathrm{H}^+ \rightarrow \mathrm{H}_2^+ + \mathrm{H}$	$k_7 = 3.0 \times 10^{-10} \exp\left(\frac{-21050}{T}\right)$ (if $T \leq 10^4$ K)	GP98
		$1.5 \times 10^{-10} \exp\left(\frac{-14000}{T}\right)$ (if $T > 10^4$ K)	
8	$\mathrm{H}_2 + e \rightarrow 2\mathrm{H} + e$	$k_{8,v=0} = 3.73 \times 10^{-9} T^{0.1121} \exp(-199430/T)$	TT02
9	$\mathrm{H}^- + e \rightarrow \mathrm{H} + 2e$	$k_9 = \exp\ [-\ 18.01849334$	AAZN97
		$+\ \ 2.3608522\ (\ln\ T_e)$	
		$-\ \ 0.28274430\ (\ln\ T_e)^2$	
		$+\ \ 1.62331664 \times 10^{-2}\ (\ln\ T_e)^3$	
		$-\ \ 3.36501203 \times 10^{-2}\ (\ln\ T_e)^4$	
		$+\ \ 1.17832978 \times 10^{-2}\ (\ln\ T_e)^5$	
		$-\ \ 1.65619470 \times 10^{-4}\ (\ln\ T_e)^6$	
		$+\ \ 1.06827520 \times 10^{-5}\ (\ln\ T_e)^7$	
		$-\ \ 2.63128581 \times 10^{-6}\ (\ln\ T_e)^8]$	
10	$\mathrm{H}^- + \mathrm{H} \rightarrow 2\mathrm{H} + e$	$k_{10} = 2.5634 \times 10^{-9}\ T^{1.78186}$ (if $T_\mathrm{e} \leq 0.1$ eV)	AAZN97
		$\exp[-\ 20.37260896$ (if $T_\mathrm{e} > 0.1$ eV)	
		$+\ \ 1.13944933\ (\ln\ T_e)$	
		$-\ \ 0.14210135\ (\ln\ T_e)^2$	
		$+\ \ 8.4644554 \times 10^{-3}\ (\ln\ T_e)^3$	
		$-\ \ 1.4327641 \times 10^{-3}\ (\ln\ T_e)^4$	
		$+\ \ 2.0122503 \times 10^{-4}\ (\ln\ T_e)^5$	
		$+\ \ 8.6639632 \times 10^{-5}\ (\ln\ T_e)^6$	
		$-\ \ 2.5850097 \times 10^{-5}\ (\ln\ T_e)^7$	
		$+\ \ 2.4555012 \times 10^{-6}\ (\ln\ T_e)^8$	
		$-\ \ 8.0683825 \times 10^{-8}\ (\ln\ T_e)^9]$	
11	$\mathrm{H}^- + \mathrm{H}^+ \rightarrow 2\mathrm{H}$	$k_{11} = 7 \times 10^{-9}\ T^{-0.5}$	GA08
12	$\mathrm{H}^- + \mathrm{H}^+ \rightarrow \mathrm{H}_2^+ + e$	$k_{12} = 6.9 \times 10^{-9}\ T^{-0.35}$ (if $T \leq 8000$ K)	GP98
		$9.6 \times 10^{-7}\ T^{-0.90}$ (if $T > 8000$ K)	
13	$\mathrm{H}_2^+ + e \rightarrow 2\mathrm{H}$	$k_{13} = 4.2278 \times 10^{-8}$	C11
		$-\ 2.3088 \times 10^{-11}\ T$	
		$+\ 7.3428 \times 10^{-15}\ T^2$	
		$-\ 7.5474 \times 10^{-19}\ T^3$	
		$+\ 3.3468 \times 10^{-23}\ T^4$	

No.	Reaction	k ($\mathrm{cm^3\ s^{-1}}$, $\mathrm{s^{-1}}$) and σ ($\mathrm{cm^2}$)	Ref.
		$- 5.528 \times 10^{-28}\ T^5$	
14	$H_2^+ + H^- \rightarrow H + H_2$	$k_{14} = 5.0 \times 10^{-6} T^{-0.5}$	AAZN97
	Three − body reactions		
15	$3H \rightarrow H_2 + H$	$k_{15} = 6 \times 10^{-32} T^{-1/4} + 2 \times 10^{-31} T^{-0.5}$	F13
16	$H_2 + H \rightarrow 3H$	$k_{16} = 1.0670825 \times 10^{-10} T_e^{2.012}$ $\cdot\ [(\exp(4.463/T_e) \times (1 + 0.2472 T_e)^{3.512}]$	AAZN97
17	$2H + H_2 \rightarrow 2H_2$	$k_{17} = k_{15}/8$	PSS83
18	$H_2 + H_2 \rightarrow 2H + H_2$	$k_{18} = k_{16}/8$	PSS83
	Deuterium reactions		
19	$D^+ + e \rightarrow D + h\nu$	$k_{19} = 3.6 \times 10^{-12} (T/300)^{-0.75}$	GP98
20	$D + H^+ \rightarrow D^+ + H$	$k_{20} = 2.00 \times 10^{-10} T^{0.402} \exp(-37.1/T)$ $- 3.31 \times 10^{-17} T^{1.48}$	Sav02
21	$D^+ + H \rightarrow D + H^+$	$k_{21} = 2.06 \times 10^{-10} T^{0.396} \exp(-33.0/T)$ $+ 2.03 \times 10^{-9} T^{-0.332}$	Sav02
22	$D + H \rightarrow HD + h\nu$	$k_{22} = 1.0 \times 10^{-25}$	Sta98
23	$D + H_2 \rightarrow H + HD$	$k_{23} = 9.0 \times 10^{-11} \exp(-3876/T)$	WS02
24	$HD^+ + H \rightarrow H^+ + HD$	$k_{24} = 6.4 \times 10^{-10}$	Sta98
25	$D^+ + H_2 \rightarrow H^+ + HD$	$k_{25} = 1.6 \times 10^{-9}$	WS02
26	$HD + H \rightarrow H_2 + D$	$k_{26} = 3.2 \times 10^{-11} \exp(-3624/T)$	Sta98
27	$HD + H^+ \rightarrow H_2 + D^+$	$k_{27} = 1.0 \times 10^{-9} \exp(-464/T)$	Sta98
28	$D + H^+ \rightarrow HD^+ + h\nu$	$k_{28} = \mathrm{dex}[- 19.38$ $- 1.523(\log T)$ $+ 1.118(\log T)^2$ $- 0.1269(\log T)^3]$	Sta98
29	$D^+ + H \rightarrow HD^+ + h\nu$	$k_{29} = k_{28}$	GP98
30	$HD^+ + e \rightarrow H + D$	$k_{30} = 7.2 \times 10^{-8} T^{-1/2}$	Sta98
31	$D + e \rightarrow D^- + h\nu$	$k_{31} = 3.0 \times 10^{-16} (T/300)^{0.95} \exp(-T/9320)$	GP98
32	$D^+ + D^- \rightarrow 2D$	$k_{32} = 5.7 \times 10^{-8} (T/300)^{-0.5}$	GP98
33	$H^+ + D^- \rightarrow H + D$	$k_{33} = 4.6 \times 10^{-8} (T/300)^{-0.5}$	GP98
34	$H^- + D \rightarrow H + D^-$	$k_{34} = 6.4 \times 10^{-9} (T/300)^{0.41}$	GP98
35	$D^- + H \rightarrow D + H^-$	$k_{35} = 6.4 \times 10^{-9} (T/300)^{0.41}$	GP98
36	$D^- + H \rightarrow HD + e$	$k_{36} = 1.5 \times 10^{-9} (T/300)^{-0.1}$	GP98
	Helium reactions		
37	$He + e \rightarrow He^+ + 2e$	$k_{37} = \exp[- 44.09864886$ $+ 23.91596563\ (\ln T_e)$ $- 10.7532302\ \ (\ln T_e)^2$ $+ 3.05803875\ (\ln T_e)^3$ $- 0.56851189\ (\ln T_e)^4$	AAZN97

No.	Reaction	k (cm^3 s^{-1}, s^{-1}) and σ (cm^2)	Ref.
		$+ \quad 6.79539123 \times 10^{-2} \ (\ln T_e)^5$	
		$- \quad 5.00905610 \times 10^{-3} \ (\ln T_e)^6$	
		$+ \quad 2.06723616 \times 10^{-4} \ (\ln T_e)^7$	
		$- \quad 3.64916141 \times 10^{-6} \ (\ln T_e)^8]$	
38	$He^+ + e \rightarrow He + h\nu$	$k_{38,A} = 3.925 \times 10^{-13} \ T_e^{-0.6353}$	C92
		$k_{38,B} = 1.26 \times 10^{-14} \ (2 \times 285335.0/T)^{0.75}$	HG97
		$k_{38,di} = 1.9 \times 10^{-3} \ T^{-1.5} \ \exp(-470000/T)$	GA08
		$\cdot \ [1 + 0.3 \ \exp(-94000/T)]$	
39	$He^+ + e \rightarrow He^{++} + 2e$	$k_{39} = \exp[-68.71040990$	AAZN97
		$+ 43.93347633 \ (\ln T_e)$	
		$- 18.4806699 \ (\ln T_e)^2$	
		$+ \quad 4.70162649 \ (\ln T_e)^3$	
		$- \quad 0.76924663 \ (\ln T_e)^4$	
		$+ \quad 8.113042 \times 10^{-2} \ (\ln T_e)^5$	
		$- \quad 5.32402063 \times 10^{36} \ (\ln T_e)^6$	
		$+ \quad 1.97570531 \times 10^{-4} \ (\ln T_e)^7$	
		$- \quad 3.16558106 \times 10^{-6} \ (\ln T_e)^8]$	
40	$He^{++} + e \rightarrow He^+ + h\nu$	$k_{40,A} = 3.36 \times 10^{-10} \ T^{-0.5} \ (T/10^3)^{-0.2}$	FK94
		$\cdot \ \left[1 + \left\{T/(4 \times 10^6)\right\}^{-0.7}\right]^{-0.1}$	
		$k_{40,B} = 2 \times k_2(T_e/4)$	AAZN97
41	$He^+ + H \rightarrow He + H^+ + h\nu$	$k_{41} = 1.20 \times 10^{-15} \ (T/300)^{0.25}$	GA08
42	$He + H^+ \rightarrow He^+ + H$	$k_{42} = 1.26 \times 10^{-9} T^{-0.75} \exp(-127500/T)$	GA08
		(if $T \leq 10^4$ K)	
		$4.0 \times 10^{-37} T^{4.74}$	
		(if $T > 10^4$ K)	
	Photon reactions		
43	$H + h\nu \rightarrow H^+ + e$	$\sigma_{43} = (A_0/Z^2) \ (\nu_{th}/\nu)^4$	SK87
		$\cdot \exp[4 - 4 \arctan(\epsilon)/\epsilon]/[1 - \exp(-2\pi/\epsilon)]$	
		$A_0 = 6.30 \times 10^{-18}$ cm^2, $Z = 1$	
		$\epsilon = (\nu/\nu_{th} - 1)^{0.5}$, $h\nu_{th} = 13.6 Z^2$ eV	
44	$H^- + h\nu \rightarrow H + e$	$\sigma_{44} = 7.928 \times 10^5 (\nu - \nu_{th})^{3/2} \nu^{-3}$	J72
45	$H_2 + h\nu \rightarrow 2H$	$k_{46} = 1.1 \times 10^8 (4\pi J(\overline{\nu}))$	AAZN97
		J [erg sec^{-1} Hz^{-1} sr^{-1}], $h\overline{\nu} = 12.87$ eV	
46	$H_2 + h\nu \rightarrow H_2^+ + e$	$\sigma_{45} = 6.2 \times 10^{-18} (h\nu) - 9.4 \times 10^{-17}$	SK87
		(if $15.42 < h\nu/\text{eV} < 16.5$)	
		$1.4 \times 10^{-18} (h\nu) - 1.48 \times 10^{-17}$	
		(if $16.5 < h\nu/\text{eV} < 17.7$)	
		$2.5 \times 10^{-14} (h\nu)^{-2.71}$	
		(if $17.7 < h\nu/\text{eV}$)	
		$h\nu_{th} = 15.42$ eV	

No.	Reaction	k (cm^3 s^{-1}, s^{-1}) and σ (cm^2)	Ref.
47	$H_2^+ + h\nu \rightarrow H + H^+$	$\sigma_{47} = \text{dex}[-40.97$	SK87
		$+ 6.03(h\nu)$	
		$- 0.504(h\nu)^2$	
		$+ 0.01387(h\nu)^3]$	
		(if $2.65 < h\nu/\text{eV} < 11.27$)	
		$\text{dex}[-30.26$	
		$+ 2.79(h\nu)$	
		$- 0.184(h\nu)^2$	
		$+ 0.003535(h\nu)^3]$	
		(if $11.27 < h\nu/\text{eV} < 21.0$)	
		$h\nu_{\text{th}} = 2.65$ eV	
48	$H_2^+ + h\nu \rightarrow 2H^+ + e$	$\sigma_{48} = \text{dex}[-16.926$	SK87
		$- 4.528 \times 10^{-2}(h\nu)$	
		$+ 2.238 \times 10^{-4}(h\nu)^2$	
		$+ 4.245 \times 10^{-7}(h\nu)^3]$	
		$h\nu_{\text{th}} = 30.0$ eV	
49	$D + h\nu \rightarrow D^+ + e$	$k_{49} = k_{43}$	GP98
50	$D^- + h\nu \rightarrow D + e$	$k_{50} = k_{44}$	Sch08
51	$HD + h\nu \rightarrow H + D$	$k_{51} = k_{46}/3$	B77
52	$HD^+ + h\nu \rightarrow H + D^+$	$k_{52} = 0.5 \times k_{47}$	Sch08
53	$HD^+ + h\nu \rightarrow H^+ + D$	$k_{53} = 0.5 \times k_{47}$	Sch08
54	$He + h\nu \rightarrow He^+ + e$	$\sigma_{54} = 7.42 \times 10^{-18}$,	SK87
		$\cdot[1.66(\nu/\nu_{\text{th}})^{-2.05} - 0.66(\nu/\nu_{\text{th}})^{-3.05}]$	
		$h\nu_{\text{th}} = 24.6$ eV	
55	$He^+ + h\nu \rightarrow He^{++} + e$	σ_{55} is the same function as σ_{43} but with $Z = 2$	SK87

Table A.1: Column 1: ID, Column 2: Chemical Reaction, Column 3: Rate coefficient and cross section, and Column 4: References; AAZN97 (Abel *et al.*, 1997), B77 (Barsuhn, 1977), C11(Coppola *et al.*, 2011b), C92 (Cen, 1992) F13 (Forrey, 2013a), FK94 (Fukugita & Kawasaki, 1994), GA08 (Glover & Abel, 2008), GP98 (Galli & Palla, 1998), HG97 (Hui & Gnedin, 1997) J72 (de Jong, 1972), PSS83 (Palla *et al.*, 1983), Sav02 (Savin, 2002), Sch08 (Schleicher *et al.*, 2008), SK87 (Shapiro & Kang, 1987), Sta98(Stancil *et al.*, 1998), TT02 (Trevisan & Tennyson, 2002), WS02 (Wang & Stancil, 2002),

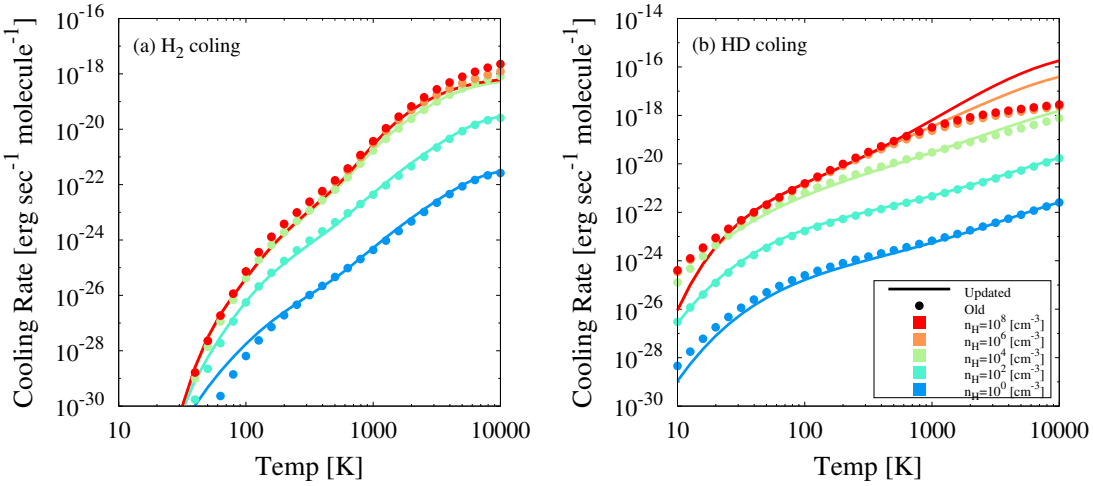

Figure A.2. Cooling rates of H_2 (panel a) and HD (b) molecules as a function of temperature at different densities. The lines show the updated functions used in this thesis whereas the dots are the previously used functions (e.g., Yoshida *et al.*, 2006). There is only a bit modification.

A.3.2 Updated Rates for H_2- and HD-Cooling

The thermal evolution of primordial, metal-free, gas cloud is dominated by H_2 and HD molecules. Recently, some updates of their cooling rates are presented (a good summary is Galli & Palla, 2013), so that the calculations in this thesis also use the updated rates accordingly.

H_2 line emission is driven by the collisional excitation of H_2 with other species. The previous scheme considered two collisional partners, atomic hydrogen (H) and molecule hydrogen (H_2). The cooling rates can be described as $\Lambda_{H_2}(\mathrm{low}, \mathrm{H_2\text{-}H})$ and $\Lambda_{H_2}(\mathrm{low}, \mathrm{H_2\text{-}H_2})$ in the low density limit whereas $\Lambda_{H_2}(\mathrm{LTE}, \mathrm{H_2\text{-}H})$ and $\Lambda_{H_2}(\mathrm{LTE}, \mathrm{H_2\text{-}H_2})$ at high densities where all energy levels are populated according to the local thermodynamic equilibrium (LTE). These rates at low- (Galli & Palla, 1998) and high-density limit (Hollenbach & McKee, 1979) are bridged as

$$\Lambda_{H_2} = \frac{\Lambda_{H_2}(\mathrm{LTE})}{1 + \Lambda_{H_2}(\mathrm{LTE})/\Lambda_{H_2}(\mathrm{low})} , \tag{A.10}$$

and the sum of two collision rates $\Lambda_{H_2} = \Lambda_{H_2}(\mathrm{H_2\text{-}H}) + \Lambda_{H_2}(\mathrm{H_2\text{-}H_2})$ is used as the H_2-cooling rate. In the updated scheme, the cooling rate in the low density limit is based on Galli & Palla (2013); fitting coefficients for H_2-cooling rates when H_2 collides with e^-, H, H^-, H^+, H_2, and He. In the high-density limit, the fraction of H_2 molecules in each level is computed by assuming LTE and the cooling rate is directly calculated. Finally, these two rates are bridged as Eq. A.10 and the total H_2-cooling rate is determined.

On the other hands, the HD-cooling rate which was based on the formula of Flower *et al.* (2000) in the previous studies is updated by bridging two rates in the low-density

limit ($\Lambda_{\rm HD}$(low); Lipovka *et al.*, 2005) and high-density limit ($\Lambda_{\rm HD}$(LTE); Coppola *et al.*, 2011a) as

$$\Lambda_{\rm HD} = \min\left[(1-{\rm rate})\times\Lambda_{\rm HD}({\rm low}) + {\rm rate}\times\Lambda_{\rm HD}({\rm LTE}),\ \Lambda_{\rm HD}({\rm LTE})\right]\ , \quad \text{(A.11)}$$

where ${\rm rate} = \min\left(n_{\rm H}/10^7,\ 1\right)$.

Figure A.2 compares the calculated cooling rates by previous (dots) and updated methods (lines). Overall, there are only a bit difference and one can consider that the thermal evolution of primordial cloud is not changed by adopting the modified rates. When the gas densities are high $n_{\rm H} = 10^6$ and 10^8 cm^{-3}, the HD-cooling rates increase at high temperature $T > 1000$ K but such dense and high temperature condition decreases the HD abundance, so that the different reaction rate cannot affect the thermal evolution of collapsing cloud.

A.3.3 H_2 and HD Self-Shielding

The simulations in Section 2.3 consider the effect of external radiation in the Lyman-Werner (LW) bands which photodissociates the main coolants: H_2 and HD molecules. The collapsing gas cloud increases its central density and finally becomes optically thick. After that, the further collapsing region is surrounded by the opaque shell and the abundances of both coolants can recover because the external radiation is consumed by photodissociating the surrounding gas (so-called *self-shielding* mechanism).

The complete treatment of such a self-shielding effect can be adopted in the hydrodynamic simulation by performing the fully radiative transfer calculation but it is computationally costly simulation. One of more simply treatments is using the analytic function, self-shielding factor, to evaluate the gas opacity. Recently, Wolcott-Green & Haiman (2011) have presented the new fitting function for H_2 and HD species depending on their column densities and local temperature. This thesis adopts their functions and calculates both the column densities of H_2 and HD by performing "six-ray approximation"; the column density is calculated by integrating the density of SPH particles which lie along six directions ($\pm X,\ \pm Y,\ \pm Z$) to account for the directional dependence of the self-shielding effect (Yoshida *et al.*, 2008). Wolcott-Green *et al.* (2011) have shown that the method can nicely approximate the detailed calculation by comparing the calculated opacities by some approximate treatments.

A.4 Numerical Resolution

To calculate the primordial star formation started from the cosmological initial condition, the simulation should treat the wide dynamic range from the large scale structure, dark matter minihalo (~ 100 kpc), to the small final object, protostellar core ($\sim 10\ R_\odot$). The calculations adopt two different methods to keep the necessary numerical resolution.

A.4.1 Hierarchical Zoom-In

One is the hierarchical zoom-in method which is applied when the cosmological initial condition is generated. After the parent, low-resolution, simulation, the zoomed-in, high-resolution, initial condition is generated by increasing the mass- and spatial-resolutions for the selected region where the target object will form. This method is useful for the case in which the target object is only a part of the simulation region and the primordial star formation is just such a problem.

A Friends-Of-Friends (FOF) halo finder locates the dense and clustered region in the parent cosmological simulation with two parameters. One is the linking length b which defines the minimum distance between particles in the same halo as $b \times L_{\rm box}/N_{\rm mesh}$. Another is the minimum particle number for FOF halo $N_{\rm halo}$ above which the selected clump is defined as FOF halo.

A.4.2 Particle Splitting

Another is the particle splitting method which is used during the cloud collapse. This thesis follows the techniques described in Kitsionas & Whitworth (2002). The procedure is summarized as below

1. In every step, the code computes the resolution condition for all SPH particles, $L_{\rm Jeans}/L_{\rm HSML}$, where $L_{\rm Jeans}$ is the local Jeans length which calculated by the thermal properties of SPH particle, and $L_{\rm HSML}$ is the smoothing length of SPH particle.
2. The parent SPH particles which do not satisfy the resolution criterion, $L_{\rm Jeans}/L_{\rm HSML} < N_{\rm res}$, are split into child particles.
3. The 13 child particles are placed on an hexagonal close-packed array; the first child is at the same position of the parent and the other twelve children are equidistant from the first. The distance between the first and other child is defined as $l = 1.5\ L_{\rm HSML}$. The particle mass is divided as $m_{\rm child} = m_{\rm parent}/13$ and the smoothing length is also divided as $L_{\rm HSML,child} = L_{\rm HSML,parent}/\sqrt[3]{13}$. The child 13 particles have the same velocity[*1] and chemical abundance of the parent particle.

By using this method, the local Jeans length is always resolved by more than a certain critical number, $N_{\rm res}$, times the local smoothing length of the SPH particles (most of simulations adopt as $N_{\rm res} = 15 - 20$). The simulations with GADGET-2 adopt the on-going splitting (on-the-fly particle splitting).

[*1] This is to avoid the computationally costly procedure. Precisely, one should calculate the velocity distribution around the parent particle and evaluate the new velocity for each child particles at their new positions.

Appendix B

Simulation of Accreting Protostar

The simulations of later accretion phase are performed by a hybrid code which consists of two parts: two-dimensional (2D) axisymmetric radiation hydrodynamic (RHD) code for the dynamics of surrounding material and protostellar evolution code for the evolution of a hydrostatic core with the variable mass accretion. The central protostar is represented as a sink cell in the RHD simulation. Two parts are interacting each other during the protostellar growth; the thermodynamic evolution of accreting envelope determine the mass accretion rate onto the central protostar whereas the state of the evolving protostar determines how efficient the stellar radiative feedback which changes the envelope's thermal state is. So one have to consistently solve the problem to obtain the accretion history and the final stellar mass.

The following two sections describe above two methods, respectively. Because the detail code descriptions can been found in the original papers (Hosokawa *et al.*, 2011, 2012a,b, 2013), these sections focus on the updated parts which is necessary to calculate various protostellar evolution with highly time-dependent accretion rates.

B.1 Radiation Hydrodynamics

The evolution of the thermodynamics of surrounding material is studied by performing a radiation hydrodynamic calculation. The code has the governing equations which are describe in the adopted cylindrical coordinate $(R,\ Z)$ as

$$\frac{\partial \rho}{\partial t} + \nabla \cdot (\rho \boldsymbol{v}) = 0 \ , \tag{B.1}$$

$$\frac{\partial (\rho \boldsymbol{v})}{\partial t} + \nabla \cdot (\rho \boldsymbol{v} \otimes \boldsymbol{v}) = -\rho \nabla \Phi - \nabla p + \frac{A^2}{\rho R^3} \boldsymbol{n}_R + \boldsymbol{K} \ , \tag{B.2}$$

$$\frac{\partial e}{\partial t} = -p \nabla \cdot \boldsymbol{v} + \Gamma - \Lambda \ , \tag{B.3}$$

$$p = (\gamma - 1) e \ , \tag{B.4}$$

where ρ is the gas density, $\boldsymbol{v} = (v_R,\ v_Z)$ is the velocity vector in the cylindrical coordinate, Φ is the gravitational potential, p is the gas pressure, $A \equiv \rho R v_\phi$ is the angular momentum per unit volume, $\boldsymbol{n}_R$ is the radial unit vector, $\boldsymbol{K}$ is the radiation force, e is the gas internal energy density, Γ and Λ are the heating and cooling rates per unit volume, and γ is the adiabatic exponent. The code treats radiative processes ($\boldsymbol{K}$ and $\Gamma - \Lambda$) and non-equilibrium chemistry (for 15 chemical reactions by five species e^-, H, H^-, H^+, and H_2) in a primordial gas. The nested-grid method is employed in order to achieve a wide spatial range (e.g., Yorke & Kaisig, 1995; Yorke & Bodenheimer, 1999; Yorke & Sonnhalter, 2002). The free flow boundary condition is adopted; the material can escape through the edges of the simulation domain assuming that the density at the boundary is the same as that of the outermost grid.

B.1.1 Angular Momentum Transport in the Accretion Disk

In a rapidly accreting circumstellar disk, the angular momentum is transferred outward by torques produced by non-axisymmetric spiral structure. Hosokawa *et al.* (2011) have adopted the so-called α-viscosity (Shakura & Sunyaev, 1973) to mimic this effect in axisymmetric 2D radiation hydrodynamic simulations. The equation of angular momentum transport is written

$$\frac{\partial A}{\partial t} + \nabla \cdot (A\vec{v}) = -\frac{1}{R}\frac{\partial}{\partial R}\left(R^3 \eta \frac{\partial \Omega}{\partial R}\right) \ , \tag{B.5}$$

where Ω is angular velocity, $\eta = 2\alpha\rho c_s^2/(3\Omega)$, and α is a dimensionless free parameter. They model the spatial distribution of the alpha-parameter with an analytic function

$$\alpha(R, Z) = \alpha_0 \ \exp\left(-\frac{Z}{H(R)}\right) \ , \tag{B.6}$$

where α_0 is a constant free parameter, and $H(R)$ is the scale height of the circumstellar disk at each radial coordinate R. The fiducial value of α_0 is 0.6 in Hosokawa *et al.* (2011).

Following the previous studies (Zhu *et al.*, 2010a; Takahashi *et al.*, 2013), this thesis improves the above description with an additional R-dependence of α_0 by adopting the functional form proposed by Gammie (1996),

$$\alpha_0(R) = \alpha_{\max}\ e^{-Q(R)^4} \ , \tag{B.7}$$

where $Q(R)$ is the Toomre Q-parameter (Toomre, 1964), which measures the gravitational stability of the disk. The underlying idea of the above dependence is as follows. With the small values of $Q < 1$, α_0 approaches $\alpha_{\max}$ because the angular momentum transport should be efficient with spiral arms emerging in such a highly unstable disk. The large α_0 promotes the mass accretion, which reduces the disk surface density and increases Q. On the other hand, α_0 has a cut-off for $Q > 1$, because the spiral arms disappear in a stable disk. Materials falling onto the disk accumulate without angular momentum transport, which enhance the disk surface density and reduce Q. With the above regulation mechanism, the self-gravitating disk hovers around the marginally stable steady state with $Q \sim 1$.

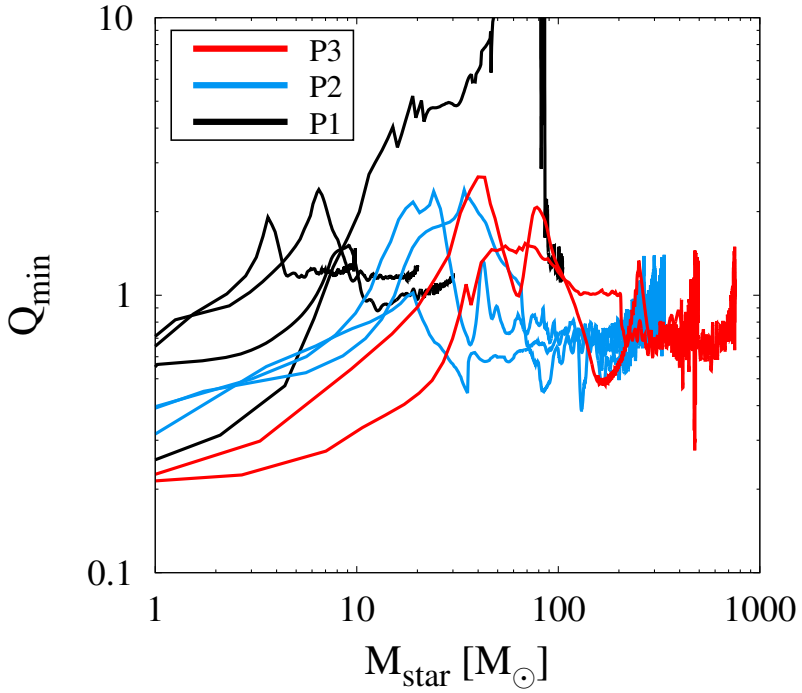

Figure B.1. Evolution of the minimum Toomre Q-parameter as a function of the stellar mass for the same cases as in Figure 2.3. $Q_{\rm min}$ is close to unity, which is generally expected for a self-gravitating circumstellar disk, in almost all the cases. Only one case, for which the cloud rotation is the slowest of the entire sample, shows a very large $Q_{\rm min}$ (see discussion in text).

All the examined cases in this thesis adopts $\alpha_{\rm max} = 2$. Figure B.1 shows the evolution of the minimum Toomre Q-values in several cases and $Q_{\rm min}$ eventually converges to around unity in each case. Only one case shows a peculiar evolution with $Q_{\rm min}$ reaching 10 at maximum. This corresponds to the most slowly rotating cloud explained in Section 2.2.5.2.1. A circumstellar disk hardly forms in this case.

Mass accretion continues smoothly without "ring-like" disk fragmentation of the disk in the simulations. In test calculations with lower values of $\alpha_{\rm max}$ ring-like fragmentation does occur occasionally with very rapid mass accretion. Such phenomena is avoided on purpose with the choice of $\alpha_{\rm max}$ because the 2D axisymmetric simulations cannot treat fragmentation. So the results are considered for very rapid mass accretion a conservative upper limit of the final stellar mass resulting from stellar UV feedback. Disk fragmentation could further reduce the final stellar masses (see also Sec. 2.2.5.3).

B.2 Protostellar Evolution

The calculations consistently follow the structure and evolution of the central accreting star and the hydrodynamics of the accreting gas which is irradiated by the stellar radia-

tion. The mass accretion rate onto the protostar is directly obtained from the inflow rate of gas into the central sink cell in the RHD simulation. The evolution of the protostar is calculated by numerically solving the interior structure with this accretion rate (e.g., Omukai & Palla, 2003; Hosokawa & Omukai, 2009). The stellar luminosity and the effective temperature are provided by the stellar model. The spectral energy distribution is calculated from these basic properties of the star.

There are four governing equations to solve the stellar structure; stellar radius r, pressure P, luminosity L, and entropy s as

$$\left(\frac{\partial r}{\partial M}\right)_t = \frac{1}{4\pi\rho r^2} \ , \tag{B.8}$$

$$\left(\frac{\partial P}{\partial M}\right)_t = -\frac{GM}{4\pi r^2} \ , \tag{B.9}$$

$$\left(\frac{\partial L}{\partial M}\right)_t = \epsilon - T\left(\frac{\partial s}{\partial t}\right)_M \ , \tag{B.10}$$

$$\left(\frac{\partial s}{\partial M}\right)_t = \frac{GM}{4\pi r^4}\left(\frac{\partial s}{\partial p}\right)_T \left(\frac{L}{L_s} - 1\right) C \ , \tag{B.11}$$

where M is the Lagrangian mass coordinate, ϵ is the energy production rate by nuclear fusion, s is the specific entropy, L_s is the radiative luminosity with adiabatic temperature gradient. The coefficient C changes according to the state of layer; unity when $L < L_s$ (radiative) and given by the mixing-length theory when $L > L_s$ (convective).

The mass accretion rate onto the protostar is given by a mass inflow rate through the surface of the sink cell in the RHD calculation. The structure of the accretion flow inside the sink cell is solved by assuming the steady state and spherical symmetry. The entire structure of both the protostar and accretion flow is consistently calculated to satisfy the jump conditions for the accretion shock at the stellar surface (Stahler *et al.*, 1980).

As described in Sec. 2.2, the stellar evolution code occasionally has convergence difficulties for the extremely high and highly variable accretion rates encountered in the P2 and P3 scenarios. Whereas for the P1 cases which can be calculated by the same method as Hosokawa *et al.* (2011), the code switches to the following simple procedure of protostellar evolution when convergence difficulties arise.

B.2.1 Oscillating Protostar (P2)

The solid line in Figure B.2 shows the numerically calculated evolution with the constant accretion rate $\dot{M} = 6 \times 10^{-3}\ M_\odot\ \mathrm{yr}^{-1}$. In this case, the stellar evolution code experienced convergence difficulties after the stellar mass exceeded 60 $M_\odot$, when the radius began to increase and the total luminosity reached the Eddington limit (see also Sec. 1.2.5). The problem worsened when the mass accretion rates became time-dependent in the simulations.

The code adopts the following simplified procedure instead. First, the protostellar evolution is numerically calculated until the protostar begins to oscillate. After that, the code analytically models the evolution of the stellar radius and luminosity using the same

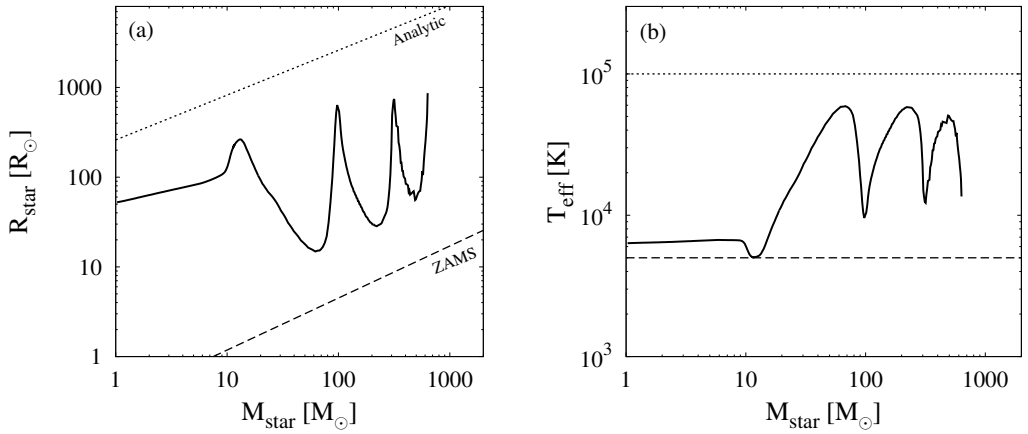

Figure B.2. Evolution of the stellar radius (panel a) and effective temperature (b) as a function of the stellar mass. The solid lines show the numerical results for $\dot{M} = 6 \times 10^{-3}\ M_\odot\ \mathrm{yr}^{-1}$ taken from Hosokawa *et al.* (2012a). The dotted and short-dashed lines are the same as in Figures 2.9(b) and (c).

power-law functions as for non-accreting ZAMS stars,

$$R(M_*) = R_{\rm edd}\ \left(\frac{M_*}{M_{\rm edd}}\right)^{0.58}\ R_\odot\ , \tag{B.12}$$

$$L(M_*) = L_{\rm edd}\ \left(\frac{M_*}{M_{\rm edd}}\right)^{1.30}\ L_\odot\ , \tag{B.13}$$

where $M_{\rm edd}$, $R_{\rm edd}$, and $L_{\rm edd}$ are the stellar quantities when the star begins to oscillate. Once the accretion rate drops below the critical value $4 \times 10^{-3}\ M_\odot\ \mathrm{yr}^{-1}$ (Eq. 1.24), the code lets the star to contract over the KH time-scale according to

$$R(M_*) = R_{\rm prev} + dt \cdot \left[\frac{R(M_*)_{\rm ZAMS} - R_{\rm prev}}{t_{\rm KH}}\right]\ R_\odot\ , \tag{B.14}$$

$$L(M_*) = L_{\rm prev} + dt \cdot \left[\frac{L(M_*)_{\rm ZAMS} - L_{\rm prev}}{t_{\rm KH}}\right]\ L_\odot\ , \tag{B.15}$$

where $R_{\rm prev}$ and $L_{\rm prev}$ are the stellar quantities at the previous step of calculation, and

$$R(M_*)_{\rm ZAMS} = 3.109 \times 10^{-1}\ \left(\frac{M_*}{M_{\rm edd}}\right)^{0.58}\ R_\odot\ , \tag{B.16}$$

$$L(M_*)_{\rm ZAMS} = 3.939 \times 10^{3}\ \left(\frac{M_*}{M_{\rm edd}}\right)^{1.30}\ L_\odot\ . \tag{B.17}$$

After the star reaches the ZAMS stage, the radius and luminosity are assumed to be the same as those of non-accreting ZAMS stars.

B.2.2 Super-Giant Protostar (P3)

The convergence difficulties described above worsen when considering P3 evolution. This thesis adopts two different methods to calculate such numerically uncertain evolution

(Secs. 2.2 and 2.3).

B.2.2.1 Using Another Numerical Code

In Section 2.2, the 2D RHD simulation without stellar UV feedback is first performed and the mass accretion history without calculating stellar evolution is recorded. Next, the stellar evolution is numerically calculated as a post process from the accretion history. The code records the stellar evolution track until the stellar total luminosity reaches the Eddington value. The RHD simulation is repeated with including UV feedback using the recorded stellar evolution track. Finally, the code switches to the same analytic model as for the path P2 for the evolution beyond the recorded stellar evolution track. UV feedback significantly affects the accretion only after the protostar enters the evolutionary path P2.

It would be very time-consuming to use the procedure described above for all twelve cases of P3 evolution. Instead, this procedure has been used for only three cases. For the other nine cases, the final stellar masses are estimated using the relation (2.4). These nine cases are designated as the path $\mathrm{P3_{pred}}$ in the captions of Figure 2.11.

B.2.2.2 Analytic Model

The evolution of mass accreting protostars greatly depends on the accretion rates. Hosokawa *et al.* (2012a) have shown that, with high accretion rates of $\dot{M} > 0.04\ M_\odot\ \mathrm{yr}^{-1}$, the protostellar evolution qualitatively differs from that at lower rates. At these high accretion rates, the stellar radius monotonically increases with increasing the stellar mass, exceeding $10^3\ R_\odot$ for $M_* > 100\ M_\odot$. The UV radiative feedback from such "super-giant protostars" is weak, because the resulting effective temperature is less than 10^4 K. In Section 2.3, this evolutionary stage frequently appears in the 2D RHD simulations of Pop $\mathrm{III.2_D}$ cases, where the accretion rates are relatively high. However, it is sometimes difficult to construct stellar models of these strongly accreting super-giant protostars by numerically solving the stellar structure equations, especially with highly variable mass accretion histories.

Instead, an analytic model for the evolution of the super-giant protostar shall be considered. It is known that, during this evolutionary stage, the evolution of the stellar radius is well described by equation (11) in Hosokawa *et al.* (2012a),

$$R_*(M_*) \simeq 260 \left(\frac{M_*}{\mathrm{M}_\odot}\right)^{1/2} R_\odot\ . \tag{B.18}$$

The calculation adopts the functional form of this description but multiply the resulting radius by 0.8 to better fit the numerical results in Section 2.2, which used a detailed stellar evolution code. The stellar effective temperature is nearly constant at $T_{\rm eff} = 5000$ K during this phase (Fig. B.2), and the stellar luminosity is calculated from

$$L_*(R_*, T_{\rm eff} = 5000\ \mathrm{K}) = 4\pi R_*^2 \sigma T_{\rm eff}^4\ , \tag{B.19}$$

where σ is the Stefan-Boltzmann constant. As long as the mass accretion rate is above the critical value $0.04\ M_\odot\ \mathrm{yr}^{-1}$ the stellar radius and luminosity are calculated by using

the above equations. Once the accretion rate falls below this value, the code switches to another analytic model of the "oscillating protostar" as in Section B.2.2.1.

After the mass accretion rate falls below $4 \times 10^{-3}\ M_\odot\ \mathrm{yr}^{-1}$, the star begins to contract on a Kelvin-Helmholtz (KH) time-scale (e.g., Omukai & Palla, 2003),

$$t_{\rm KH} = \frac{GM_*^2}{R_* L_*}\ . \tag{B.20}$$

The changes of stellar radius and luminosity during a timestep dt are written

$$R_*^{\rm new} = R_* + \frac{{\rm d}t}{t_{\rm KH}} \cdot [R(M_*)_{\rm ZAMS} - R_*]\ , \tag{B.21}$$

$$L_*^{\rm new} = L_* + \frac{{\rm d}t}{t_{\rm KH}} \cdot [L(M_*)_{\rm ZAMS} - L_*]\ , \tag{B.22}$$

where the properties of Zero-Age Main Sequence (ZAMS) stars are

$$R(M_*)_{\rm ZAMS} = 3.109 \times 10^{-1} \left(\frac{M_*}{\rm M_\odot}\right)^{0.58}\ , \tag{B.23}$$

$$L(M_*)_{\rm ZAMS} = 3.939 \times 10^{3} \left(\frac{M_*}{\rm M_\odot}\right)^{1.30}\ . \tag{B.24}$$

If Eq. B.21 yields a value $R_*^{\rm new}(M_*) < R_{\rm ZAMS}$, the code uses another relationship to get the stellar properties at the next step

$$R_*^{\rm new} = \left[R_* + \frac{{\rm d}t}{t_{\rm KH}} R(M_*)_{\rm ZAMS}\right] \left(1 + \frac{{\rm d}t}{t_{\rm KH}}\right)^{-1}, \tag{B.25}$$

$$L_*^{\rm new} = \left[L_* + \frac{{\rm d}t}{t_{\rm KH}} L(M_*)_{\rm ZAMS}\right] \left(1 + \frac{{\rm d}t}{t_{\rm KH}}\right)^{-1}. \tag{B.26}$$

By using the above-mentioned formulae for protostars going through the super-giant phase, the mass growth of a rapidly accreting Pop III.2$_{\rm D}$ star can be computed.

Appendix C

Thermal Evolution Depending on the Collapsing time-scale

As described in Section 2.2.2.2, HD line cooling, which has been thought to be unimportant in Pop III.1 star formation, is actually quite effective during the early run-away collapse stage in several of these cases. HD molecules form when rotational support of the cloud can sufficiently slow the collapse. This chapter tests this hypothesis using a simple one-zone model, which follows the thermal evolution at the center of the collapsing cloud (e.g., Omukai, 2000; Chiaki *et al.*, 2013). Figure C.1 shows the results for different collapsing time-scales, $t_{\rm coll} = f \cdot t_{\rm ff}$, with $f = 0.6$, 1.0, 1.8, 3.2, 5.6, and 10.0 (solid lines). Several examples of the thermal evolution obtained in the 3D hydrodynamic simulations (colored dashed lines with filled circles) are also plotted in this figure. The one-zone results can well explain the diversity of thermal evolution. The following paragraphs briefly describe the essence of the evolution in each density range below.

Low Density ($n_{\rm H,cen}/{\rm cm}^{-3} < 10^8$)

In this stage, HD cooling could significantly affect the thermal evolution for the slowly collapsing cloud. HD cooling becomes efficient when the gas temperature falls below 100 K. The additional coolant HD further reduces the temperature to the cosmological temperature floor, $T_{\rm CMB}$. Figure C.1 shows that the gas temperature falls more strongly for the longer collapse time-scale. The gas temperature falls below the critical temperature via H_2 and HD coolings when $f > 1.8$. Indeed, this critical value of f can be analytically derived by requiring the collapse time-scale $t_{\rm coll} = f \cdot t_{\rm ff}$ to be equal to the H_2 cooling time at $T = 100$ K (and $n_{\rm H} = 10^3$ cm^{-3}). The resulting value of $f_{\rm crit} = 1.2$ is close to the numerical result.

Intermediate Density ($10^8 < n_{\rm H,cen}/{\rm cm}^{-3} < 10^{12}$)

At densities above 10^8 cm^{-3} the three-body H_2 formation reaction becomes quite efficient, and H_2 formation heating becomes more important than heating by compression. Nevertheless, the equilibrium temperature is lower for cases with a higher abundance of hydrogen molecules. The middle panel of Figure C.1 shows that the more slowly collapsing clouds have a higher H_2 fraction at densities 10^8 cm$^{-3} < n_{\rm H,cen} < 10^{12}$ cm^{-3}, because more H_2 is formed when the collapse time is longer. H_2 cooling dominates the cooling, so

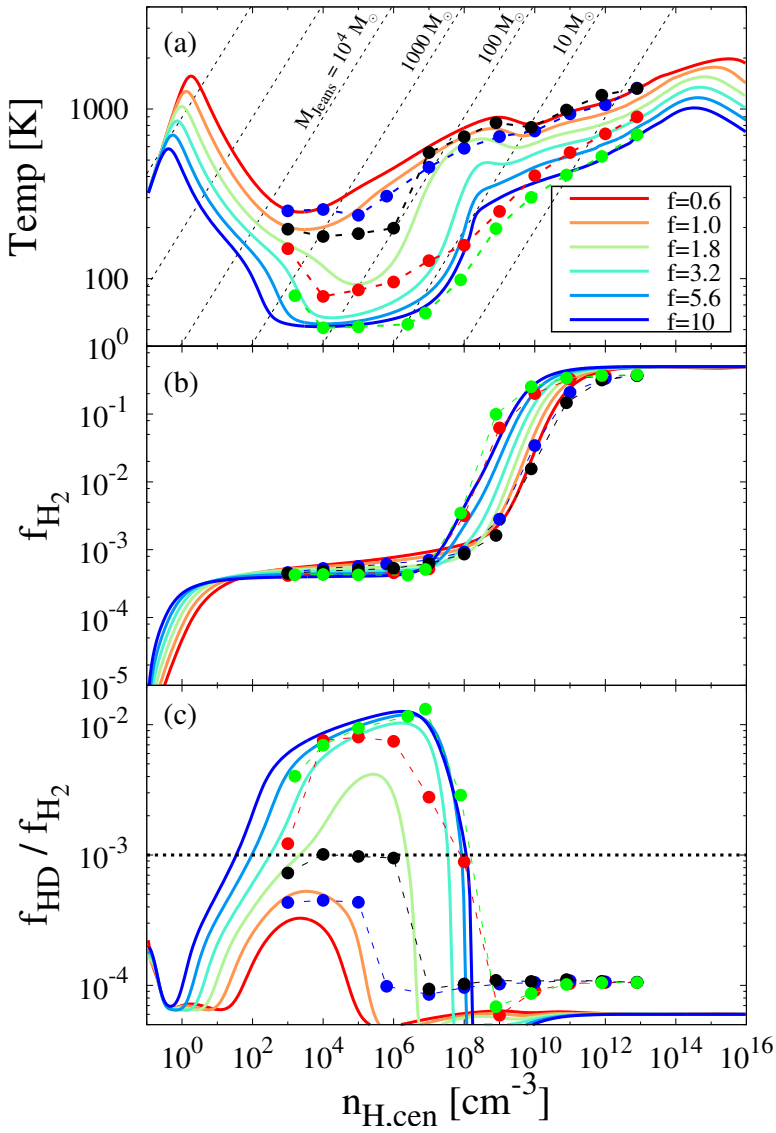

Figure C.1. Comparison of the thermal evolution during the cloud collapse between the simulation results (dashed lines and filled circles) and one-zone models (solid lines). The solid lines with the different colors represent the different collapse time-scales, $t_{\rm coll} = f \cdot t_{\rm ff}$, with f = 0.6, 1.0, 1.8, 3.2, 5.6, and 10, which is a parameter for one-zone modeling. The red, blue, and black dashed lines represent the same 3D simulation cases shown in Figure 2.10, whereas the green line is for the most rapidly rotating cloud shown in Figure 2.15. The black dashed lines in the top panel present $\rho - T$ relations for given values of the Jeans mass.

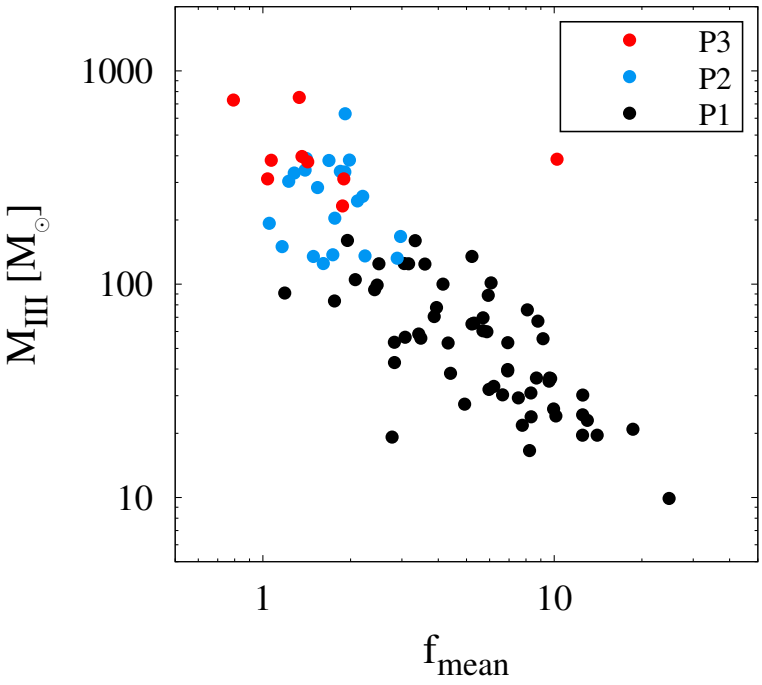

Figure C.2. Correlation between the ratio $f = t/t_{\rm ff}$ of the averaged relative collapse time-scale to the free-fall time-scale and the final stellar masses in the numerical simulations.

the temperature is lower with the larger f in this density range.

High Density ($10^{12} < n_{\rm H,cen}/{\rm cm}^{-3}$)

At these high densities all of the hydrogen has been converted into its molecular form. Compression heating, which increases with decreasing collapse time-scale, becomes the dominant heating process. The heating rate is thus lower for the longer collapse time-scale. This explains why the temperature remains lower with the larger f in the highest density range.

Figure C.2 shows the correlation between f and the final stellar masses in the numerical results. f is the ratio of the collapsing time-scale, $t_{\rm coll}$, between two snapshots during which the central density decouples, $n_{\rm H,cen} \rightarrow 10 \times n_{\rm H,cen}$, to the free-fall time,

$$t_{\rm ff} = \left(\frac{3\pi}{32 G \rho} \right)^{1/2} . \tag{C.1}$$

The averaged ratios at $n_{\rm H,cen} = 10^4$ to 10^{12} cm^{-3} are assumed as the characteristic parameters of the collapsing clouds f. The good correlation presented here suggests that the thermal evolution in the 3D cosmological simulations really depends on f.

McKee & Tan (2008) have adopted the rotational degree of the cloud $f_{\rm Kepler}$ as a key parameter which determines the final stellar mass in their semi-analytic model. However, they only consider that the rotational support of the cloud slows down the mass accretion

onto the star. It have been shown that the rotational support reduces the accretion rate by changing the chemo-thermal evolution as well as the gas dynamics.

Appendix D

110 Population III.1 Stars

This chapter shows the 110 simulation results shown in Section 2.2. Figure D.1 shows the diversity of minihalos' density structure: isolated or clustered, lie on the filament or at the knot of the cosmic web. Table D.1 shows the resultant data list which is used to derive the correlations.

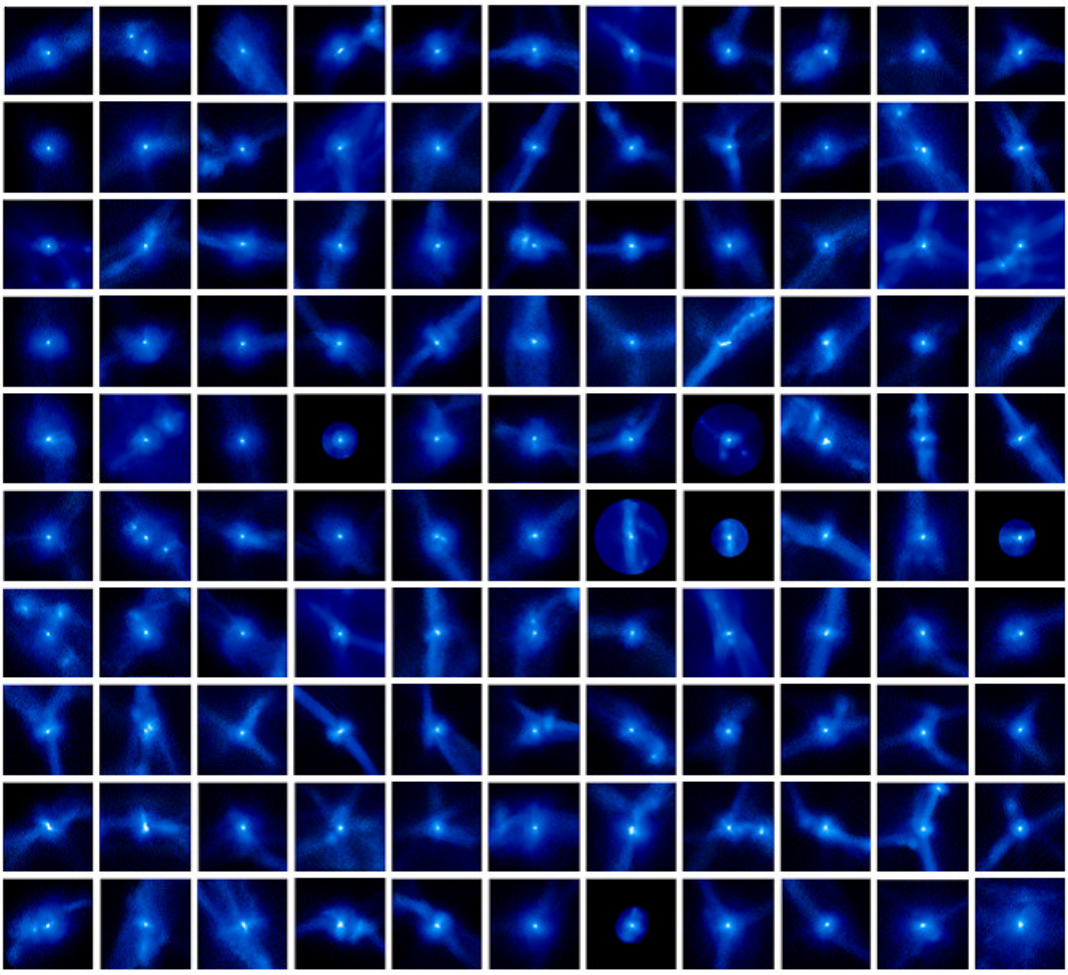

Figure D.1. Density maps of 110 dark matter with a physical 500 pc in a side.

ID	$z_{\rm form}$	$M_{\rm vir}$ ($M_\odot$)	$\lambda_{\rm DM}$	$\lambda_{\rm gas}$	θ	$\dot{M}_{\rm vir}$ ($M_\odot$ yr^{-1})	$M_{\rm Jeans}$ ($M_\odot$)	β	$\dot{M}_{\rm Jeans}$ ($M_\odot$ yr^{-1})	$M_{\rm III.1}$ ($M_\odot$)	P
001	35.5	4.2E5	0.093	0.072	5.3	3.42E-3	666	0.14	20.80E-3	236.9	2
002	34.7	0.3E5	0.035	0.051	70.1	0.50E-3	945	0.23	3.74E-3	78.0	1
003	31.0	1.4E5	0.045	0.065	15.2	0.67E-3	590	0.34	0.45E-3	100.0	1
004	29.9	0.3E5	0.035	0.018	43.5	0.25E-3	434	0.32	0.40E-3	38.2	1
005	29.8	0.3E5	0.024	0.054	86.3	0.28E-3	1650	0.33	1.91E-3	99.6	1
006	28.9	6.1E5	0.038	0.035	9.9	5.98E-3	260	0.34	6.96E-3	1041.0	2
007	26.8	1.2E5	0.057	0.046	8.3	1.51E-3	529	0.63	0.39E-3	20.0	1
008	25.2	2.4E5	0.072	0.038	17.3	0.99E-3	926	1.15	0.53E-3	100.0	1
009	24.1	2.2E5	0.022	0.019	19.2	0.96E-3	230	0.55	1.15E-3	90.9	1
010	23.8	2.5E5	0.011	0.013	67.9	1.06E-3	858	0.69	2.15E-3	160.3	1
011	22.8	3.1E5	0.054	0.043	3.3	1.50E-3	688	0.37	4.47E-3	300.0	3
012	21.6	4.0E5	0.023	0.019	10.7	2.63E-3	395	0.35	3.87E-3	302.3	2
013	21.5	2.2E5	0.046	0.030	4.6	1.05E-3	317	0.51	1.32E-3	135.0	2
014	21.4	5.2E5	0.036	0.061	23.7	2.22E-3	243	0.27	1.34E-3	99.0	1
015	21.3	1.8E5	0.048	0.012	15.3	0.52E-3	79	0.44	0.16E-3	39.2	1
016	21.2	1.8E5	0.049	0.011	15.1	0.52E-3	124	0.58	0.21E-3	67.1	1
017	21.2	2.7E5	0.025	0.020	12.0	0.81E-3	208	0.63	0.43E-3	75.8	1
018	21.0	4.2E5	0.093	0.072	5.3	3.42E-3	666	0.14	20.80E-3	342.8	2
019	20.7	2.9E5	0.054	0.023	22.7	0.81E-3	574	0.84	1.01E-3	132.3	2
020	20.5	3.5E5	0.044	0.021	24.1	1.50E-3	1080	0.56	2.78E-3	283.9	2
021	20.2	2.9E5	0.044	0.023	16.9	0.69E-3	527	0.79	1.20E-3	125.0	1
022	20.2	2.6E5	0.024	0.015	99.8	0.58E-3	514	0.80	1.90E-3	167.3	2
023	20.2	2.4E5	0.045	0.016	57.5	0.87E-3	428	0.53	1.32E-3	124.3	1
024	20.2	3.9E5	0.063	0.060	28.4	1.57E-3	1100	0.07	11.10E-3	655.6	3
025	20.1	2.2E5	0.029	0.025	42.2	0.38E-3	103	0.45	0.17E-3	56.4	1
026	19.9	3.1E5	0.011	0.005	48.6	1.47E-3	1030	0.26	4.14E-3	500.0	3
027	19.8	4.2E5	0.045	0.035	32.1	1.99E-3	775	0.17	4.07E-3	219.5	2
028	19.3	2.6E5	0.038	0.022	44.3	0.67E-3	197	0.20	1.60E-3	125.0	2
029	19.3	2.9E5	0.033	0.021	27.0	1.16E-3	753	0.35	5.51E-3	398.2	2
030	19.2	3.6E5	0.027	0.009	58.5	1.29E-3	360	0.29	0.93E-3	132.4	1
031	19.2	5.2E5	0.047	0.056	16.2	2.44E-3	686	0.28	3.30E-3	219.5	1
032	19.1	2.2E5	0.038	0.027	15.9	0.42E-3	268	0.47	3.27E-3	258.1	2
033	19.0	6.1E5	0.038	0.035	9.9	5.98E-3	260	0.34	6.96E-3	338.0	2
034	18.9	4.0E5	0.106	0.073	19.0	3.42E-3	153	0.39	0.55E-3	77.7	1
035	18.8	4.2E5	0.031	0.002	136.0	1.63E-3	211	0.22	0.87E-3	137.4	2
036	18.7	3.3E5	0.045	0.023	10.0	0.65E-3	2040	0.74	2.02E-3	381.8	2
037	18.7	5.5E5	0.074	0.052	19.3	2.39E-3	1390	0.54	2.87E-3	193.0	2
038	18.5	4.6E5	0.048	0.023	38.0	1.50E-3	1590	0.57	1.61E-3	204.0	2
039	18.4	4.6E5	0.032	0.024	2.0	2.06E-3	362	0.23	0.62E-3	42.9	1
040	18.4	3.1E5	0.049	0.031	11.4	0.58E-3	289	0.24	2.67E-3	124.7	1

ID	$z_{\rm form}$	$M_{\rm vir}$ ($M_\odot$)	$\lambda_{\rm DM}$	$\lambda_{\rm gas}$	θ	$\dot{M}_{\rm vir}$ ($M_\odot$ yr^{-1})	$M_{\rm Jeans}$ ($M_\odot$)	β	$\dot{M}_{\rm Jeans}$ ($M_\odot$ yr^{-1})	$M_{\rm III.1}$ ($M_\odot$)	P
041	18.4	4.2E5	0.027	0.034	51.3	0.76E-3	130	0.41	0.76E-3	55.5	1
042	18.4	3.0E5	0.062	0.022	5.8	1.09E-3	46	0.33	0.08E-3	24.1	1
043	18.3	3.9E5	0.096	0.070	7.8	4.05E-3	77	0.16	0.49E-3	30.9	1
044	18.3	3.0E5	0.021	0.010	20.9	1.13E-3	709	0.41	4.25E-3	332.2	2
045	18.1	3.9E5	0.043	0.025	56.2	2.98E-3	604	0.20	2.83E-3	270.0	2
046	18.1	2.9E5	0.018	0.013	47.7	0.54E-3	712	0.82	1.13E-3	83.4	1
047	18.1	4.3E5	0.035	0.045	59.8	1.86E-3	1110	0.75	2.29E-3	475.0	3
048	17.8	7.9E5	0.027	0.052	8.8	3.67E-3	455	0.25	3.71E-3	650.0	2
049	17.7	3.2E5	0.022	0.010	92.2	0.30E-3	365	0.84	0.30E-3	36.3	1
050	17.5	3.2E5	0.052	0.050	18.9	0.80E-3	415	0.75	1.80E-3	124.7	1
051	17.5	5.9E5	0.070	0.062	17.4	1.58E-3	558	0.88	0.52E-3	59.9	1
052	17.4	3.2E5	0.030	0.014	17.8	0.83E-3	24	0.24	0.16E-3	69.6	1
053	17.4	3.1E5	0.040	0.028	7.7	0.49E-3	139	0.48	0.53E-3	55.8	1
054	17.3	4.6E5	0.047	0.034	14.6	1.62E-3	225	0.18	1.14E-3	269.9	2
055	17.3	2.9E5	0.016	0.005	27.5	0.57E-3	184	0.57	0.23E-3	53.0	1
056	17.2	3.1E5	0.032	0.043	161.0	0.38E-3	157	0.34	0.55E-3	58.4	1
057	17.2	4.2E5	0.039	0.063	23.9	1.00E-3	114	0.63	0.14E-3	35.1	1
058	17.2	4.0E5	0.049	0.037	9.0	2.06E-3	54	0.23	0.15E-3	33.9	1
059	17.1	5.6E5	0.017	0.015	12.5	2.81E-3	116	0.95	0.26E-3	730.0	3
060	17.1	4.6E5	0.057	0.033	35.5	1.62E-3	695	0.80	0.83E-3	135.0	1
061	17.1	6.7E5	0.055	0.058	41.4	1.90E-3	1390	0.66	2.46E-3	340.0	3
062	17.1	3.0E5	0.057	0.050	29.0	0.61E-3	20	0.22	1.38E-3	32.1	1
063	16.9	3.5E5	0.017	0.022	114.0	0.82E-3	121	0.45	0.22E-3	36.3	1
064	16.7	8.2E5	0.111	0.139	13.4	3.51E-3	521	0.78	1.12E-3	160.0	1
065	16.6	8.2E5	0.064	0.084	18.1	3.03E-3	1130	0.64	1.16E-3	135.7	2
066	16.5	4.8E5	0.044	0.039	24.9	2.36E-3	785	0.10	7.86E-3	423.3	2
067	16.5	7.5E5	0.064	0.056	7.4	2.17E-3	3360	0.72	5.22E-3	490.0	3
068	16.4	2.7E5	0.062	0.079	20.5	0.22E-3	97	0.74	0.15E-3	30.2	1
069	16.3	4.2E5	0.032	0.016	62.2	1.15E-3	855	0.06	0.52E-3	430.0	3
070	16.3	4.6E5	0.005	0.018	97.5	0.63E-3	136	0.41	1.15E-3	94.3	1
071	16.3	4.0E5	0.025	0.019	10.9	0.31E-3	90	0.13	0.29E-3	44.6	1
072	16.3	5.0E5	0.020	0.022	27.9	1.38E-3	630	0.23	19.30E-3	380.3	2
073	16.2	7.4E5	0.056	0.053	12.9	2.20E-3	2070	0.62	2.45E-3	388.5	2
074	16.2	1.9E5	0.049	0.019	68.5	0.18E-3	226	0.41	0.55E-3	88.7	1
075	16.2	4.2E5	0.019	0.020	2.8	1.00E-3	737	0.92	0.64E-3	70.5	1
076	16.2	8.3E5	0.074	0.049	23.6	2.95E-3	972	0.48	5.16E-3	751.3	3
077	16.1	4.1E5	0.051	0.047	25.0	0.75E-3	98	0.68	0.11E-3	19.6	1
078	16.0	3.1E5	0.013	0.011	77.0	0.62E-3	120	0.17	0.52E-3	340.0	3
079	15.9	3.8E5	0.022	0.094	19.6	0.63E-3	84	0.89	0.15E-3	36.1	1
080	15.9	4.9E5	0.112	0.111	16.0	1.49E-3	140	0.50	0.46E-3	65.7	1

ID	$z_{\rm form}$	$M_{\rm vir}$ ($M_\odot$)	$\lambda_{\rm DM}$	$\lambda_{\rm gas}$	θ	$\dot{M}_{\rm vir}$ ($M_\odot$ yr^{-1})	$M_{\rm Jeans}$ ($M_\odot$)	β	$\dot{M}_{\rm Jeans}$ ($M_\odot$ yr^{-1})	$M_{\rm III.1}$ ($M_\odot$)	P
081	15.8	2.5E5	0.024	0.041	70.0	0.50E-3	133	0.68	0.15E-3	23.9	1
082	15.8	1.6E5	0.043	0.034	28.7	0.07E-3	83	0.41	0.12E-3	30.3	1
083	15.8	7.3E5	0.066	0.041	17.0	1.83E-3	6490	0.63	3.06E-3	266.0	3
084	15.6	2.1E5	0.019	0.008	73.1	0.19E-3	42	0.39	0.21E-3	24.4	1
085	15.6	4.5E5	0.053	0.062	30.3	0.70E-3	203	0.60	0.20E-3	53.2	1
086	15.6	4.2E5	0.009	0.021	31.2	0.53E-3	78	0.19	1.03E-3	65.1	1
087	15.5	3.1E5	0.072	0.048	7.4	0.49E-3	371	0.48	0.85E-3	101.4	1
088	15.3	3.1E5	0.038	0.020	4.3	0.69E-3	260	0.29	1.68E-3	150.0	2
089	15.3	2.8E5	0.013	0.038	30.7	0.33E-3	186	0.91	0.24E-3	39.8	1
090	15.2	7.7E5	0.052	0.036	22.0	5.07E-3	3400	0.12	8.19E-3	1621.0	2
091	15.1	4.8E5	0.102	0.071	10.7	0.75E-3	121	0.38	0.45E-3	60.5	1
092	14.9	9.8E5	0.033	0.010	72.0	4.09E-3	1970	0.90	3.04E-3	264.8	3
093	14.9	5.8E5	0.057	0.041	17.0	0.93E-3	25	0.47	0.04E-3	9.9	1
094	14.5	6.8E5	0.048	0.035	16.8	0.78E-3	146	0.57	0.13E-3	26.0	1
095	14.4	4.7E5	0.039	0.065	39.4	0.32E-3	253	0.34	2.10E-3	245.8	2
096	14.3	8.3E5	0.089	0.100	15.9	2.50E-3	2470	0.60	0.53E-3	27.4	1
097	14.2	7.1E5	0.050	0.048	20.8	1.19E-3	1180	0.52	3.20E-3	303.9	2
098	14.1	5.4E5	0.055	0.036	14.4	0.67E-3	115	0.58	0.20E-3	29.3	1
099	14.1	1.9E5	0.024	0.035	28.9	0.09E-3	65	0.58	0.15E-3	23.0	1
100	14.0	3.3E5	0.046	0.062	20.4	0.52E-3	39	0.24	0.14E-3	19.2	1
101	14.0	10.4E5	0.038	0.039	31.4	4.90E-3	927	0.14	29.00E-3	335.7	2
102	14.0	3.5E5	0.024	0.040	33.0	0.56E-3	21	0.29	0.12E-3	20.9	1
103	13.9	6.8E5	0.014	0.037	50.7	0.23E-3	67	0.18	0.18E-3	53.4	1
104	13.9	3.8E5	0.068	0.035	22.1	0.82E-3	108	0.71	0.20E-3	21.8	1
105	13.8	3.0E5	0.017	0.014	4.1	0.30E-3	67	0.02	0.45E-3	105.0	1
106	13.8	7.5E5	0.121	0.130	18.8	0.32E-3	216	1.09	0.23E-3	33.2	1
107	13.2	9.0E5	0.121	0.141	4.6	1.60E-3	919	0.56	6.52E-3	629.4	2
108	13.0	3.0E5	0.097	0.061	27.0	0.24E-3	87	0.09	0.90E-3	19.6	1
109	11.9	7.2E5	0.050	0.184	21.1	0.08E-3	29	0.30	0.16E-3	16.6	1
110	11.6	4.2E5	0.032	0.041	12.3	0.15E-3	87	0.67	0.11E-3	38.2	1

Table D.1: Column 1: ID, Column 2: Formation redshift, Column 3: Virial mass of minihalo Columns 4 and 5: Spin parameters of DM and gas components, Column 6: Offset angle, Column 7: Gas infall rate at the virial scale, Column 8: Gravitationally unstable cloud mass, Column 9: Rotation parameter, Column 10: Gas infall rate at the Jeans scale, Column 11: Final stellar mass, and Column 12: Evolutionary path of the accreting protostar.

Appendix E

Remaining Pop III.2$_{\mathrm{D}}$ Cases

Section 2.3 shows the detail calculation results for only 3 initial conditions (Figs. 2.19 and 2.20). This chapter represents the thermal and dynamical properties for remaining cases (ID = 1, 2, 3, 5, 6, and 7) in Figures E.1 and E.2. Their complicated evolution can be recognized as the explanations in Section 2.3.4.

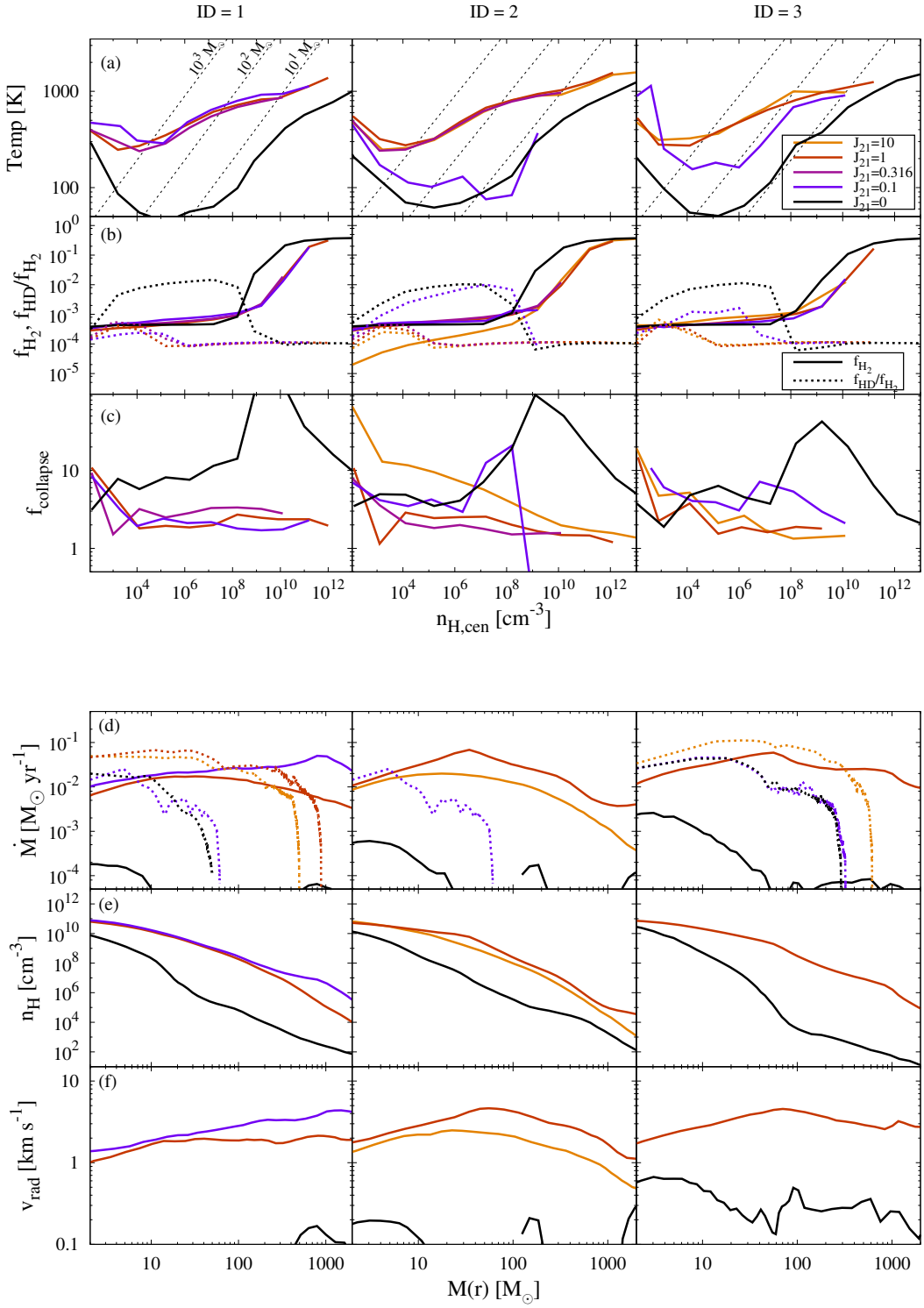

Figure E.1. Same as Figures 2.19 and 2.20 for ID = 1, 2, and 3 cases.

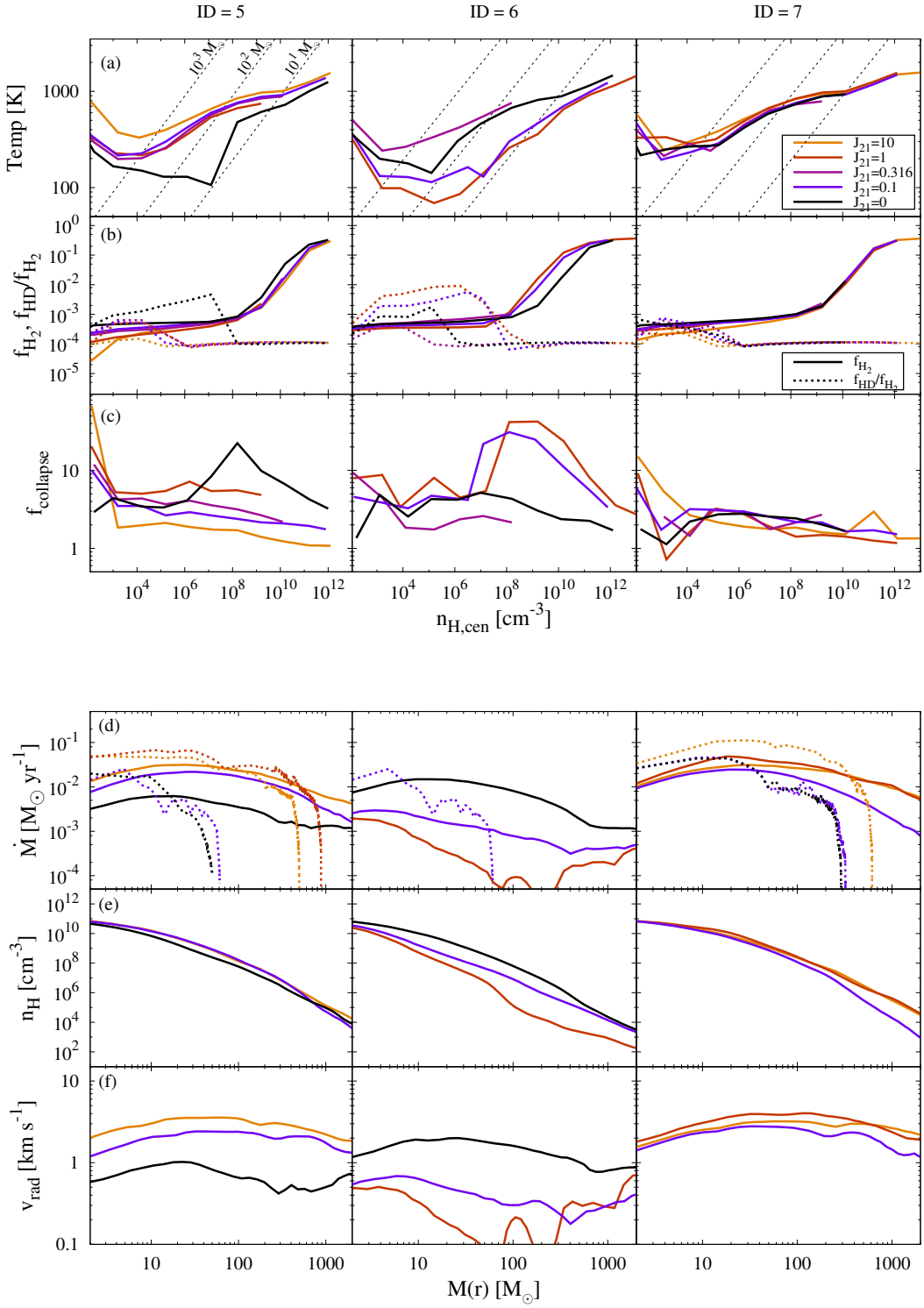

Figure E.2. Same as Figures 2.19 and 2.20 for ID = 5, 6, and 7 cases.

Acknowledgments

I express my sincere gratitude to my supervisor Hideyuki Umeda, who has introduced me to this research field and let me tackle on problems by his tenacious schooling during my Ph.D. course. I would like to thank the main collaborators Naoki Yoshida and Takashi Hosokawa, who teach me the cosmological simulation and protostellar simulation. Their great perspective on the field has kept correctly the progress of this study and discussions with them motivates the daily calculations. This work is finished with the help of other collaborators, Kazuyuki Omukai, Gen Chiaki, and Harold W. Yorke, whose wisdom and pointed indication polish the overall discussion of the study. I also thank Masahiro N. Machida, Kenji Hasegawa, Ikko Shimizu, Kei Tanaka, Kohei Inayoshi, and Sanemichi Z. Takahashi for stimulating discussions and Ralf S. Klessen, Paul C. Clark, and Thomas H. Greif for helpful comments on this study. I would like to thank the examiners, Yuzuru Yoshii (chief), Tomonori Totani, Masami Oouchi, Masayuki Umemura, and Hajime Susa for their indications which improve the quality of this thesis.

I spent my five year Ph.D. course in Hongo campus of the University of Tokyo and I would like to thank all the members of the Department of Astronomy for their supports and every discussions. In particular, I express special thanks to my laboratory members. All workshops and colloquium I participated in were exciting and educational. Also, I get a lot of assistance from the members of the University of Tokyo Theoretical Astrophysics (UTAP). The experience of oral and poster presentations and discussions with researchers broadened my perspective in the astronomy. Again, I express thanks to all for experiences during my doctor course.

Finally, I would like to thank my family for their understanding and continuous support during my life.

The numerical calculations were in part carried out on Cray XT4, XC30, and the general-purpose PC farm at Center for Computational Astrophysics (CfCA) of National Astronomical Observatory of Japan, T2K-Tsukuba System at Center for Computational Sciences, University of Tsukuba, and SR16000 at YITP in Kyoto University. All the figures are generated by Gnuplot [*1], PGPLOT [*2], VisIt [*3], and Oosawa [*4]. The work is supported in part by the Global COE Program "The Physical Sciences Frontier," MEXT, Japan, and Grant-in-Aid for JSPS Fellows.

[*1] http://www.gnuplot.info/
[*2] http://www.astro.caltech.edu/ tjp/pgplot/
[*3] https://wci.llnl.gov/simulation/computer-codes/visit/
[*4] http://qcganime.web.fc2.com/OOSAWA/oosawaE.html

Bibliography

Abel, T., Anninos, P., Zhang, Y. & Norman, M. L. (1997). *Modeling primordial gas in numerical cosmology.* Nature, **2**, 181–207.

Abel, T., Bryan, G. L. & Norman, M. L. (2002). *The Formation of the First Star in the Universe.* Science, **295**, 93–98.

Agarwal, B., Khochfar, S., Johnson, J. L., Neistein, E., Dalla Vecchia, C. & Livio, M. (2012). *Ubiquitous seeding of supermassive black holes by direct collapse.* Monthly Notices of the Royal Astronomical Society, **425**, 2854–2871.

Alpher, R. A., Bethe, H. & Gamow, G. (1948). *The Origin of Chemical Elements.* Physical Review **73**, 803–804.

Alvarez, M. A., Bromm, V. & Shapiro, P. R. (2006). *The* $\mathrm{H_{II}}$ *Region of the First Star.* The Astrophysical Journal, **639**, 621–632.

Aoki, W., Tominaga, N., Beers, T. C., Honda, S. & Lee, Y. S. (2014). *A chemical signature of first-generation very massive stars.* Science, **345**, 912–915.

Barkana, R. & Loeb, A. (2001). *In the beginning: the first sources of light and the reionization of the universe.* Physics Reports **349**, 125–238.

Barkana, R. & Loeb, A. (2007). *The physics and early history of the intergalactic medium.* Reports on Progress in Physics **70**, 627–657.

Barkat, Z., Rakavy, G. & Sack, N. (1967). *Dynamics of Supernova Explosion Resulting from Pair Formation.* Physical Review Letters **18**, 379–381.

Barsuhn, J. (1977). *Molecular and thermal equilibrium in low density interstellar clouds. I - The chemical reaction network.* Astronomy & Astrophysics, **28**, 453–461.

Bond, J. R., Arnett, W. D. & Carr, B. J. (1984). *The evolution and fate of Very Massive Objects.* The Astrophysical Journal, **280**, 825–847.

Bouwens, R. J., Illingworth, G. D., Labbe, I., Oesch, P. A., Trenti, M., Carollo, C. M., van Dokkum, P. G., Franx, M., Stiavelli, M., González, V., Magee, D. & Bradley, L. (2011). *A candidate redshift z˜10 galaxy and rapid changes in that population at an age of 500Myr.* Nature, **469**, 504–507.

Bovino, S., Latif, M. A., Grassi, T. & Schleicher, D. R. G. (2014). *Dark-matter halo mergers as a fertile environment for low-mass Population III star formation.* Monthly Notices of the Royal Astronomical Society, **441**, 2181–2187.

Bromm, V. (2013). *Formation of the first stars.* Reports on Progress in Physics **76**(11), 112901.

Bromm, V., Coppi, P. S. & Larson, R. B. (2002). *The Formation of the First Stars. I. The Primordial Star-forming Cloud.* The Astrophysical Journal, **564**, 23–51.

Bromm, V. & Loeb, A. (2004). *Accretion onto a primordial protostar.* Nature, **9**, 353–364.

Bromm, V. & Yoshida, N. (2011). *The First Galaxies.* Annual Review of Astronomy & Astrophysics, **49**, 373–407.

Bromm, V., Yoshida, N., Hernquist, L. & McKee, C. F. (2009). *The formation of the first stars and galaxies.* Nature, **459**, 49–54.

Bullock, J. S., Dekel, A., Kolatt, T. S., Kravtsov, A. V., Klypin, A. A., Porciani, C. & Primack, J. R. (2001). *A Universal Angular Momentum Profile for Galactic Halos.* The Astrophysical Journal, **555**, 240–257.

Burbidge, E. M., Burbidge, G. R., Fowler, W. A. & Hoyle, F. (1957). *Synthesis of the Elements in Stars.* Reviews of Modern Physics **29**, 547–650.

Caffau, E., Bonifacio, P., François, P., Sbordone, L., Monaco, L., Spite, M., Spite, F., Ludwig, H.-G., Cayrel, R., Zaggia, S., Hammer, F., Randich, S., Molaro, P. & Hill, V. (2011). *An extremely primitive star in the Galactic halo.* Nature, **477**, 67–69.

Capak, P., Faisst, A., Vieira, J. D., Tacchella, S., Carollo, M. & Scoville, N. Z. (2013). *Keck-I MOSFIRE Spectroscopy of the z ˜ 12 Candidate Galaxy UDFj-39546284.* The Astrophysical Journal, Letters, **773**, L14.

Cen, R. (1992). *A hydrodynamic approach to cosmology - Methodology.* The Astrophysical Journal, Supplement, **78**, 341–364.

Chatzopoulos, E. & Wheeler, J. C. (2012). *Effects of Rotation on the Minimum Mass of Primordial Progenitors of Pair-instability Supernovae.* The Astrophysical Journal, **748**, 42.

Chiaki, G., Yoshida, N. & Kitayama, T. (2013). *Low-mass Star Formation Triggered by Early Supernova Explosions.* The Astrophysical Journal, **762**, 50.

Ciardi, B. & Ferrara, A. (2005). *The First Cosmic Structures and Their Effects.* Space Science Reviews, **116**, 625–705.

Clark, P. C., Glover, S. C. O., Klessen, R. S. & Bromm, V. (2011a). *Gravitational Fragmentation in Turbulent Primordial Gas and the Initial Mass Function of Population III Stars.* The Astrophysical Journal, **727**, 110.

Clark, P. C., Glover, S. C. O., Smith, R. J., Greif, T. H., Klessen, R. S. & Bromm, V. (2011b). *The Formation and Fragmentation of Disks Around Primordial Protostars.* Science, **331**, 1040.

Coe, D., Zitrin, A., Carrasco, M., Shu, X., Zheng, W., Postman, M., Bradley, L., Koekemoer, A., Bouwens, R., Broadhurst, T., Monna, A., Host, O., Moustakas, L. A., Ford, H., Moustakas, J., van der Wel, A., Donahue, M., Rodney, S. A., Benítez, N., Jouvel, S., Seitz, S., Kelson, D. D. & Rosati, P. (2013). *CLASH: Three Strongly Lensed Images of a Candidate z ≈ 11 Galaxy.* The Astrophysical Journal, **762**, 32.

Cooke, R. J. & Madau, P. (2014). *Carbon-enhanced Metal-poor Stars: Relics from the Dark Ages.* The Astrophysical Journal, **791**, 116.

Coppola, C. M., Lodi, L. & Tennyson, J. (2011a). *Radiative cooling functions for*

primordial molecules. Monthly Notices of the Royal Astronomical Society, **415**, 487–493.

Coppola, C. M., Longo, S., Capitelli, M., Palla, F. & Galli, D. (2011b). *Vibrational Level Population of H_2 and H_2^+ in the Early Universe.* The Astrophysical Journal, Supplement, **193**, 7.

Cucchiara, A., Levan, A. J., Fox, D. B., Tanvir, N. R., Ukwatta, T. N., Berger, E., Krühler, T., Küpcü Yoldaş, A., Wu, X. F., Toma, K., Greiner, J., Olivares, F. E., Rowlinson, A., Amati, L., Sakamoto, T., Roth, K., Stephens, A., Fritz, A., Fynbo, J. P. U., Hjorth, J., Malesani, D., Jakobsson, P., Wiersema, K., O'Brien, P. T., Soderberg, A. M., Foley, R. J., Fruchter, A. S., Rhoads, J., Rutledge, R. E., Schmidt, B. P., Dopita, M. A., Podsiadlowski, P., Willingale, R., Wolf, C., Kulkarni, S. R. & D'Avanzo, P. (2011). *A Photometric Redshift of $z \sim 9.4$ for GRB 090429B.* The Astrophysical Journal, **736**, 7.

de Jong, T. (1972). *The Density of H2 Molecules in Dark Interstellar Clouds.* Astronomy & Astrophysics, **20**, 263.

de Souza, R. S., Ciardi, B., Maio, U. & Ferrara, A. (2013). *Dark matter halo environment for primordial star formation.* Monthly Notices of the Royal Astronomical Society, **428**, 2109–2117.

Ellis, R. S., McLure, R. J., Dunlop, J. S., Robertson, B. E., Ono, Y., Schenker, M. A., Koekemoer, A., Bowler, R. A. A., Ouchi, M., Rogers, A. B., Curtis-Lake, E., Schneider, E., Charlot, S., Stark, D. P., Furlanetto, S. R. & Cirasuolo, M. (2013). *The Abundance of Star-forming Galaxies in the Redshift Range 8.5-12: New Results from the 2012 Hubble Ultra Deep Field Campaign.* The Astrophysical Journal, Letters, **763**, L7.

Fan, X., Strauss, M. A., Schneider, D. P., Becker, R. H., White, R. L., Haiman, Z., Gregg, M., Pentericci, L., Grebel, E. K., Narayanan, V. K., Loh, Y.-S., Richards, G. T., Gunn, J. E., Lupton, R. H., Knapp, G. R., Ivezić, Ž., Brandt, W. N., Collinge, M., Hao, L., Harbeck, D., Prada, F., Schaye, J., Strateva, I., Zakamska, N., Anderson, S., Brinkmann, J., Bahcall, N. A., Lamb, D. Q., Okamura, S., Szalay, A. & York, D. G. (2003). *A Survey of z5.7 Quasars in the Sloan Digital Sky Survey. II. Discovery of Three Additional Quasars at z6.* The Astronomical Journal, **125**, 1649–1659.

Federrath, C., Sur, S., Schleicher, D. R. G., Banerjee, R. & Klessen, R. S. (2011). *A New Jeans Resolution Criterion for (M)HD Simulations of Self-gravitating Gas: Application to Magnetic Field Amplification by Gravity-driven Turbulence.* The Astrophysical Journal, **731**, 62.

Flower, D. R. & Harris, G. J. (2007). *Three-body recombination of hydrogen during primordial star formation.* Monthly Notices of the Royal Astronomical Society, **377**, 705–710.

Flower, D. R., Le Bourlot, J., Pineau des Forêts, G. & Roueff, E. (2000). *The cooling of astrophysical media by HD.* Monthly Notices of the Royal Astronomical Society, **314**, 753–758.

Forrey, R. C. (2013a). *Rate of Formation of Hydrogen Molecules by Three-body Recombination during Primordial Star Formation.* The Astrophysical Journal, Letters, **773**, L25.

Forrey, R. C. (2013b). *Sturmian theory of three-body recombination: Application to the formation of H_2 in primordial gas.* Physical Review A, **88**(5), 052709.

Frebel, A., Johnson, J. L. & Bromm, V. (2009). *The minimum stellar metallicity observable in the Galaxy.* Monthly Notices of the Royal Astronomical Society, **392**, L50–L54.

Fukugita, M. & Kawasaki, M. (1994). *Reionization during Hierarchical Clustering in a Universe Dominated by Cold Dark Matter.* Monthly Notices of the Royal Astronomical Society, **269**, 563.

Furlanetto, S. R., Oh, S. P. & Briggs, F. H. (2006). *Cosmology at low frequencies: The 21 cm transition and the high-redshift Universe.* Physics Reports **433**, 181–301.

Galli, D. & Palla, F. (1998). *The chemistry of the early Universe.* Astronomy & Astrophysics, **335**, 403–420.

Galli, D. & Palla, F. (2002). *Deuterium chemistry in the primordial gas.* Planetary Space Science, **50**, 1197–1204.

Galli, D. & Palla, F. (2013). *The Dawn of Chemistry.* Annual Review of Astronomy & Astrophysics, **51**, 163–206.

Gammie, C. F. (1996). *Layered Accretion in T Tauri Disks.* The Astrophysical Journal, **457**, 355.

Gao, L., White, S. D. M., Jenkins, A., Frenk, C. S. & Springel, V. (2005). *Early structure in ΛCDM.* Monthly Notices of the Royal Astronomical Society, **363**, 379–392.

Gao, L., Yoshida, N., Abel, T., Frenk, C. S., Jenkins, A. & Springel, V. (2007). *The first generation of stars in the Λ cold dark matter cosmology.* Monthly Notices of the Royal Astronomical Society, **378**, 449–468.

Glover, S. (2008). Chemistry and Cooling in Metal-Free and Metal-Poor Gas. In: *First Stars III* (O'Shea, B. W. & Heger, A., eds.), vol. 990 of *American Institute of Physics Conference Series.*

Glover, S. (2013). The First Stars. In: *Astrophysics and Space Science Library* (Wiklind, T., Mobasher, B. & Bromm, V., eds.), vol. 396 of *Astrophysics and Space Science Library.*

Glover, S. C. O. & Abel, T. (2008). *Uncertainties in H_2 and HD chemistry and cooling and their role in early structure formation.* Monthly Notices of the Royal Astronomical Society, **388**, 1627–1651.

Greif, T. H. (2014). *Multifrequency radiation hydrodynamics simulations of H_2 line emission in primordial, star-forming clouds.* Monthly Notices of the Royal Astronomical Society, **444**, 1566–1583.

Greif, T. H., Bromm, V., Clark, P. C., Glover, S. C. O., Smith, R. J., Klessen, R. S., Yoshida, N. & Springel, V. (2012). *Formation and evolution of primordial protostellar systems.* Monthly Notices of the Royal Astronomical Society, **424**, 399–415.

Greif, T. H., Springel, V. & Bromm, V. (2013). *On the operation of the chemoth-*

ermal instability in primordial star-forming clouds. Monthly Notices of the Royal Astronomical Society, **434**, 3408–3422.

Greif, T. H., Springel, V., White, S. D. M., Glover, S. C. O., Clark, P. C., Smith, R. J., Klessen, R. S. & Bromm, V. (2011a). *Simulations on a Moving Mesh: The Clustered Formation of Population III Protostars.* The Astrophysical Journal, **737**, 75.

Greif, T. H., White, S. D. M., Klessen, R. S. & Springel, V. (2011b). *The Delay of Population III Star Formation by Supersonic Streaming Velocities.* The Astrophysical Journal, **736**, 147.

Haiman, Z., Thoul, A. A. & Loeb, A. (1996). *Cosmological Formation of Low-Mass Objects.* The Astrophysical Journal, **464**, 523.

Hanawa, T. & Matsumoto, T. (2000). *Stability of a Dynamically Collapsing Gas Sphere.* Publications of the Astronomical Society of Japan, **52**, 241.

Hartwig, T., Clark, P. C., Glover, S. C. O., Klessen, R. S. & Sasaki, M. (2014). *A new approach to determine optically thick H_2 cooling and its effect on primordial star formation.* ArXiv e-prints .

Hattori, K., Yoshii, Y., Beers, T. C., Carollo, D. & Lee, Y. S. (2014). *Possible Evidence for Metal Accretion onto the Surfaces of Metal-poor Main-sequence Stars.* The Astrophysical Journal, **784**, 153.

Heger, A. & Woosley, S. E. (2002). *The Nucleosynthetic Signature of Population III.* The Astrophysical Journal, **567**, 532–543.

Hirano, S., Hosokawa, T., Yoshida, N., Umeda, H., Omukai, K., Chiaki, G. & Yorke, H. W. (2014). *One Hundred First Stars: Protostellar Evolution and the Final Masses.* The Astrophysical Journal, **781**, 60.

Hirano, S., Umeda, H. & Yoshida, N. (2011). *Evolution of Primordial Stars Powered by Dark Matter Annihilation up to the Main-sequence Stage.* The Astrophysical Journal, **736**, 58.

Hirano, S. & Yoshida, N. (2013). *Radiative Cooling Implementations in Simulations of Primordial Star Formation.* The Astrophysical Journal, **763**, 52.

Hollenbach, D. & McKee, C. F. (1979). *Molecule formation and infrared emission in fast interstellar shocks. I Physical processes.* The Astrophysical Journal, Supplement, **41**, 555–592.

Hosokawa, T. & Omukai, K. (2009). *Evolution of Massive Protostars with High Accretion Rates.* The Astrophysical Journal, **691**, 823–846.

Hosokawa, T., Omukai, K. & Yorke, H. W. (2012a). *Rapidly Accreting Supergiant Protostars: Embryos of Supermassive Black Holes?* The Astrophysical Journal, **756**, 93.

Hosokawa, T., Omukai, K., Yoshida, N. & Yorke, H. W. (2011). *Protostellar Feedback Halts the Growth of the First Stars in the Universe.* Science, **334**, 1250.

Hosokawa, T., Yorke, H. W., Inayoshi, K., Omukai, K. & Yoshida, N. (2013). *Formation of Primordial Supermassive Stars by Rapid Mass Accretion.* The Astrophysical Journal, **778**, 178.

Hosokawa, T., Yoshida, N., Omukai, K. & Yorke, H. W. (2012b). *Protostellar Feedback and Final Mass of the Second-generation Primordial Stars.* The Astrophysical Journal, Letters, **760**, L37.

Hoyle, F. (1946). *The synthesis of the elements from hydrogen.* Monthly Notices of the Royal Astronomical Society, **106**, 343.

Hui, L. & Gnedin, N. Y. (1997). *Equation of state of the photoionized intergalactic medium.* Monthly Notices of the Royal Astronomical Society, **292**, 27.

Johnson, J. L., Dalla, V. C. & Khochfar, S. (2013). *The First Billion Years project: the impact of stellar radiation on the co-evolution of Populations II and III.* Monthly Notices of the Royal Astronomical Society, **428**, 1857–1872.

Johnson, J. L., Greif, T. H. & Bromm, V. (2007). *Local Radiative Feedback in the Formation of the First Protogalaxies.* The Astrophysical Journal, **665**, 85–95.

Karlsson, T., Bromm, V. & Bland-Hawthorn, J. (2013). *Pregalactic metal enrichment: The chemical signatures of the first stars.* Reviews of Modern Physics **85**, 809–848.

Kashlinsky, A., Arendt, R. G., Mather, J. & Moseley, S. H. (2005). *Tracing the first stars with fluctuations of the cosmic infrared background.* Nature, **438**, 45–50.

Keller, S. C., Bessell, M. S., Frebel, A., Casey, A. R., Asplund, M., Jacobson, H. R., Lind, K., Norris, J. E., Yong, D., Heger, A., Magic, Z., da Costa, G. S., Schmidt, B. P. & Tisserand, P. (2014). *A single low-energy, iron-poor supernova as the source of metals in the star SMSS J031300.36-670839.3.* Nature, **506**, 463–466.

Kitayama, T., Yoshida, N., Susa, H. & Umemura, M. (2004). *The Structure and Evolution of Early Cosmological H II Regions.* The Astrophysical Journal, **613**, 631–645.

Kitsionas, S. & Whitworth, A. P. (2002). *Smoothed Particle Hydrodynamics with particle splitting, applied to self-gravitating collapse.* Monthly Notices of the Royal Astronomical Society, **330**, 129–136.

Komatsu, E., Dunkley, J., Nolta, M. R., Bennett, C. L., Gold, B., Hinshaw, G., Jarosik, N., Larson, D., Limon, M., Page, L., Spergel, D. N., Halpern, M., Hill, R. S., Kogut, A., Meyer, S. S., Tucker, G. S., Weiland, J. L., Wollack, E. & Wright, E. L. (2009). *Five-Year Wilkinson Microwave Anisotropy Probe Observations: Cosmological Interpretation.* The Astrophysical Journal, Supplement, **180**, 330–376.

Komatsu, E., Smith, K. M., Dunkley, J., Bennett, C. L., Gold, B., Hinshaw, G., Jarosik, N., Larson, D., Nolta, M. R., Page, L., Spergel, D. N., Halpern, M., Hill, R. S., Kogut, A., Limon, M., Meyer, S. S., Odegard, N., Tucker, G. S., Weiland, J. L., Wollack, E. & Wright, E. L. (2011). *Seven-year Wilkinson Microwave Anisotropy Probe (WMAP) Observations: Cosmological Interpretation.* The Astrophysical Journal, Supplement, **192**, 18.

Larson, D., Dunkley, J., Hinshaw, G., Komatsu, E., Nolta, M. R., Bennett, C. L., Gold, B., Halpern, M., Hill, R. S., Jarosik, N., Kogut, A., Limon,

M., Meyer, S. S., Odegard, N., Page, L., Smith, K. M., Spergel, D. N., Tucker, G. S., Weiland, J. L., Wollack, E. & Wright, E. L. (2011). *Seven-year Wilkinson Microwave Anisotropy Probe (WMAP) Observations: Power Spectra and WMAP-derived Parameters.* The Astrophysical Journal, Supplement, **192**, 16.

Li, Y., Hernquist, L., Robertson, B., Cox, T. J., Hopkins, P. F., Springel, V., Gao, L., Di Matteo, T., Zentner, A. R., Jenkins, A. & Yoshida, N. (2007). *Formation of z˜6 Quasars from Hierarchical Galaxy Mergers.* The Astrophysical Journal, **665**, 187–208.

Lipovka, A., Núñez-López, R. & Avila-Reese, V. (2005). *The cooling function of HD molecule revisited.* Monthly Notices of the Royal Astronomical Society, **361**, 850–854.

Lucy, L. B. (1977). *A numerical approach to the testing of the fission hypothesis.* The Astronomical Journal, **82**, 1013–1024.

Machida, M. N. & Doi, K. (2013). *The formation of Population III stars in gas accretion stage: effects of magnetic fields.* Monthly Notices of the Royal Astronomical Society, **435**, 3283–3305.

Machida, M. N., Omukai, K. & Matsumoto, T. (2010). Magnetohydrodynamics of Population III Star Formation. In: *American Institute of Physics Conference Series* (Whalen, D. J., Bromm, V. & Yoshida, N., eds.), vol. 1294 of *American Institute of Physics Conference Series.*

Machida, M. N., Omukai, K., Matsumoto, T. & Inutsuka, S.-i. (2008). *Conditions for the Formation of First-Star Binaries.* The Astrophysical Journal, **677**, 813–827.

Maio, U., Khochfar, S., Johnson, J. L. & Ciardi, B. (2011). *The interplay between chemical and mechanical feedback from the first generation of stars.* Monthly Notices of the Royal Astronomical Society, **414**, 1145–1157.

Matsuda, T., Satō, H. & Takeda, H. (1969). *Cooling of Pre-Galactic Gas Clouds by Hydrogen Molecule.* Progress of Theoretical Physics **42**, 219–233.

Matsumoto, T., Seo, H. J., Jeong, W.-S., Lee, H. M., Matsuura, S., Matsuhara, H., Oyabu, S., Pyo, J. & Wada, T. (2011). *AKARI Observation of the Fluctuation of the Near-infrared Background.* The Astrophysical Journal, **742**, 124.

McGreer, I. D. & Bryan, G. L. (2008). *The Impact of HD Cooling on the Formation of the First Stars.* The Astrophysical Journal, **685**, 8–20.

McKee, C. F. & Tan, J. C. (2008). *The Formation of the First Stars. II. Radiative Feedback Processes and Implications for the Initial Mass Function.* The Astrophysical Journal, **681**, 771–797.

Meiksin, A. A. (2009). *The physics of the intergalactic medium.* Reviews of Modern Physics **81**, 1405–1469.

Monaghan, J. J. (2005). *Smoothed particle hydrodynamics.* Reports on Progress in Physics **68**, 1703–1759.

Mortlock, D. J., Warren, S. J., Venemans, B. P., Patel, M., Hewett, P. C., McMahon, R. G., Simpson, C., Theuns, T., Gonzáles-Solares, E. A., Adamson, A., Dye, S., Hambly, N. C., Hirst, P., Irwin, M. J., Kuiper, E.,

Lawrence, A. & Röttgering, H. J. A. (2011). *A luminous quasar at a redshift of z = 7.085.* Nature, **474**, 616–619.

Omukai, K. (2000). *Protostellar Collapse with Various Metallicities.* The Astrophysical Journal, **534**, 809–824.

Omukai, K. (2001). *Primordial Star Formation under Far-Ultraviolet Radiation.* The Astrophysical Journal, **546**, 635–651.

Omukai, K. & Inutsuka, S.-i. (2002). *An upper limit on the mass of a primordial star due to the formation of an Hii region: the effect of ionizing radiation force.* Monthly Notices of the Royal Astronomical Society, **332**, 59–64.

Omukai, K. & Nishi, R. (1998). *Formation of Primordial Protostars.* The Astrophysical Journal, **508**, 141–150.

Omukai, K. & Palla, F. (2001). *On the Formation of Massive Primordial Stars.* The Astrophysical Journal, Letters, **561**, L55–L58.

Omukai, K. & Palla, F. (2003). *Formation of the First Stars by Accretion.* The Astrophysical Journal, **589**, 677–687.

Omukai, K. & Yoshii, Y. (2003). *The Mass Spectrum of Metal-free Stars Resulting from Photodissociation Feedback: A Scenario for the Formation of Low-Mass Population III Stars.* The Astrophysical Journal, **599**, 746–758.

O'Shea, B. W. & Norman, M. L. (2007). *Population III Star Formation in a ΛCDM Universe. I. The Effect of Formation Redshift and Environment on Protostellar Accretion Rate.* The Astrophysical Journal, **654**, 66–92.

O'Shea, B. W. & Norman, M. L. (2008). *Population III Star Formation in a ΛCDM Universe. II. Effects of a Photodissociating Background.* The Astrophysical Journal, **673**, 14–33.

Palla, F., Salpeter, E. E. & Stahler, S. W. (1983). *Primordial star formation - The role of molecular hydrogen.* The Astrophysical Journal, **271**, 632–641.

Peters, T., Klessen, R. S., Mac Low, M.-M. & Banerjee, R. (2010). *Limiting Accretion onto Massive Stars by Fragmentation-induced Starvation.* The Astrophysical Journal, **725**, 134–145.

Planck Collaboration, Ade, P. A. R., Aghanim, N., Armitage-Caplan, C., Arnaud, M., Ashdown, M., Atrio-Barandela, F., Aumont, J., Baccigalupi, C., Banday, A. J. & et al. (2014). *Planck 2013 results. XVI. Cosmological parameters.* Astronomy & Astrophysics, **571**, A16.

Prieto, J., Jimenez, R. & Martí, J. (2012). *Dark matter merging induced turbulence as an efficient engine for gas cooling.* Monthly Notices of the Royal Astronomical Society, **419**, 3092–3108.

Prieto, J., Jimenez, R. & Verde, L. (2014). *Overcooled haloes at $z \geq 10$: a route to form low-mass first stars.* Monthly Notices of the Royal Astronomical Society, **437**, 2320–2327.

Reed, D. S., Bower, R., Frenk, C. S., Jenkins, A. & Theuns, T. (2007). *The halo mass function from the dark ages through the present day.* Monthly Notices of the Royal Astronomical Society, **374**, 2–15.

Rees, M. J. (1999). The end of the 'dark age'. In: *After the Dark Ages: When Galaxies were Young (the Universe at 2 < Z < 5)* (Holt, S. & Smith, E., eds.), vol. 470 of *American Institute of Physics Conference Series*.

Ripamonti, E. (2007). *The role of HD cooling in primordial star formation.* Monthly Notices of the Royal Astronomical Society, **376**, 709–718.

Ripamonti, E. & Abel, T. (2004). *Fragmentation and the formation of primordial protostars: the possible role of collision-induced emission.* Monthly Notices of the Royal Astronomical Society, **348**, 1019–1034.

Ripamonti, E., Haardt, F., Ferrara, A. & Colpi, M. (2002). *Radiation from the first forming stars.* Monthly Notices of the Royal Astronomical Society, **334**, 401–418.

Ritter, J. S., Safranek-Shrader, C., Gnat, O., Milosavljević, M. & Bromm, V. (2012). *Confined Population III Enrichment and the Prospects for Prompt Second-generation Star Formation.* The Astrophysical Journal, **761**, 56.

Robertson, B. E., Ellis, R. S., Dunlop, J. S., McLure, R. J. & Stark, D. P. (2010). *Early star-forming galaxies and the reionization of the Universe.* Nature, **468**, 49–55.

Sabano, Y. & Yoshii, Y. (1977). *Thermal Instability in a Pre-Galactic Gas Cloud.* Publications of the Astronomical Society of Japan, **29**, 207–220.

Saigo, K., Tomisaka, K. & Matsumoto, T. (2008). *Evolution of First Cores and Formation of Stellar Cores in Rotating Molecular Cloud Cores.* The Astrophysical Journal, **674**, 997–1014.

Salvaterra, R., Della Valle, M., Campana, S., Chincarini, G., Covino, S., D'Avanzo, P., Fernández-Soto, A., Guidorzi, C., Mannucci, F., Margutti, R., Thöne, C. C., Antonelli, L. A., Barthelmy, S. D., de Pasquale, M., D'Elia, V., Fiore, F., Fugazza, D., Hunt, L. K., Maiorano, E., Marinoni, S., Marshall, F. E., Molinari, E., Nousek, J., Pian, E., Racusin, J. L., Stella, L., Amati, L., Andreuzzi, G., Cusumano, G., Fenimore, E. E., Ferrero, P., Giommi, P., Guetta, D., Holland, S. T., Hurley, K., Israel, G. L., Mao, J., Markwardt, C. B., Masetti, N., Pagani, C., Palazzi, E., Palmer, D. M., Piranomonte, S., Tagliaferri, G. & Testa, V. (2009). *GRB090423 at a redshift of z˜8.1.* Nature, **461**, 1258–1260.

Santos, M. R., Bromm, V. & Kamionkowski, M. (2002). *The contribution of the first stars to the cosmic infrared background.* Monthly Notices of the Royal Astronomical Society, **336**, 1082–1092.

Savin, D. W. (2002). *Rate Coefficients for D(1s)+H^+ rightleftarrow D^++H(1s) Charge Transfer and Some Astrophysical Implications.* The Astrophysical Journal, **566**, 599–603.

Savin, D. W., Brickhouse, N. S., Cowan, J. J., Drake, R. P., Federman, S. R., Ferland, G. J., Frank, A., Gudipati, M. S., Haxton, W. C., Herbst, E., Profumo, S., Salama, F., Ziurys, L. M. & Zweibel, E. G. (2012). *The impact of recent advances in laboratory astrophysics on our understanding of the cosmos.* Reports on Progress in Physics **75**(3), 036901.

Schaerer, D. (2002). *On the properties of massive Population III stars and metal-free stellar populations.* Astronomy & Astrophysics, **382**, 28–42.

Schleicher, D. R. G., Galli, D., Palla, F., Camenzind, M., Klessen, R. S., Bartelmann, M. & Glover, S. C. O. (2008). *Effects of primordial chemistry on the cosmic microwave background.* Astronomy & Astrophysics, **490**, 521–535.

Seager, S., Sasselov, D. D. & Scott, D. (1999). *A New Calculation of the Recombination Epoch.* The Astrophysical Journal, Letters, **523**, L1–L5.

Seager, S., Sasselov, D. D. & Scott, D. (2000). *How Exactly Did the Universe Become Neutral?* The Astrophysical Journal, Supplement, **128**, 407–430.

Shakura, N. I. & Sunyaev, R. A. (1973). *Black holes in binary systems. Observational appearance.* Astronomy & Astrophysics, **24**, 337–355.

Shapiro, P. R. & Kang, H. (1987). *Hydrogen molecules and the radiative cooling of pregalactic shocks.* The Astrophysical Journal, **318**, 32–65.

Shchekinov, Y. A. & Vasiliev, E. O. (2006). *Formation of HD molecules in merging dark matter haloes.* Monthly Notices of the Royal Astronomical Society, **368**, 454–460.

Silk, J. (1983). *The first stars.* Monthly Notices of the Royal Astronomical Society, **205**, 705–718.

Smidt, J., Whalen, D. J., Chatzopoulos, E., Wiggins, B. K., Chen, K.-J., Kozyreva, A. & Even, W. (2014). *Finding the First Cosmic Explosions. IV. 90 - 140 M$_{\odot}$ Pair-Instability Supernovae.* ArXiv e-prints .

Smith, R. J., Iocco, F., Glover, S. C. O., Schleicher, D. R. G., Klessen, R. S., Hirano, S. & Yoshida, N. (2012). *Weakly Interacting Massive Particle Dark Matter and First Stars: Suppression of Fragmentation in Primordial Star Formation.* The Astrophysical Journal, **761**, 154.

Solomon, P. M. & Woolf, N. J. (1973). *Interstellar Deuterium: Chemical Fractionation.* The Astrophysical Journal, Letters, **180**, L89.

Spolyar, D., Bodenheimer, P., Freese, K. & Gondolo, P. (2009). *Dark Stars: A New Look at the First Stars in the Universe.* The Astrophysical Journal, **705**, 1031–1042.

Spolyar, D., Freese, K. & Gondolo, P. (2008). *Dark Matter and the First Stars: A New Phase of Stellar Evolution.* Physical Review Letters **100**(5), 051101.

Springel, V. (2005). *The cosmological simulation code GADGET-2.* Monthly Notices of the Royal Astronomical Society, **364**, 1105–1134.

Stacy, A. & Bromm, V. (2013). *Constraining the statistics of Population III binaries.* Monthly Notices of the Royal Astronomical Society, **433**, 1094–1107.

Stacy, A., Bromm, V. & Loeb, A. (2011a). *Effect of Streaming Motion of Baryons Relative to Dark Matter on the Formation of the First Stars.* The Astrophysical Journal, Letters, **730**, L1.

Stacy, A., Bromm, V. & Loeb, A. (2011b). *Rotation speed of the first stars.* Monthly Notices of the Royal Astronomical Society, **413**, 543–553.

Stacy, A., Greif, T. H. & Bromm, V. (2010). *The first stars: formation of binaries and small multiple systems.* Monthly Notices of the Royal Astronomical Society, **403**,

45–60.

Stacy, A., Greif, T. H. & Bromm, V. (2012a). *The first stars: mass growth under protostellar feedback.* Monthly Notices of the Royal Astronomical Society, **422**, 290–309.

Stacy, A., Greif, T. H., Klessen, R. S., Bromm, V. & Loeb, A. (2013). *Rotation and internal structure of Population III protostars.* Monthly Notices of the Royal Astronomical Society, .

Stacy, A., Pawlik, A. H., Bromm, V. & Loeb, A. (2012b). *Effect of Population III multiplicity on dark star formation.* Monthly Notices of the Royal Astronomical Society, **421**, 894–907.

Stahler, S. W., Palla, F. & Salpeter, E. E. (1986). *Primordial stellar evolution - The protostar phase.* The Astrophysical Journal, **302**, 590–605.

Stahler, S. W., Shu, F. H. & Taam, R. E. (1980). *The evolution of protostars. I - Global formulation and results.* The Astrophysical Journal, **241**, 637–654.

Stancil, P. C., Lepp, S. & Dalgarno, A. (1998). *The Deuterium Chemistry of the Early Universe.* The Astrophysical Journal, **509**, 1–10.

Sur, S., Federrath, C., Schleicher, D. R. G., Banerjee, R. & Klessen, R. S. (2012). *Magnetic field amplification during gravitational collapse - influence of turbulence, rotation and gravitational compression.* Monthly Notices of the Royal Astronomical Society, **423**, 3148–3162.

Sur, S., Schleicher, D. R. G., Banerjee, R., Federrath, C. & Klessen, R. S. (2010). *The Generation of Strong Magnetic Fields During the Formation of the First Stars.* The Astrophysical Journal, Letters, **721**, L134–L138.

Susa, H. (2013). *The Mass of the First Stars.* The Astrophysical Journal, **773**, 185.

Susa, H., Hasegawa, K. & Tominaga, N. (2014). *The Mass Spectrum of the First Stars.* The Astrophysical Journal, **792**, 32.

Takahashi, K., Umeda, H. & Yoshida, T. (2014). *Stellar Yields of Rotating First Stars. I. Yields of Weak Supernovae and Abundances of Carbon-enhanced Hyper-metal-poor Stars.* The Astrophysical Journal, **794**, 40.

Takahashi, S. Z., Inutsuka, S.-i. & Machida, M. N. (2013). *A Semi-analytical Description for the Formation and Gravitational Evolution of Protoplanetary Disks.* The Astrophysical Journal, **770**, 71.

Tanaka, M., Moriya, T. J. & Yoshida, N. (2013). *Detectability of high-redshift superluminous supernovae with upcoming optical and near-infrared surveys - II. Beyond $z = 6$.* Monthly Notices of the Royal Astronomical Society, **435**, 2483–2493.

Tanvir, N. R., Fox, D. B., Levan, A. J., Berger, E., Wiersema, K., Fynbo, J. P. U., Cucchiara, A., Krühler, T., Gehrels, N., Bloom, J. S., Greiner, J., Evans, P. A., Rol, E., Olivares, F., Hjorth, J., Jakobsson, P., Farihi, J., Willingale, R., Starling, R. L. C., Cenko, S. B., Perley, D., Maund, J. R., Duke, J., Wijers, R. A. M. J., Adamson, A. J., Allan, A., Bremer, M. N., Burrows, D. N., Castro-Tirado, A. J., Cavanagh, B., de Ugarte Postigo, A., Dopita, M. A., Fatkhullin, T. A., Fruchter, A. S., Foley, R. J., Gorosabel, J., Kennea, J., Kerr, T., Klose, S., Krimm, H. A., Komarova, V. N.,

Kulkarni, S. R., Moskvitin, A. S., Mundell, C. G., Naylor, T., Page, K., Penprase, B. E., Perri, M., Podsiadlowski, P., Roth, K., Rutledge, R. E., Sakamoto, T., Schady, P., Schmidt, B. P., Soderberg, A. M., Sollerman, J., Stephens, A. W., Stratta, G., Ukwatta, T. N., Watson, D., Westra, E., Wold, T. & Wolf, C. (2009). *A γ-ray burst at a redshift of $z \sim 8.2$.* Nature, **461**, 1254–1257.

Tegmark, M., Silk, J., Rees, M. J., Blanchard, A., Abel, T. & Palla, F. (1997). *How Small Were the First Cosmological Objects?* The Astrophysical Journal, **474**, 1.

Tominaga, N., Iwamoto, N. & Nomoto, K. (2014). *Abundance Profiling of Extremely Metal-poor Stars and Supernova Properties in the Early Universe.* The Astrophysical Journal, **785**, 98.

Toomre, A. (1964). *On the gravitational stability of a disk of stars.* The Astrophysical Journal, **139**, 1217–1238.

Trevisan, C. S. & Tennyson, J. (2002). *Calculated rates for the electron impact dissociation of molecular hydrogen, deuterium and tritium.* Plasma Physics and Controlled Fusion **44**, 1263–1276.

Tseliakhovich, D. & Hirata, C. (2010). *Relative velocity of dark matter and baryonic fluids and the formation of the first structures.* Physical Review D, **82**(8), 083520.

Tumlinson, J., Venkatesan, A. & Shull, J. M. (2004). *Nucleosynthesis, Reionization, and the Mass Function of the First Stars.* The Astrophysical Journal, **612**, 602–614.

Turk, M. J., Abel, T. & O'Shea, B. (2009). *The Formation of Population III Binaries from Cosmological Initial Conditions.* Science, **325**, 601.

Turk, M. J., Clark, P., Glover, S. C. O., Greif, T. H., Abel, T., Klessen, R. & Bromm, V. (2011). *Effects of Varying the Three-body Molecular Hydrogen Formation Rate in Primordial Star Formation.* The Astrophysical Journal, **726**, 55.

Turk, M. J., Oishi, J. S., Abel, T. & Bryan, G. L. (2012). *Magnetic Fields in Population III Star Formation.* The Astrophysical Journal, **745**, 154.

Uehara, H. & Inutsuka, S.-i. (2000). *Does Deuterium Enable the Formation of Primordial Brown Dwarfs?* The Astrophysical Journal, Letters, **531**, L91–L94.

Umeda, H. & Nomoto, K. (2003). *First-generation black-hole-forming supernovae and the metal abundance pattern of a very iron-poor star.* Nature, **422**, 871–873.

Umeda, H. & Nomoto, K. (2005). *Variations in the Abundance Pattern of Extremely Metal-Poor Stars and Nucleosynthesis in Population III Supernovae.* The Astrophysical Journal, **619**, 427–445.

Umeda, H., Yoshida, N., Nomoto, K., Tsuruta, S., Sasaki, M. & Ohkubo, T. (2009). *Early Black Hole formation by accretion of gas and dark matter.* Journal of Cosmology and Astroparticle Physics, **8**, 24.

Umemura, M., Susa, H., Hasegawa, K., Suwa, T. & Semelin, B. (2012). *Formation and radiative feedback of first objects and first galaxies.* Progress of Theoretical and Experimental Physics **2012**(1), 010000.

Vorobyov, E. I., DeSouza, A. L. & Basu, S. (2013). *The Burst Mode of Accretion*

in Primordial Protostars. The Astrophysical Journal, **768**, 131.

Wang, J. G. & Stancil, P. C. (2002). *Hydrogen Ion-Molecule Isotopomer Collisions: Charge Transfer and Rearrangement.* Physica Scripta Volume T **96**, 72.

Weinberg, S. (1977). *The first three minutes. A modern view of the origin of the universe.*

Whalen, D. J., Even, W., Frey, L. H., Smidt, J., Johnson, J. L., Lovekin, C. C., Fryer, C. L., Stiavelli, M., Holz, D. E., Heger, A., Woosley, S. E. & Hungerford, A. L. (2013a). *Finding the First Cosmic Explosions. I. Pair-instability Supernovae.* The Astrophysical Journal, **777**, 110.

Whalen, D. J., Joggerst, C. C., Fryer, C. L., Stiavelli, M., Heger, A. & Holz, D. E. (2013b). *Finding the First Cosmic Explosions. II. Core-collapse Supernovae.* The Astrophysical Journal, **768**, 95.

Whalen, D. J., Smidt, J., Even, W., Woosley, S. E., Heger, A., Stiavelli, M. & Fryer, C. L. (2014). *Finding the First Cosmic Explosions. III. Pulsational Pair-instability Supernovae.* The Astrophysical Journal, **781**, 106.

Willott, C. J., Delorme, P., Reylé, C., Albert, L., Bergeron, J., Crampton, D., Delfosse, X., Forveille, T., Hutchings, J. B., McLure, R. J., Omont, A. & Schade, D. (2010). *The Canada-France High-z Quasar Survey: Nine New Quasars and the Luminosity Function at Redshift 6.* The Astronomical Journal, **139**, 906–918.

Wise, J. H., Turk, M. J., Norman, M. L. & Abel, T. (2012). *The Birth of a Galaxy: Primordial Metal Enrichment and Stellar Populations.* The Astrophysical Journal, **745**, 50.

Wolcott-Green, J. & Haiman, Z. (2011). *Suppression of HD cooling in protogalactic gas clouds by Lyman-Werner radiation.* Monthly Notices of the Royal Astronomical Society, **412**, 2603–2616.

Wolcott-Green, J., Haiman, Z. & Bryan, G. L. (2011). *Photodissociation of H_2 in protogalaxies: modelling self-shielding in three-dimensional simulations.* Monthly Notices of the Royal Astronomical Society, **418**, 838–852.

Wong, W. Y., Moss, A. & Scott, D. (2008). *How well do we understand cosmological recombination?* Monthly Notices of the Royal Astronomical Society, **386**, 1023–1028.

Yoon, S.-C., Dierks, A. & Langer, N. (2012). *Evolution of massive Population III stars with rotation and magnetic fields.* Astronomy & Astrophysics, **542**, A113.

Yorke, H. W. (1986). *The dynamical evolution of H II regions - Recent theoretical developments.* Annual Review of Astronomy & Astrophysics, **24**, 49–87.

Yorke, H. W. & Bodenheimer, P. (1999). *The Formation of Protostellar Disks. III. The Influence of Gravitationally Induced Angular Momentum Transport on Disk Structure and Appearance.* The Astrophysical Journal, **525**, 330–342.

Yorke, H. W. & Kaisig, M. (1995). *Use of multiply nested grids for the solution of flux-limited radiation diffusion and hydrodynamics.* Computer Physics Communications **89**, 29–44.

Yorke, H. W. & Sonnhalter, C. (2002). *On the Formation of Massive Stars.* The Astrophysical Journal, **569**, 846–862.

Yoshida, N., Abel, T., Hernquist, L. & Sugiyama, N. (2003). *Simulations of Early Structure Formation: Primordial Gas Clouds.* The Astrophysical Journal, **592**, 645–663.

Yoshida, N., Oh, S. P., Kitayama, T. & Hernquist, L. (2007). *Early Cosmological H_{II}/He_{III} Regions and Their Impact on Second-Generation Star Formation.* The Astrophysical Journal, **663**, 687–707.

Yoshida, N., Omukai, K. & Hernquist, L. (2008). *Protostar Formation in the Early Universe.* Science, **321**, 669.

Yoshida, N., Omukai, K., Hernquist, L. & Abel, T. (2006). *Formation of Primordial Stars in a ΛCDM Universe.* The Astrophysical Journal, **652**, 6–25.

Yoshii, Y. (1981). *Metal enrichment in the atmospheres of extremely metal-deficient dwarf stars by accretion of interstellar matter.* Astronomy & Astrophysics, **97**, 280–290.

Zhu, Z., Hartmann, L. & Gammie, C. (2010a). *Long-term Evolution of Protostellar and Protoplanetary Disks. II. Layered Accretion with Infall.* The Astrophysical Journal, **713**, 1143–1158.

Zhu, Z., Hartmann, L., Gammie, C. F., Book, L. G., Simon, J. B. & Engelhard, E. (2010b). *Long-term Evolution of Protostellar and Protoplanetary Disks. I. Outbursts.* The Astrophysical Journal, **713**, 1134–1142.

Zinnecker, H. & Yorke, H. W. (2007). *Toward Understanding Massive Star Formation.* Annual Review of Astronomy & Astrophysics, **45**, 481–563.